Characterization and detection of traces of energetic materials by Nanocalorimetry

Nelly Piazzon

To cite this version:

Nelly Piazzon. Characterization and detection of traces of energetic materials by Nanocalorimetry. Other. Université de Haute Alsace - Mulhouse, 2010. English. NNT : 2010MULH5932 . tel-00702242

HAL Id: tel-00702242
https://theses.hal.science/tel-00702242
Submitted on 29 May 2012

FRENCH-GERMAN RESEARCH INSTITUTE OF SAINT-LOUIS

CHARACTERIZATION AND DETECTION OF TRACES OF ENERGETIC MATERIALS BY NANOCALORIMETRY

Nelly PIAZZON

MULHOUSE, 2010

THÈSE

Présentée pour obtenir le titre de

DOCTEUR DE L'UNIVERSITÉ DE HAUTE-ALSACE

spécialité :

Chimie des Matériaux

par

Nelly PIAZZON

Sujet :

Characterization and detection of traces of energetic materials by nanocalorimetry

Soutenue le 19 novembre 2010 devant le jury composé de :

Prof. C. POPESCU	Rapporteur	DWI an der RWTH e. V, Aachen, Germany
Prof. M. PYDA	Rapporteur	Rzeszow University of Technology, Poland
Dr. L. OLMEDO	Examinateur	CEA / Le Ripault, Monts, France
Dr. C. BARAS	Membre invité	ISL, Saint-Louis, France
Ing. D. DILHAN	Membre invité	CNES, Toulouse, France
Dr. D.A. IVANOV	Promoteur	IS2M, Mulhouse, France
Dr. D. SPITZER	Promoteur	ISL, Saint-Louis, France

Acknowledgments

First, I would like to thank my advisors Dr. Dimitri IVANOV and Dr. Denis SPITZER for sharing their knowledge, for their patience, for their encouragements, for giving me freedom in my research, for their trust. You were always present along these three years.

I would particularly thank Alexander BONDAR who has built the nanocalorimeter and who teaches me how to use it.

I would like to thank the members of my jury for reading this manuscript.

I would like to thank ISL for their financial support of my thesis.

It was a pleasure to share the office at IS2M with Guillaume COLOMBE, Yaroslav ODARCHENKO, Dr. Matthieu DEFAUX, Dr. Houssam HAMIE, Dr. Denis ANOKHIN and Dr. Martin ROSENTHAL.

I am grateful to my colleagues from ISL: Dr Sigo Scharnholtz and Frank SCHERRER for their help in white room, Michaël SCHÄFER, Fabien SCHNELL for SEM micrographs, Dr Lionel BORNE and Julien MORY for energetic material samples, Yves SUMA for fast CCD camera.
I am grateful to my colleagues from IS2M: Dr Loïc VIDAL for SEM micrographs, Simon GREE for electronic part.

I would like to thank especially Drs. Karine MOUGIN, Vincent PICHOT (poker master), Karine BONNOT Marc COMET and also Dominique HASSLER, Benny SIEGERT, Loïc SCHMIDLIN, Benedikt RISSE.

I wanted to finish with several personal thanks: my parents for their support to arrive where I am today, my brother. I would like to thank Patrice. I am grateful to my friends, especially Annie (…11…), Stella, Céline, Didier, Zhiqiang, Damien, Gaël, Sylvain and the poker team.

List of abbreviations, acronyms and symbols

Techniques

AFM	Atomic Force Microscopy
DSC	Differential Scanning Calorimetry
DIC	Differential Interference Contrast
EDX	Energy-Dispersive X-ray spectroscopy
FTIR	Fourier Transform Infrared spectroscopy
GC	Gas Chromatography
IMS	Ion Mobility Spectrometry
MDSC	Modulated Differential Scanning Calorimetry
MP-85	Micromanipulator MP-85 from Sutter Instruments
MS	Mass spectrometry
POM	Polarized Optical Microscopy
SAXS	Small-Angle X-ray Scattering
SEM	Scanning Electron Microscopy

Materials

CL-20	2,4,6,8,10,12-hexanitro-2,4,6,8,10,12-hexaazaisowurtzitane
NC	Nitrocellulose
NC11.9	Nitrocellulose with a nitrogen content of 11.9 %
NC12.5	Nitrocellulose with a nitrogen content of 12.5 %
NC13.49	Nitrocellulose with a nitrogen content of NC13.49 %
PETN	Penthrite = Pentaerythritol tetranitrate
RDX	Hexogen = Cyclotrimethylenetrinitramine = Cyclonite
TNT	Trinitrotoluene

Other notations

AC mode	Alternating Current mode
C_p	Heat capacity at constant pressure
DC mode	Direct Current mode
DS	Substitution Degree (for nitrocellulose)
HOPG	Highly Oriented Pyrolitic Graphite
k	Cantilever spring constant
LOD	Limit Of Detection
PID	Proportional Integral Differential Regulator
PSD	Power Spectral Density
Q’ or G	Heat exchange parameter
SAM	Signal Access Module
SAMs	Self-Assembled Monolayers
SR	Sampling Rate
TO-5	Transistor housing (obsolete) of nanocalorimetric chip from Xensor
Thtr	Heater temperature
Ttpl	Thermopile temperature
U_{tpl}	Voltage of the thermopile
XEN-3970	Nanocalorimetric chip from Xensor with an active area of 30x30 µm²
XEN-3971	Nanocalorimetric chip from Xensor with an active area of 60x60 µm²
XEN-3972	Nanocalorimetric chip from Xensor with an active area of 100x100 µm²
XEN-3977	Nanocalorimetric chip from Xensor with an active area of 62x62 µm² and with aluminium coating

Table of contents

1. Introduction

1.1. General background

Calorimetry is one of the main techniques of thermal analysis. Most of physical or chemical modifications of material are associated with thermal effects whereby heat is absorbed (i.e., endothermic phenomena such as melting) or released (i.e., exothermic phenomena such as crystallization or thermal decomposition). For such transitions, calorimetry allows determining the transition heats and temperatures.

Calorimetric experiments are most often performed with Differential Scanning Calorimetry (DSC), which measures the heat flux absorbed or released by the sample to follow the same heat program as the reference material. In these experiments, measurements are typically carried out on a few milligrams of sample. However, for many applications one has to handle nanograms or even picograms of sample. One of such applications is relevant to studies of materials which can release a significant amount of energy during their decomposition (energetic materials). The release of energy is obtained by mechanisms of intramolecular oxydoreduction. Different ways can trigger this release: heating the materials till the decomposition temperature, impact, friction. Moreover, calorimetry able to handle nanograms of sample could find potential applications in the field of explosives detection.

The temperature increase can initiate several phenomenon in energetic material, therefore the calorimetry is a good technique to characterize and to detect energetic materials such as nitrocellulose (NC), hexogen (RDX), 2,4,6,8,10,12-hexanitro-2,4,6,8,10,12-hexaazaisowurtzitane (CL-20) and penthrite (PETN).

The energetic materials detection by calorimetry has attracted quite some interest. Thus, a brief communication appeared in Nature, which was entitled “A microsensor for trinitrotoluene vapour”[1], is a proof of the scientific community interest. In the referenced work, the authors use a heated microcantilever to detect traces of TNT.

1.2. Calorimetry

This section describes the basics of DSC, the typical characteristics of a calorimeter and the main equations used to analyze the results of calorimetric experiments.

1.2.1. Introduction

Calorimetry measures the amount of energy exchanged in the form of a heat flow between two interacting systems over the experiment duration. Calorimeters can be classified according to the different characteristics such as[2] :

(a) Measuring principle:

  (i) Measurement of the energy required for compensation of a thermal effect (compensation calorimeters)

  (ii) Measurement of the temperature change of the calorimeter substance due to the thermal effect (temperature-changing calorimeters)

  (iii) Measurement of the heat exchange between calorimeter substance and surroundings (heat-exchanging calorimeters)

(b) Mode of operation:

  (i) Isothermal (the sample temperature remains constant: $\Delta T = 0$, the housing of the calorimeter stays in thermal contact with the environment)

  (ii) Isoperibolic (refers to calorimeter in contact with a constant temperature body/liquid)

  (iii) Adiabatic (no heat exchange with the environment)

(c) The principle of construction:

  (i) Single calorimeter

  (ii) Twin or differential calorimeter which uses two crucibles (the first one for reference and the second one for sample).

For **compensation calorimeters**, the electric energy is supplied separately to the sample and reference.

For **temperature-changing calorimeters**, the heat to be measured changes the temperature of the calorimeter substance with which the heat is exchanged. In this kind of calorimeter, the signal ΔT is maximized by decreasing the heat exchange with the environment.

For **heat-exchanging calorimeters**, the sample temperature changes (ΔT) are measured. ΔT is maximized by decreasing the heat exchange with the surroundings.

In the field of materials science, the most currently used DSC is the heat-flux DSCs which record the temperature difference between the sample and reference. The next section gives some basics on the DSC instrumentation and experiments.

1.2.2. Differential Scanning Calorimetry[3, 4]

Differential Scanning Calorimetry (DSC) allows measuring thermal properties of materials such as heat capacity at a constant pressure, enthalpies and temperatures of thermal transitions. In the field of materials science, the most commonly used DSC is the heat-flux DSCs which record the temperature difference between the sample and reference. In this study, one of the used calorimeters is a heat-flux calorimeter DSC 822E (Mettler-Toledo) shown on figure 1.

The essential of this technique lies in the measurement of the heat flux absorbed or released by the sample during execution of a thermal program defined by the user (heating and cooling ramps, or isothermal segments). In a heat flux calorimeter, the difference between the sample and reference temperatures is measured with the help of a thermal sensor array. The sample and reference are placed together in the measuring cell enclosed in a single furnace. The reference is typically chosen to be an inert material, which does not exhibit thermal transitions in the studied temperature range. In some cases, it can be an empty pan. Both sample and reference are placed on a thermal sensor disk having a good thermal conductivity. The thermal sensor array contains 56 (28+28) thermocouples connected in series. The heat exchange between the furnace and the sample is mainly due to the thermal sensor.

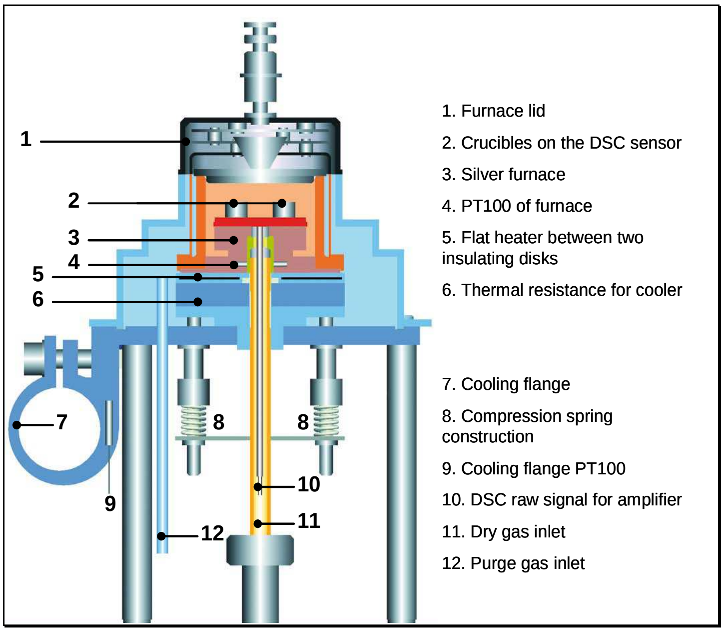

Figure 1. Schematic drawing of a Mettler-Toledo DSC measuring cell.[5] The thermal sensor array contains 56 (28+28) thermocouples. The absolute temperature probes (PT100) measure the temperature of the furnace and cooling flange.

When a thermal transition occurs in the sample, the associated heat release or absorption induces a change in the resulting heat flux between the sample (Φ_{fs}) and the furnace. The heat exchange between the furnace and the sample is mainly due to conduction across the thermal sensor. In the approximation of small heat fluxes, the measured signal ΔT

is proportional to the difference of the heat fluxes Φ_{fr} and Φ_{fs} from the furnace to the reference and from the furnace to the sample, respectively (cf. equation 1).

$$\Delta\Phi = \Phi_{fs} - \Phi_{fr} = -K.\Delta T \qquad (1)$$

The proportionality factor in equation (1) is determined during the system calibration. The preliminary calibration of the instrument was carried out using melting enthalpies and temperatures of indium and zinc.

1.2.3. Thermodynamic considerations

The enthalpy variation (dH) expresses the quantity of heat released or absorbed during transformation of a system at constant pressure:

$$\begin{aligned} &H = U + P.V \\ &dH = dU + P.dV + V.dP \\ &dH = dU + P.dV (2) \end{aligned}$$

As the pressure is constant, V.dP = 0.

The first law of thermodynamics says that the state of a system can be changed by allowing the system to do the mechanical work or to exchange heat with its surroundings. The work W (= -P.dV at constant pressure) and heat Q are the two possible forms of energy transfer, they determine the energy change dU of the system[2]:

$$\begin{aligned} &dU = Q + W \\ &dU\big|_P = Q - P.dV (3) \end{aligned}$$

By replacing dU in equation (2) by its expression (3), we obtain:

$$\delta Q\big|_P = dH$$

The heat capacity is defined as the temperature increase of a unit mass of substance as a result of supply of a unit of heat. At constant pressure, the heat capacity (C_p) is written as the partial derivative of enthalpy over temperature:

$$dH\big|_P = C_p.dT$$

The power given to the system corresponds to:

$$P = \frac{dH}{dt}\bigg|_P = C_P.\frac{dT}{dt}$$

This expression shows that the sensitivity of a calorimeter increases with the heating rate.

1.2.4. Characteristics of DSC

The efficiency of a DSC is described by five characteristics.

The **zero-line repeatability** describes the DSC behaviour without the sample.

The **noise** of the DSC is due to the heating rate, the temperature, the atmosphere and the electronics. In order to detect the smallest heat-flow rate for a given sample, it is crucial to have the highest signal-to-noise ratio.

The **system linearity** characterizes the functional relation between the measured signal Φ_m and the true reaction heat flux Φ_r determined through calibration. Usually the ratio Φ_r/Φ_m is represented as a function of the mass or the temperature.

The **time constant τ** is defined as the time interval necessary to reach 63.2%[6] of the temperature change after an abrupt thermal event.

Usually the measurements by DSC are performed with heating rates in the range of 1 to 40°C/min. It typically corresponds to a good compromise between the precision, resolution, sensitivity and measurement rate. In 2004, Mettler Toledo has built a new device – DSC822E – which allows to perform measurements with a maximum heating rate of 400 °C/min.[7] The use of high heating rates presents several advantages. For example, one can increase the signal intensity for small samples and for samples which exhibit low-enthalpy transitions. Also, in some instances the kinetically-controlled (such as cold crystallisation) can be suppressed. Experiments with high heating rates have some disadvantages: the temperature resolution is reduced, and it could be more difficult to separate peaks. High heating rates need higher final temperature because of the peak broadening, which may be problematic since the sample can be decomposed at these high temperatures. In the following part, we present a new technique of thermal analysis: the nanocalorimetry which allows achieving high heating rates (up to 10^6 °C/s) on small samples of a few nanograms.

1.3. Nanocalorimetry

In this section, we describe the design of a calorimetric sensor used in the measurements, some applications of Nanocalorimetry and operation modes of our home-built nanocalorimeter.

1.3.1. Introduction

The nanocalorimeter allows analyzing small amounts of materials (nanograms or picograms) such as thin films with thickness varying from a few nanometers to some microns. The heating and cooling rates employed are much higher than in the classical DSC: they are comprised between 10^3 and 10^6 °C/s [8,9,10,11]. As a result, the measurements performed by nanocalorimetry are really fast (i.e., on the order of a few milliseconds). Besides, the nanocalorimeter built in our lab can also perform experiments with the same heating rates as in the classical DSC.

1.3.2. Calorimetric sensor

The calorimetric sensor is built of a thin silicon-nitride membrane (900 x 900 x 1 µm, figure 2b) where the heating elements (in red and orange on figure 2c) and thermocouples (in violet on figure 2c) are assembled.

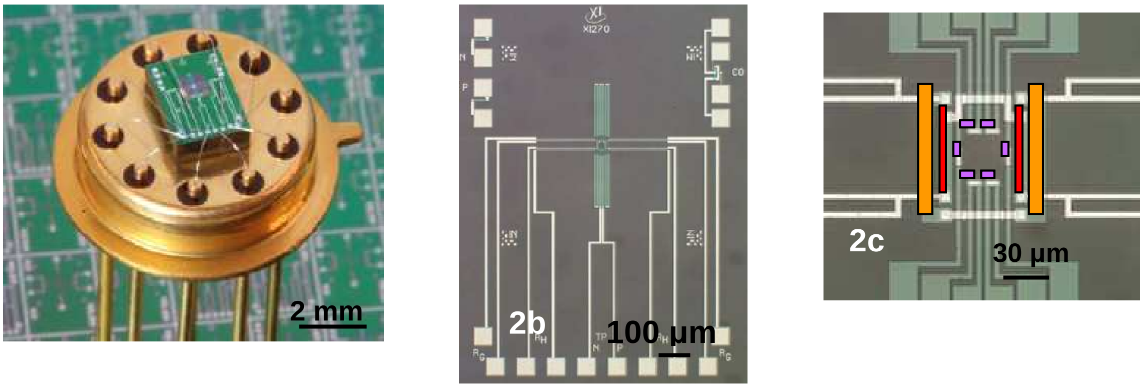

Figure 2. Calorimetric chip sensor from Xensor company (general view) and zoom on the suspended membrane and the active area.

The nanocalorimeter can perform experiments in the AC mode at classical heating rates like for the case of MDSC and experiments in the DC mode at fast heating rates: 10^3 to 10^6 °C/s[8, 11, 12]. The temperature modulation frequencies can be as high as 3.0-10.0 kHz. The heating rates can be reached thanks to the small membrane and sample sizes. Two internal heaters (in red on figure 2c) heat the sample during modulation experiments whereas two external heaters (in orange on figure 2c) are used during fast DC experiments. The six thermocouples (in violet on figure 2c) are connected in series in order to increase thermopile sensitivity to ca. 2 mV/K at 273 K.

The part of the sensor located between the thermocouples constitutes the active area or measurement area of the sensor. The thermopile measures the temperature difference between its cold junction and its hot junction. As shown on figure 3, the hot junction is placed on the active area whereas the cold junction is on the edge of the sensor housing. The dimensions of the active area vary from 14 x 14 µm² to 130 x 130 µm².

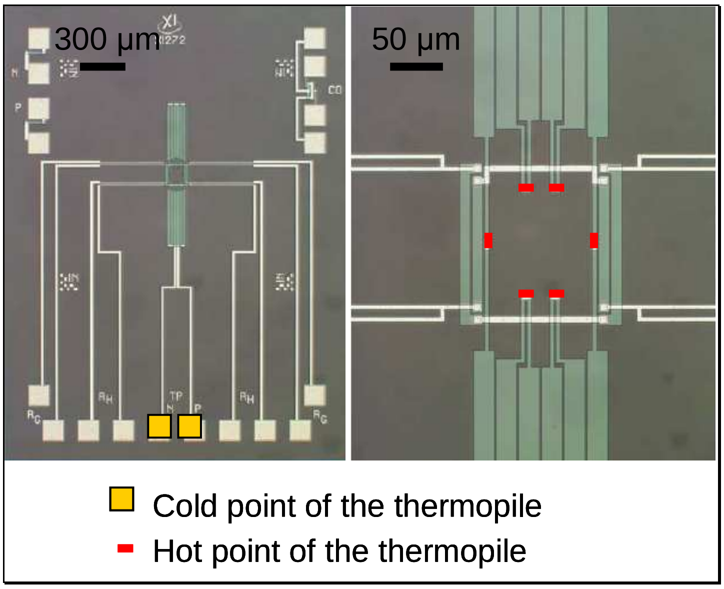

Figure 3. Hot and cold points of the thermopile.

The roughness of the membrane surface was measured by AFM (figure 4).

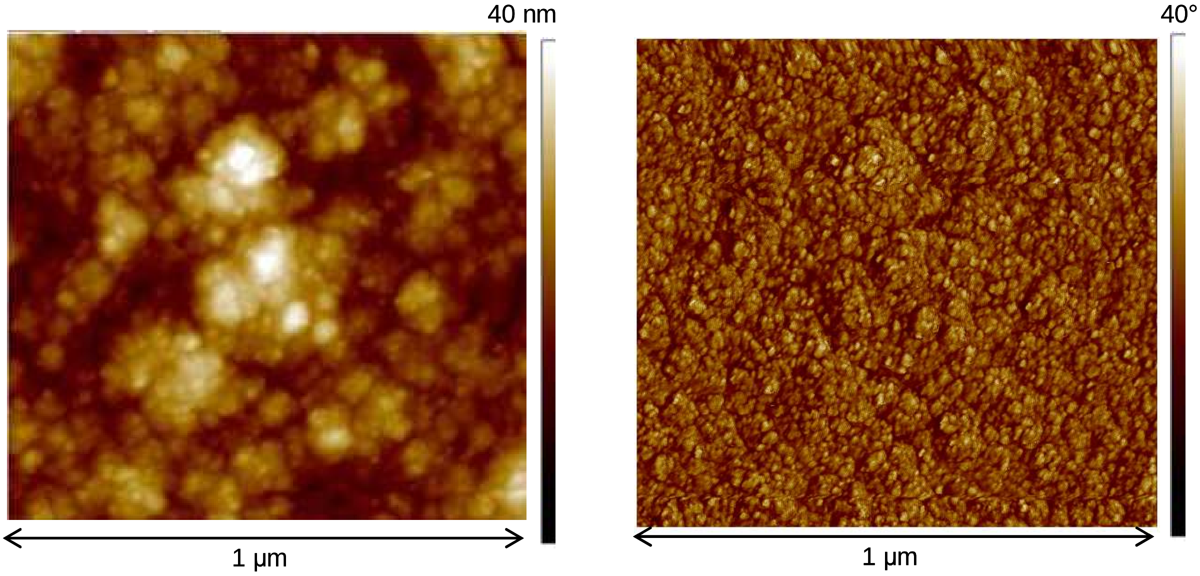

Figure 4. Tapping mode AFM, topographic and phase images of the sensor membrane (cf. the previous figure).

The average roughness (Ra) is 4 nm, Rq is equal to 4.94 nm and the maximal roughness is 35,6 nm.

1.3.3. State of art in Nanocalorimetry

In this section, we will describe different nanocalorimeter devices and different types of nanocalorimeter sensors. Afterwards, we will focus on some applications of nanocalorimetry.

- The nanocalorimeter devices: the nanocalorimetry was introduced by L.H. Allen et al. in 1993. The authors built this technique for thermal analysis of thin films and termed it electrical thermal annealing.[13] A MEMS sensor was developed as a calorimetric cell for differential scanning nanocalorimeter.[14] The schematics MEMS sensor is shown on figure 5. The sensor is an amorphous silicon nitride (SiN_x) membrane of 50 nm thick supported by a Si frame. A strip of platinum is used as a resistive heater and resistive thermometer. This Pt strip is 50 nm thick and 500 μm wide. The platinum is used because of the superior stability of its electrical resistance. Two voltage senses are made on the membrane in order to measure the voltage across the working part of heater. Four contact pads connected with the strip and the senses are used for electrical measurements on the sensor. The calorimetric cell is the region between the Pt strip and the SiN_x membrane directly beneath it. A non-conductive sample can be deposited on either the platinum or the silicon nitride surface whereas a conductive sample is placed on the silicon nitride side in order to not change the electrical properties of the heater/thermometer strip. A short pulse (1.5 – 16 ms) of electric current (20 – 100 mA) is applied to the Pt strip, the temperature of the calorimetric sensor and of the sample increase by Joule heating. The calorimeter sensitivity is 1 nJ/K [15].

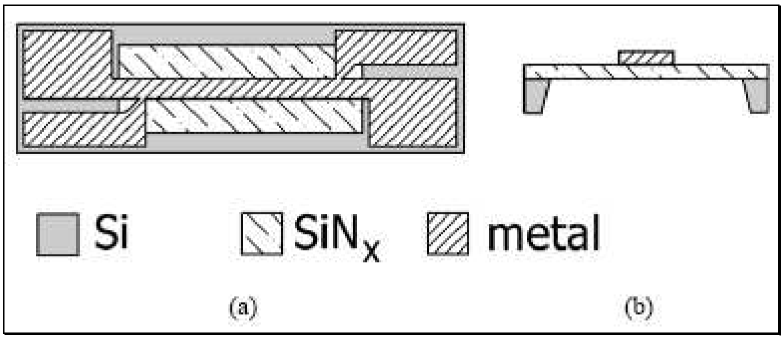

Figure 5. Schematics of a calorimetric chip sensor. View from top is shown in (a) and cross section in (b). Metallized area extends onto the Si frame in order that electrical connections can be made

Some nanocalorimeters can work in a frequency range covering two decades (0.06 to 15 Hz) and with high resolution. The sensors allow very low noise measurement (limited by Johnson noise in thermometer). The resolution on the heat capacity is ± 5.10^{-6} J/K which is less than the nanocalorimeter described before, the device allows the detection of a variation of ± 100 nJ/K, which represents an energy variation of ± 25 nJ for an amplitude of temperature oscillation of 0.25°C.[16] A cell measurement of 5 μL is employed to study biological samples.[17]

Another kind of nanocalorimeter was built, which is an advanced construction of a two-channel AC calorimeter for simultaneous measurements of frequency-dependent complex heat capacity C(ω) and complex thermal conductivity λ(ω). This technique was illustrated by the measurements of complex effusivity, diffusivity, heat capacity and thermal conductivity of glycerol in the glass transition region. The double-channel ac calorimetry can be used for relaxation processes related to relaxing thermal conductivity or relaxing heat capacity.[18]

One of the first calorimetric sensors commercialized by Xensor (TCG 3880) was used to perform fast heating and fast cooling in non-adiabatic conditions and in ambient gas atmosphere. The device reaches a maximum cooling rate of 10^3 °C/s. This rate can be increased by decreasing the cell-sample dimensions. Such nanocalorimeter had a sensitivity of 1 nJ/K and a time resolution of 5 ms.[19] The conditions to obtain a maximum cooling rate of 10^6 °C/s were optimized by using nanogram samples and other commercially sensors which have an active area in the range of 10 – 100 μm. The maximum cooling rate can be calculated with the following equation:

$$\left|\frac{dT}{dt}\right|_{\max} = \frac{(T_{\max} - T_t)G}{(C_S + C_A)}$$

where $T_{\max}$ is the maximum sample temperature, G is the heat exchange parameter, C_S is the sample heat capacity and C_A is the addenda heat capacity. For a disk-like sample with a thickness d_S, a radius r_0, a density ρ_0 and a specific heat capacity c_S, the maximum cooling rate is

$$V_{\max} \approx \frac{4(T_{\max} - T_t)\lambda_g}{r_0 d_S \rho_S c_S}$$

This equation shows that the cooling rate is inversely proportional to the radius of the active area of the sensor.[20] It is noteworthy that Nanocalorimetry is also used for studies at very low temperatures (from -273.10°C to 126.85°C) in physics of solid.[21]

At the moment, the maximum heating and cooling rates reach by a nanocalorimeter is 10^6 K/s with a sensitivity of 1 nJ/K.

In the next section, we are going to review some applications of nanocalorimetry in several fields such as studies of single particles, nanoparticles, polymers and thin-films.

- Applications of nanocalorimetry

The research with nanocalorimetry implies a multidisciplinary character because it covers a lot of different materials. Importantly, the fast cooling rates allow to prepare materials in nonequilibrium states. The amorphous state in metals, semiconductors or polymers can be thus reached with fast cooling rates up to 0.1 MK/s.

Single particles and nanoparticles

The cooling rate dependence of undercooling was studied for SnAgCu particles by fast scanning chip calorimetry. Particle size and cooling rates are crucial factors for the solidification. By using DSC, one need several mg (which represent a lot of particles) to be studied at once so the particle size distribution has to be taken in account. In this way, it is not easy to distinguish the influence of the cooling rate and particle size on the solidification process. By using chip calorimeter, it is possible to address solidification of a single micro-particles. The authors[22] observed that after several heating and cooling cycles the particles keep their spherical shape and do not wet the surface of the measurement area. The nanocalorimetry thus offers the possibility to study the size dependence of undercooling of single micro-particles.[22]

The size-dependent melting of Bi nanoparticles was also investigated by nanocalorimetry. As the fast calorimetric experiments are performed in situ with the Bi deposition, it is possible to perform calorimetry during the film growth. The melting point depression of nanoparticles was explained by Pawlov in 1909. This phenomenon is caused by the influence of the surface energy. At the nanoscale, the surface-to-volume ratio is very high whereas in bulk material, surfaces and interfaces usually have only a slight effect on the material properties.

The melting temperature of small particles is given as follows:

$$\Delta T = T_m^{bulk} - T_m(r) = \left(\frac{2T_m^{bulk}}{H_m^{bulk}\rho_S}\right)\left(\frac{\alpha}{r}\right) = \frac{A}{r}$$

where T_m^{bulk} is the melting temperature of the bulk, $T_m(r)$ is the size-dependent melting temperature, H_m^{bulk} is the fusion heat of the bulk, ρ_S is the solid phase density, r the particle radius, A is a constant, α depends on the melting model.

The nanocalorimetric experiments show that the particles smaller than 7 nm melt 50 K above the predicted temperature given by the equation. This difference is attributed to superheating due to suppression of surface melting. [23]

The melting of nanostructures (indium clusters on a SiN_x surface) was investigated by nanocalorimetry during the early stages of thin film growth. The nanostructures have a size in the range of 1000 to 10 000 atoms. Some discontinuities in the heat of melting below 100°C were found and related to the number of atoms (magic number) which are necessary to form a complete shell at the particle surface.[24]

In polymer science: nanocalorimetry is an interesting technique allowing to vary in a wide range the rates of solidification/melting. Thus, the high cooling rates and supercoolings on polyethylenes during processing allow to reach higher productivity. Heating and cooling rates at 3000 K/s were applied to polyethylenes. During fast crystallization, some crystal defects remain whereas during moderate supercooling, macromolecules have time for rearrangement so the material has fewer defects.[25]

In reference[26], nanocalorimetry was used to study the crystallization kinetics of isotactic polypropylene and melting of its mesophase. The high cooling rate (1000 K/s) reached with the nanocalorimeter allows to prevent crystallization during cooling so the crystallization kinetics of i-PP can be addressed under quiescent conditions. The isothermal experiments were performed after fast cooling each 5°C within the temperature in the range -15 to 90°C, they observed a local exothermal overheating. After crystallization from the melt, the i-PP presents three crystalline polymorphs: α-monoclinic, β-hexagonal and γ-triclinic.

The mesomorphic phase in i-PP presents some nodules which have a size in the range of 5 to 20 nm. At ambient temperature, the percentage of mesophase is of the order of 25 – 50 %. They observed that during fast heating (1000 $K.s^{-1}$) the mesophase is transformed into a supercooled liquid at temperatures lower about 77 – 87 K, so the mesophase of i-PP is a metastable partially ordered phase. Besides an increase of the heating rate increases the temperature of the mesomorphic – liquid phase transition.[27]

As far as polymer crystals are concerned, the nanocalorimetry was used to study the melting of isolated polyethylene single crystals presented on figure 6.[28]

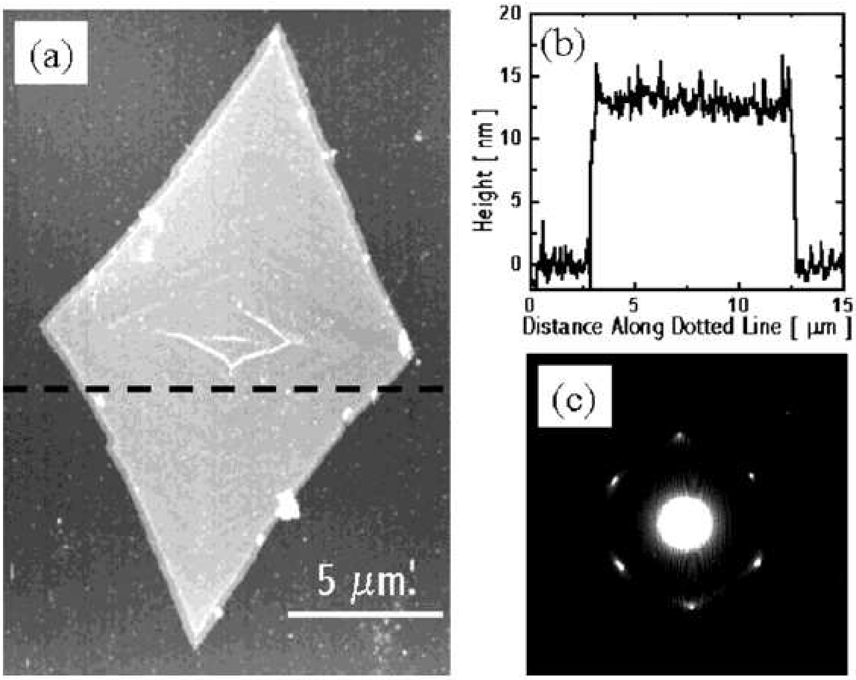

Figure 6. (a) AFM micrograph of a typical polymer single crystal. (b) The section profile of the crystal. The profile corresponds to the dotted line in A. (c) A diffraction pattern of a similar crystal obtained by TEM.

The dimension of one crystal is 20 μm x 13 μm x 12 nm. The lowest amount of crystals detected by nanocalorimetry was 25, it represents 0.1% of the surface coverage of the sensor. The melting temperature of the isolated single crystals of PE was 123 ± 2 °C which is 9 °C lower than the melting temperature of bulk PE. The isolation of crystals allows to limit interactions between crystals, to measure crystal thickness with AFM, to take diffraction pattern on individual crystals by TEM.

In studies of thin-films nanocalorimetry holds promise to study the finite size effects on the glass transition.

The study of ultra-thin polystyrene films with thickness in the range of 4 nm to 60 nm has showed that a reduction in heat capacity (c_p) for small film thickness supports the idea of a layer-like mobility profile consisting of both cooperative bulk dynamics and non-cooperative surface mobility.[29] The measurements of superheating phenomenon in linear polymers performed by nanocalorimetry have shown that there is a power law relation between the superheating and the heating rate in the range 10^{-2} to 10^{5} K/s. Generally, melting is accompanied by recrystallization at low heating rate that is why ultrafast heating rates are required for such experiments.[30]

Usually glass transition in polymers is studied by DSC, the samples are bulk and have a weight of several milligrams. It is not possible to study the behaviour of thin polymer films by DSC. The glass transition of ultrathin polymer films (less than 1 – 400 nm) was investigated by nanocalorimetry[32]. The solutions of polystyrene, poly(2-vinyl pyridine) and poly(methyl methacrylate) were spin-coated on the platinum surface of the nanocalorimetric sensor. Different film thicknesses were obtained by varying the concentration of solution and the speed of rotation. The thin polymer films were heated at very fast heating rates in the range of 20 to 200 °C/ms, which allow to perform experiments in nearly adiabatic conditions. The film thickness is determined according to the heat capacity (C_p) of the film at room temperature and the specific heat capacity of the bulk. The glass transition was observed in films which have a thickness of 1 to 3 nm and even thicker films but there is no dependence of the glass transition temperature on the thickness. As the films are heated very fast, there is no size dependence of the glass transition temperature on the millisecond timescale. Experiments show a broadening of the glass transition and a loss of transition contrast effects with the decreasing of film thickness. [31-32]

The measurement of heat capacity and enthalpy of formation of nickel silicide using nanocalorimetry was useful to study the interfacial reactions in thin films. The technique allowed to measure quantitatively the heat capacity and enthalpy of solid state reactions. Nickel forms several phases with silicon. The nanocalorimetric measurements of heat capacity and enthalpy of Ni-Si thin film interfacial reactions show several phase reactions during the first heating cycle and that samples below 800°C have predominantly NiSi phase whereas samples above 850°C formed θ-Ni_2Si. [33]

The use of nanocalorimetry for investigations of 2D SAMs has the advantage to determine the intrinsic melting properties of SAMs on individual separated nanoparticles without the effect of cluster-cluster melting (as it is the case for 3D SAMs in conventional DSC). [34]

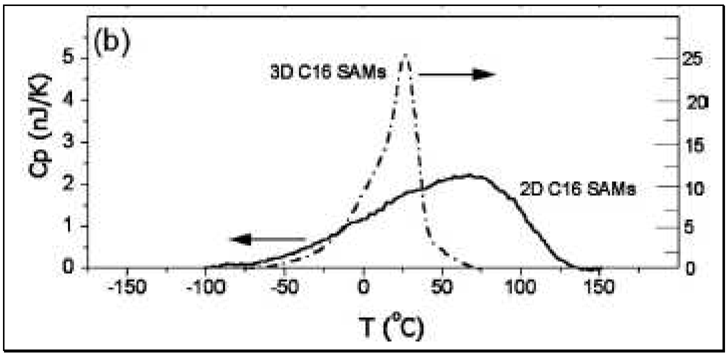

Figure 7. Comparison of the Cp value for 2D and 3D SAMs.

On figure 7, one observes that the transition temperature for 2D SAMs is higher and broader than for 3D SAMs. The heat of fusion for 2D and 3D SAMs is comparable (H_{m2D} = 20 ± 4 kJ/mol and H_{m3D} = 16 ± 5 kJ/mol) and lower than the bulk value (H_{mBulk} = 53 kJ/mol).

In conclusion, we have seen through these examples of applications that nanocalorimetry is complementary to DSC. It can address individual micro-particles, thin-films and single polymer crystals. Moreover, the high heating and cooling rates allow to generate the metastable states of materials.

1.3.4. Working modes of the Nanocalorimeter

The Nanocalorimeter can work in two modes: the mode with temperature modulation (AC) and the pulse mode (DC).

1. Temperature modulation: AC mode

In the AC mode, the sample is subject to a superposition of a linear temperature program and to a periodical temperature program. The power delivered to the sample has the form $P = p_0 + p.\sin(\omega t)$, the sample temperature oscillates around the mean temperature T_0 [35]. The theory of the modulated calorimetry was developed by Corbino in 1910. At that time, he considered a wire heated by an alternating current. During a short time interval Δt, the heat brought to the system is used to heat the sample and to heat the environment. This can be expressed by equation (4):

$$(p_0 + p.\sin(\omega t)).\Delta t = mc.\Delta T + Q(T).\Delta t \qquad (4)$$

Where m, c, T are the mass, heat capacity and sample temperature, respectively. Q(T) is the power of the heat losses, ω the angular frequency of modulation (ω = 2πf), and ΔT is the temperature variation during the time interval Δt. If we consider $T_0 + \Theta$ (with $\Theta << T_0$) and $Q(T) = Q(T_0) + Q.\Theta$ (where $Q = \frac{dQ}{dT}$ is the heat exchange parameter), we obtain :

$$p_0 + p.\sin(\omega t) = mc.\left(\frac{d\theta}{dt}\right) + Q(T_0) + Q'.\Theta \qquad (5)$$

If p_0 is used to heat the environment then mc.ΔT = 0.

The conditions of equation (5) are: $Q(T_0) = p_0$ and $\Theta = \Theta_0.\sin(\omega t - \Phi)$

By substituting it in equation (5), one finds:

$$\Theta_0 = \frac{P}{\sqrt{(mc\omega)^2 + Q^2}} \quad \text{and} \quad \tan\Phi = \frac{mc\omega}{Q}$$

where Θ is the amplitude of the temperature modulation, Φ is the phase difference between the temperature oscillations of the power dissipated in the sample and the temperature oscillations applied to the sample.

2. *Pulse mode: DC mode*

The possibility to perform fast heating experiments is one of the main advantages of Nanocalorimetry. A typical fast heating experiment takes only a few milliseconds. For such an experiment, a voltage ramp is applied to the external heater. Experiments at extremely fast heating rates could enable us to detect and differentiate energetic materials based on their thermal behaviour (melting, evaporation, sublimation and other transitions).

1.4. Energetic materials[36, 37]

The following part of this chapter provides some introductory information on energetic materials and basic definitions such as the explosive power and strength, deflagration, detonation and combustion, oxygen balance and activation energy of thermal decomposition.

1.4.1. Introduction

Energetic materials store a significant amount of energy that can be released during their highly exothermic decomposition induced by temperature, impact or friction. The release of energy is obtained by mechanisms of intramolecular oxydoreduction. An explosion results from a sudden release of energy.

1.4.2. Classification of energetic materials

Energetic materials are classified according to their applications, as shown on figure 8. In this case, the same explosive molecule can enter in the formulation of propergols and explosives. The munition powders provide an impulsion to the projectile, propergols provide the pushing force to a missile. The decomposition of primary explosives such as TATP, lead azoture can be easily initiated and lead to detonation whereas secondary explosives such as TNT, RDX are less susceptible to be initiated. Commercial explosives are used in mining operations and for demolition of buildings. One can see through their applications that energetic materials are employed to produce a work rather than heat.

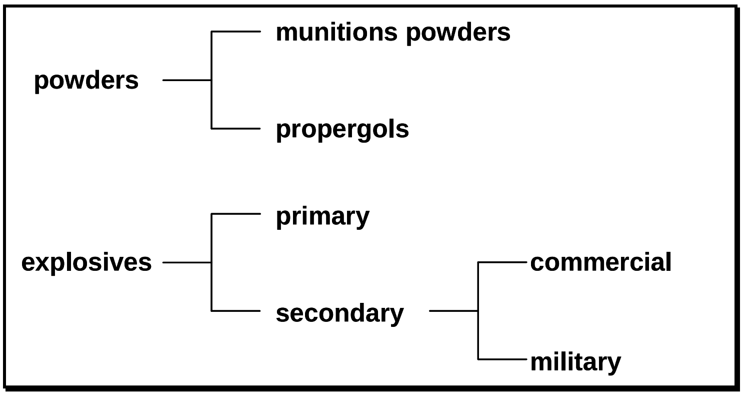

Figure 8. Classification of energetic materials.

1.4.3. *Explosive power – Explosive strength*

The explosive power refers to the ability of the explosive to do the work, it is also used to compare different energetic materials. The explosive power corresponds to the energy produced by the adiabatic decomposition of the material (Q) with the volume of combustion gaz (V_g) measured at ambient pressure and at 15°C. The explosive power[38] can be expressed as:

$$ExplosivePower = Q \times V$$

The explosive power is reported to the one of picric acid (figure 9), which is one of the most stable secondary explosives. The power index is:

$$Power \quad index = \frac{Q \times V}{Q_{\left(picric \;\; acid\right)} \times V_{\left(picric \;\; acid\right)}}$$

where $Q_{(\text{picric acid})} = 3250$ kJ/kg, $V_{(\text{picric acid})} = 0.831$ dm^3/g.

The explosive strength of energetic material is the magnitude of the explosion relative to that from the same quantity of reference (TNT). The explosive strength of TNT is $2{,}72.10^6$ J/kg. Experimentally, the explosive strength is determined with the Trauzl block test, which consists in the measurement of the expansion caused by an explosion contained within a block of lead or aluminium.

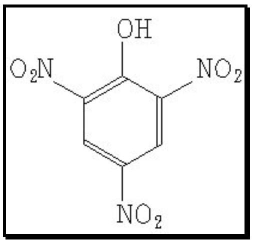

Figure 9. Structure of picric acid.

1.4.4. Combustion, deflagration, detonation

Explosives release their energy quickly (in a few microseconds) during their decomposition. Combustion, deflagration and detonation differ by the speed of their flame front. The flame front is a thin zone where the exothermic reaction takes place. It separates the area which contains the combustible from the area which contains the combustion products. For the combustion, the speed of the flame front is in the range of m/s to cm/s, and the combustion burns the material progressively. The speed of the flame front is lower than the sound speed (about a few decimetres to hundreds meters per second) for the deflagration and higher than the sound speed (about kilometres by second) for detonation. For the deflagration, the part of the explosive upstream of the flame front is sensitized. For the detonation, the shockwave crosses the explosive and its speed is auto-supported by the chemical reactions that it produces. The detonation process acts through shock pressure forces. The resulting impact on neighbouring materials is the basis for the detonation mechanism. Detonation is relatively independent of ambient conditions but is sensitive to density of the explosive. There is no propagation of detonation below a critical diameter or a critical thickness of the energetic material. This parameter depends on the confinement and the density of explosive.[39,40] The deflagration process transfers its energy by thermal means through a temperature difference, this process depends on external conditions such as ambient pressure.

The initiation of decomposition reaction after the passage of the shock wave is explained by the increasing temperature when the shock wave propagates across the energetic material through hot spots. Hot spots are small volumes in the material in which if the release of chemical energy is greater than that dissipated by heat losses, whereby the reaction amplifies.[41] These hot spots are created whether by friction between two particles which have a high melting point or by adiabatic compression of interstitial gaz.[42]

1.4.5. Activation energy of thermal decomposition of explosives

The decomposition of energetic materials is associated with the activation energies of the reaction process. For some energetic materials, the decomposition is initiated by the break-up of fragile bonds (explosophore bonds), this step determines the decomposition kinetics.

Explosophore bonds are often X – NO_2 bonds like in TNT (figure 10). The activation energy of decomposition depends on the molecular structure, the environment of the molecule in the condensed phase and the addition of some compounds which can initiate the decomposition.

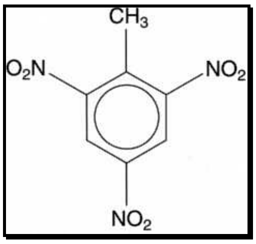

Figure 10. Structure of trinitrotoluene.

1.4.6. Oxygen balance

An energetic material is also characterized by its oxygen balance (Ω). The oxygen balance is equal to the difference between the proportion of oxygen in the material and the proportion of oxygen which could allow complete oxidation of the compound. For a compound $C_aH_bN_cO_d$, the oxygen balance is the following:

$$\Omega = (16/M) \times [d - (2a) - (b/2)]$$

The explosion products are formed either in direct explosion reaction or in reaction with the surrounding atmosphere. The products from chemical explosives include the usual combustion products (CO_2, CO, H_2O, N_2) as well as molecular hydrogen (H_2), molecular oxygen (O_2), nitric oxide (NO), hydroxyl (OH), monoatomic hydrogen (H), monoatomic oxygen (O), monoatomic nitrogen (N) and small amounts of ionized gases and associated electrons.[36]

1.5. Actual explosives traces detection devices

1.5.1. Traces of explosives

Explosive traces can consist of particles that remain for example on a person who handled explosives or when he/she has been near explosives or when he/she has hidden explosives on him/herself. The main difficulty to detect explosives is due to their low vapour pressure at ambient temperature and pressure for some of them. The vapour pressure of common explosives is presented on figure 11.

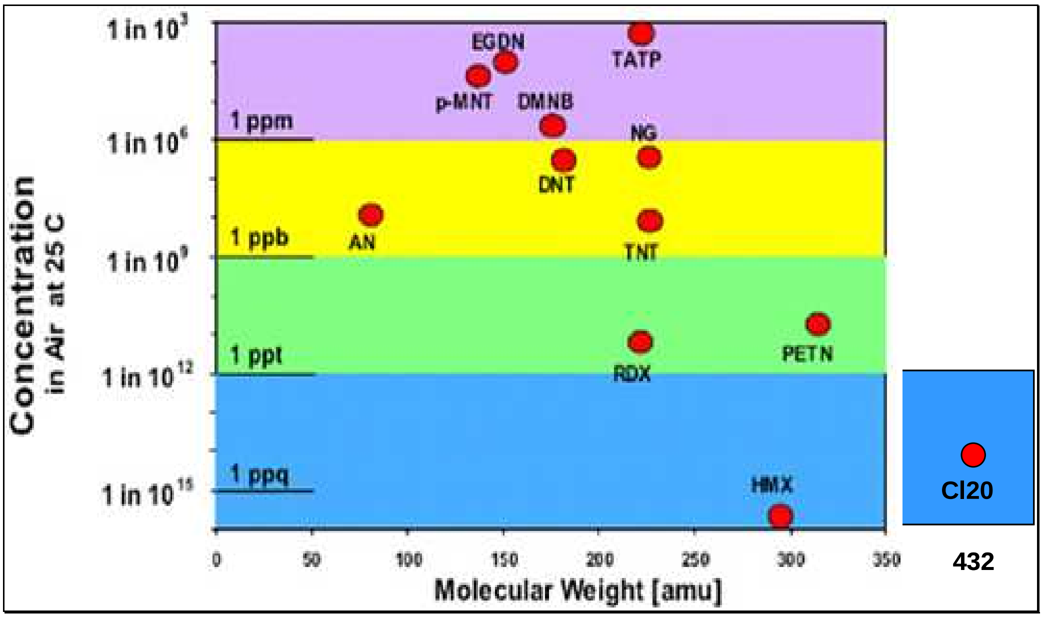

Figure 11. Concentration of explosives in air at 25 °C.[43]

The low concentration of explosives in air results in difficulties for the vapour phase detection without concentrating the explosives.

1.5.2. The three steps required for explosive detection devices

The explosive detection is typically constituted of three steps: sample collection, pre-concentration and detection. The relationship between these three steps can be described by equation (6):

$$S = M_0 \eta_r \eta_C C_1 \ldots C_n \left(\frac{Q_d}{Q_n} \right) k \qquad (6)$$

where S is the signal output from the detector, M_0 is the initial mass of explosive residue on a person, η_r is the fraction of explosive that is removed from the person by sample collection system, η_C is the fraction of explosive removed that is collected in the pre-concentration system, C_1 is the concentration gain of the first pre-concentration stage, C_n is the concentration gain of the nth pre-concentration stage, Q_d is the inlet (sampling) flow rate of the detector, Q_n is the output flow rate from the final pre-concentration stage, k is the proportionality term relating signal strength to concentration at the detector.[44]

The first step of the explosive detection is the sample collection: the explosives are removed from the person either by mechanical methods (rubbing, wiping, agitation), by ionization (explosive particles are statically remove), by airflow or by heat (the temperature elevation enhances the explosive vapour production). Then the explosive traces are transported to a pre-concentration system by airflow.

The second step, which is the pre-concentration, serves to increase the concentration of explosives in order to reach the limit of detection of the detector. We observe on figure 11 that the concentration of common explosives in air is in the range of 1 in 10^3 to 1 in 10^{15}. The pre-concentrator adsorbs explosives, then the pre-concentrator is heated to allow the explosives desorption from its surface into a smaller volume than the volume of the sample collection airflow.

The third step is the detection itself: the sample arrives from the pre-concentrator and is analyzed on the detector.

1.5.3. Sensors used for explosives detection

The principle of a sensor relies on a sensitive material which presents variation of one or more physical properties (fluorescence, conductivity, mass modification, shift frequency, optical properties…) in contact with the substance of interest.

The gas sensors of energetic materials can be divided in three groups. There are resistive sensors (based on conductivity variation of the sensitive material), acoustic and gravimetric sensors (the mass variation is link to a variation in the oscillation frequency), optical sensors (variation of optical properties such as colour, fluorescence).[45] The explosives detection methods are classified on figure 12 according to the properties used by the sensor.

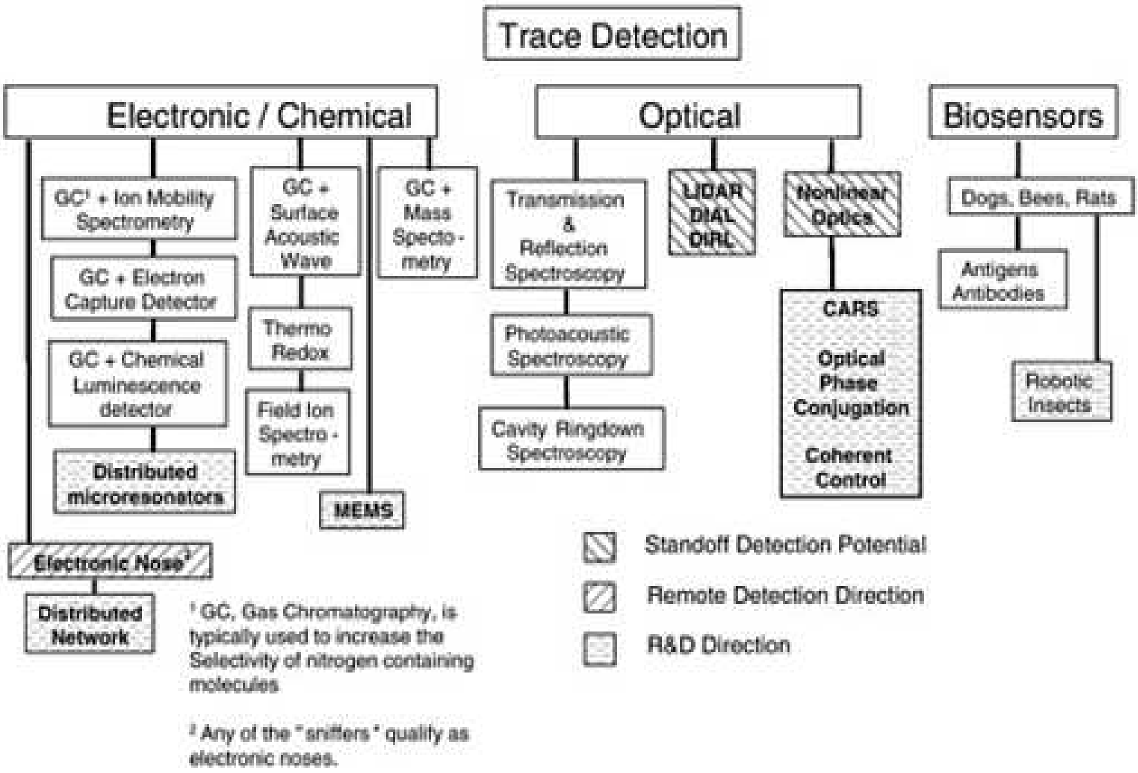

Figure 12. Explosives detection methods.

The trace detector based on electronic / chemical sensors are often coupled to a GC in order to separate explosives from potential interferents and to increase the selectivity of the device. Among the different instrumental techniques, mass spectrometry methods have the best selectivity and sensitivity. Their analysis time can be about 5s by reducing or eliminating the sample preparation time. Pan et al. reached a limit of detection of 0.78 pg for HMX in solution.[46] The limit of detection for TNT, RDX and PETN are about 1, 5 and 20 pg respectively. [47] The disadvantages of mass spectrometry (MS) are high cost and complexity. Ion mobility spectrometry (IMS) is similar to mass spectrometry except that the ions are dispersed by gas-phase viscosity and not by molecular weight. Comparatively to MS, IMS is smaller and cheaper (because there is no vacuum system) but its accuracy is less than MS. The analysis by Ion Mobility Spectrometry takes 1 min and the detection limit for TATP is 187 µg/mL.[48] The common explosive compounds produce negative ions. Surface acoustic wave detectors are based on shifts in the resonant frequency of a piezoelectric crystal based on mass and properties of materials condensed on the crystal. Optical spectroscopy can be used for explosive identification but the sensitivity is not very high comparatively to MS. Biosensors such as dogs are probably the best explosives detectors to date. They can recognize up to 19000 smells associated with explosives such as nitrate compounds, chlorates, peroxides and acids. However, their performance is diminished by boredom, distraction, unfamiliar signals, and tiredness. In comparison to instrumental methods, dogs have the advantages to detect faster explosives and to go to the source where they find the explosives. Table 1 compares instrumental detection devices and dogs.

Aspect	Instrument	Canine
Duty cycle	24 h day^{-1} (theoretical)	Ca. 8 h day^{-1} (20 min on/40 min break dependent on conditions)
Calibration standards	Can be run simultaneously (i.e. chromatography based)	Run individually
I.D. of explosive	Presumptive I.D. possible (limited by selectivity factors)	Not trained to I.D. with different alerts
Operator/handler influence	Less of a factor	A potential factor
Environmental conditions	Less affected	May adversely affect (i.e. high temperatures)
Instrument lifetime	Generally ca. 10 years	Generally 6–8 years
State of scientific knowledge	Relatively mature	Late emerging
Courtroom acceptance	Generally unchallenged	Sometimes challenged
Selectivity (vs. interferents)	Sometimes problematic	Very good
Overall speed of detection	Generally slower	Generally faster
Mobility	Limited at present	Very versatile
Integrated sampling system	Problematic/inefficient	Highly efficient
Scent to source	Difficult with present technology	Natural and quick
Intrusiveness	Variable (apprehensiveness not uncommon)	Often innocuous (breed dependent)
Initial cost	ca. $45 000	ca. $6000
Annual cost (excluding personnel)	ca. $4000 (service contract)	ca. 2000 (vet and food bill)
Sensitivity	Very good/well known	Very good/few studies
Target chemical(s)	Parent explosive(s)/well studied	Odorant signatures/mostly unknown
Toxicological considerations	Minimal (operator may be affected at excessive levels)	Minimal (team may be affected at excessive levels)
Downtime	Varies with instrument, operator and manufacturer	Varies with breed, handler and medical condition
Instrument components	Varies with manufacturer (variable sampling, separation, detection, I.D. technology)	Varies with agency (variable breed, training, alert and reward systems)
Initial calibration	Generally performed by manufacturer (specifications vary by manufacturers)	Generally performed by supplier (specifications vary by supplier with minimum 6 weeks training)
Operator training	Typically a 40 h course	Typically 40 h course minimum
Certifications	Varies, annually to biannually	Annually to biannually
Re-calibrations	Daily to weekly	Daily to weekly
Scientific foundations	Electronics, computer science, analytical chemistry	Neurophysiology, behavioral psychology, analytical chemistry
Potential affects on performance	Electronics/mechanical	Disease conditions

Table 1. Comparison between instrumental explosives detection devices and detector dogs.[49]

Some insects such as bees are also trained to detect explosives. In order to train these insects, researchers feed them with a mixture of sugar, water and the explosive molecules.[47] So, when the bees detect explosives, they fly over the suspected area to indicate the presence of explosives.

1.5.4. Detection device based on amplifying fluorescent polymers

A detection device which has a level of detection comparable to that of dog has been developed by the Nomadics Inc. company. It is a system of real-time detection based on fluorescent polymers.[50] The amplifying fluorescent polymers (AFP) were invented by T.M. Swager from MIT.[51] Instead of pre-concentrating explosives, this fluorescent polymers amplify a few femtograms of explosives (~ ppq) to create a detectable signal. AFP are chromophores linked together in polymer chains which fluoresce when they are stimulated by light of the correct wavelength. Explosives binding to the AFP will reduce (quench) the brightness of the fluorescence. As the chromophores are linked in series, the quenching effect is amplified (see figure 13), that is why a few femtograms of explosives can be detected.

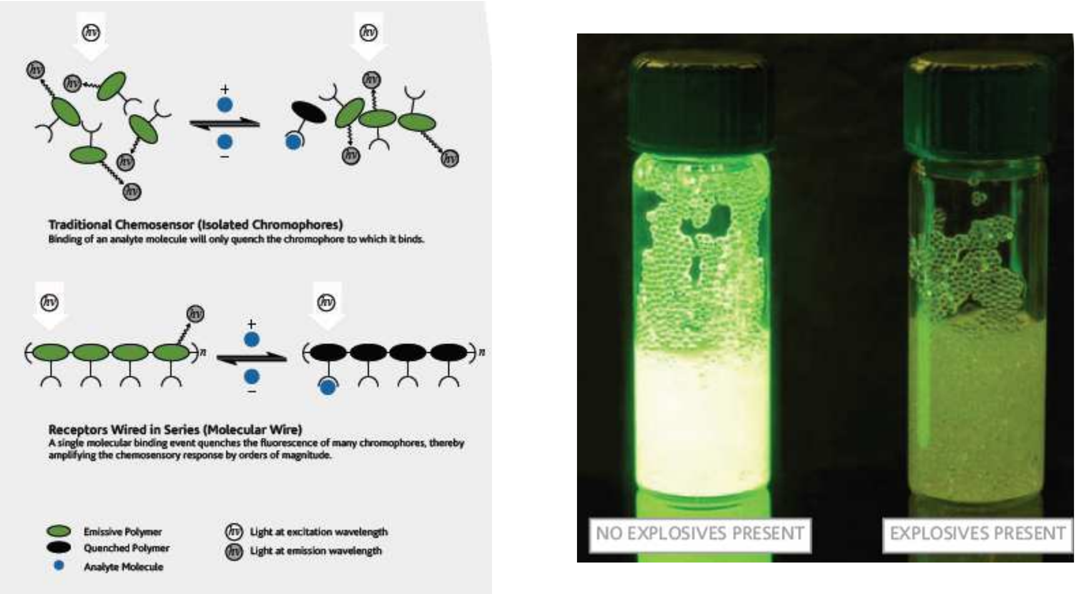

Figure 13. AFP for explosive detection.

The analysis time in this case is short: a film of polymer in figure is quenched by 50% within 30s of exposure to TNT and by 75% within 60s.

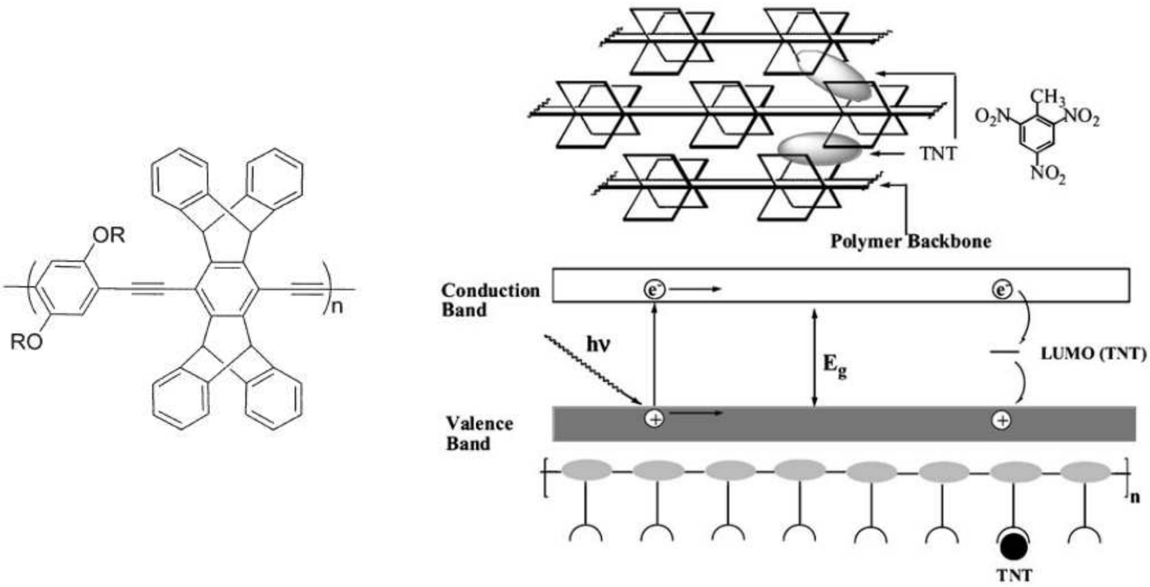

Figure 14. Monomer of poly(phenylene ethynylene) on the left, schematic representation of porous polymer films allowing TNT detection and band diagram depicting quenching resulting from electron transfer from PPE to TNT (on the right).

As shown on figure 14, the rigidity and the three-dimensional structure of the polymer forms cavities in the sensor films in which small molecules of TNT are diffused. The selectivity of this device is based on three paths.[47] First, the steric constraints allow only small molecules to fit in the cavities of the porous film. Secondly, the electron-rich polymer binds reversibly to electron-deficient explosives through an electrostatic-type interaction. To enhance binding of target compounds, receptor sites that are electrostatic mirror images of the target molecule have been specifically synthesized into the polymer backbone. Thirdly, the free energy change (ΔG^0) must be negative for the process of the electron transfer to the bound molecule. Thus the magnitude of fluorescence quenching (FQ) can be approximated as:

$$(FQ) \sim C.[\exp(-\Delta G^0)^2].K_b$$

where K_b is the binding constant and C is the concentration of the quencher in the sample. This equation shows that compounds which are weakly bound to the polymer films and those without favourable reduction potentials are not able to quench the polymer, except in very high concentrations.

Figure 15. Fido XT (on the left) and Fido-robot (on the right).

Nowadays, Fido device seems to be the most sensitive explosive detector and it can be incorporated onto a robot as shown on figure 15, so the Fido-robot is able to locate explosive devices and to disarm them.

1.6. Detection of energetic materials by calorimetry

There has been an important interest and development of systems for explosive trace detection in the past years.[52] These instruments use mass spectrometry[53], Raman spectroscopy[54, 55], ion mobility spectroscopy[56], gaz sensors constituted in organic materials[57], porous substrates[58]. This section is focused on systems using calorimetric principles to detect explosive traces which are microcantilever sensor and miniature calorimeter. The functionalisation of the cantilevers is also mentioned.

1.6.1. Microcantilever sensor: lab on a tip

Microcantilever sensors have a sensitivity of a few picograms. They have several advantages such as a surface area of the order of 10^{-4} cm² and a high surface-to-volume ratio (the order of 10^{3}). The mass loading can be observed by bending of the cantilever and by a shift in the resonant frequency, microcantilevers can be produced in mass at a relatively low cost.

- Cantilever working.

In 2003, L.A. Pinnaduwage and T. Thundat developed a microcantilever sensor which can detect the deflagration of 70 pg of TNT. The article was published in Nature.[1] The equipment included a piezoresistive heater on the microcantilever surface. The mass of explosive is measured by deflection of the cantilever with an optical beam-bounce technique.[59]

A system based on microcantilever[60] has lead to development of another system using suspended microfabricated bridges.[61, 62] This is a combination of a resonating microcantilever and of suspended microfabricated bridges which are in the same plane. The microcantilever allows measuring the mass of adsorbed explosives and the bridges make it possible to heat in order to address the thermal behaviour of the adsorbed explosives. The sample temperature is given by resistances of the sensor bridges. This system can reach a heating rate of 10^7 °C/s and detect a limit mass of 600 pg. During the heating, the adsorbed molecules are decomposed and desorbed as a function of temperature. The mass loss detected by the microcantilever looks like a sigmoid function. The microcantilever deflection allows determining the mass of adsorbed molecules thanks to formula (7):

$$\delta m = \frac{K}{4\pi^2 n} . \left(\frac{1}{\nu_1{}^2} - \frac{1}{\nu_2{}^2} \right) \qquad (7)$$

where υ_1 and υ_2 are the resonance frequencies before and after adsorption, K the spring constant, δm the mass of adsorbed molecules, n corresponds to the coefficient between the effective mass m* and the mass m of the cantilever (m* = n.m).[63] When microcantilevers oscillate in fluids, there is a mass effect, which explains the usefulness of the effective mass notion[64]. In air at ambient pressure, this effect is negligible.

Nowadays, nanoelectrochemical devices (NEMS) can detect a mass on the order of a zeptogram[65]. This kind of devices are very high frequency (VHF) NEMS which have a fundamental resonant frequency of 190 MHz and a quality factor of 5000 in the temperature range of the experiment. The experiments to detect such mass are performed in situ within a cryogenically cooled, ultrahigh vacuum apparatus at pressures below 10^{-10} Torr. Nanocantilevers with very high mechanical resonance frequency allow detecting less than 1 attogram (10^{-18}g).[66] The cantilevers integrated electronic displacement transducers based on piezoresistive thin metal films, permitting straightforward and optimal device readout. Two legs link the cantilever to the chip. These legs serve as an electrical path for piezoresistive transduction and, upon cantilever deflection, as strain concentrators. Nanocantilevers are fabricated using electron-beam lithography, metal-film deposition and lift-off methods.

- Cantilever functionalisation

Studies on the functionalisation of microcantilevers have lead to selective detection of energetic materials. Two papers were found on this topic.

In the first one[67], the authors use self-assembled monolayers of 4-mercaptobenzoic acid (4-MBA also known as thiosalicylic acid). These surfaces are believed to fix nitro-molecules of explosives via hydrogen bonding.[68] The thiol compounds have as general formula $CH_3(CH_2)_nSH$. These molecules have a capacity to graft on gold surfaces thanks to the head SH. The silanes ($CH_3(CH_2)nSiCl_3$) are preferably grafted on silicon, silicon oxide, aluminium oxide surfaces. When the molecules are sufficiently close to each other, the Van der Waals interactions are strong enough to order molecules in a dense layer.[69] Scanning Tunneling Microscopy studies of 4-MBA SAMs have shown that these surfaces have domains with a periodic row structure and no hole defects.[70] Such characteristics are convenient for the detection of explosives. Before to deposit 4-MBA SAMs on the cantilevers, the cantilevers are cleaned with the method described in literature[71]. Then, the cantilevers are immersed in a 6.10^{-3} M solution of 4-MBA in absolute ethanol for 2 days. The PETN and RDX vapour streams are generated by introducing ambient air through a reservoir containing PETN or RDX. For the experiments, the vapour concentrations for PETN and RDX are 1400 ppt and 290 ppt. The generator delivers 660 pg of PETN in 20 s and 96 pg of RDX in 25 s. The bending signal of the cantilever and the shift frequency for each explosive are presented on figure 16.

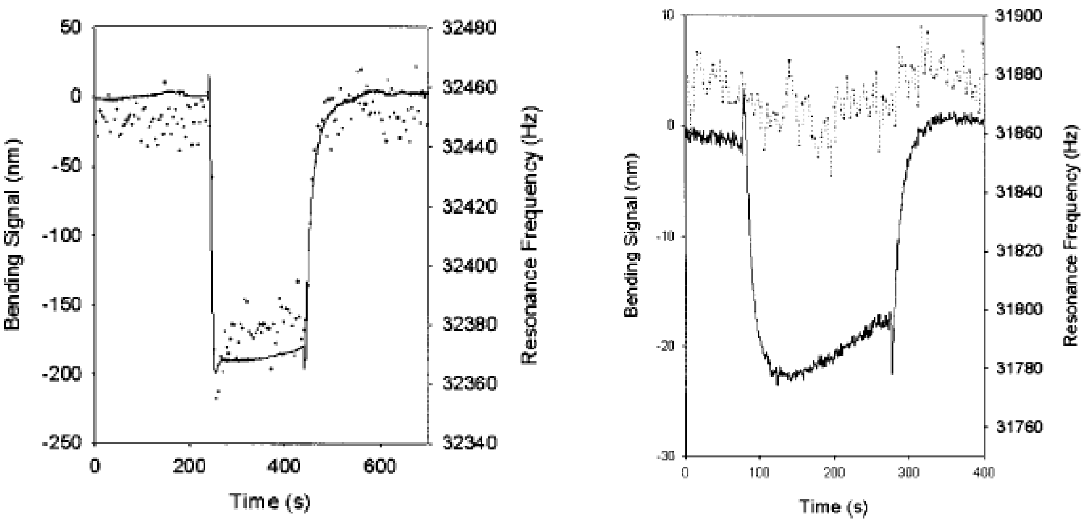

Figure 16. Response of a 4-MBA-coated silicon cantilever loaded with 660 pg of PETN (on the left) and with 96 pg of RDX (on the right). The solid curves represent the bending signal, the dots represents the resonant frequency.

The deflection of the cantilever and the shift frequency are due to the adsorption of energetic materials on the 4-MBA SAMs. The graph on the right panel of figure 16 shows that the bending signal is more sensitive to the RDX adsorption than the shift of resonant frequency. The adsorption of the explosives molecules on the SAMs are easily reversible; it is probably due to hydrogen bonding between the nitrogroups of the explosives and the carboxyl groups of 4-MBA.

The second paper is focused on zeolite-coated cantilevers.[72] Zeolites are silicon-based solids with nanometric or subnanometric pores. These compounds act like sieves because molecules which are larger than the pore size keep outside the zeolite. Furthermore, the adsorption properties of the zeolite can be adjusted by adjusting their Si/Al ratio or by exchanging the cation presents in pores. As shown on figure 17, the addition of cobalt to the BEA zeolite increases the sensitivity to nitrotoluene.

The zeolites used in this work are MFI (silicalite and ZSM-5), zeolite A (LTA), zeolite Y (FAU), Beta (BEA) and mordenite (MOR) zeolites. Different methods are tested to deposit layers of zeolites on silicon substrates: evaporation,

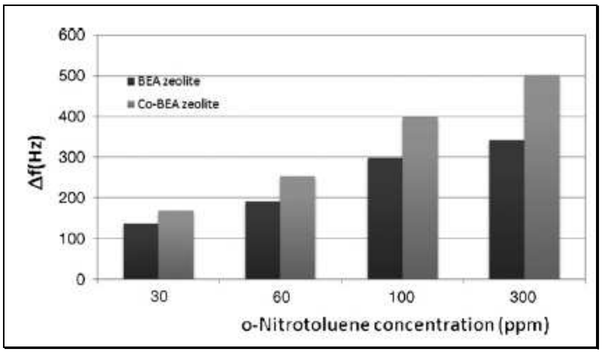

Figure 17. Detection of o-nitrotoluene at room temperature on QCMs loaded with NH4-BEA and Co-BEA zeolites.

micro-dropping of zeolite suspensions, covalent bonding of the zeolite crystals (by using chemical linkers which connect the OH groups of the zeolite to those on the surface of different materials) and spin coating. Evaporation and microdropping lead to a coating of several layers of zeolitic material, the coating thickness is thicker and more uniform by evaporation than by microdropping. Covalent bonding produces a zeolitic monolayer on the substrate.

1.6.2. Miniature calorimeter for explosives detection and identification

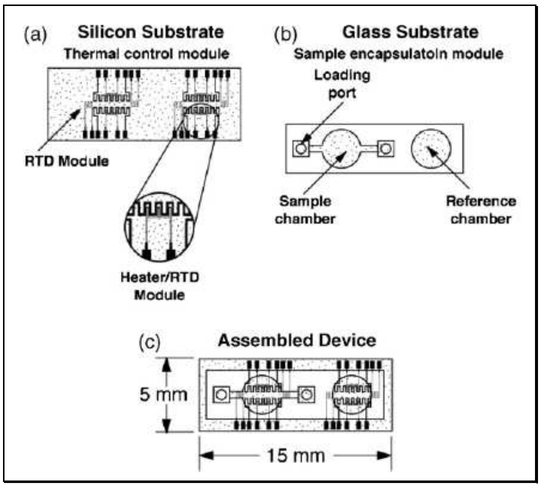

Figure 18. Schematic drawing of the calorimeter cell.

One calorimeter was built to study and to detect energetic materials. Figure 18 presents a system of thermal control and a system of compound encapsulation.[73] The calorimetric cell consists of a thermal control module (cf. figure 18a) and a sample encapsulation module (cf. figure 18b). As shown on figure 18, the thermal control and the sample encapsulation components are separated, the assembly of these two parts constitutes the calorimetric cell whose dimensions are 5 x 15 mm². The resistive heaters on the thermal control module allow to heat the sample. The temperature sensitivity of the device is 0,2°C.[74] This calorimeter allows analyzing solid and liquid samples of a few nanograms or nanoliters. It was tested with the evaporation of 350 nL of acetone and with energetic materials of a few nanograms. The heating rate used for these experiments is 1 °C/min like for classical DSC. A micrograph of the nanocalorimetry prototype is given on figure 19.

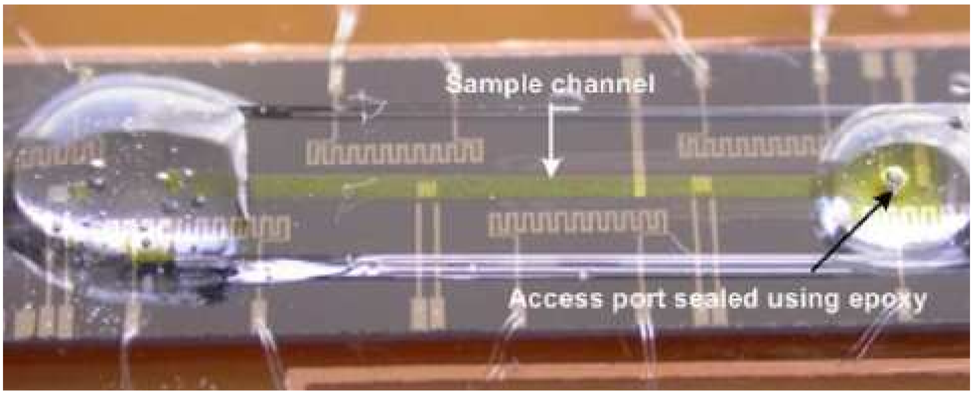

Figure 19. Nanocalorimetry prototype loaded with a sample of ammonium iron (III) sulphate dodecahydrate sealed using epoxy.

The volume of gas produced during the decomposition reaction can be 100 – 1000 times of the original sample, so the pressure inside the analysis cell increases. The cell can resist at pressure until 800 psi i.e. 50 times the atmospheric pressure. The nanocalorimetric cell can be damaged during the decomposition or combustion reaction of energetic materials.[73]

For now, this nanocalorimeter is the only one which was developed specifically for detection and identification of energetic compounds. Nevertheless, we were not able to find any calorimetric curve of energetic materials measured with this device even though it was specifically made for explosives detection (to our knowledge, there is only curve with evaporation of acetone). As mentioned in publication[73], samples of ~ 1 µg were successfully characterised by this calorimeter.

---

1 Pinnaduwage, L.A.; Gehl, A.; Hedden, D. L.; Muralidharan, G.; Thundat, T.; Lareau, R.T.; Sulchek, T.; Manning, L.; Rogers, B.; Jones, M.; Adams, J.D. *Nature* **2003**, *425*, 474.

2 Mathot, V.B.F. *Calorimetry and thermal analysis of polymers*; Hanser Publishers: München, 1994.

3 Operating Instructions – Mettler Toledo, DSC 822E Module, Mettler-Toledo, technical datasheet, **2002**

4 Defaux, M. Thesis, Université de Haute-Alsace, Mulhouse, **2008**.

5 Analyse calorimétrique différentielle pour toutes les exigences, Support technique, Mettler-Toledo, Schwertzenbach, **2007**

6 Traité de thermométrie par thermocouple et résistance, TC S.A, version 6.0., **2007**.

7 Wagner, M.; Bottom, R.; Larbanois, P.; Schawe, J. *User Comm. Mettler Toledo*, **2004**

8 Merzlyakov, M. *Thermochimica Acta* **2006**, *442*, 52–60.

9 Lopeandìa, A.F.; Rodrìguez-Viejo, J. *Thermochimica Acta* **2007,** *461*, 82–87.

10 Minakov, A.A.; van Herwaarden, A.W. ; Wien, W. ; Wurm, A. ; Schick, C. ; *Thermochimica Acta* **2007,** *461*, 96–106.

11 Minakov, A.; Schick, C. *Review of Scientific Instruments* **2007**, *78*, 073902

12 Minakov, A.A.; van Herwaarden, A.W.; Wien, W.; Wurm, A.; Schick, C. *Thermochimica Acta* **2007**, *461*, 96–106.

13 Allen, L.H.; Ramanath, G.; Lai, S.L.; Ma, Z.; Lee, S.; Allman, D.D.J.; Fuchs, K.P. *Applied Physical Letters* **1994,** *64* (4), 417 – 419.

14 Olson, E.A.; Efremov, Yu. M.; Zhang, M.; Zhang, Z.; Allen, L.H. *Journal of microelectromechanical systems*, **2003**, *12* (3), 355 – 364.

15 Efremov, M. Yu.; Olson, E.A.; Zhang, M.; Allen, L.H.; *Thermochimica Acta* **2003**, *403*, 37 – 41.

16 Château, E.; Garden, J.-L.; Bourgeois, O.; Chaussy, J.; *Applied Physics Letters* **2005**, *86*, 151913.

17 Garden, J.-L.; Château, E.; Chaussy, J.; *Applied Physics Letters*, **2004**, *84* (18), 3597 – 3599.

18 Minakov, A.A.; Adamovsky, S.A.; Schick, C. *Thermochimica Acta* **2003**, *403*, 89 – 103.

19 Minakov, A.A.; Adamovsky, S.A.; Schick, C. *Thermochimica Acta* **2005**, *432*, 177 – 185.

20 Minakov, A.A.; Schick, C. *Review of Scientific Instruments* **2007**, *78*, 073902.

21 Ong F., Thesis, Université Joseph Fourier, Grenoble, 2007.

22 Gao, Y.L.; Zhuralev, E.; Zou, C.D.; Yang, B.; Zhai, Q.J.; Schick, C. *Thermochimica Acta* **2009**, *482*, 1 – 7.

23 Olson, E.A.; Efremov, M.Yu.; Zhang, M.; Allen, L.H. *Journal of Applied Physics* **2005**, *97*, 034304.

24 M. Yu. Efremov, M.Yu.; Schiettekatte, F.; Zhang, M.; Olson, E.A.; Kwan, A.T.; Berry, R.S.; Allen, L.H. *Physical Review Letters*, **2000**, *85* (17), 3560 – 3563.

25 Krumme, A.; Lehtinen, A.; Adamovsky, S.; Schick, C.; Roots, J.; Viikna, A. *Journal of Polymer Science Part B. Polymer physics*, **2008**, 46 (15), 1577 – 1588.

26 De Santis, F. ; Adamovsky, S. ; Titomanlio, G. ; Schick, C. Macromolecules **2007**, *40*, 9026 – 9031.

27 Mileva, D.; Androsch, R.; Zhuravlev, E.; Schick, C. *Macromolecules* **2009**, *42*, 7275 – 7278.

---

28 Kwan, A.T.; Efremov, M.Yu.; Olson, E.A.; Schiettekatte, F.; Zhang, M.; Geil, P.H.; Allen, L.H. *Journal of Polymer Science. Part B. Polymer Physics* **2001**, *39* (11), 1237 – 1245.

29 Lupaşcu, V.; Huth, H.; Schick, C.; Wübbenhorst, M. *Thermochimica Acta* **2005**, *432,* 222 – 228.

30 Minakov, A.A.; van Herwaarden, A.W.; Wien, W.; Wurm, A.; Schick, C. *Thermochimica Acta* **2007**, *461*, 96 – 106.

31 Efremov, M. Yu.; Warren, J.T.; Olson, E.A.; Zhang, M.; Kwan, A.T.; Allen, L.H. *Macromolecules* **2002**, *35* (5), 1481 – 1483.

32 Efremov, M. Yu.; Olson, E.A.; Zhang, M.; Zhang, Z.; Allen, L.H. *Physical Review Letters* **2003**, *91* (8), 085703.

33 Kummamuru, R.K.; De La Rama, L.; Hu, L.; Vaudin, M.D.; Efremov, M.Y.; Green, M.L.; LaVan, D.A.; Allen, L.H. *Applied Physics Letters* **2009**, *95*, 181911.

34 Zhang, Z.S.; Wilson, O.M.; Efremov, M.Yu.; Olson, E.A.; Braun, P.V.; Senaratne, W.; Ober, C.K.; Zhang, M.; Allen, L.H. *Applied Physics Letters* **2004**, *84* (25), 5198 – 5200.

35 Kraftmakher Y., *Modulation calorimetry : theory and applications*, **2004**, Springer, Heidelberg.

36 Kinney, G.F., Graham K.J., *Explosive shocks in air, Second Edition*, **1985**, Springer, New York.

37 Mathieu, D.; Beaucamp, S. *Matériaux énergétiques*, *Techniques de l'ingénieur*, **2004**

38 http://www.globalspec.com/reference/55654/203279/explosive-power-and-power-index

39 Boileau, J. *J. Phys. Colloques* **1987,** *48*, C4-99-C4-104.

40 Estimation du diamètre critique de détonation – Méthode des éprouvettes cylindriques et coniques, www.ixarm.com, FMD-141-B-1, **1987**

41 Field, J.E. *Acc. Chem. Res*. **1992**, *25*, 489 – 496.

42 Van Tiggelen A., Burger J., Clément G., De Soete G., Feugier A., Karr C., Monnot G. *Oxydations et Combustions*. Editions Technip, Paris, **1968**.

43 Committee on the Review of Existing and Potential Standoff Explosives Detection Techniques, National Research Council, *Existing and potential standoff explosives detection techniques*, the National Academies Press, **2004,** Washington.

44 Yinon, J. *Counterterrorist detection techniques of explosives*, **2007**, Elsevier Science, Amsterdam.

45 Montmeat,P.; Thery-Merland, F.; Hairault, L. Capteurs chimiques pour la détection d'explosifs, *Techniques d'ingénieur*, **2003**

46 Pan X.-P.; Tian K.; Jones L.E.; Cobb G.P. *Talanta*, **2006**, *70*, 455 – 459.

47 Woodfin, R.L. *Trace chemical sensing of explosives*, Wiley Interscience, **2007**, Hoboken, New Jersey.

48 Buttigieg, G.A.; Knight, A.K.; Denson, S.; Pommier, C.; Bonner Denton, M. *Forensic Science International* **2003**, *135*, 53 – 59.

49 Furton, K.G.; Myers, L.J. *Talanta* **2001**, *54*, 487 – 500.

50 http://www.icxt.com/products/icx-detection/explosives/fido/

51 Zheng, J.; Swager, T.M.; *Adv Polym. Sci.* **2005**, 177, 151 – 179.

52 Moore, D.S.; *Sens Imaging* **2007**, *8*, 9 – 38.

53 Hitachi Review **2004**, *53* (2), 88 – 91.

54 Moore, D.S.; Scharff, R.J. *Anal. Bioanal. Chem.* **2009**, *393*, 1571 – 1578.

55 Golightly, R.S.; Doering, W.E.; Natan, M.J. *Nano focus* **2009**, *3* (10), 2859 – 2869.

56 Khayamian, T.; Tabrizchi, M.; Jafari, M.T. *Talanta* **2003**, *59* (2), 327 – 333.

57 Hairault L. Détection d’explosifs : vers des capteurs sélectifs à fonctionnement continu, CEA Techno(s), **2003**, *65*.

58 Ko, H.; Chang, S.; Tsukruk, V.V. *ACS Nano* **2009**, *3* (1), 181 – 188.

59 Thundat, T.; Chen, G.Y.; Warmack, R.J.; Allison, D.P.; Wachter, E.A. *Anal. Chem.* **1995**, *67*, 519 – 521.

60 Pinnaduwage, L.A.; Hedden, D.L.; Gehl, A.; Boiadjiev, V.I.; Hawk, J.E.; Farahi, R.H.; Thundat, T.; Houser, E.J.; Stepnowski, S.; McGill, R.A.; Deel, L.; Lareau, R.T. *Review of Scientific Instruments* **2004**, 75 (11), 4554 – 4557.

61 Yi, D.; Greve, A.; Hales, J.H.; Senesac, L.R.; Davis, Z.J.; Nicholson, D.M.; Boisen, A.; Thundat, T. *Applied Physics Letters* **2008**, *93*, 154102.

62 Senesac, L.R.; Yi, D.; Greve, A.; Hales, J.H.; Davis, Z.J.; Nicholson, D.M.; Boisen, A.; Thundat, T. *Review of Scientific Instruments* **2009**, *80*, 035102.

63 Chen, G.Y.; Thundat, T.; Wachter, E.A.; Warmack, R.J. *Journal of Applied Physics* **1995**, *77* (8), 3618 – 3622.

64 Dareing, D.W.; Tian, F.; Thundat, T. *Ultramicroscopy* **2006**, *106*, 789 – 794.

65 Yang, Y.T.; Callegari, C.; Feng, X.L.; Ekinci, K.L.; Roukes, M.L. *Nano Letters* **2006**, *6*, 583 – 586.

66 Li, M.; Tang, H.X.; Roukes, M.L. *Nature Nanotechnology*, **2007**, *2*, 114 – 120.

67 Pinnaduwage, L.A.; Boiadjiev, V.; Hawk, J.E.; Thundat, T. *Applied Physics Letters* **2003**, *83* (7), 1471 – 1473.

68 Houser, E.J.; Mlsna, T.E.; Nguyen, V.K.; Chung, R.; Mowery, R.L.; McGill, R.A. *Talanta* **2002**, *54*, 469.

69 Rouaï, L.; Trapes, C. Elaboration et caractérisation de nanocapteurs, *Techniques de l’ingénieur*, **2006**

70 Schafer, A.H.; Seidel, C.; Chi, L.F.; Fuchs, H. *Advanced Materials* **1998**, *10* (11), 839 – 842.

71 A. Ulman, An Introduction to Ultrathin Organic Films, Academic, New York, **1991**

72 Urbiztondo, M.A.; Pellejero, I.; Villarroya, M.; Sesé, J.; Pina, M.P.; Dufour, I.; Santamaria, J. *Sensors and actuators B* **2009**, *137*, 608-616.

73 Liu, Y.-S.; Ugaz, V.M.; North, S.W.; Rogers, W.J.; Sam Mannan, M. *Journal of Hazardous Materials* **2007**, *142*, 662–668.

74 Liu, Y.-S., Ugaz, V.M., Rogers, W.J., Mannan, M.S., Saraf, S.R. *Journal of loss prevention in the process industries* **2005**, *18*, 139 – 144.

2. Materials and methods

In the first part of the chapter, the energetic materials used in this study are briefly specified. In the second part of the chapter, the main experimental techniques employed are introduced. These techniques are complementary to nanocalorimetry and are used for understanding the thermal behaviour of the explosives during nanocalorimetric experiments and for sample preparation.

2.1. Materials

This part describes several energetic materials of which we have studied the thermal behaviour by nanocalorimetry. The sample specifications and most important characteristics of the used materials will be given in the following.

2.1.1. Nitrocellulose (NC)

Cellulose is the most abundant polymer on the planet. The wool is the natural source of the purest cellulose contains 94% of cellulose. Generally, the cellulose is associated with other substances as lignin and hemicellulose.[1] This natural semi-crystallized polymer is a polysaccharide ($M_n \sim 10^{-6}$ g.mol^{-1}) constituted of cellobiose units shown on figure1.[2] Figure 2 gives an optical micrograph of a spin-cast nitrocellulose film.

Hydrogen links between hydroxyl groups of the same molecule or between the molecules lead to organisation of polymeric chains in bundles of 3.5 mm diameter. They also result in insolubility of cellulose in water (and in organic solvents). Numerous studies have shown that elementary fibrils aggregate in micro-fibrils of cellulose as it is illustrated in figure 3.

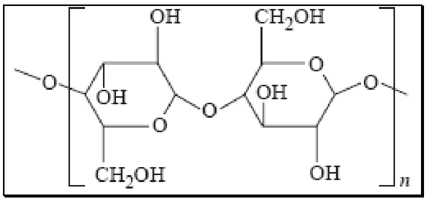

Figure 1. Cellobiose unit.

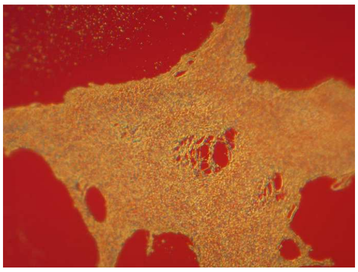

Figure 2. Optical micrograph of a nitrocellulose film.

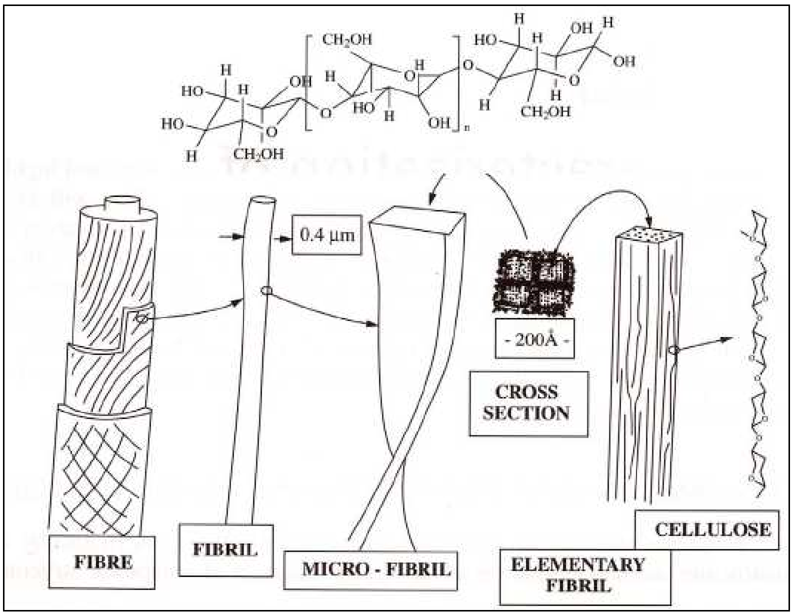

Figure 3. Morphology of a cellulose fiber.[3]

The partial or total substitution of hydroxyl functions allows to form a great number of cellulosic derivates. They possess properties which are rather different from those of cellulose. The oldest cellulosic derivate was discovered in 1846 by the German chemist Christian Friedrich Schonbein. It is an organic ester of cellulose, the nitrocellulose. Contrary to cellulose, the nitrocellulose is soluble in a wide number of organic solvents. The chemical structure of the monomer is shown on figure 4.

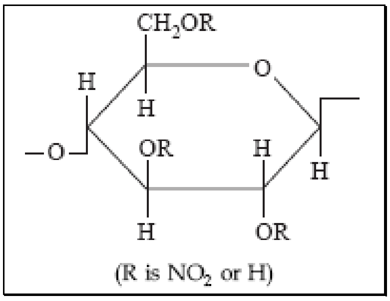

Figure 4. Monomer of nitrocellulose.

When all groups R are hydrogen atoms, the elementary motif corresponds to cellobiose. The hydroxides of the cellobiose are replaced by nitro groups to form nitrocellulose. If the substitution degree (DS) is three, the nitrogen content reaches 14.14%. Nevertheless in practice, the nitrogen proportion in nitrocellulose never exceeds 13.8%[4] (the reaction of esterification is not complete), so the nitrocellulose still contains some hydroxyl groups. The different types of nitrocellulose are characterized by their nitrogen content as presented on figure 5.

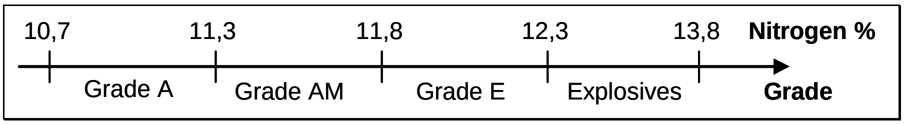

Figure 5. Nitrocellulose grades.

The nitrocellulose grade gives information about solubility. Thus, nitrocelluloses A, AM and E are all soluble in esters and ketones. The designation A means that the nitrocellulose is soluble in alcohol too, the designation AM means Alcohol Medium soluble, E means soluble in esters. The nitrocellulose grades containing more than 12.3% of nitrogen are classified as explosives, whereas the ones having the nitrogen contents between 10.7% and 12.3% are used for lacquers and varnishes. For these applications, the nitrocellulose presents advantage of forming strong and flexible films. The nitrocellulose grades with more than 12.3% of nitrogen are typically stabilized by amines such as diphenylamine. The amines act as nitrogen oxides absorbers thereby hindering the auto-catalytic decomposition of nitrocellulose. The different grades of nitrocellulose are obtained by adjusting the ratio nitric acid / sulphuric acid as well as the water fraction in the acid mixture. A mixture of nitric and sulphuric acids allows to synthesize nitrocellulose with a nitrogen content below 13,5%. The nitrocellulose with nitrogen content above 13.5% is obtained by replacing sulphuric acid with phosphoric acid or acetic anhydride.

A number of techniques have been developed for the synthesis of nitrocellulose, the most known and the oldest among them being nitration of activated cellulose by a mixture of nitric and sulphuric acids.[5] From the chemical point of view, it is in fact not nitration but esterification, nevertheless the word nitration is currently used to specifically term the cellulose esterification by nitric acid. The activation of cellulose fibers is carried out by heating them under pressure in a sodium hydroxide bath till the fibers are dry. The activated cellulose is then dipped in a mixture of nitric and sulphuric acid or phosphoric acids. The hydroxyl groups are substituted by nitro groups. The reactions are outlined in figure 6.[6]

The nitronium ions come from reaction between nitric acid and sulphuric acid. Afterwards they react with alcohol functions (see figure 7).

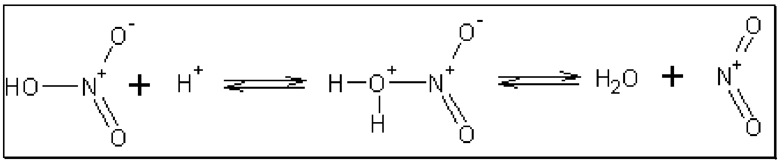

Figure 6. Formation of nitronium ion.

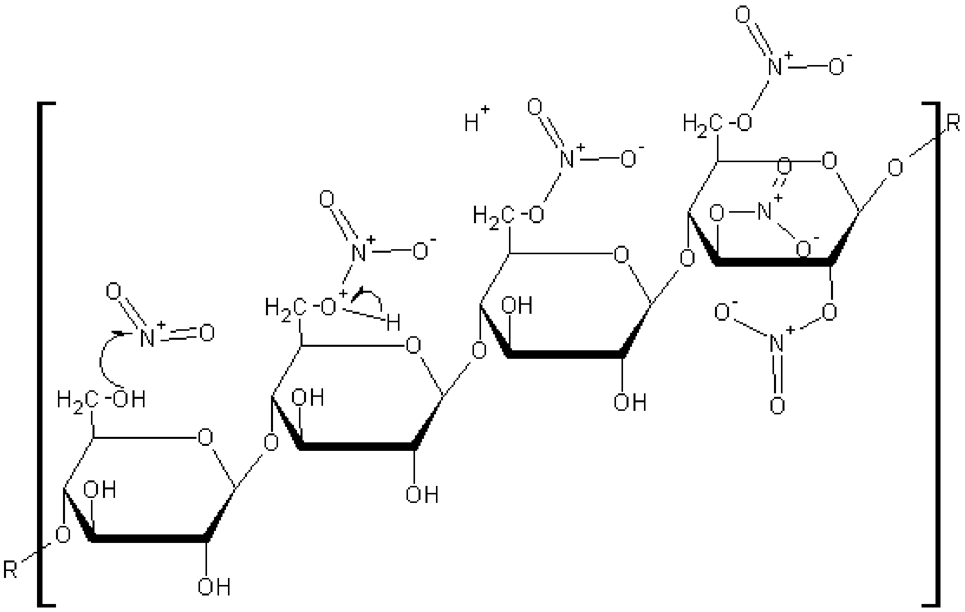

Figure 7. Esterification of activated cellulose.

The dip time of activated cellulose should be sufficient to allow the nitration of cellulose by nitric acid. After the nitration, the nitrocellulose fibers are rinsed with water to remove the acid traces. The adsorbed water on fibers is removed by heating them to 100°C.

- Decomposition of nitrocellulose.

The energy release during decomposition of nitrocellulose is due to the mechanism of intra-molecular oxydo-reduction. This leads to formation of stable small molecules (N_2, CO_2, CO, H_2O).[7] In the regime of detonation of nitrocellulose, the detonation velocity is about 8,5 $km.s^{-1}$. The explosion takes place when a temperature of 185 – 190°C is reached by the system.[8] The high energy released through the nitrocellulose decomposition is due to combustive and combustible elements. The latter are typically highly electronegative elements such as oxygen. These elements can also be linked with weak bonds as it is the case of nitrogen dioxide. They can burn up combustible elements such as the carbon skeleton of nitrocellulose.[9] Therefore an increase of the nitrogen content (NO_2 groups) enhances the combustive ability of nitrocellulose, which explains why this kind of nitrocellulose is ranked as an explosive grade.

- Nitrocellulose characterization.

X-ray diffraction analysis of oriented nitrocellulose fibers indicates that the molecule crystallizes in a right-handed helical conformation 5_2, i.e. the chain makes two turns over the length of five monomers (cf. figures 8 and 9).[10] The crystallographic data in table 1 correspond to a highly substituted nitrocellulose (substitution degree is 3).

Lattice	Elementary cell			γ
	a (Å)	b (Å)	c (Å)	
Orthorhombic	12,25	25,4	9,0	–
Orthorhombic	9,0	14,6	25,4	–
Monoclinic	12,3	8,55	25,4	91°

Table 1. Crystallographic data for nitrocellulose.[11]

It is noteworthy that the c-parameter is not always chosen in the chain direction, which is a more recent crystallographic convention for polymers. This explains why there is an apparent discrepancy between the different unit cells. The molecular model of the 5_2 conformation of nitrocellulose (the second line in table 1) and its lattice is given in figure 8.

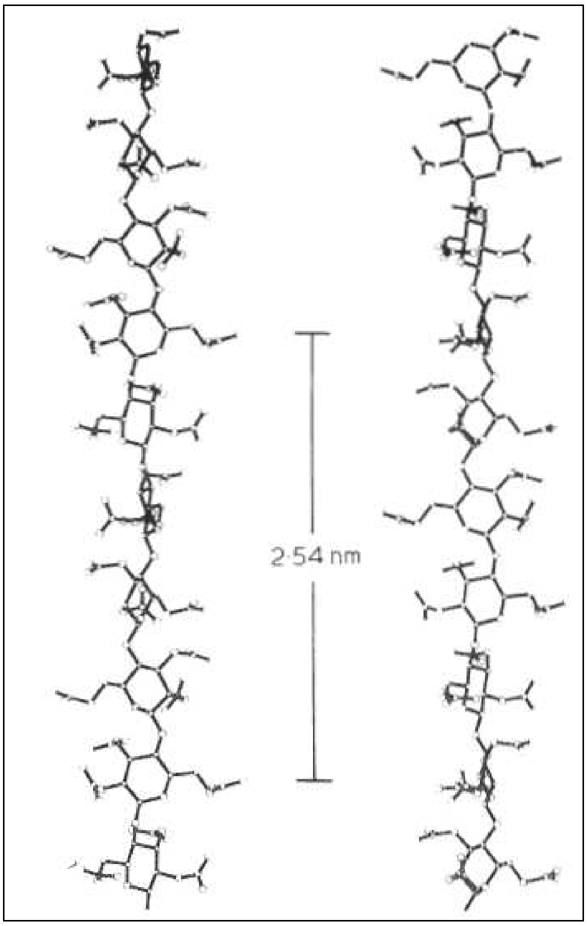

Figure 8. Spiral conformation (5_2) of nitrocellulose.[10]

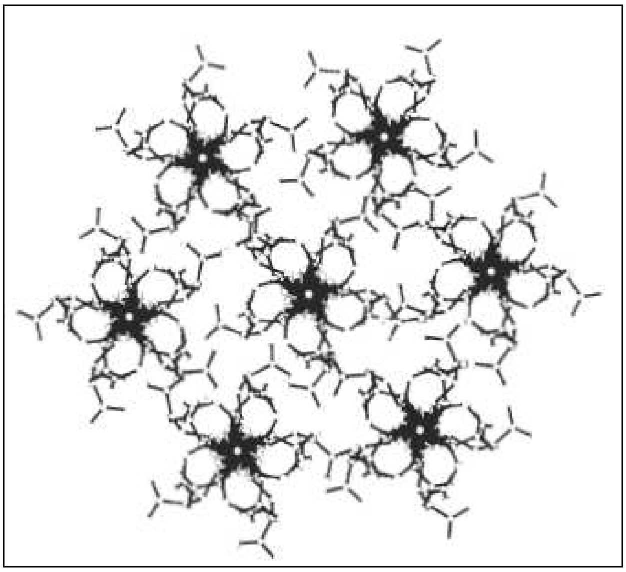

Figure 9. Crystalline lattice of nitrocellulose (DS = 3, a = 9 Å, b = 14,6 Å).

2.1.2. Hexogen (RDX)

Hexogen, also known as RDX, cyclonite, cyclotrimetylenetrnitramine, 1,3,5-trinitri-1,3,5-triazacyclohexane and T4, was synthesized for the first time in 1898 by Georg Friedrich Henning for the medical use. It was recognized as an explosive in 1920. The detonation velocity of RDX at the density of 1.76 g/cm³ is 8750 m/s. This compound is as well used in armament and demolition as in medicine.[12] RDX is a white crystalline solid. The explosive C4 contains around 91% RDX (percentage in weight of C4).[13] The chemical structure of RDX and a typical micrograph of RDX are presented on figures 10 and 11.

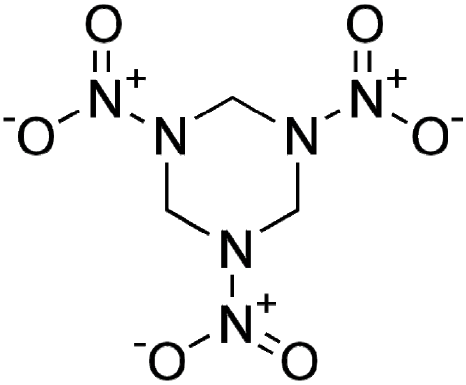

Figure 10. Chemical structure of RDX.

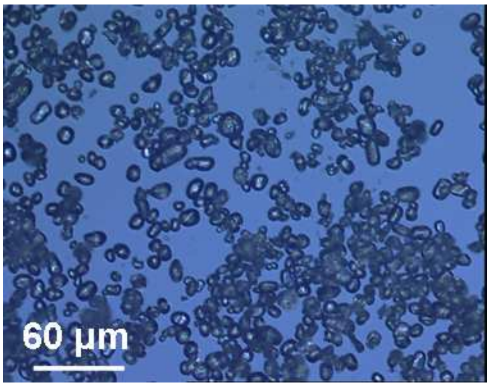

Figure 11. RDX crystals used in the present study.

The chemical reaction between hexamine and nitric acid to produce RDX reads as following :

$$C_6H_{12}N_4 + 10HNO_3 \rightarrow C_3H_6N_6O_6 \textbf{\textit{ (RDX)}} + 3CH_2(ONO_2)_2 + NH_4NO_3 + 3H_2O$$

It is produced in a batch reactor. For example, one can mix 110 g of nitric acid and 10 g of hexamine, i.e. the weight percentage of nitric acid is 98 %. After reaction time of 10 min at a temperature of 30°C the RDX yield is 80% (for the given example it corresponds to 12.75g).[14]

RDX can be crystallised from different solvents including benzene, nitromethane, acetone, acetic acid, nitric acid.[15] It exists in four polymorphic phases. The α-RDX is the room-temperature ambient-pressure phase, its heat capacity at room temperature is 1.126 J/(g.K).[16] The α and ß phases can be thermally decomposed. The γ phase is transformed during a heating ramp either in α or β phase, then the decomposition follows. The decomposition rate of α-RDX increases with increasing pressure, this fact suggests a bimolecular-type reaction mechanism. The activation energy of α-RDX for decomposition is 213 kJ/mol[17], and 144 ± 4.3 kJ/mol in unsealed crucibles.[18] The α-RDX crystallizes in orthorhombic structure with eight molecules per unit cell with the following unit cell parameters: a = 13.182 Å, b = 11.574 Å, c = 10.709 Å.[19] The crystalline lattice consists of pairs of RDX molecules in which the association of the NO_2 groups dominates the intermolecular cohesion.[20,21,22] RDX forms the α phase below 4 GPa and is in the γ phase above this pressure. The α-γ transition is a reversible first-order phase transition.[23,24] Above 18.8 GPa, a new phase (δ-RDX) is formed. The observation of δ-RDX is based on the appearance of new vibrational bands in high-pressure infrared spectra.[25] The β-RDX is prepared by evaporation of a high boiling solution such as thymol-RDX or nitrobenzene-RDX. Nevertheless the β phase is transformed in α phase upon contact with α-RDX or during sharp agitation. The β → α transition induces shear stresses and/or crystal defects, which affects the performance of α-RDX. After crystallization, dendritic crystals of β-RDX are obtained. The β-RDX crystals can be distinguished from the plates of α-RDX by their birefringence and morphology.[26,27]

2.1.3. Pentrite (PETN)

Pentrite, also known as nitropenta or pentaerythritol tetranitrate, was discovered in 1891 by Tollens and Wiegand. This energetic material is also used in medicine as a vasodilator for heart conditions treatment[28]. PETN has a detonation velocity over 7620 $m.s^{-1}$. It is more sensitive to shock or friction than TNT.[29] The chemical structure and morphology of PETN crystals are given in figures 12 and 13.

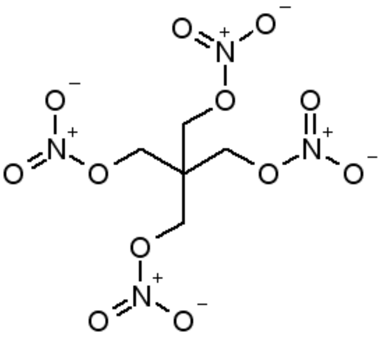

Figure 12. Chemical structure of PETN.

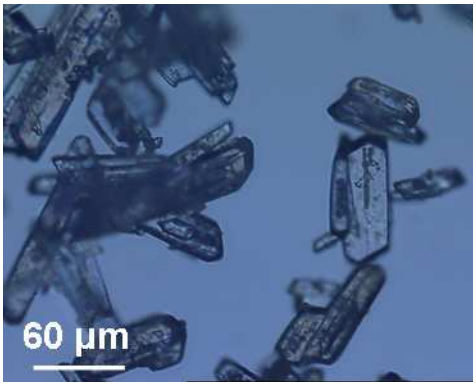

Figure 13. PETN crystals used in the present study.

The following reaction (nitration of pentaerythritol in a mixture of concentrated nitric and sulphuric acids in ratio 2:1) is used for synthesis of PETN:

$$C(CH_2OH)_4 + 4HNO_3 \rightarrow C(CH_2ONO_2)_4 + 4H_2O$$

The temperature of solution is kept below 25 – 30 °C during 30 min, then the PETN is filtered, washed with water and neutralized with sodium carbonate solution. It is subsequently purified by dissolving in acetone, recrystallization and air-drying.[30] At ambient pressure and temperature, PETN crystallizes in tetragonal structure, the lattice parameters are the following: a = b = 9.38 Å and c = 6.71 Å.[31, 32, 33] The activation energy of the PETN decomposition is 175.0 ± 3.3 kJ/mol in unsealed crucibles.[18]

2.1.4. *Hexanitrohexaazaisowurtzitane (CL-20)*

2,4,6,8,10,12-hexanitro-2,4,6,8,10,12-hexaazaisowurtzitane, also called CL-20, is a relatively new energetic material synthesised by Arnold Nielsen in 1986. CL-20 is a polycyclic nitramine with a three-dimensional cage structure and is probably the highest energetic single component compound. The molecular structure of this cage-shaped molecule and its crystals are shown on figures 14 and 15.

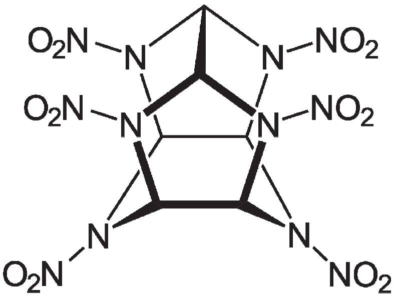

Figure 14. Chemical structure of CL-20.

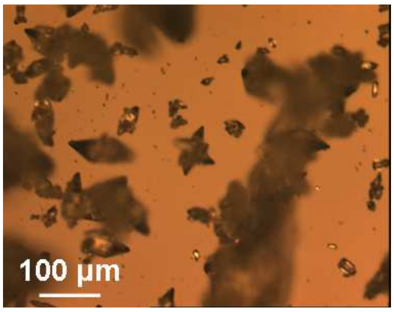

Figure 15. CL-20 crystals used in the present study.

The starting reagents for synthesis reaction[34,35] of CL-20 are N,N-dimethylformamide, acetic anhydride, HBIW and nitric acid. The reaction is sketched in figure 16.

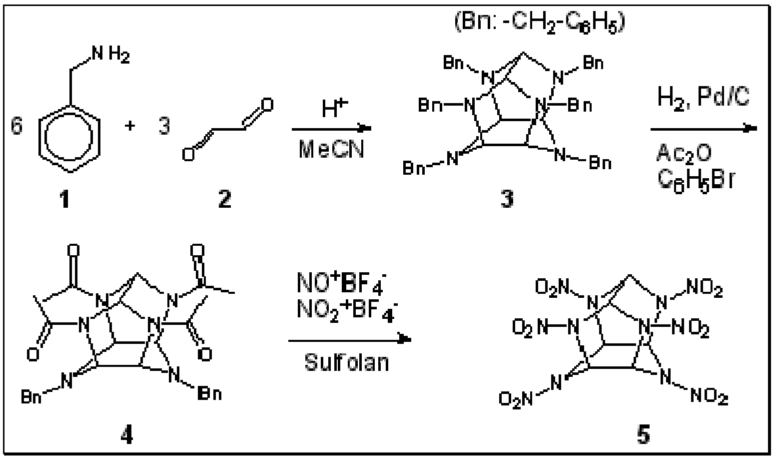

Figure 16. Synthesis of CL-20.

Six polymorphs of CL-20 (α to ζ) have been identified.[36, 37] At ambient pressure and room temperature, the ε-phase is the most stable. The crystal structure of the ε-phase is monoclinic. It contains four molecules per unit cell. The lattice parameters are the following: a = 13.696 Å, b = 12.554 Å, c = 8.833 Å and β = 111.18°.[38] During DSC heating ramps, a solid – solid ε → γ phase transition occurs at 160 – 170°C. It is followed by thermal decomposition of the γ-phase at temperatures above 210°C.[39] The activation energy parameter is found for γ-Cl20: $E_a = 207 \pm 18$ kJ.mol^{-1} (in nitrogen atmosphere)[39]. The gaseous products of the CL-20 decomposition at 240°C are identified as N_2, N_2O, CO_2, CO. The main gaseous products at 250°C - 400°C are NO_2 (50%) and NO (25%) whereas CO, HCN, N_2O, CO_2 are produced in small quantities.[40] An amorphous solid residue (17% of the weight of the starting sample) is present at the end of the CL-20 decomposition. The molecular formulas corresponding to the residue are $H_3C_3N_2O_2$ and $C_6H_5N_5O_2$. It was observed that the residue contains C=O, C=N, N – H and amide functions. In reference[41] the authors found the molecular formula of the residue formed at 285°C, which was $C_2H_2N_2O$. In addition, they found that the unreacted CL-20 is more thermally unstable than the original CL-20.

2.1.5. *Summary on the thermodynamic data of the energetic materials studied in this work*

The thermodynamic data of the energetic materials is listed in table 2. The melting temperature and the melting enthalpy, the decomposition temperature and decomposition enthalpy are determined from DSC curves at different heating rates. The curves are given in appendix 2.1 to 2.4.

Material	Nitrocellulose	RDX	PETN	CL-20
Cp at 298 K (J/(g.K))		1.126		
$T_{melting}$ (°C)	–	205	141	–
Melting enthalpy (J/g)	–	95	157	–
$T_{decomposition}$ (°C)	192 to 195.5	205 to 209	170 to 185	200 to 231
Decomposition enthalpy (J/g)	1518 to 2308	4688 to 5041	3750 to 3840	1200 to 4542

Table 2. Thermoanalytical data of the studied energetic materials.[42-43]

2.2. Characterization techniques

2.2.1. Nanocalorimetry

The nanocalorimeter designed for performing thermal analysis at high heating rates employs a commercial thermal sensor (www.xensor.nl) and a controller (www.nanotlab.com). The unique feature of the NanoCalorimeter is that it can handle extremely small amounts of sample such as pico- and nano-grams. The samples are for example spin-coated polymer films, one micrometric crystal: such samples cannot be studied by DSC.

The extension of the sample size to the nano- and pico-range can be interesting for development of new surface-related technologies that require modification of nanometer-thick surface layers in a controllable way. It can also be useful in pharmaceutics where new material production and purification is a time-limiting step and the amounts of sample are sometimes very small. It should be noted that the speed of heating/cooling is not only crucial for the investigation of small samples but also opens the way to carry out real-time analysis for example for an on-line quality control. In addition, having access to extremely high rates of thermal treatment is of fundamental scientific importance as it can produce materials in unusual state (e.g., amorphisized materials obtained by rapid cooling from the isotropic melt).

1. Technical characteristics of the Nanocalorimeter

The main technical characteristics of the nanocalorimeter are the following:[44]

- temperature range for the sample: 173 – 523 K (-100 to +250 °C); short-term (i.e. for some minutes) heating up to +500 °C (773 K),
- absolute sample temperature is better than 1.0 K,
- the sample temperature resolution is better than 0.001 K,
- the maximum heating rate of the sample depends on the membrane size of the sensor (e.g., for XEN-3977 sensor, the maximum heating rate in DC mode is approximately 1 000 000 K/s),
- there are two operation modes: the AC mode using temperature modulation with a constant offset or temperature modulation with synchronous detection at double frequency and the DC mode using rectangular pulse or a pulse of arbitrary form,
- there are three heating modes: external, internal (i.e. using a heater assembled on the silicon nitride membrane) or combined,
- the frequency range of the sample temperature modulation is 1.0 Hz to 40 kHz,
- the precision of the phase lag of the sample temperature response is better than 0.05°,
- the maximum sampling rate (time resolution) is 200 kHz (5 μs),
- the maximum buffer capacity is 100 000.

Two kinds of calorimetric sensors are used for our experiments. The first one mounted on a TO-5 housing are used for experiments followed by optical microscope in reflexion. The second type of sensor are flat sensors with hole in the housing behind the membrane to allow monitoring with optical microscope in transmission. Both sensors are presented on figure 17.

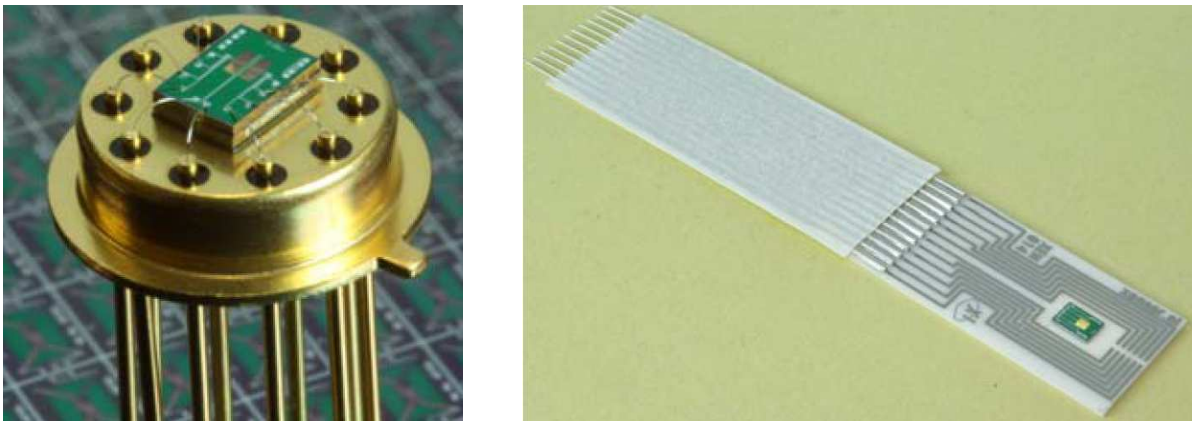

Figure 17. Sensor mounted on TO-5 housing (left image) and flat sensor (right image).

The setup on figure 18 allows imaging the sample during calorimetric experiment with an optical microscope in reflexion equipped with a Photron high speed CCD camera.

For fast-heating measurements, the CCD camera is triggered by a signal of 4.5V delivered by the nanocalorimeter.

Figure 19 shows the trigger and heater voltage signals for an experiment performed with a sampling rate (SR) of 20 kHz. There is a delay of 0.5 ms between the trigger of the high speed CCD camera and the beginning of the heating ramp. This delay corresponds to $\frac{1}{SR}$, which shows that the triggering system operates properly.

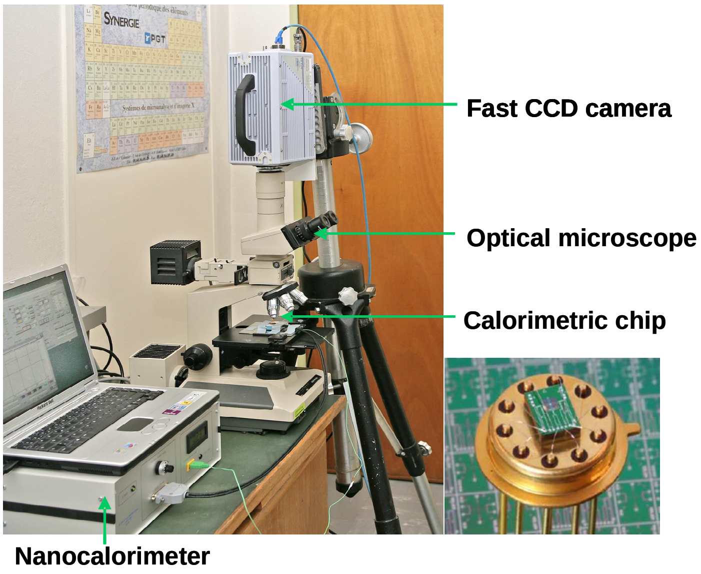

Figure 18. Laboratory setup for fast-heating measurements monitored with a high speed CCD camera.

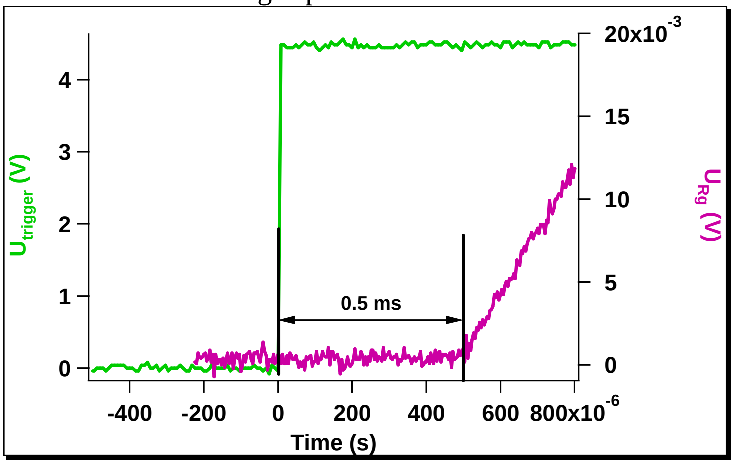

Figure 19. Nanocalorimetric trigger and heater voltage signals.

2. *Types of nanocalorimetric experiments*

Several types of experiments can be performed with our nanocalorimetric device. The main menu panel of the Nanocalorimeter software is shown on figure 20.

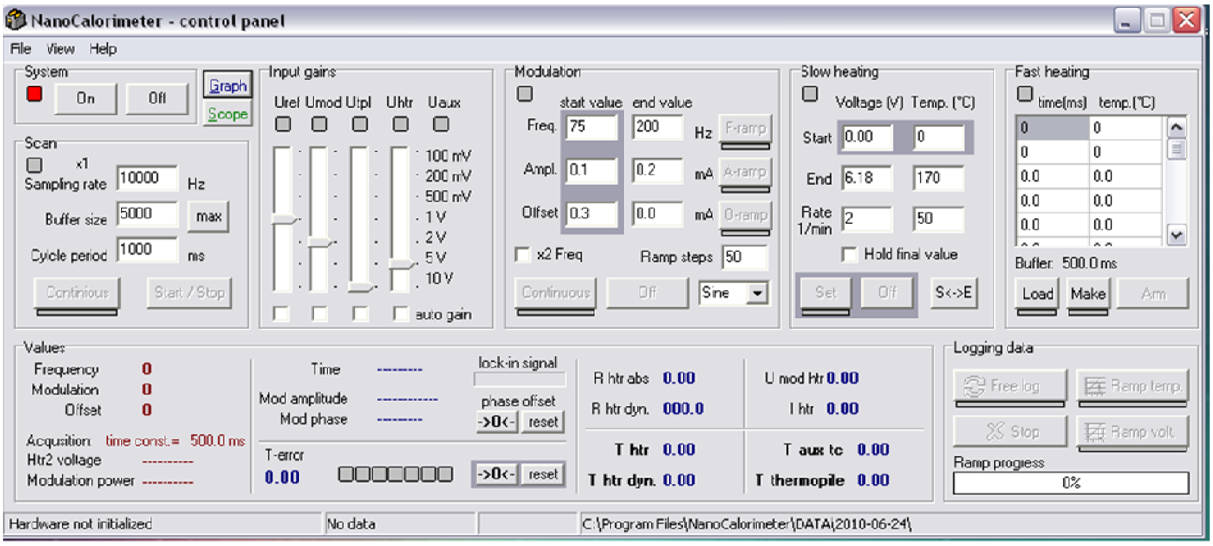

Sampling rate 10000 Hz
Buffer size 5000
Cycle period 1000 ms
Freq. 75 200 Hz
Ampl. 0.1 0.2 mA
Offset 0.3 0.0 mA
Ramp steps 50
Sine
Start 0.00 0
End 6.18 170
Rate 1/min 2 50
Buffer: 500.0 ms
Frequency 0
Modulation 0
Offset 0
Acquisition time const.= 500.0 ms
Htr2 voltage ---------
Modulation power ---------
Time ---------
Mod amplitude ---------
Mod phase ---------
T-error 0.00
R htr abs 0.00
R htr dyn. 000.0
T htr 0.00
T htr dyn. 0.00
U mod Htr 0.00
I htr 0.00
T aux tc 0.00
T thermopile 0.00
Hardware not initialized
No data
C:\Program Files\NanoCalorimeter\DATA\2010-06-24\

Figure 20. Main control panel of the Nanocalorimeter program.

Continuous logging regime is used to record data for example during an isotherm. To this end, the button “free log” in the logging data part is engaged as shown on figure 21.

Different types of ramps can be executed to determine the influence of the modulation parameters on the thermal behaviour of the sample such as frequency, modulation amplitude and modulation offset ramps. The corresponding panel is given on figure 22.

The modulation panel makes it possible to control the current flowing through the heater. The button “continuous” starts the oscillator in a continuous mode with the frequency, amplitude and offset indicated in the “start value” column.

The values in the column “end value” are only used to perform frequency ramp, amplitude ramp or offset ramp in the range indicated.

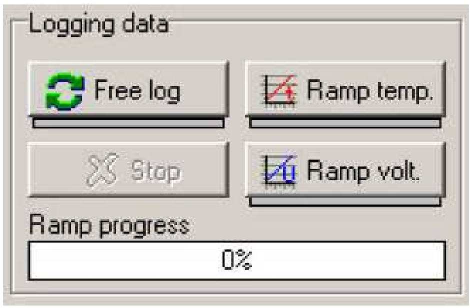

Figure 21. Logging data part of the menu.

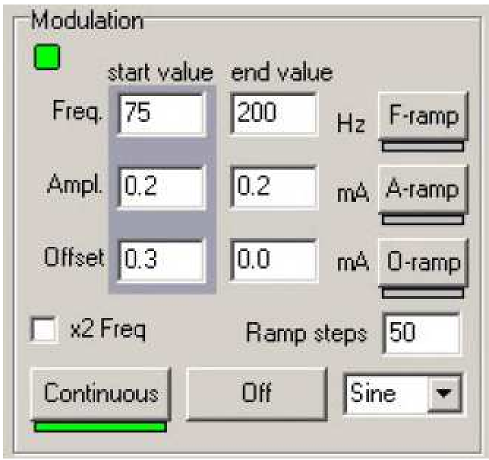

Freq. 75 200 Hz
Ampl. 0.2 0.2 mA
Offset 0.3 0.0 mA
Ramp steps 50
Sine

Figure 22. Modulation panel.

Heating of the sample can be realized with two different methods. Using the internal heater (cf. “Slow Heating” panel shown on figure 23), the assessable heating rates are in the range of those used in classical DSC.

With the elements of this group, one can control the second (or “guard”) heater of the sensor. One can set the temperature, voltage and ramp parameters. When the voltage value is set, it will be automatically recalculated into the temperature and vice versa using the calibration file. If “Hold final value” is checked, the heater will hold its final temperature after execution of the ramp, otherwise it will be set back to the “start” value.

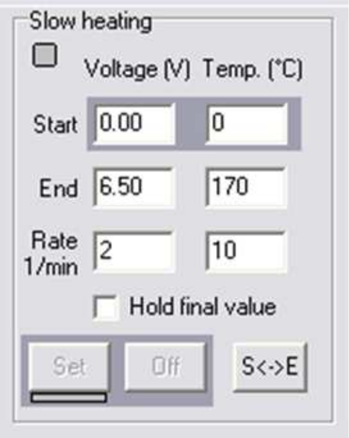
Slow heating

☐	Voltage (V)	Temp. (°C)
Start	0.00	0
End	6.50	170
Rate 1/min	2	10

☐ Hold final value

Figure 23. Slow heating panel.

In the other method, a voltage ramp is applied to the heater, which is suitable for high heating rates. For fast heating measurements, the voltage ramp is defined either in the table “Fast Heating” presented on figure 24 or by an arbitrary waveform (voltage ramp).

The button “Load” allows downloading the arbitrary waveform from an external heater (one column of floating point values in volts). The heating rate of the fast heating experiment can be adjusted with the point number of the wave and the used sampling rate. The faster heating ramps are obtained with fewer points in the wave and with a higher sampling rate. The highest heating rate of a sensor mainly depends on the corresponding membrane size as all sensors have the same membrane thickness.

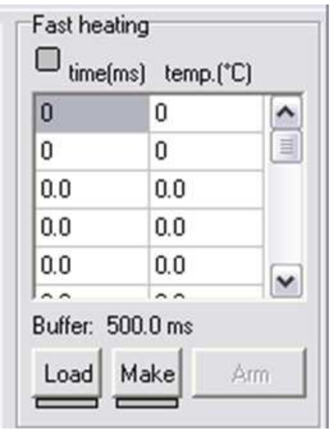
Fast heating

☐

time(ms)	temp.(°C)
0	0
0	0
0.0	0.0
0.0	0.0
0.0	0.0

Buffer: 500.0 ms

Figure 24. “Fast heating” table panel.

Interestingly, the calorimetric chip can also detect the approach or disengagement of the AFM tip onto the membrane surface. The graphic on figure 25 presents nanocalorimetric curves obtained at different z positions of the tip above the membrane surface. The nanocalorimetric curves are recorded with free log at ambient temperature with a modulation frequency of 75 Hz, an amplitude modulation of 0.1 mA, an offset of 0.3 mA.

At the beginning, the tip is above the membrane and far from the membrane surface (part 1). Then the tip approaches the surface during engagement (part 2). In part 3, the tip sweeps the surface. Finally, the tip is disengaged (part 4), and in part 5, the tip is far from the membrane surface.

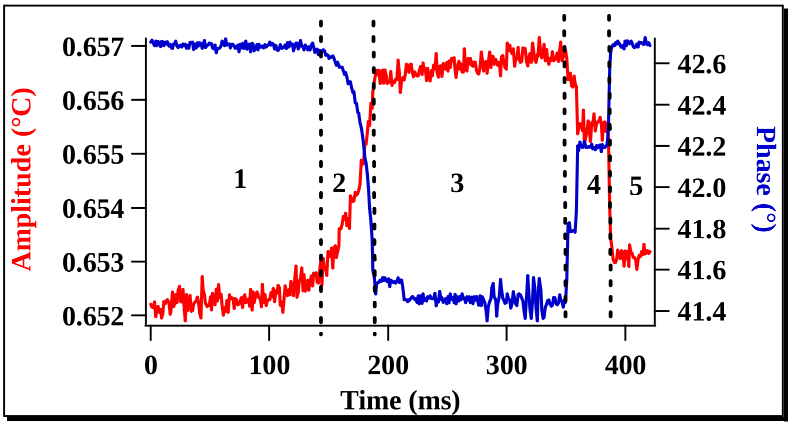

Figure 25. Nanocalorimetric curves obtained at different z positions of the tip.

3. *Calibration standards for the Nanocalorimeter*

Usually, the substances used to calibrate DSC have to be pure, non-volatile and should not react with material of the crucible or with the purge gas. They should show a well-defined phase transition (as a melting) with no measurable hysteresis, a high transition velocity and they should not be influenced by grain size, particle size or shape.[45] Typically these compounds are indium, tin, gallium, bismuth, zinc, aluminium. The chosen substances must cover the temperature range of the experiment.

For our nanocalorimetric experiments, two substances were chosen to check the calibration: indium and zinc powders from Strem Chemicals. The optical and SEM micrographs of these particles are given on figures 26 and 27.

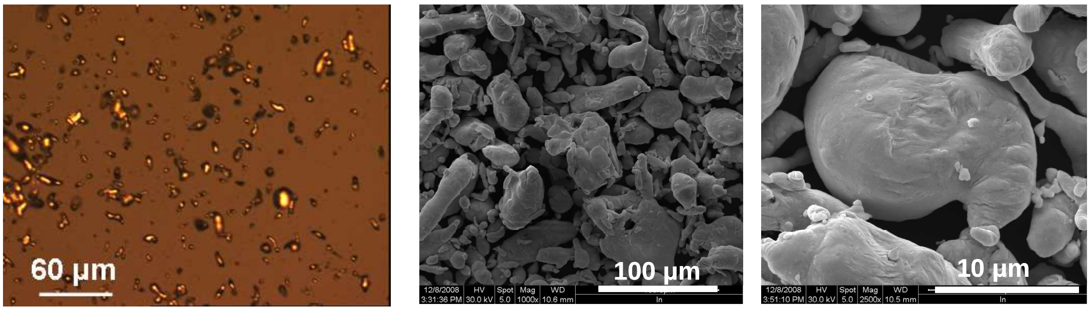

Figure 26. Indium microparticles (optical micrograph on the left, and SEM micrographs in the middle and on the right).

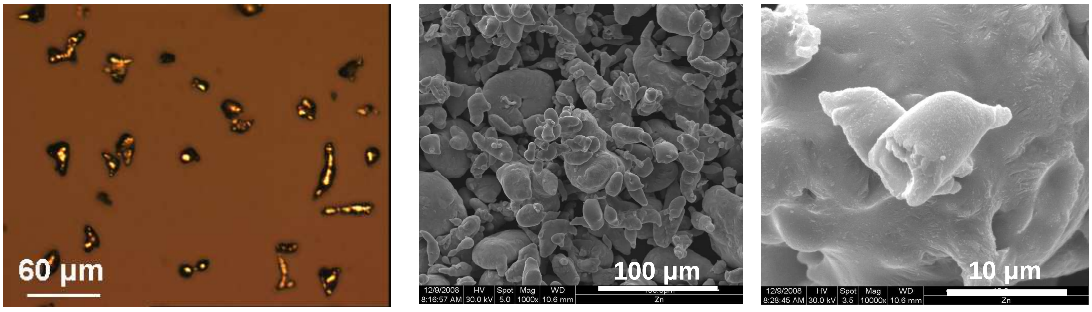

Figure 27. Zinc microparticles (optical micrograph on the left, and SEM micrographs in the middle and on the right).

It is clear that there is a wide range of particle size and variety of shapes. By heating the particles above the melting temperature, the particle shape is not observed to change dramatically. In our experimental protocol, an indium particle was deposited in the membrane center then a first heating ramp is performed. Afterwards the indium particle was removed and a zinc particle was deposited at the same place. The heating ramps of indium particle and zinc particle allow to check the temperature calibration. The thermodynamic data[46, 47] of indium and zinc are listed in table 3:

	$T_{melting}$ (°C)	ΔH_m ($J.g^{-1}$)	Heat capacity ($J.g^{-1}.K^{-1}$)
indium	156.6	28.62	0.233
zinc	419.5	102.02	0.387

Table 3. Thermoanalytical data for In and Zn.

To check the purity of the materials, EDX experiments were performed on the used indium and zinc particles. The obtained spectra are given on figures 28 and 29.

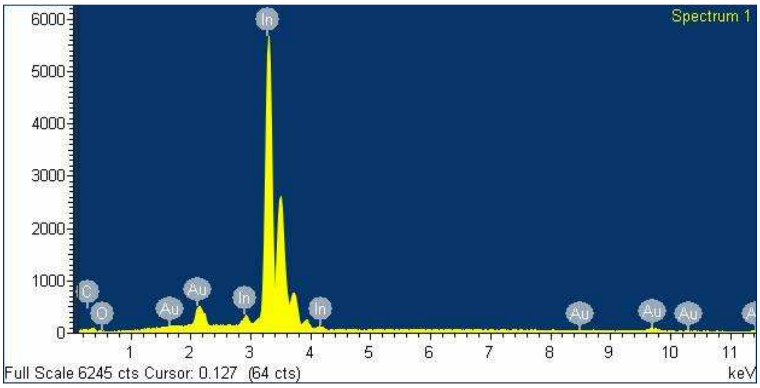

Figure 28. EDX spectrum of In particle.

On figure 28, the three peaks between 3,5 and 4 keV are attributed to tin.

The spectra show that particles are rather pure. The purity of each metallic powder is calculated based on six measurements, and is 92% for indium and 90.6% for zinc powder. In particular, the oxidation layer on the particle surface is really negligible: the oxygen peak on graphs 28 and 29 looks really small. Therefore these particles can be used as calibration standards.

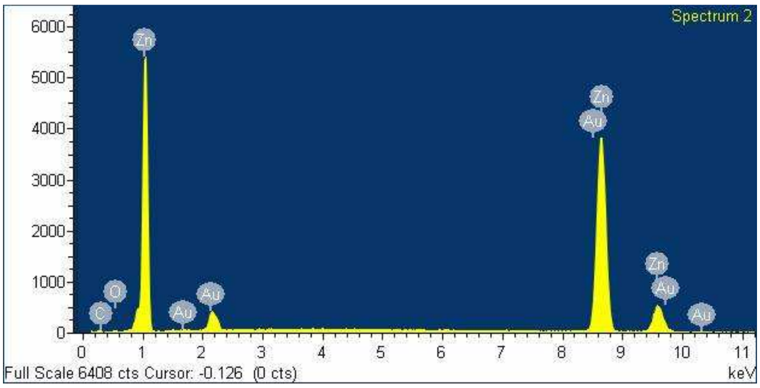

Figure 29. EDX spectrum of Zn particle.

2.2.2. Differential Scanning Calorimetry

In this work, DSC was used to characterize energetic materials in open and closed crucibles. The measured heat capacity was used to calculate the sample mass of the energetic material deposited on the nanocalorimetric sensor.

The DSC Q1000 from TA Instruments at ISL was used to study energetic materials in closed crucibles to determine the kinetic parameters of the decomposition reaction. This instrument has a temperature precision of 0.05 °C and a sensitivity of 0.2 µW. The crucibles used for this device are closed so the pressure inside the crucible can reach a few hundreds bars. These crucibles are used to perform DSC measurements through the decomposition of energetic materials.

The Mettler-Toledo DSC 822E was used at IS2M in order to obtain experimental DSC curves on inert materials such as polystyrene. The resolution is of 0.4 µW and 0.2 °C. The sample can be heated from 0.01 °C/min to 20 °C/min.[48]

In both DSC devices, the sample mass is typically about few mg, whereas the mass is about few nanograms for the Nanocalorimeter.

2.2.3. Atomic Force Microscopy (AFM)

AFM is a surface characterization technique suitable for studies of both conductive and non-conductive surfaces. The principle of AFM consists to sweep the surface sample with a sharp tip mounted on the extremity of a micro-cantilever. The tip shape can be assimilated to a sphere with a curvature radius of one to several nanometers. The interactions between the atoms of the tip and the atoms of the sample surface allow determining the sample topography.

During operation, the horizontal and vertical deflections of the cantilever are transmitted to a position-sensitive photo-diode using a laser beam bounced from the cantilever. A piezo-electric scanner allows performing controlled motion along x, y and z-axes.[49] AFM can be used in three modes: contact mode, tapping mode and non-contact mode. In the contact mode, the tip is in permanent contact with the sample surface. In tapping mode, the contact between the tip and the sample surface is intermittent, with the cantilever being driven at its resonant frequency. In non-contact mode, the cantilever also vibrates near its resonant frequency however the interactions with the sample surface are mainly attractive. In this work, the sample surface was imaged in tapping mode. To visualize isolated nitrocellulose chains, the three kinds of nitrocellulose are solubilised in acetone at different concentrations, then the samples are deposited on HOPG (Highly Oriented Pyrolitic Graphite) in ambient conditions and observed by AFM in Tapping mode with DLCS tips.

2.2.4. Microbalance

AFM cantilevers are characterized by the probe dimensions (width, length, thickness) and the elastic properties (Young’s modulus). These parameters determine the resonant frequency (ω) and spring constant (k). The cantilever stiffness varies with the thickness and length. The largest error on the spring constant is due to the measurement of the cantilever thickness.[50]

1. Mass measurement

In this work, AFM and more precisely micro-cantilevers are used as a microbalance to determine the weight of microparticle.

The SEM micrographs given on figures 26 and 27 show that particles used for calibration have irregular shape and unsmooth surface so one cannot easily estimate their mass. The LSM 700 Bio/Mat (Zeiss) confocal microscope has lateral resolution of 200 nm and z-resolution of 20 nm.

To use a microcantilever as a microbalance, one can assimilate the cantilever to a spring with a spring constant *k*. In this way, when a particle with a mass *m* is attached to the cantilever, the resonant frequency of the cantilever decreases. The mass determination with AFM cantilever is based on the frequency difference between the resonant frequency of the cantilever with and without the particle:

$$m = k_{lev} \cdot \left(\frac{1}{\omega^2} - \frac{1}{\omega_0^2} \right)$$

In the equation m is the mass of the particle, k_{lev} is the spring constant of the cantilever, ω_0 is the angular frequency of the empty cantilever and ω is the angular frequency of the cantilever loaded with particle. To weight the particle it is thus necessary to accurately know the spring constant of the cantilever. The latter is defined as the force required to bend the cantilever per unit distance. According to the cantilever manufacturer (in this case, www.spmtips.com/csc/c12/tipless), the spring constant can significantly vary even between cantilevers of the same batch because of manufacturing variability.[51] The spring constant strongly depends on the thickness of the cantilever which can vary from 20% or more in the same batch.[52] We used cantilevers with low spring constants in order to have a higher sensitivity of the resonant frequency to the added mass.

2. *Calibration of the cantilever spring constant*

A summary of the different techniques used to determine the spring constant is given by Burnham and al.[53] The authors describe the advantages and disadvantages of each technique as well as the uncertainty on the spring constant value. In the following part, we are going to explain the five most frequent methods used to determine the spring constant of a cantilever.

- The **Cleveland method**[54, 55] uses tungsten beads with different diameters. When a mass m is added to the end of the cantilever, the resonant frequency is given by :

$$\upsilon = \frac{\omega}{2\pi} = \frac{1}{2\pi} \sqrt{\frac{k}{m + m*}}$$

Where m* is the effective mass of a uniform cantilever of rectangular cross section ($m^* = 0.24m_b$ where m_b is the mass of the cantilever). This equation can be rearranged as follows:

$$M = k(2\pi\upsilon)^{-2} - m*$$

According to this last equation, a linear plot of the added mass versus $(2\pi\upsilon)^{-2}$ gives a line the slope of which gives the spring constant of the cantilever. The tungsten beads used in this method come from a polydisperse tungsten powder with a mean particle diameter of 20 μm and a standard deviation of 15 μm. The particle mass is determined according to the diameter of the bead (measured by optical microscope) and the bulk density of tungsten (19.3 g/cm^3). With this method, the errors on spring constant can be due to the diameter measurement of the spherical beads and to the position of the bead on the cantilever[56,57] :

$$k = k_E \left(\frac{L}{L - \Delta L} \right)^3$$

where k_E is the end spring constant, L the length of the cantilever and ΔL is the distance between the particle and the end of the cantilever.

- The **Sader method** requires to know the density or mass of the cantilever and its dimensions, the unloaded resonant frequency and the quality factor of the fundamental mode of vibration. The thermal noise spectrum of the cantilever is measured to obtain the quality factor (Q).[58] This value depends on the density and viscosity of the cantilever environment. Air damping leads to a shift of 4% in the resonant frequency down from its value in vacuum. Gold coating used to increase the laser beam reflection is also known to influence the resonant frequency.[56]

- The **reference lever method of spring constant calibration** proposed by Torii[52] uses calibrated cantilevers the spring constant of which are already known. This method can measure the force constant of cantilevers (k between 0.1 and 10 N/m) with a precision of 20%. The cantilever of unknown spring constant is pressed against three calibrated cantilevers with different spring constants. These three cantilevers are tipless rectangular silicon levers with nominal spring constants of 0.16, 1.3, and 10.4 N/m. They are manufactured with extremely well controlled dimensions and material properties and have an ideal rectangular shape. A force curve is performed on the calibrated cantilever with the cantilever of unknown spring constant (called the uncalibrated sensor in the following). The spring constant is deduced from the slope of the curve force performed against different calibrated cantilevers. Experimentally, the spring constant is measured as follows. The uncalibrated cantilever is first press against a hard surface, and the cantilever deflection (δ_{tot}) is measured. Then, the uncalibrated cantilever is pressed against the end of the reference cantilever, and the cantilever deflection (δ_{test}) is measured.

The spring constant of the uncalibrated cantilever is determined by:

$$k_{test} = k_{ref} \frac{\delta_{tot} - \delta_{test}}{\delta_{test} \cos\theta}$$

In the above equation k_{ref} is the spring constant of the reference cantilever and θ is the angle between the uncalibrated cantilever and the reference cantilever. The resulting k_{test} can be influenced by the stick-slip motion when one spring is pushed against another one[53] and by the contact position of the two cantilevers.

- The **thermal noise method**[59] is based on the equipartition theorem which states that the total energy of a system at equilibrium is shared in equal parts between its different components. For the cantilever, the thermal energy stored in the cantilever oscillation equals its potential energy. The quantity $k_B.T/2$ is associated with one degree of freedom. So according to this theorem and by considering the cantilever as an ideal spring of constant k, we have :

$$k = \frac{k_B T}{\left\langle A^2 \right\rangle} \qquad (1)$$

A² is the mean square displacement of the cantilever, T is the absolute temperature (K), k_B is the Boltzmann constant. Since the cantilever is not a perfect simple harmonic oscillator because of other vibration modes, a correction is brought to the equation:

$$k = \frac{0.971 k_B T}{\left\langle A^2 \right\rangle} \qquad (2)$$

If we take into account bending of the cantilever in the chip holder of the AFM with an angle α and the correction due to the other vibration modes, the equation becomes:

$$k = \frac{0.817 k_B T \cos^2\alpha}{\left\langle A^2 \right\rangle} \qquad (3)$$

Experimentally, the optical sensitivity is first determined by pushing the cantilever against a hard surface. The slope of the force curve corresponds to the optical sensitivity. In this method, the main source of error comes from the deflection sensitivity measurement, the resulting uncertainty in the spring constant is about 8%.[60] Then, the signal of the thermal noise (figure 30) is acquired with a sampling frequency of 122 Hz.

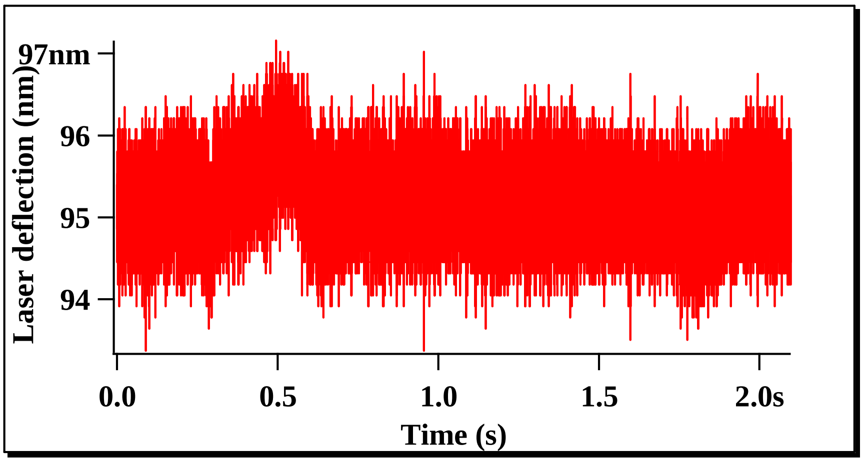

Figure 30. Thermal noise signal for a cantilever (k = 0.026 N/m).

A power spectral density function (PSD) is calculated from the acquired data (figure 31). The Fourier transform of the signal recorded during a time period t allows to determine the frequency range contained in the signal. The PSD of the thermal noise image is peaked on the resonant frequency of the cantilever fundamental mode as shown on the figure 31.

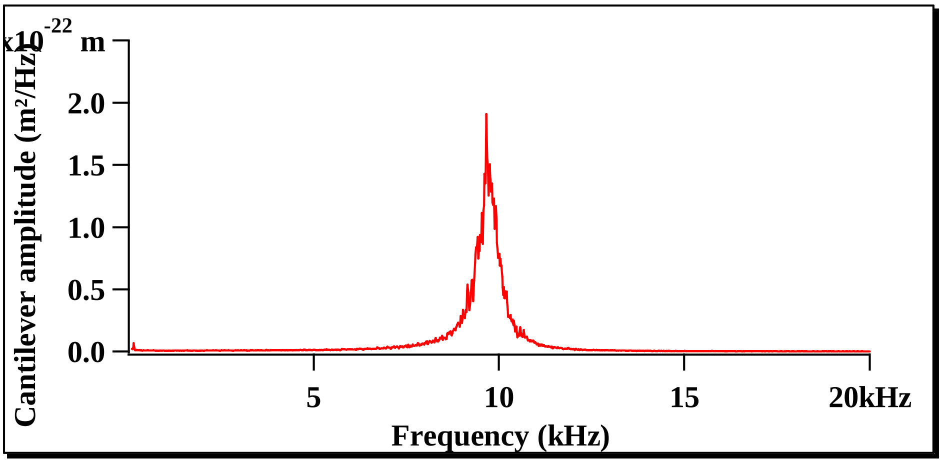

Figure 31. PSD of the thermal noise signal.

The segment length of the PSD influences the smoothing of the curve whereas the window function type can control the frequency leakage between the frequency bins[61]. To exclude the problems with aliasing it is preferential to check for each measurement if the frequency peak is centred on the frequency resonance determined with the AFM auto tune function.

In the next step, the PSD of the thermal noise image is integrated (figure 32).

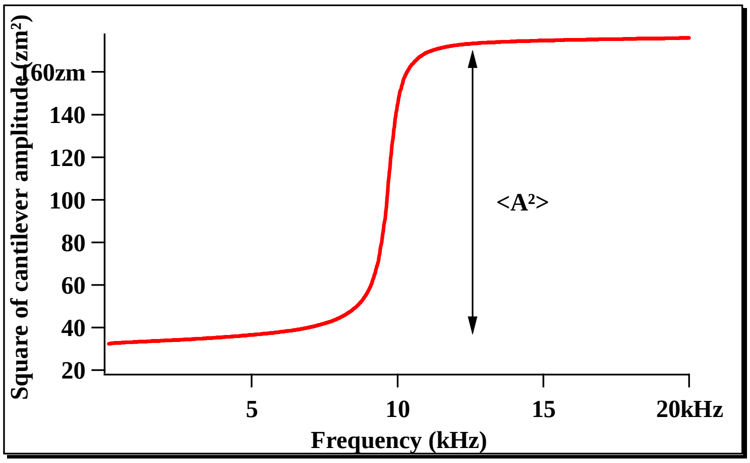

Figure 32. Integrated the thermal noise spectrum.

The step in the integrated curve corresponds to the mean amplitude square of the cantilever. The integration limits corresponds to five times the peak width.

The spring constant of the cantilever is then calculated thanks to the equation (1).

This method is rapid and easy experimentally but it is only valid for cantilevers with a resonant frequency smaller than 61 kHz because of the Nyquist frequency. Indeed, the sampling frequency has to be equal or superior to the double of the maximal frequency contained in the signal. The highest scan rate obtained with Nanoscope IV is 122 Hz. This value is obtained by applying zero to the rounding parameter in the scanner calibration file and by acquiring the thermal noise image with 256 lines. The cantilevers used in the work have resonant frequencies of 14, 10 and 20 kHz. All frequencies are given in appendix 2.5.

The software used with the controller Nanoscope IV is Nanoscope V5.12b41. According to Veeco specifications, the sensitivity of the laser on photodiodes can be enhanced by decreasing the deflection limit in the panel “Other controls” before acquiring a thermal noise image. The deflection limit clips and amplifies the residual cantilever deflection signal.[62] The deflection setpoint in feedback control panel is negative in order to perform a false engagement. The absolute value must be superior to the vertical value on the microscope (vertical position of the laser spot on the photodiode). It must be smaller than the value of deflection limit otherwise a part of the deflection signal is cut. A false engagement can also be done by clicking on engage and when the dialogue box appears on the screen hitting Ctrl-F.

The following experiment was performed on a cantilever E (resonant frequency = 12 kHz).

On figure 33, we can observe that the resonance peak disappears and another peak appears at 4 kHz for a deflection limit smaller than 1 V. This alias can be also generated by decreasing the scan rate of the thermal noise image (see figure 34).

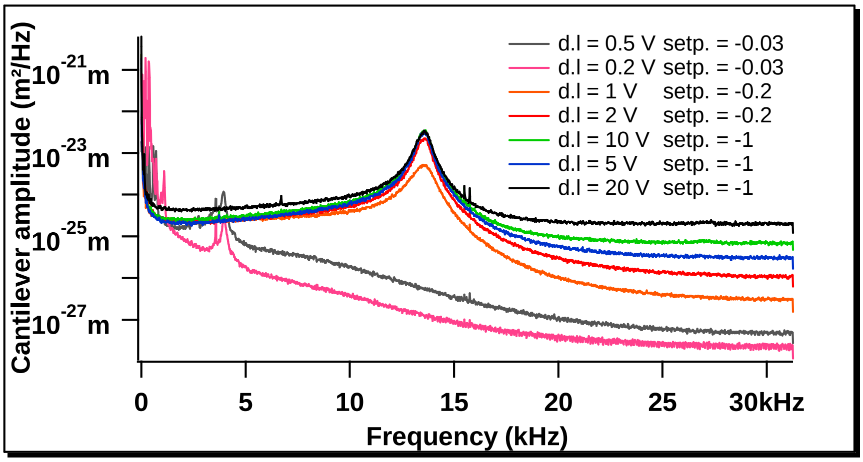

Figure 33. Resonance peak for several deflection limits.

The presence of the alias at 4 kHz indicates that there is a filter at 8 kHz

$$f_{filter} = \frac{f_{resonance} + f_{alias}}{2}$$

The area of the resonance peak is in this case incorrect because a part of the peak is removed by the filter.

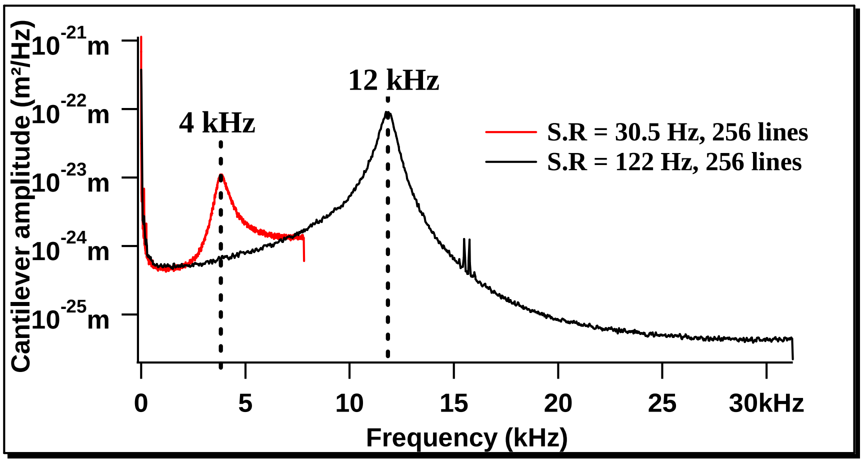

Figure 34. Aliasing of the resonance peak.

According to Veeco, the filter is located in the controller. The measurement can be performed without this filter by placing a Signal Access Module (SAM) between the controller and the microscope as shown on figure 35.

The “input 1” BNC on the back of the controller is connected to the “In 0 Output” BNC on the front panel of the SAM. The thermal noise image is recorded with the signal of the Input 1.

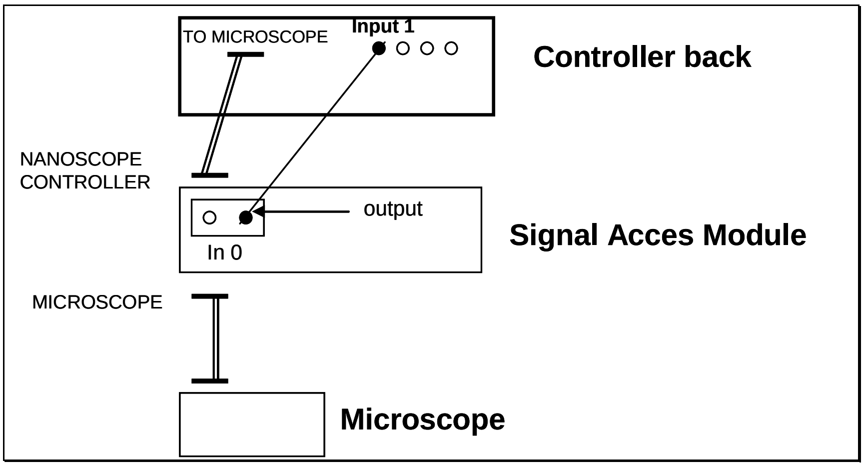

Figure 35. Electrical scheme of the experimental setup.

- The cantilever spring constant can be also calibrated using **laser Doppler vibrometry** (LDV)[63]. This technique is used to perform non-contact vibration measurements of a surface. The principle is based on the Doppler shift for an object which moves from the source of the wave (laser beam). The vibrometer has a subpicometer resolution, the laser spot has a diameter of about 2.5 μm.

The measurement of the cantilever displacement by LDV allows eliminating some uncertainties caused by optical lever detection with photodiodes on an AFM. Experiments were performed with model CLFC AFM probes from Veeco Probes. The tipless rectangular silicon probes have three cantilevers with nominal spring constants of 0.16, 1.3, and 10.4 N/m. This technique enhances the signal-to-noise measurements of the deflection as shown on figures 36.[68]

B. Ohler explained in his publication that for these experiments, the laser spot is positioned at the end of the cantilever. Displacement data are collected with a frequency in the range of 256 to 1280 kHz, depending on the resonance frequency of the cantilever. For each cantilever, a power spectral density function is measured, the resonance peak is fitted and the spring constant is calculated with the equation of the Sader method and with the equation of the thermal tune method.

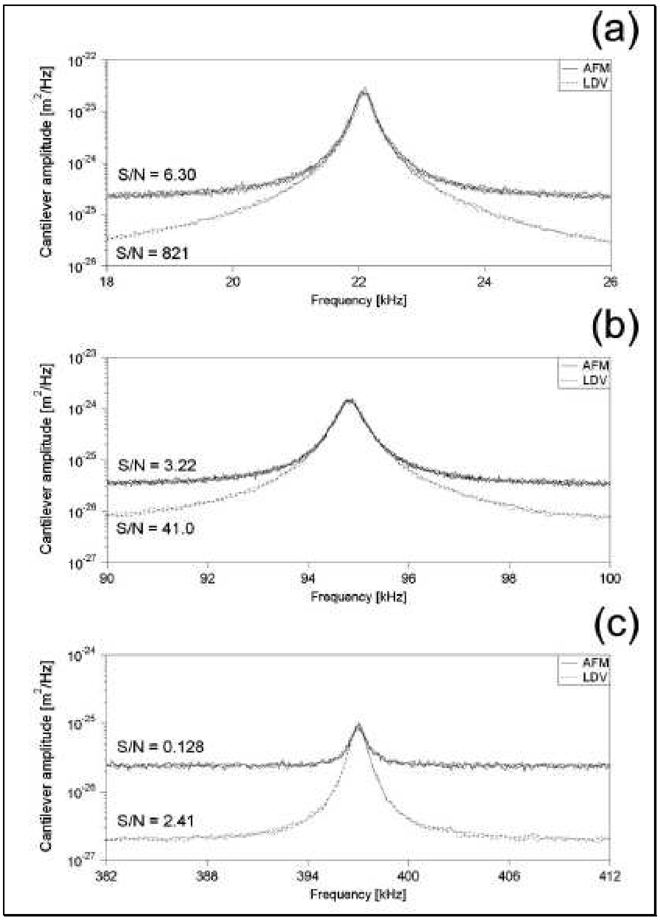

Figure 36. Three typical resonance peaks for the (a) 400 μm long cantilever, (b) 200 μm long cantilever, and (c) 100 μm long cantilever of an AFM probe are shown as collected by both AFM and LDV. The signal to noise ratios shown are the averages for each group of three curves over the bandwidths indicated by the frequency scale.[68]

2.2.5. X-Ray analysis

The X-ray analysis were performed using two devices : Small Angle X-ray Scattering (SAXS) [64,65] and powder diffractometer. [66]

Small Angle X-ray Scattering is an essential characterization technique to elucidate structure of semi-crystalline polymers. This technique allows studying the material structure at different scales from ca. hundred nanometers to four nanometers.

The powder diffractometer is equipped with an X-ray tube, detector, goniometer, collimating slits. The detector receives the X-ray photons diffracted by the sample, the diffracted beam has an angle θ with the sample reticular plane (the angle between the incident beam and the diffracted beam is 2θ). In the case of crystalline powder, the diffracted beam direction is given by the Bragg law nλ = 2dsinθ where d is the reticular distance, λ is the wavelength and n is the diffraction order.

2.2.6. Optical microscopy

Optical microscopy studies were carried out with several microscopes.

At IS2M, an Olympus BX51 microscope equipped with Olympus DP70 digital colour camera and a Leica microscope are used. Differential Interference Contrast (DIC) is employed to study thin deposited films of polystyrene and nitrocellulose. In the DIC accessory, the polarized light is separated into two beams, which results in an image with a pseudo-3D contrast. DIC microscopy allows to observe the uniformity of the deposited films.

The Leica microscopes from IS2M and ISL are used in combination with the micromanipulator to place particles on the membrane sensor.

An Olympus microscope from ISL is used in Polarized Optical Microscopy (POM) to identify the variation of birefringence in energetic material crystals during nanocalorimetric measurements. Figure 37 illustrates the operation of the microscope in polarized light.

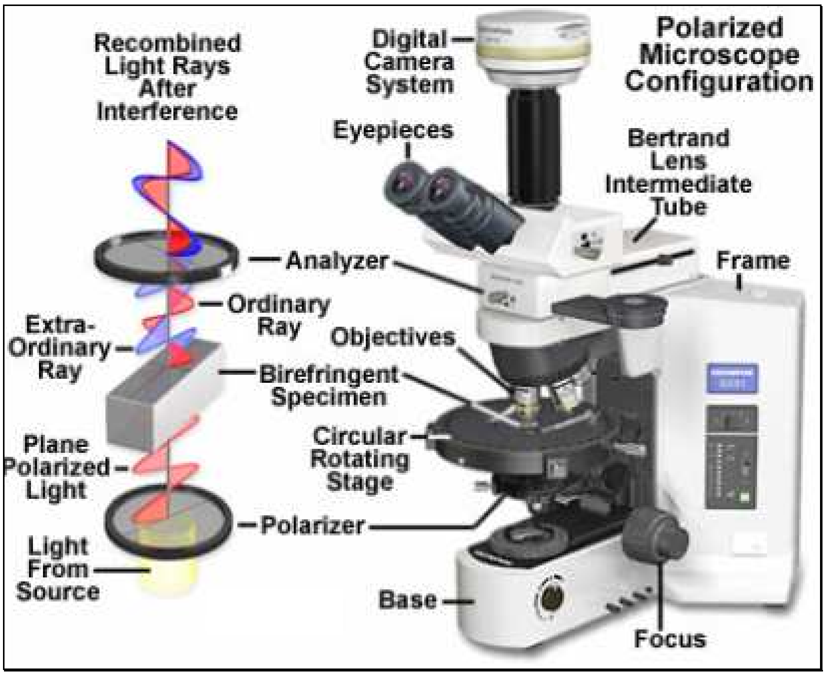

Figure 37. Schematics of the polarized light optical microscopy.

The polarizer and the analyzer have to be crossed to perform observation in polarized light.

At ISL, fast heating measurements of energetic materials are filmed with a high speed CCD camera placed on the microscope (with natural or polarized light). Usually, the high speed CCD camera takes 5000 frames per second for fast heating experiments (but the camera is in fact able to acquire even more images per second). The recorded films are used to interpret the nanocalorimetric curves.

2.2.7. Raman

A Renishaw inVia Raman microscope with a 514 nm laser for excitation wavelength was used to obtain the local-scale spectra of explosives at ISL.

The Raman technique is a vibrational molecular spectroscopy. The principle of this technique is based on scattering of an incident electromagnetic wave on molecules. The scattered light has either the same frequency as the incident electromagnetic wave (elastic scattering) or a different frequency (inelastic scattering). The Raman technique derives from an inelastic light scattering process. The energy loss is characteristic of the bond energy in the molecule, therefore Raman spectra can be used as fingerprints of molecules.

The Raman shift spectra were obtained from 200 cm^{-1} to 3200 cm^{-1}. The system was calibrated using a silicon wafer (vibration at 520.56 cm^{-1}). The acquisition of each spectrum was performed by varying the acquisition time. Preliminary experiments were performed to determine the maximal laser power one can use without destroying sample, the laser power was then fixed at 10% for the experiments.

2.3. Sample preparation

Before sample preparation, the extraneous fragments on the sensor are removed with the micromanipulator then the sensor is rinsed with ethanol and acetone followed by heating at 200°C during one hour. The fragments found on the sensor surface are probably pieces of silicon coming from the edges of the chip or wires. Ethanol and acetone are used to remove dust particles. The applied heating allows to dry the sensor and to eliminate internal tensions which can affect the value of the heater resistance and the heat capacity of the membrane.

The sensor can be reused after some experiments with energetic materials which are completely decomposable. In these cases, no residue remains on the membrane active area while the sublimated material outside the measurement area is removed by cleaning the sensor in a good solvent (for example, acetone is a good solvent for RDX and PETN).

Several methods were tested to place a particle or a crystal in the membrane centre. The micro particles and crystals for nanocalorimetric experiments are placed on the membrane sensor by micromanipulation, the thin films are deposited by spin-coating on the whole sensor surface or by micro-injection on the measurement area of the sensor.

2.3.1. Micro-manipulation of particles and crystals

The sample preparation of a particle or crystal is performed by placing the object in the membrane center. This was carried out with a micromanipulator MP-85 from Sutter Instrument Company. As shown on figure 38, the micromanipulator is constituted of six independent Huxley screws and one tip fixed on an instrument holder. The tip movements are governed by the screws.

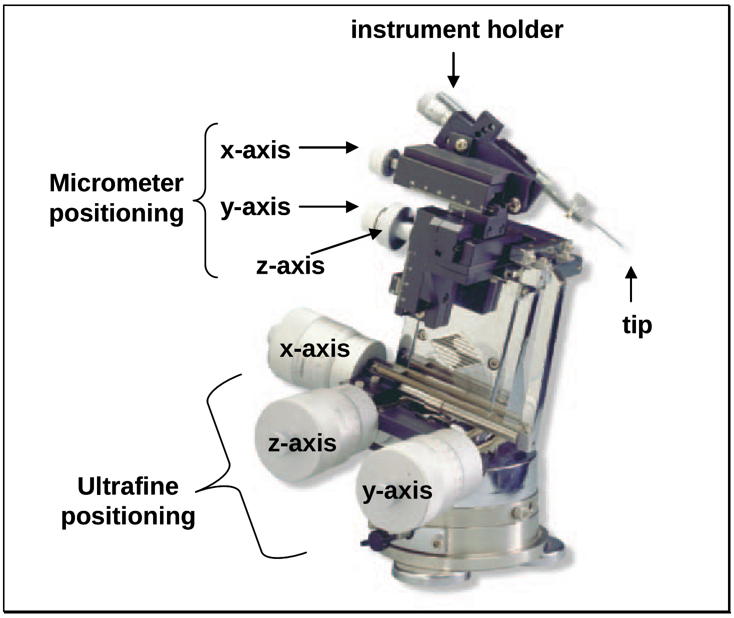

Figure 38. Micromanipulator MP-85 from Sutter Instrument Company.

The three screws in the upper part of the micromanipulator are used for the micrometer tip displacement, the three others allow smooth, precise and ultrafine tip displacements through a 10:1 reduction mechanism. The micromanipulator is a heavy and solid device which ensures that there is no tip drift during movements. The MP-85 dimensions are 25 cm x 25 cm x 28 cm.

The X-axis can vary from 0 to 45 degrees in 15 degrees increments. The resolution from the micrometer screws is 10 µm whereas the resolution from ultrafine screws is 0.2 µm.[67] A number of instruments can be fixed on the instrument holder (micro-needles, micro-scalpel, micro-hook, …) but these instruments are typically too rigid to prepare sample on the sensor membrane. Indeed, this kind of tools can break the membrane or sputtered circuitry. Therefore it is convenient to fix a thin metal wire or a hair on a micro-needle. The metal wires are either gold wire with diameter of 12.7 µm (Alfa Aesar) or platinum wire with diameter of 25 µm or a copper/nickel alloy wire with diameter of 12 µm. The tip used to pick and place an object depends on the interaction (Van der Waals forces) between the object (particle or crystal) and the tip.

Figure 39 shows the experimental setup which combines the micromanipulator with an optical microscope in order to place the object in the membrane center.

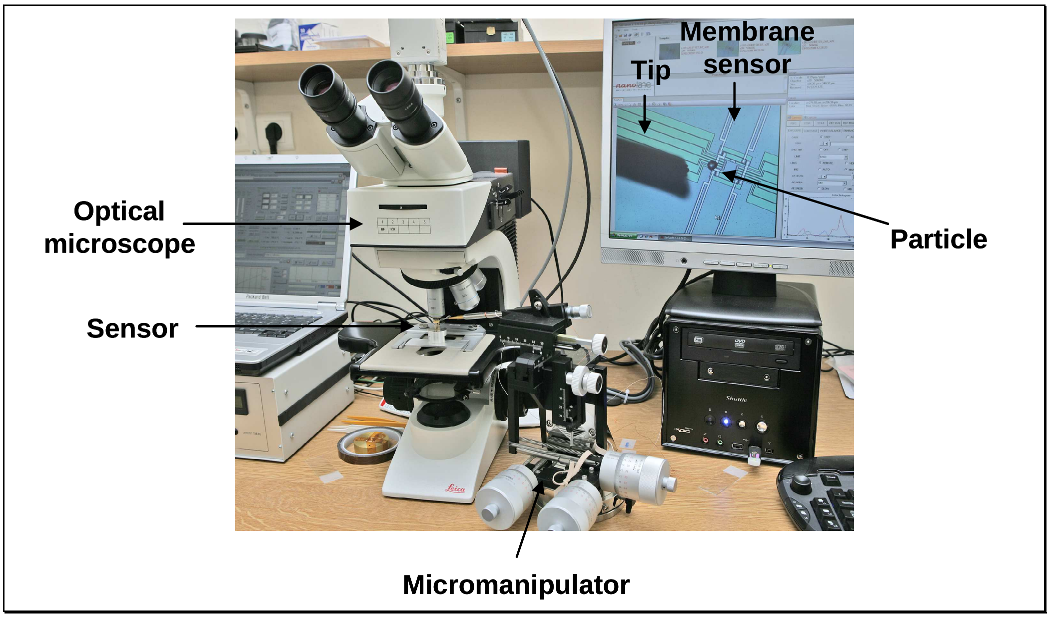

Figure 39. Experimental setup used to load the calorimetric chip sensor.

In order to prepare the sample, we focus the long distance objective first on the tip. The tip is placed in the center of the image, then it is withdrawn by turning the z-axis screw until its shadow is visible. Then, the studied powder (energetic materials or calibration standards) is spilled over the microscope slide. The object which has the desired characteristics (size and shape) is picked up with the micromanipulator tip. After that, the sensor is placed under the microscope and the objective is focalized on the sensor membrane. The tip with the particle is approached from the membrane surface and is rubbed over the surface until the particle gets released from the tip onto the membrane surface. Finally, the particle is gently pushed with the tip toward the membrane center.

2.3.2. Deposition of continuous thin films by spin-coating

Spin-coating was used to prepare supported polymer films. Nitrocellulose solutions in acetone were deposited by spin-coating on the sensor membrane. The parameters of spin-coating are 3000 rpm for 90s and an acceleration ramp of 1000 rpm/s. The film uniformity was checked with optical microscope equipped with a DIC filter.

The film thickness is measured by AFM with the scratch method on films deposited on silicon wafer. (The solutions are deposited by the same manner on silicon wafer than on calorimetric chip).

---

1 Polymeric materials encyclopedia, J. C. Salamone

2 Polymer Data Handbook, **1999**, Oxford University Press

3 Department of materials science and engineering of MIT, Course 3.94 Polymer Morphology, Lecture 20, Pethrick & Viney **2003**

4 www.azom.com

5 Miles, F. D. Cellulose nitrate, **1955**, London, Interscience.

6 http://ger001.ge.funpic.de/Nitrogenium/index.php?datei=./main/exp/nitrocellulose.htm

7 A propos des matériaux énergétiques, groupe SNPE

8 A study of propellant decomposition by differential scanning calorimetry, House J.E. Jr.; Flentge, C.; Zack, P.J. *Thermochimica Acta* **1978**,

9 Heats of decomposition, combustion and explosion of nitrocelluloses derived from wood and cotton, Lemieux, E.; Prud'homme, R.E. *Thermochimica Acta* **1985**,

10 Meader, D.; Atkins, E.D.T.; Happey, F. *Polymer* **1978,** 12, 1371 – 1374.

11 *Polymer Data Handbook*, *Cellulose nitrate* by Yong YANG, Oxford University Press, Inc

12 The Chemistry of Explosives, Akhavan, J. RSC Paperbacks : Athenaeum Press, Ltd. : Manchester, U.K 1998

13 www.wikipedia.org

14 Luo, K.M.; Lin, S.H.; Chang, J.G.; Huang, T.H. *Journal of loss prevention in the process industries* **2002**, *15*, 119 – 127.

15 McCrone W.C. *Analytical Chemistry*, **1950**, *22* (7), 954 – 955.

16 Botcher, T.R.; Wight, C.A. *Journal Physical Chemistry* **1993**, *97*, 9149 – 9153.

17 Chandra Shekar, N.V.; Govinda Rajan, K. *Bull. Mater. Sci.* **2001**, *24* (1), 1 – 21.

18 Lee, J.S.; Hsu, C.K.; Chang, C.L. *Thermochimica Acta* **2002**, *392-393*, 173 – 176.

19 Goto, N.; Fujihisa, H; Yamawaki, H.; Wakabayashi, K.; Nakayama, Y.; Yoshida, M.; Koshi, M. *J. Phys. Chem. B* **2006**, *110*, 23655 – 23659.

20 Karpowicz, R.J.; Brill, T.B. *J. Phys. Chem.* **1984**, *88*, 348 – 352.

21 Choi, C.S.; Prince, H. *Acta Crystallogr.*, *Sect. B* **1972**, *28*, 2857-62.

22 Karpowicz, R.J ; Brill, T.B. *J. Phys. Chem.* **1983**, *87*, 2109-12.

23 Olinger, B.; Roof, B.; Cady, H.H. Symposium on high dynamic pressures ; Paris, France, **1978**

24 Davidson, A.J.; Oswald, I.D.H.; Francis, D.J.; Lennie, A.R.; Marshall, W.G.; Millar, D.I.A.; Pulham, C.R.; Warren, J.E.; Cumming, A.S. *CrystEngComm* **2008**, *10* (2), 162 – 165.

25 Ciezak, J.A.; Jenkins, T.A.; Liu, Z.; Hemley, R.J. *J. Phys. Chem. A*, **2007**, *111*, 59 – 63.

26 Karpowicz, R.J.; Serglo, S.T.; Brill, T.B. *Ind. Eng. Chem. Prod. Res. Dev*. **1983**, *22*, 363 – 365.

27 Millar, D.I.A.; Oswald, I.D.H.; Francis, D.J.; Marshall, W.G.; Pulham, C.R.; Cumming, A.S. *Chem. Commun* **2009**, 562 – 564.

28 Russek H. I., *American Journal of Medical Science* **1966**, 252

29 Jaw, K.-S., Lee, J.-S., *Journal of Thermal Analysis and Calorimetry* **2008**, *93* (3), 953-957.

30 Zhuang, L.; Gui, L.; Gillham, R.W.; *Environ. Sci. Technol.* **2008**, *42*, 4534 – 4539.

31 Halfpenny, P.J.; Roberts, K.J.; Sherwood, J.N.; *J. Appl. Crystallogr*. **1984**, *17*, 320 – 327.

32 Gruzdkov, Y.A.; Dreger, Z.A.; Gupta, Y.M. *J. Phys. Chem. A* **2004**, *108*, 6216-6221.

33 Cady, H.H.; Larson, A.C. *Acta Crystallogr. B* **1975**, *31*, 1864 - 1869

34 www.wikipedia.org

35 Ledgard, J. The preparatory manual of explosives, Third edition, Seattle, **2007**

36 Russel, T.P.; Miller, P.J.; Piermarini, G.J.; Block, S. *J. Phys. Chem*. **1993**, *97*,

---

37 Foltz, M.F.; Coon, C.L.; Garcia, F.; Nichols III A.L. *Propell. Explos. Pyrotech*. **1994**, *19*, 133

38 van der Heijden, A.E.D.M; Bouma, R.H.B. *Crystal growth and design* **2004**, *4* (5), 999 – 1007.

39 Turcotte, R.; Vachon, M.; Kwok, Q.S.M.; Wang, R.; Jones, D.E.G. *Thermochimica Acta* **2005**, *433*, 105 – 115.

40 Korsounskii, B.L.; Nedel'ko, V.V.; Chukanov, N.V.; Larikova, T.S.; Volk, F. *Russian Chemical Bulletin* **2000**, *49* (5), 812 – 818.

41 Dong, L.-M.; Li, X.-D.; Yang, R.-J. *Acta Phys. Chim. Sin*. **2009**, *25* (5), 981 – 986.

42 Appendix 2.1 to 2.4

43 Explosivstoffe, 3. Auflage, Rudolf Meyer, **1973**, Verlag Chemie GmbH, Weinheim

44 Nanocalorimeter, User manual

45 Gmelin, E.; Sarge, St.M.; *Pure & Appl. Chem*., **1995**, *67* (11), 1789 – 1800.

46 www.ktf-split.hr/periodni/fr

47 www.wikipedia.org

48http://www.pt.ctw.utwente.nl/organisation/facilities/analysis/Mettler%20Differential%20Scanning%20Calorimeter%20(DSC822E).doc/

49 Defaux, M. Thesis, Université de Haute-Alsace, Mulhouse, **2008**.

50 Mendels, D.A.; Lowe, M.; Cuenat, A.; Cain, M.G.; Vallejo, E.; Ellis, D.; Mendels, F. *J. Micromech. Microeng.* **2006**, *16*, 1720-1733

51 Johnson, W.T. Support Note from Agilent Technologies, USA, **2008**.

52 Characterization of application specific probes for SPMs, M. Tortonese, M. Kirk, *Proceeding Micromachining and imaging* **1997**,

53 Burnham, N.A.; Chen, X.; Hodges, C.S.; Matei, G.A.; Thoreson, E.J.; Roberts, C.J.; Davies, M.C.; Tendler, S.J.B. *Nanotechnology* **2003**, *14*, 1-6.

54 Cleveland, J.P.; Manne, S.; Bocek, D.; Hansma, P.K. *Review Scientific Instruments* **1993**, *64* (2), 403 – 405.

55
http://www.nyu.edu/fas/dept/chemistry/wardgroup/Instructions,%20Calibrating%20AFM%20Cantilevers.pdf

56 Sader, J.E.; Larson, I.; Mulvaney, P.; White, L.R. *Review Scientific Instruments* **1995**, *66* (7), 3789 – 3798.

57 Green, C.P.; Lioe, H.; Cleveland, J.P.; Proksch, R.; Mulvaney, P.; Sader, J.E. *Review Scientific Instruments* **2004**, *75* (6), 1988 – 1996.

58 Sader, J.E.; Chon, J.W.M.; Mulvaney, P. *Review Scientific Instruments* **1999**, *70* (10), 3967 – 3969.

59 http://www.physics.uwo.ca/~hutter/calibration/afmcal.html

60 Practical advice on the determination of cantilever spring constants, B. Ohler, Veeco, **2007**.

61 Numerical recipes, the art of scientific computing, Third edition, W.H. Press, S.A. Teukolsky, W.T. Vetterling, B.P. Flannery, Cambridge University Press, **2007**

62 Nanoscope Iva controller manual, **2004**, Digital Instruments Veeco Metrology Group

63 Ohler, B. *Review of Scientific Instruments* **2007**, *78*, 063701.

64 Amalou, Z. Thesis, Université Libre de Bruxelles, Bruxelles, **2006.**

65 Daubigny, V. Dissertation de Licence, Université Libre de Bruxelles, Bruxelles, **2003.**

---

66 Caractérisation de solides cristallisés par diffraction X, Techniques de l’ingénieur, Norbert Broll.

67 Catalogue from Sutter Instrument, **2008**

3. Calibration of the Nanocalorimeter

In the first part of the chapter, the procedure of the temperature calibration is explained. Then the calibration of the power scale is introduced for each kind of experiments (i.e., the AC and DC modes). After that, the temperature calibration for fast heating experiments and the PID procedure used to refine linear heating ramps are presented. In the last parts of the chapter, the temperature gradient on sensors is measured by placing an indium microparticle at different places on the membrane and an original method to determine the mass of unknown particle is described.

3.1. Temperature calibration procedure

The temperature calibration step is essential for calorimetric measurements. This step allows to calibrate and control the heaters temperature, as well as the temperature and sensitivity of the thermopiles. According to the approaches described in the literature[1-2], the sensor is placed in an oven to calibrate the heater temperature, then the calibration is checked with indium films sputtered on the whole sensor membrane.

In the first step of this protocol, an external thermocouple is fixed on the sensor housing. During a temperature increase, the external thermocouple temperature and electrical resistance of the heater are simultaneously recorded. A typically parabolic fit through the experimental points is used:

$$T = A + B \times R_{htr} + C \times R_{htr}{}^{2}$$

where R_{htr} is the resistance of the heating elements at temperature T reading of the external thermocouple. The coefficients A, B, C are constants to be found for each sensor or sensor batch. Such an analytical fit sometimes allows reasonably extending the temperature range of the calibration beyond the experimental temperature limits. The main imprecision of this calibration method comes from the fact that the external thermocouple is placed approx. 1 cm away from the measurement area, which could introduce a significant error if there is a temperature gradient between the external thermocouple and the elements of the active area (e.g., heaters resistances, thermopiles). To circumvent this problem, we propose a calibration method based on the melting temperatures of metallic microparticles (indium and zinc).

In the following section, an example of the sensor calibration is given for sensor XEN-3972 which has a measurement area of 100 x 100 μm². The calibration depends on the membrane size, the type of the membrane (the membrane can be e.g. from bare silicon nitride or contain aluminium coating), and the sensor batch.

- Cleaning procedure.

Before calibration and before each measurement, the sensor is washed with deionised water and acetone to remove dust and other impurities. Some silicon pieces coming from fabrication of the sensor are removed with the micromanipulator. Then the sensor is prebaked in an oven at 200 °C during 30 min in order to relax the remaining internal stresses and to dry it.

- *Calibration file.*

The main calibration window of the Nanocalorimeter software is shown in figure 1. At the beginning it contains only zeroes and units as calibration coefficients.

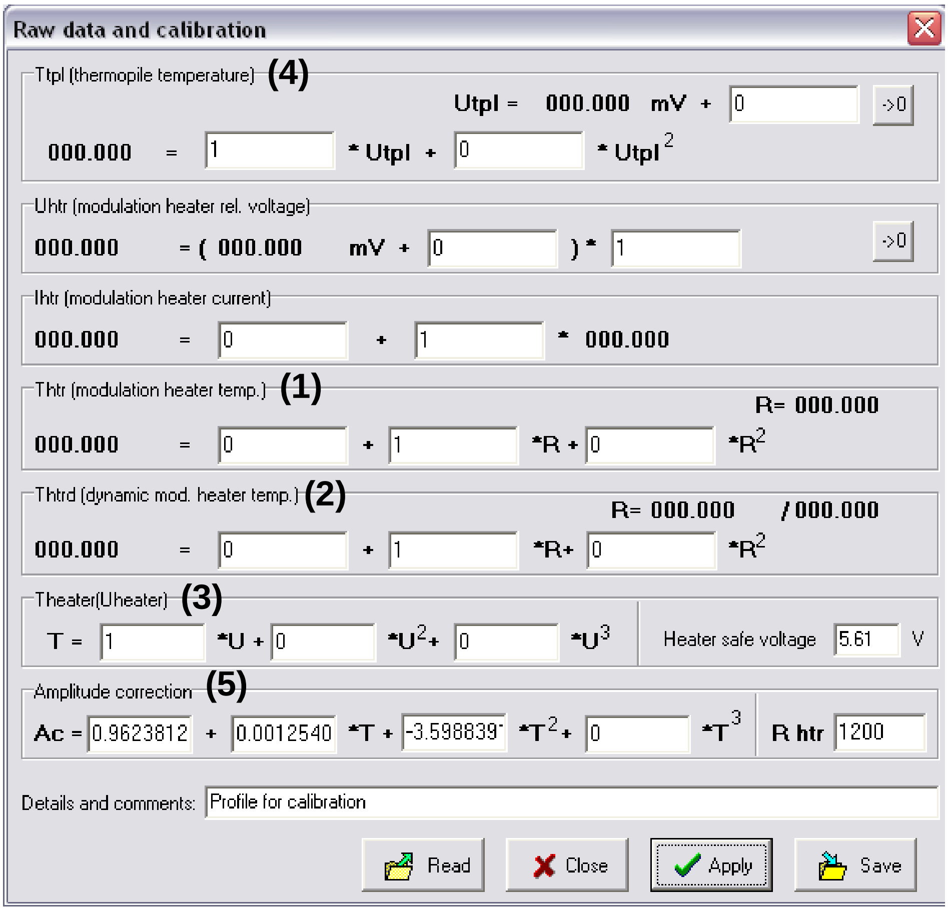

Utpl = 000.000 mV + 0

000.000 = 1 * Utpl + 0 * Utpl^2

000.000 = (000.000 mV + 0) * 1

000.000 = 0 + 1 * 000.000

R= 000.000

000.000 = 0 + 1 *R + 0 *R^2

R= 000.000 / 000.000

000.000 = 0 + 1 *R+ 0 *R^2

T = 1 *U + 0 *U^2+ 0 *U^3

Heater safe voltage 5.61 V

Ac = 0.9623812 + 0.0012540 *T + -3.598839 *T^2+ 0 *T^3

R htr 1200

Details and comments: Profile for calibration

Figure 1. Calibration window of the Nanocalorimetric software.

In the calibration window, “Ttpl” stands for the thermopile temperature, “Thtr” and “Thtrd” are the heater temperature measured by two different ways explained in appendix 3.1, “Theater(Uheater)” is the relation which correlates the temperature of the heater to the applied voltage. The heater maximum safe voltage (i.e. the maximum voltage that one can apply on the heater without destroying the sensor by melting the aluminium thermocouples) and the value “R htr” (i.e. the resistance of the heater measured at 22°C) are specified by Xensor[3, 4].

- *The five-step temperature calibration of the sensor*

The calibration we propose contains five steps. First, we calibrate the temperature of the heater resistances (1 and 2 on figure 1), then we determine the dependence of the heater voltage on its temperature (3). The internal thermopile sensitivity is then calibrated by heating the sensor with a heater resistance, and the heater temperature is linked to the voltage on the thermopile (4). The amplitude correction function is eventually determined (5). At the end, the calibration is cross-checked with melting temperatures of indium and zinc microparticles.

Step 1: temperature calibration of the heater resistance

During temperature calibration, the sensor is placed in a metal cylinder thermostated at 250°C. An external thermocouple (K-type) is fixed on the edge of the sensor housing with a kapton tape. The thermal contact between the external thermocouple and the sensor is found to be sensibly enhanced using a special heat sink compound (Radiospare 554-311). The value of the resistance and the temperature of the external thermocouple are recorded using the Nanocalorimeter during cooling of the cylinder.

Figure 2 shows typical plots obtained for a XEN-3972 sensor.

The curves T = f(resistances) are fitted with a parabolic expression. The found parameters such as the ones given below are introduced in the calibration file:

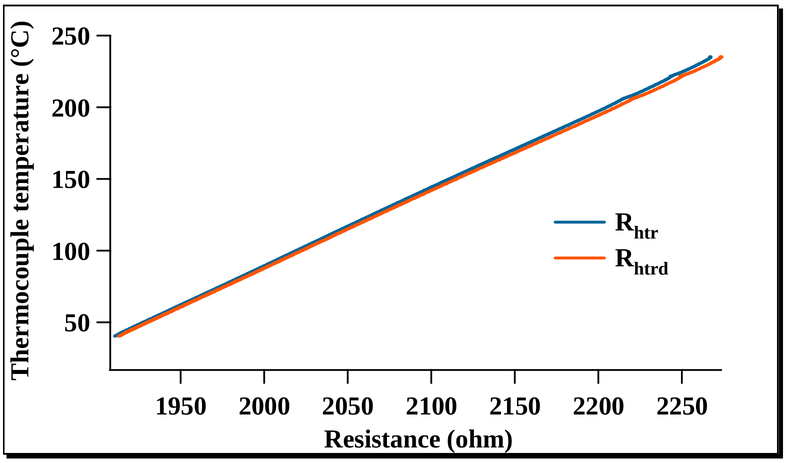

Figure 2. Temperature of the external thermocouple as a function of the heater resistance (R_{htr} and R_{htrd}) for a XEN-3972 sensor.

$$T_{htr} = -1083 + 0.62691 \times R_{htr} - 2.0317.10^{-5} \times R_{htr}{}^{2}$$

$$T_{htrd} = -1098.1 + 0.64522 \times R_{htrd} - 2.6124.10^{-5} \times R_{htrd}{}^{2}$$

Step 2: determining the relation between the voltage on the heater and its temperature

This calibration step allows establishing the relation between the voltage applied on the heater and its temperature, which is essential for performing temperature programs. Figure 3 shows the dependence of the voltage on the heater on its temperature. Before the determination of the voltage dependence on the heater temperature, the sensor is equilibrated for several minutes with the environment. A voltage ramp typically from 0 to 6 V is performed to determine the calibration parameters on the curve given in figure 3.

For each calibration it is checked which heater temperature (i.e., static or dynamic temperature) represents better the fit “heater temperature” = f(heater voltage). For the given example, it was the static temperature, which reads as:

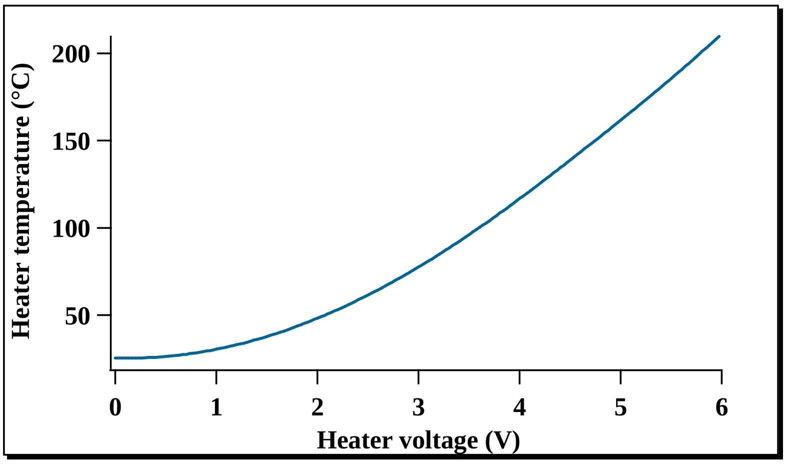

Figure 3. Heater temperature as a function of the heater voltage.

$$T = 26.114 - 3.78 \times U_{htr} + 8.2642 \times U_{htr}^{2} - 0.41764 \times U_{htr}^{3}$$

Upon completion of this step, the calibration coefficients are stored in the calibration file.

Step 3: calibration of the thermopile sensitivity

Before determining the thermopile sensitivity, the current modulation is firstly turned off in order to measure the offset voltage remaining on the thermopile. The latter is compensated for in the calibration file as follows:

$$U_{tpl} = 0.000mV - OffsetVoltage$$

In the second step, the modulation is turned on. The thermopile sensitivity is obtained by performing a temperature ramp. Before launching this experiment, the sensor must be equilibrated for several minutes with the environment. The temperature ramp allows correlating the heater temperature to the thermopile voltage as shown on figure 4.

The obtained correlation Heater temperature = f(Thermopile voltage) is fitted with a polynomial function, e.g. as shown below:

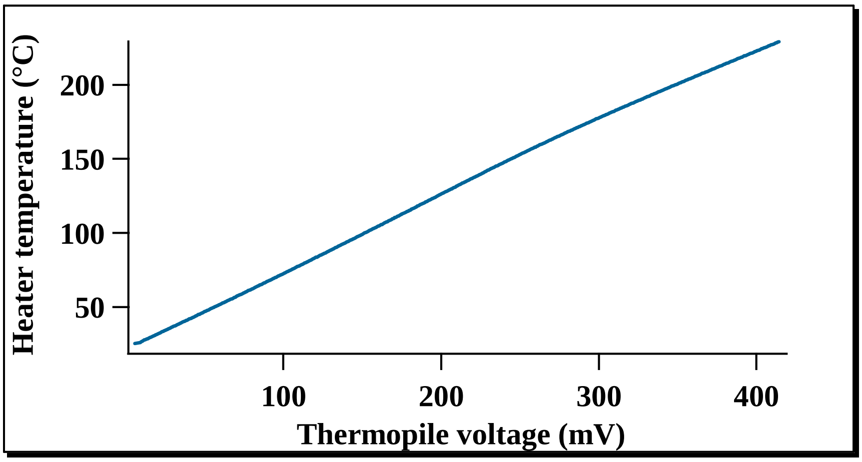

Figure 4. Heater temperature as a function of the thermopile voltage.

$$T_{tpl} = 18.726 + 0.56313 \times U_{tpl} - 0.00012391 \times U_{tpl}^{2}$$

Upon completion of the protocol, the calibration coefficients are stored in the calibration file.

Step 4: calibration of the amplitude correction

In this calibration step, the modulation response of an empty sensor as a function of temperature is fitted with a polynomial equation for use as a correction function. The obtained calibration parameters are saved in the calibration profile.

- Remarks regarding steps 2 and 3.

The heater temperature as a function of the voltage applied on it and as a function of the thermopile signal obviously depend on the surroundings temperature as shown in figure 5, as at zero applied voltage the heater is equilibrated with the ambient atmosphere. The latter also determines the temperature of the thermopile cold junction.

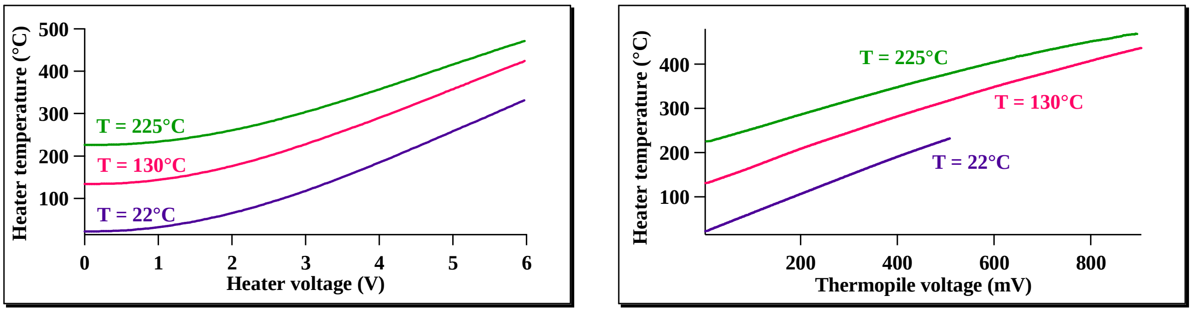

Figure 5. Dependence of the heater temperature on the heater voltage (left) and on the thermopile voltage (right) measured at different ambient temperatures.

Step 5 : verification of the temperature calibration

After completion of the four calibration steps previously described, the calibration parameters are checked with melting temperatures of indium and zinc microparticles. The particles are placed in the centre of the active area with a micromanipulator. Then two heating ramps at 20°C/min are successively performed. A slow heating rate is chosen to avoid thermal gradients which exist between the centre and the edges of the active area. The first heating ramp removes the internal stresses in the particle and enhances the thermal contact between the particle and the membrane. Melting of an indium particle (second heating ramp) is shown on figure 6.

It can be seen that the melting onset temperature is different from the tabulated one, i.e. 156.5°C.

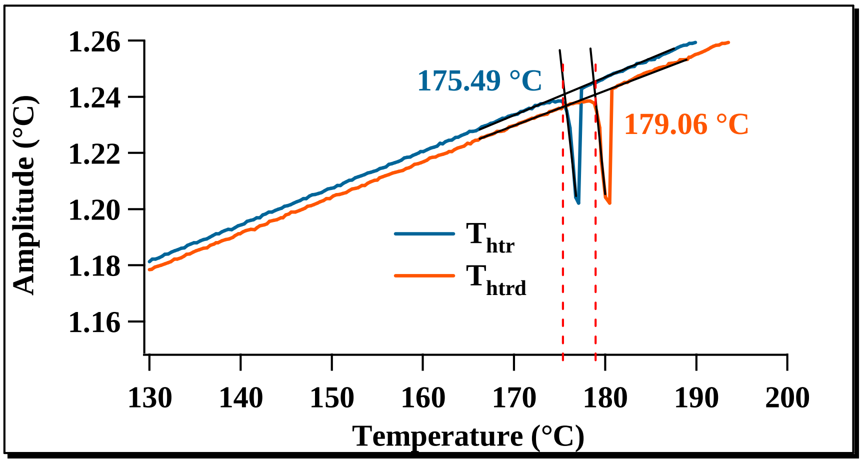

Figure 6. Heating ramp of an indium microparticle used for temperature calibration.

Since the heater resistances (static and dynamic) can be calculated from the equation of the calibration file, the resistances corresponding to the melting points can be easily found.

The equation below exemplifies the temperature dependence of the static heater resistance:

$$T_{htr} = -1083 + 0.62691 \times R_{htr} - 2.0317.10^{-5} \times R_{htr}{}^{2}$$

Therefore the static resistance of the heater corresponding to 175.49°C is 2157.9 Ω. Similarly, the equation for the dynamic resistance is given below:

$$T_{htrd} = -1098.1 + 0.64522 \times R_{htrd} - 2.6124.10^{-5} \times R_{htrd}{}^{2}$$

The dynamic resistance of the heater corresponding to 179.06°C is found to be 2163.7 Ω. The same experiments are subsequently performed on a zinc microparticle. The sensor is placed in the cylinder at 170°C in order to be able to reach the zinc melting temperature as shown on figure 7.

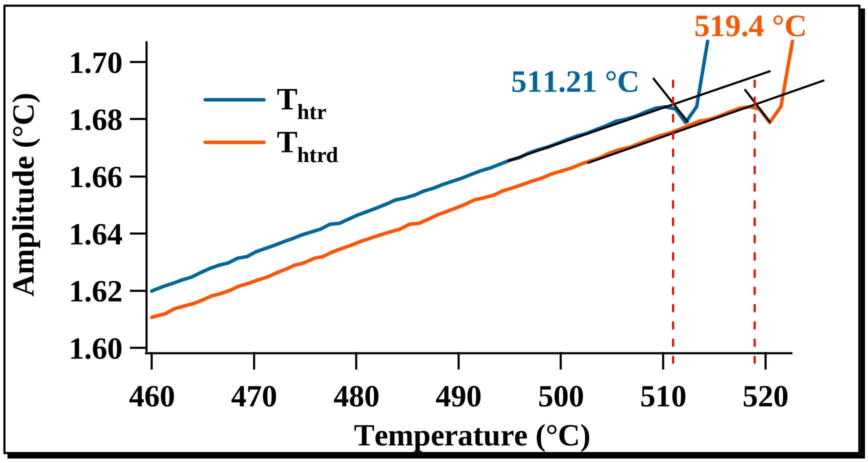

Figure 7. Heating ramp of a zinc microparticle used for temperature calibration.

Based on the initial calibration file, the static resistance of the heater corresponding to 511.21°C is 2794.5 Ω and the dynamic resistance at 519.4 °C is 2810.6 Ω. These resistance values corresponding to the melting temperature of indium and zinc microparticles are used to refine the temperature calibration. Thus, the statistical weight of these points is chosen to be much higher than the weight of other points to force the fit to pass through them (figure 8).

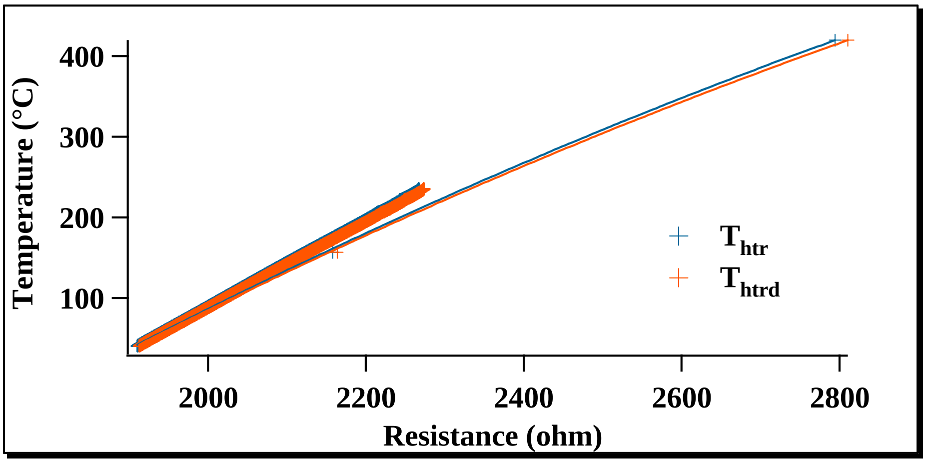

Figure 8. Temperature dependence of the heater resistances obtained in the first calibration step and those upon calibration with indium and zinc microparticles.

The difference between the temperature measured with a thermocouple placed on the edge of the sensor housing and the temperature measured with indium microparticle is approx. 18°C. This difference is most probably due to the temperature gradient existing across the active area and due to the imperfect thermal contact between the external thermocouple and the sensor. The calibration method using metallic microparticles provides us with more precise temperature values measured in the centre of the sensor active area.

After the calibration of the heater temperature, other calibration steps are performed in the same manner as before, i.e. from step 2 to step 4. Finally, the temperature calibration is checked again in the AC mode using melting of indium microparticle placed in the membrane centre. A typical AC curve is shown in figure 9. In this case, the membrane temperature is calculated as the sum of the external thermocouple temperature and the thermopile temperature.

It can be seen that the onset of melting is at 156.5°C, i.e. it is now much more correct. It is noteworthy that the onset temperature determined from the amplitude and phase curves is the same.

Figure 10 shows a similar AC experiment carried out on a tin microparticle.

The melting temperature is found to be 231.9 °C, i.e. equal to the tabulated one[5]. This result is considered satisfactory for our purpose.

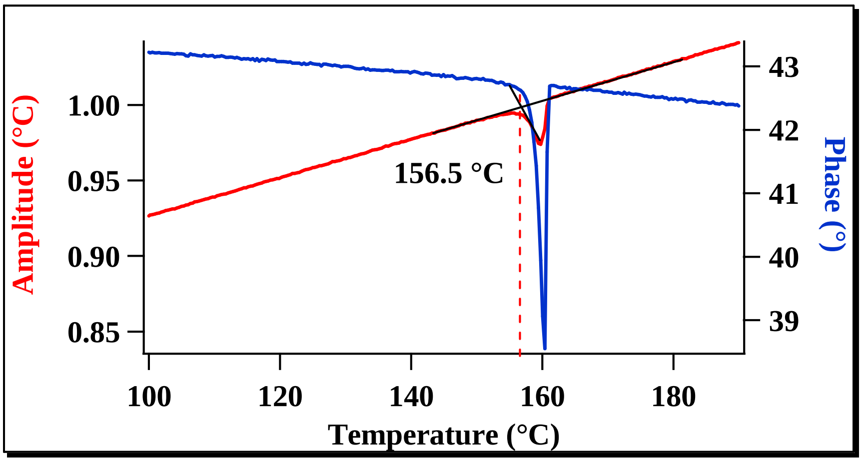

Figure 9. Heating ramp of an indium microparticle at 20°C/min.

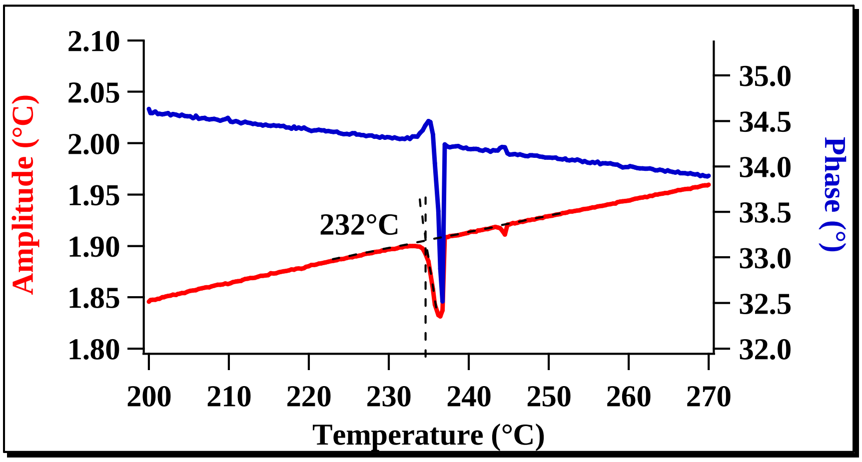

Figure 10. Heating ramp of a tin microparticle at 20°C/min.

Generally, our experience shows that the temperature calibration has to be performed not only for different types of sensors but also for each sensor batch. Thus, we found that the heater resistances can vary for about 10 % from one batch to another. Also, in establishing the calibration protocol, it was found that the optical control of the particle position on the active area of the sensor is important. It was observed that particles can change their position or even jump out of the active area during heating ramps. One of the reasons for such behaviour could be the release of internal stress in the particle.

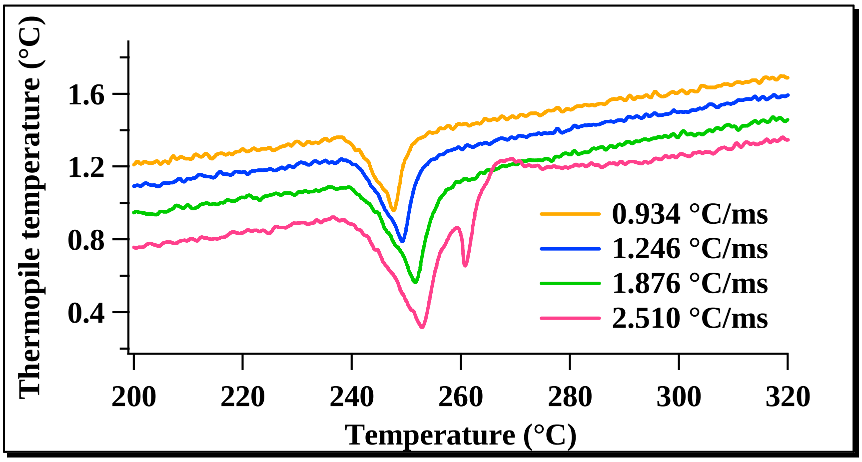

Figure 11. Heating ramp of a tin microparticle at heating rates from 0.934 to 2.510°C/ms.

Figure 11 shows two melting peaks on the curve measured at 2510 °C/s: the first peak corresponds to melting of the particle positioned in the membrane center and the second peak is melting of the same particle moved to another position.

The micrographs on figure 12 show the position of an indium microparticle before and after a heating ramp at 20°C/min.

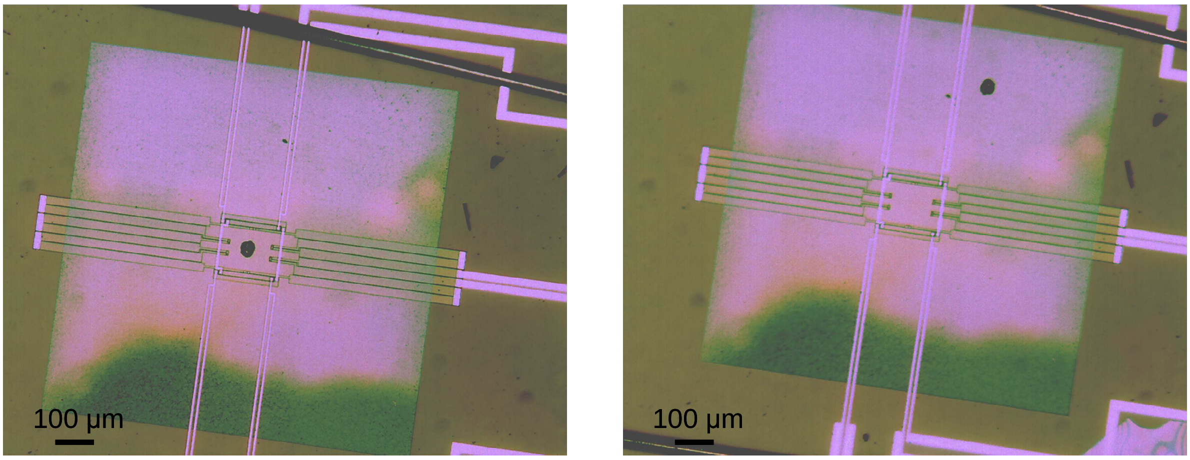

Figure 12. Indium microparticle positioned on the membrane before (left) and after the heating ramp (right).

It is visible that the indium particle is about 240 µm from its initial position after the heating ramp. The nanocalorimetric curves corresponding to this experiment are presented on figure 13.

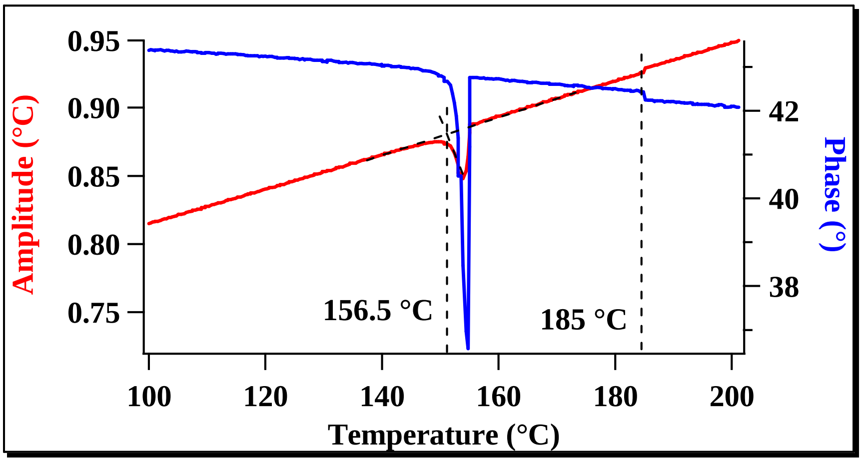

Figure 13. Nanocalorimetric curves of an indium particle heated at 20°C/min.

Here one can see a melting peak of the indium particle located at the initial position (membrane center) at 156.5°C, and a second thermal event at 185°C. The latter most probably results from the particle displacement during the heating ramp. The melting peak of the moved particle is not observed because it left the active area.

3.2. Calibration of the power scale

The power calibration is obviously as important as the temperature calibration, as it allows to calculate the enthalpy of thermal transitions and heat capacity of the samples. On DSC or nanocalorimetric curve, the heat capacity is measured from the instantaneous power absorbed by the sample during a linear heating ramp while the enthalpy corresponds to the time integral of the power through the temperature range of transition.

3.2.1. Quasi-static conditions

The quasi-static conditions correspond to situation where the sensor is kept in equilibrium with the environment and there is only a small perturbation generated by the current modulation passing through the heater resistance. The expression for the electric power dissipated on resistance R is $P = I^2.R$. The modulation current is $I = I_0 + I_1.\sin(\omega t)$, where I_0 is the current offset and I_1 is the modulation amplitude. The modulation power reads as:

$$P = I^2.R$$

or

$$P = \frac{(I_0{}^2.R)}{2} + 2.I_0 I_1.\sin(\omega t).R + I_1{}^2.\sin^2(\omega t).R$$

It is thus clear that in the Fourier space one has terms at the single and double frequency. After integration over oscillation period, one gets:

$$P = I_0{}^2.R + \frac{I_1{}^2.R}{2} \qquad (1)$$

In the absence of modulation, in equation (1) there are evidently no terms dependent on I_1 anymore. The power can be varied then only by changing the offset current (I_0). The power function expressed in this manner is named $P_1(I_0)$. In the presence of a constant amplitude modulation, the power can also be varied by varying the offset current I_0 (the function is named P_2). However, in addition one can vary the amplitude current I_1. This results in the power function termed $P_3(I_1)$. If the double frequency is employed, there is no offset current to be used. The power function (P_4) expresses the dependence on the modulation amplitude I_1 for this case. The described methods are used to determine the heat exchange parameter Q according to equation (2):

$$P = Q.T_{tpl} \qquad (2)$$

where T_{tpl} is the temperature of the thermopile.

The values of Q determined by the described four methods for a 30x30µm² sensor are given in table 1.

Method	P_1	P_2	P_3	P_4
Q (10^{-5} W/K)	3.62	3.59	3.39	3.56

Table 1. Heat exchange parameter determined according to four methods at ambient temperature (see text for more details).

The average measurement uncertainty is ca. 2.10^{-7} W/K. It is clear that, within the error-bar, the three methods result in almost the same value of Q.

1. *Determination of the heat exchange parameter (Q)*

The heat exchange parameter (Q) corresponds to the heat loss of the system through the environment and the membrane. The equation (3) links the heat exchange parameter to the electrical parameters measured by the nanocalorimeter:

$$P = R.I^2 = Q.\Delta T \qquad (3)$$

where P is the electrical power, R is the heater resistance, I is the intensity of the current which pass through the heater, and ΔT is the temperature difference between the membrane and the cold point on the edge of the sensor. This temperature difference is given by the thermopile. As shown on figure 14, we see that the slope of the line $P = f(\Delta T)$ corresponds to the heat exchange parameter Q.

The line passes through the origin, i.e. when no power is applied on the sensor, there is no temperature difference which is detected.

In the literature[6], we find that the heat exchange parameter is equal to 2.10^{-5} W/K in normal conditions of temperature and pressure, which is close to our experimental value 3.6 10^{-5} W/K.

The heat exchange parameter is proportional to the thermal conductivity of the gas. The general expression of Q is the following[7]:

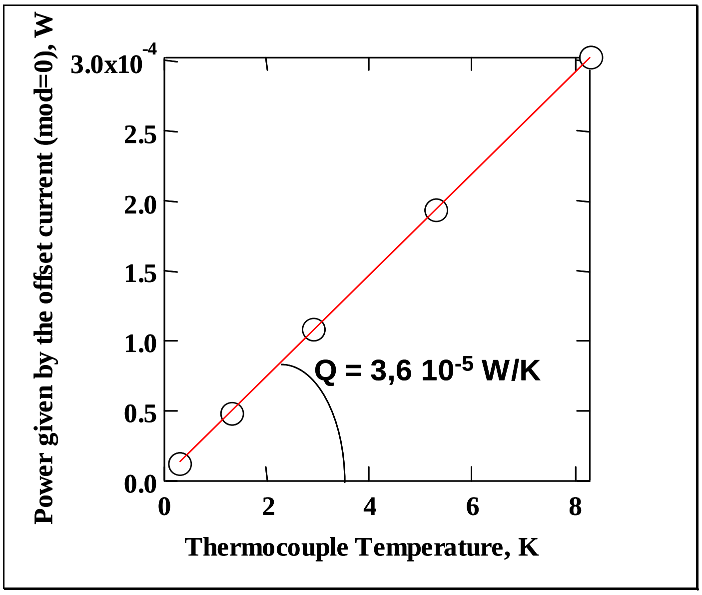

Figure 14. Electric power generated by the offset current versus thermocouple temperature.

$$Q = \frac{(n.C_v.\nu.\lambda)}{(N_A.4)}$$

where n is the number of molecules in the unit volume of gas, ν is the mean speed of a molecule, λ is the mean free path, N_A is the Avogadro number.

On figure 15, the heat exchange parameter was determined on five sensors from the same batch and with the same calibration file.

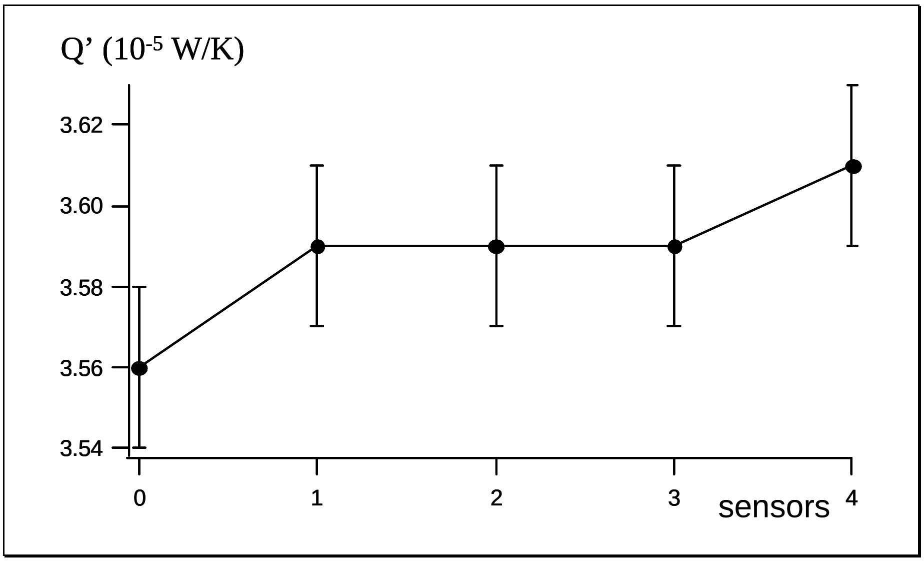

Figure 15. Heat exchange parameter determined on five different sensors.

We observe that there is nearly no difference on the value of the heat exchange parameter on five sensors from the same batch and calibrated with the same calibration file. The average of the heat exchange parameter is 3.59 ± 0.02 10^{-5} W/K.

The variation of the heat exchange parameter according to the frequency of modulation is given on figure 16.

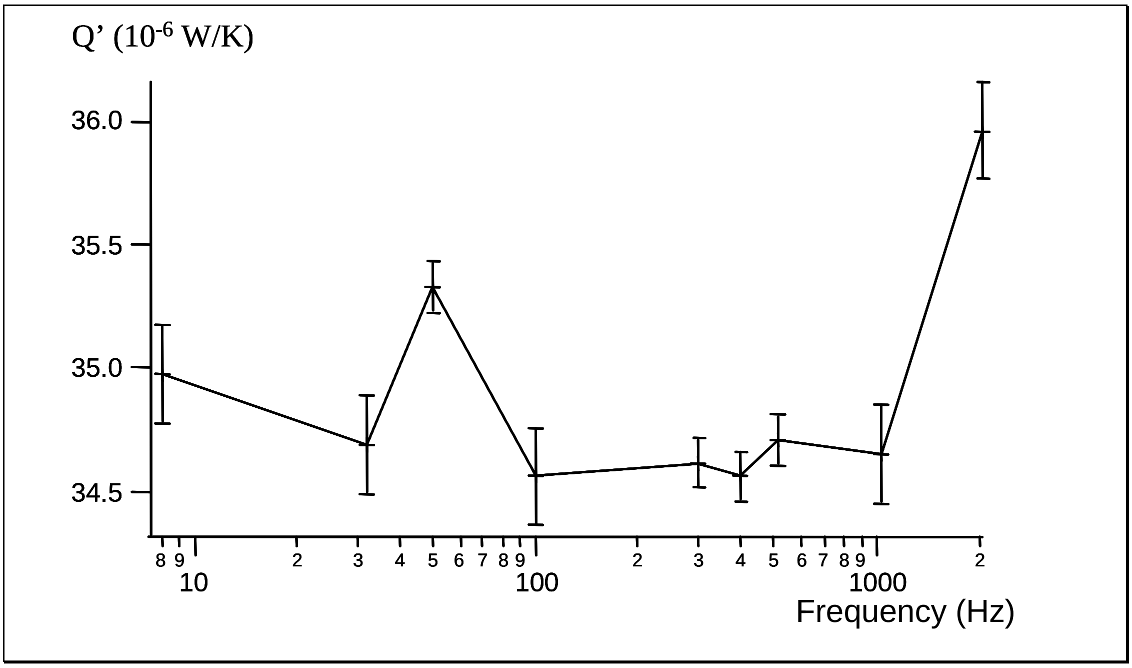

Figure 16. Variation of the heat exchange parameter with modulation frequency.

We observe that the point at 50 Hz is far from the others, it is because of the noise of the mains at this frequency. The value of the heat exchange parameter is almost constant in the range of 1 to 1000 Hz.

Some experiments were performed under vacuum in order to exclude the heat exchange parameter through the air.

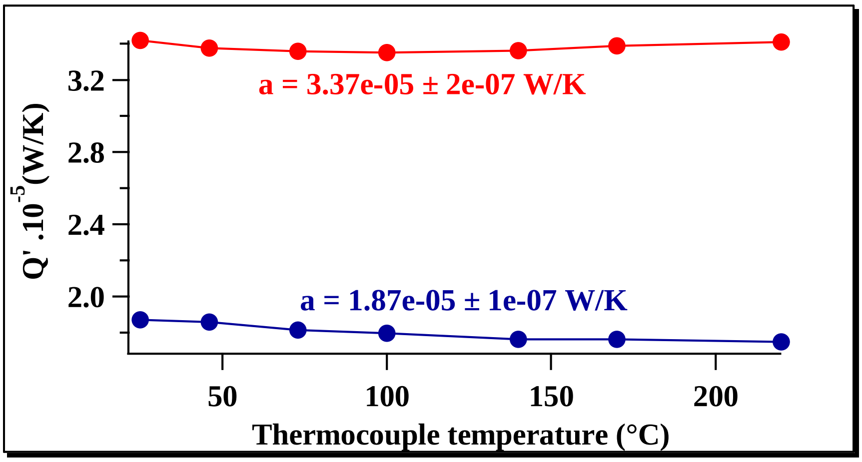

Figure 17. Heat exchange parameter at several temperatures in air and in vacuum.

According to the measurements given on figure 17, the value of the heat exchange parameter is constant with the temperature of the membrane.

In air atmosphere, Q = Q(membrane) + Q(air) = 3.38 10^{-5} ± 0.02 10^{-5} W/K. In vacuum, Q = Q(membrane) = 1.87 10^{-5} ± 0.01 10^{-5} W/K. In vacuum, the heat losses are produced via the heat exchange membrane and by radiation (the heat losses by radiation are equivalent in air atmosphere and in vacuum). So the heat losses through the air atmosphere is 1.50 10^{-5} W/K, which is about one half of the total value.

2. *Determination of the heat capacity (Cp)*

The heat capacity, expressed in J/(g.K), corresponds to the heat required to increase the temperature of one gram of sample by one degree. There are several methods to determine the heat capacity of the membrane and of the added mass. The first method uses the curves power versus temperature obtained by fast heating. This method is explained below.

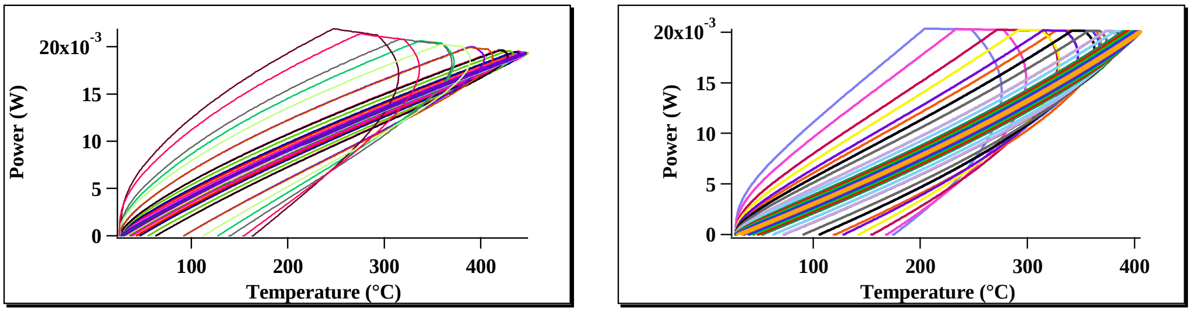

Figure 18. Power as a function of temperature for different heating rates (from 700°C/s to 57000°C/s) for a 30x30 µm² XEN-3970 sensor ((left) and XEN-3971 60x60 µm² (right).

The heat capacity of the empty membrane can be determined from the curves presented on figure 18. The power is calculated according to the following equation: $P = U^2 / R_g$ where U is the voltage in the heaters and R_g the guard resistance.

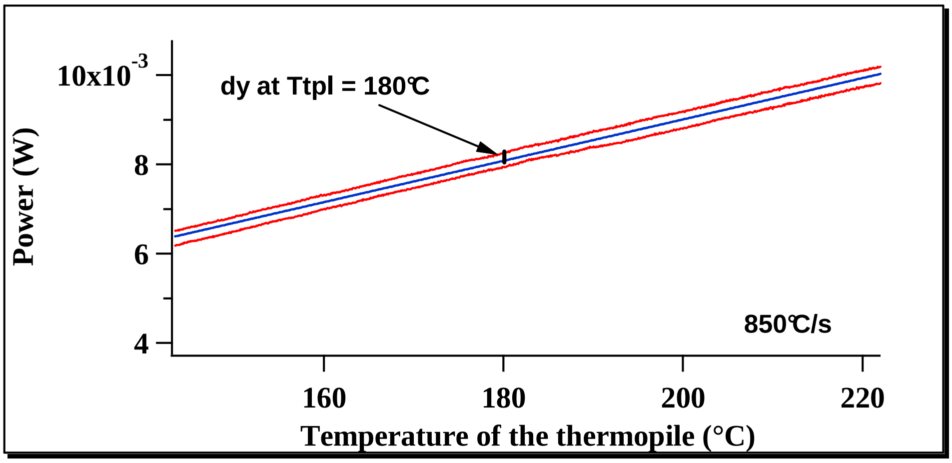

Figure 19. Heat capacity calculation based on fast heating measurements.

The heat capacity (C_p) can be found from the following expression:

$$\Phi = C_p.\beta$$

The Φ stands for the heat flow, the heating rate is ß. The heating and cooling ramps of the membrane are shown on figure 19. It is convenient to trace half the sum of the two curves to calculate the heat capacity of the membrane.

Another method can directly use the thermopile temperature difference obtained after subtraction of the experiment with a blank sensor (ΔT_{tpl}). This resulting data is multiplied by the heat exchange parameter (Q) to calculate the heat flow, as reads:

$$\Phi = Q.\Delta T_{tpl}$$

The second method to determine the heat capacity uses quasi-static measurements with application of a temperature modulation. In this case, the amplitude modulation (θ_0) is linked to the heat capacity (C_p) and the amplitude of the heat flux (P):

$$\Theta_0 = \frac{P}{\sqrt{(mc\omega)^2 + Q^2}}$$

So the Cp is given by:

$$C_P = mc = \frac{1}{\omega}\sqrt{\left(\frac{1}{x}\right)^2 - Q^2}\ .$$

In this equation, x corresponds to the slope of the line representing the amplitude modulation (θ_0) versus the amplitude of the heat flux (P).

The heat capacity of bare membranes is shown for different modulation frequencies on figure 20.

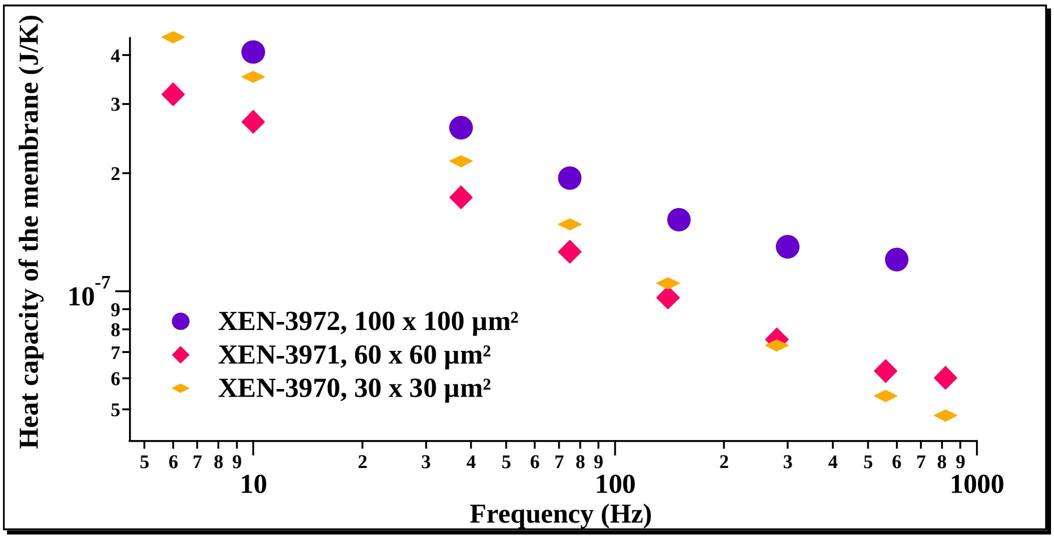

Figure 20. Membrane heat capacity at different frequencies for sensors XEN-3970 30x30µm², XEN-3971 60x60µm² and XEN-3972 100x100µm².

It can be seen that the heat capacity of the membrane decreases with the frequency increase. This trend is understandable as at high frequencies the tested area is smaller than that at small frequencies. The heat capacity increases after 1kHz, which probably means that other uncontrollable factors come into play at these high frequencies.

3.2.2. AC calorimetric experiments

In the presentation of the AC amplitude on the complex plane, the norm and phase of the amplitude are given (cf. Chapter I):

$$\Theta_0 = \frac{P}{\sqrt{(mc\omega)^2 + Q^2}} \qquad \text{and} \qquad \tan\Phi = \frac{mc\omega}{Q}$$

Here Φ (phase) is the phase difference between the temperature oscillation of the sample and that applied externally, m, c, T are the mass, heat capacity and sample temperature, respectively. Q is the power of the heat losses (or the heat exchange parameter), ω the angular frequency of modulation.

3.2.3. Fast heating experiments

For fast heating experiments, the instantaneous power can be calculated in two ways:

(1) the sample temperature after subtraction of the empty membrane temperature (this temperature difference with the blank curve is named ΔT_{tpl}) is multiplied by the heat exchange parameter (Q) to obtain the power absorbed or released by the sample:

$$P = Q.\Delta T_{tpl}$$

(2) the supplied power is calculated from the value of the guard resistance (R_g). The graph on figure 21 gives the evolution of the two resistances (i.e. the heater and the guard) as a function of temperature.

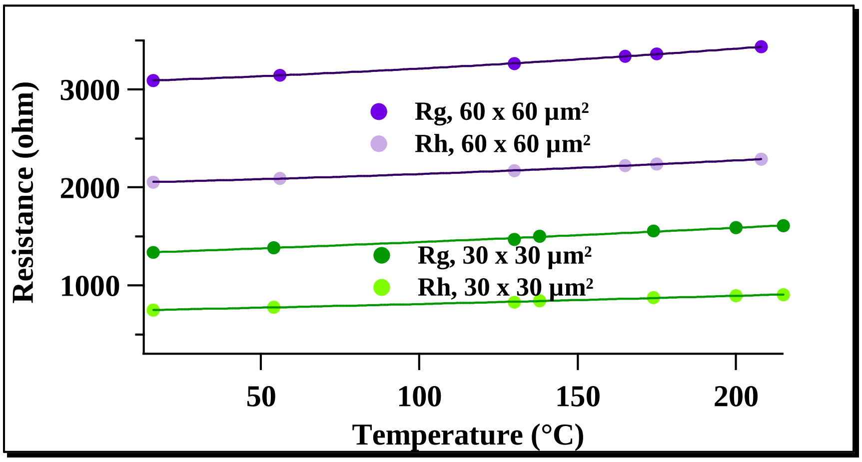

Figure 21. Evolution of the resistances as a function of the temperature for two kinds of sensors (XEN-3970 and XEN-3971).

The data points are obtained by measuring the two resistances with a multimeter (the electrical scheme is given in appendix 3.2.) at each isotherm. To this end, an external thermocouple is placed on the sensor edge while the sensor is placed in a heated cylinder. The two resistances R_h and R_g follow approx. the same linear law, the ratio between them staying constant. Therefore one can find the value of R_g from R_h.

Usually, we used the first way to determine the instantaneous power in fast heating measurement.

3.3. Temperature calibration for fast heating experiments

The sensor calibration for fast heating experiments was refined in a way similar to what was used in the previous section. The shape of the voltage pulse was determined for each type of sensor. To improve the signal to noise ratio, the voltage wave was applied successively nine times on the sensor before and after deposition of the particle. The average of the curves measured on the empty sensor constitutes the blank sensor curve (T_{tpl}(blank)). The average of the thermopile temperature obtained on the sensor loaded with a metal (e.g., indium) microparticle (T_{tpl}(exp)) is corrected for the blank curve.

The power is obtained after the multiplication of the particle temperature by the heat exchange parameter (Q).

Figure 22 shows nanocalorimetric curves for an indium particle heated at different heating rates ranging from 45000 °C/min to 740000 °C/min.

The peak broadening reflects the time required to melt the particle.

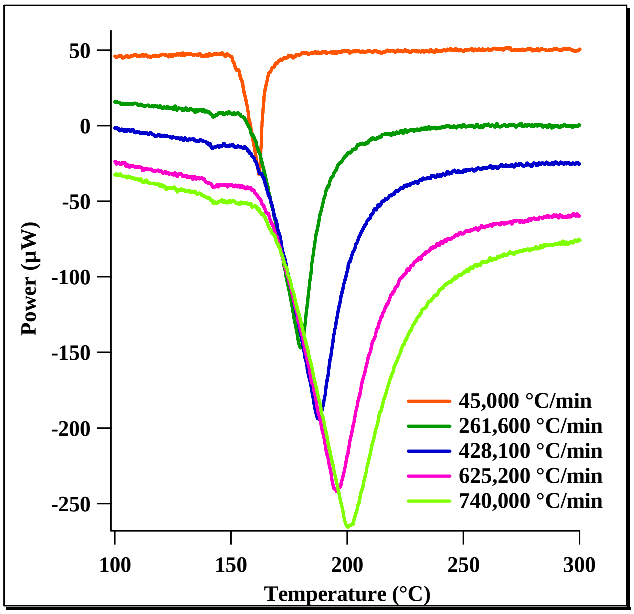

Figure 22. Heating ramps of indium microparticle.

- Characteristic time of the nanocalorimeter

Figure 23 gives the melting onset temperature of an indium microparticle as a function of the heating rate applied.

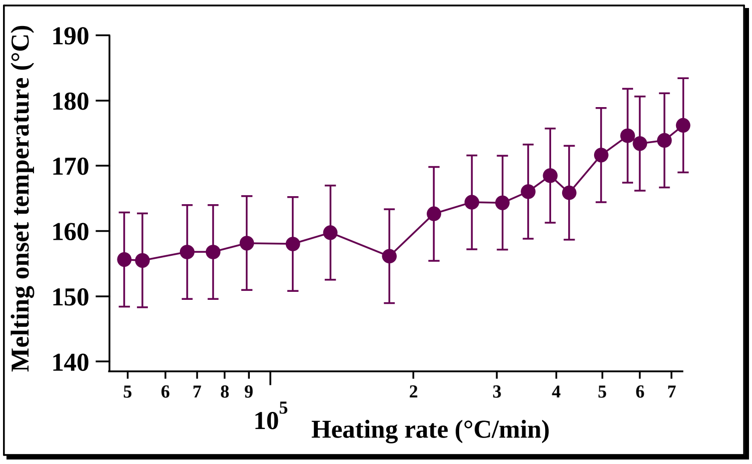

Figure 23. Melting temperature of an indium microparticle measured at different heating rates.

It can be seen that the onset temperature increases from 155.6 °C to 176.2 °C.

Figure 24 shows the same data as in figure 23 but in linear coordinates. The slope of the linear fit through the data points provides the characteristic time of the device, which is in this case equal to 1.9 ms.

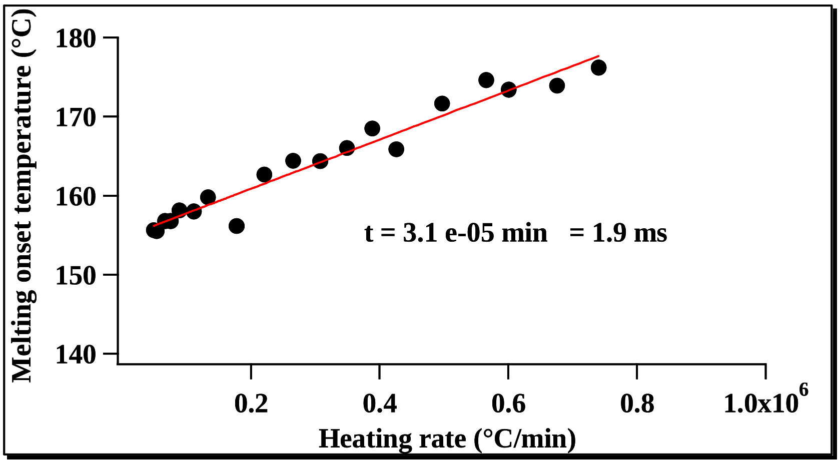

Figure 24. Determination of the nanocalorimeter characteristic time.

3.4. PID procedure used to refine the linear heating ramps

Generally, a PID regulator allows adjusting the measurement signal relative to the programmed signal. The error signal here is defined as the difference between the two signals. The PID regulator can undertake three actions to minimize the error signal:

- Proportional action: the error signal is multiplied by a respective gain;
- Integral action: the error signal is integrated according with respect to time, then it is multiplied by a respective gain;
- Differential action: the error signal is first differentiated with respect to time, then it is multiplied by a respective gain.

In this work, the proportional action is found sufficient for refining the linear heating ramps at high heating rates. In the following, we describe an example of such refinement on a sensor XEN-3970.

The graphs on figure 25 display the heating and cooling rates obtained on two types of sensors using the temperature calibration data.

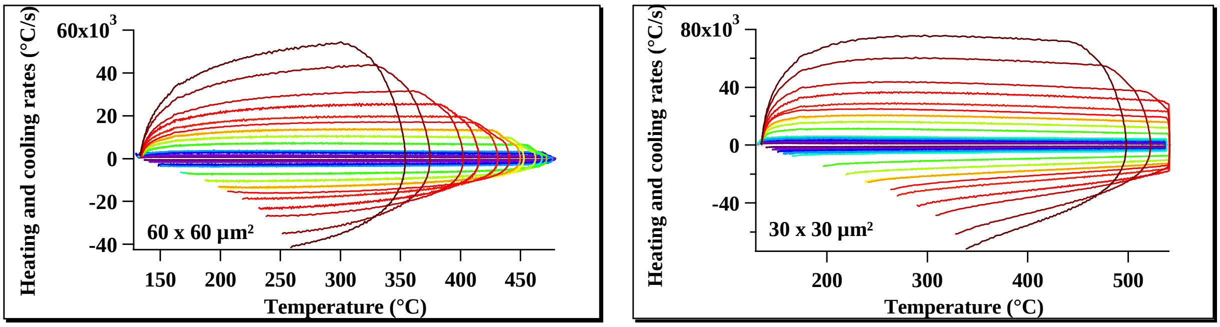

Figure 25. Heating and cooling rates versus temperature for sensor XEN-3971 60x60µm² (left) and sensor XEN-3970 30x30 µm² (right).

One can see that for high heating rates, especially for sensor XEN-3971, the heating program is not linear.

Figure 26 presents the experimental heating ramp (in orange) and the target heating ramp (in blue) to reach. The heating rate corresponds to the slope of the target line. In this case, the heating rate is 14.6 °C/ms (= 876 000 °C/min) to be applied on a sensor with a membrane size of 30 x 30 µm².

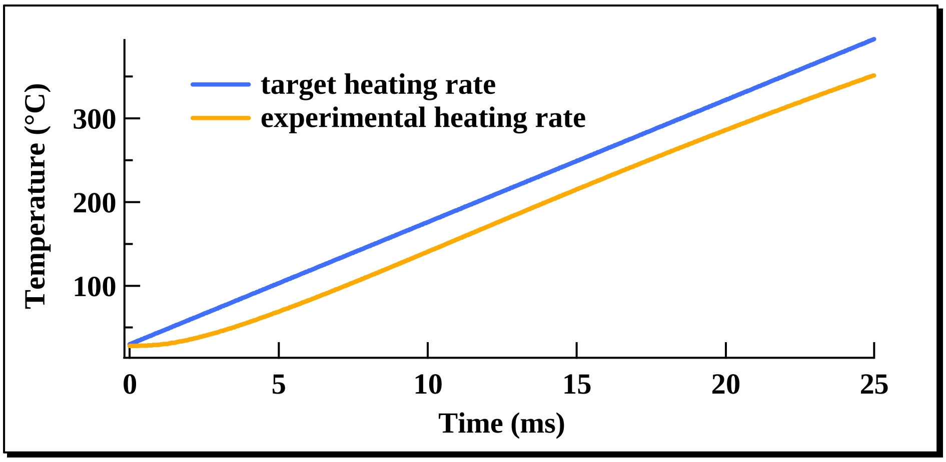

Figure 26. Experimental heating ramp and target heating ramp before PID correction.

By comparing the experimental and target programs, one can see that there is a curvature on the experimental curve between 0 and 2 ms. The temperature difference between the two curves after 5 ms is 36°C. The non-linearity of the heating rate – especially at the beginning of the temperature program – is due to the thermal inertia of the membrane. This problem can be circumvented thanks to the PID procedure. Thus, if the experimental heating ramp is lower than the theoretical heating ramp, the voltage applied on the heater should be increased. On the other hand, if the experimental data points are higher than the theoretical heating ramp, the heater voltage should be decreased. The PID procedure with the proportional action can be implemented in several steps explained below.

After sensor calibration, we first perform a voltage ramp in order to have the heater voltage versus its temperature as shown on figure 27.

Then we interpolate the heater voltage in order to have a wave of the heater voltage versus the number of points of the wave. In the example on figure 28, the wave has 1000 points.

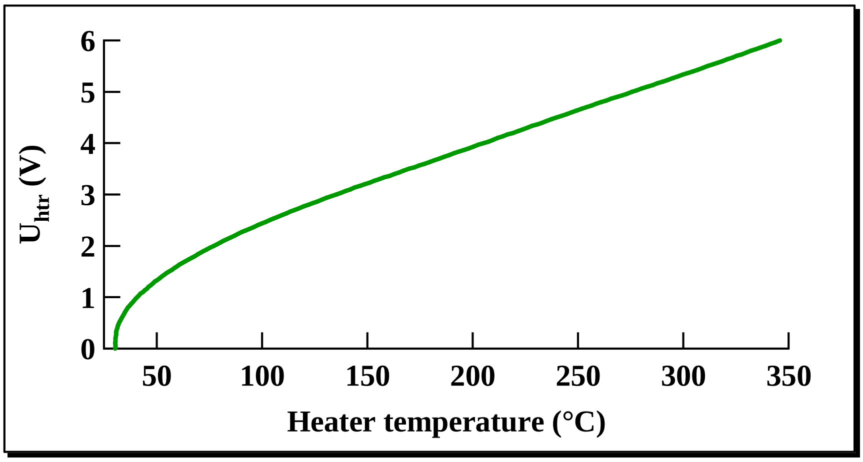

Figure 27. Step 1, voltage ramp on the heater.

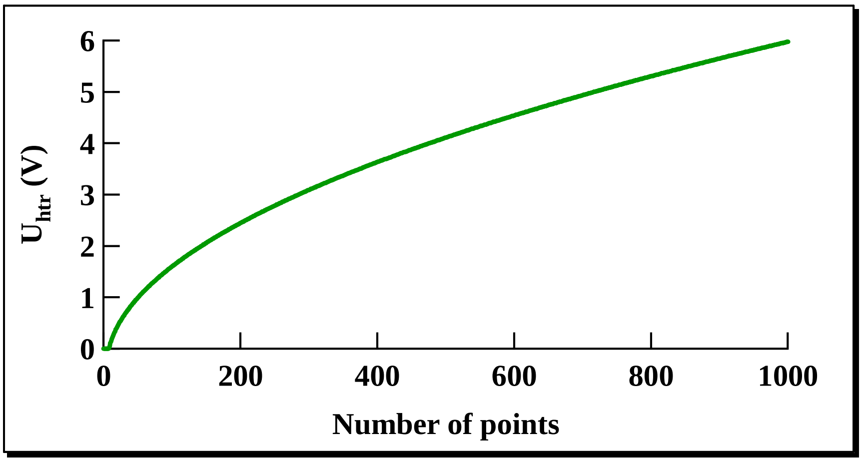

Figure 28. Step 2, heater waveform.

In the third step, the voltage wave obtained through step 2 is applied on the sensor. We obtain similar curves as those presented on figure 26.

The target temperature (blue curve on figure 26) is the membrane temperature we want to reach after the PID correction in order to have linear heating rate. To this end, we calculate the temperature difference between the target and the experimental curves for the membrane temperature as shown on figure 29.

Here delta T represents the temperature difference between the target temperature and the experimental temperature.

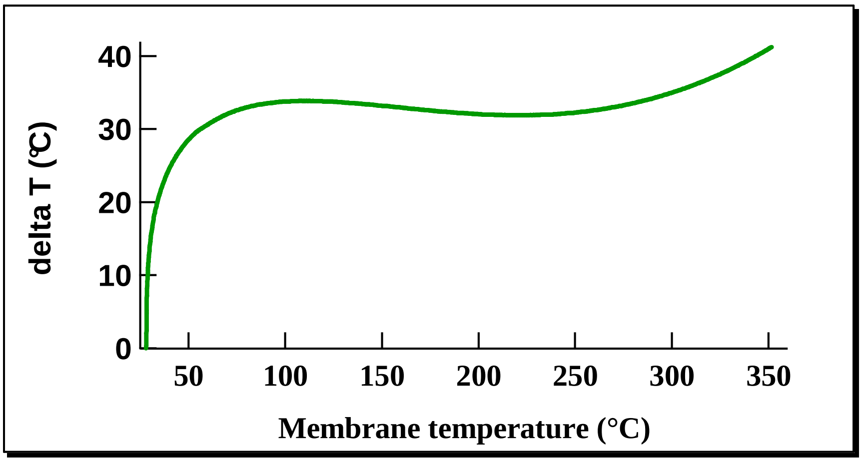

Figure 29. Step 4, temperature difference between the target and the experimental membrane temperature.

In the fifth step (figure 30), we interpolate the curve U_{htr} = f(Temperature) obtained after the voltage ramp of step 1, thus we have U_{htr} = f(Temperature).

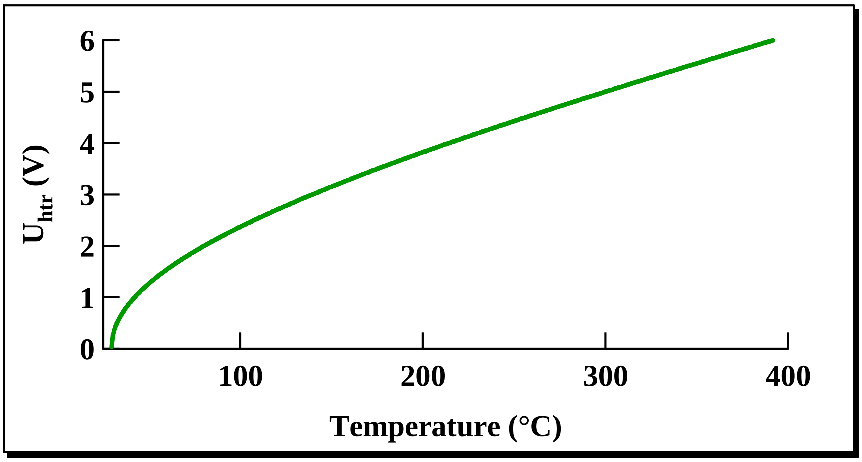

Figure 30. Step 5, heater voltage as a function of temperature.

In step 6, we differentiate the heater voltage (Uhtr) with the temperature in order to have $\frac{dU_{htr}}{dT} = f(Temperature)$ as shown on figure 31.

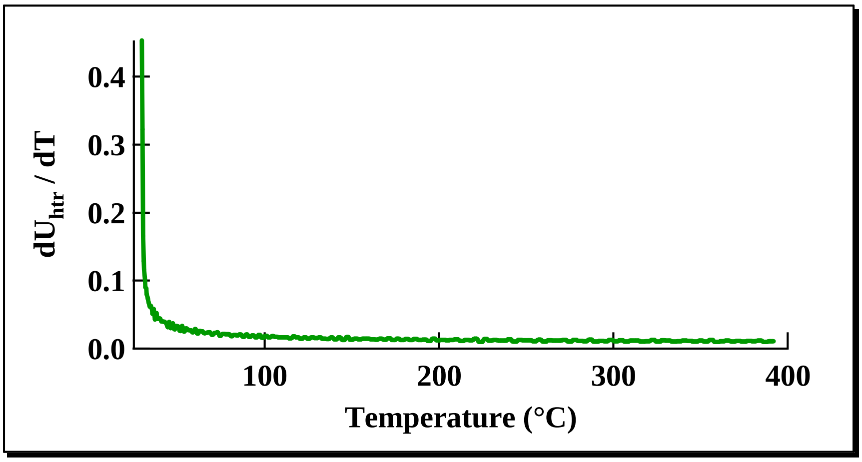

Figure 31. Step 6, derivative of the heater voltage over temperature as a function of temperature.

The next step (figure 32) consists in the calculation of the voltage correction which has to be added from the initial voltage ramp (step 1).

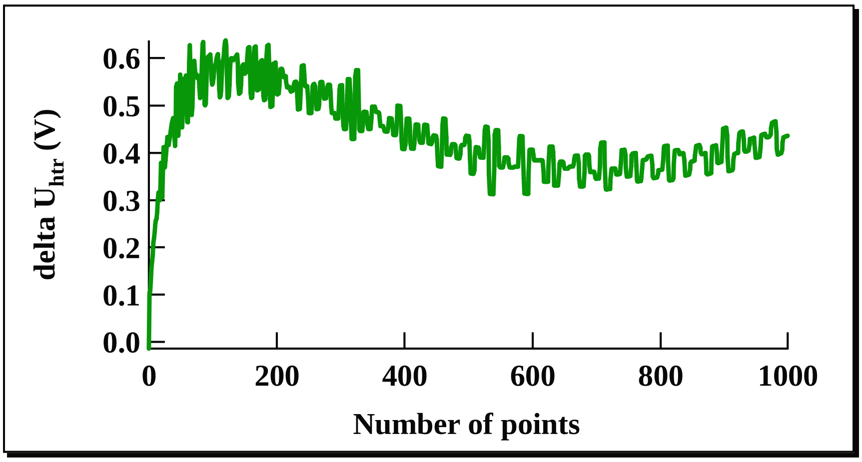

Figure 32. Step 7, voltage delta waveform used to subtract at the initial heater voltage of step 2.

The ΔU_{htr} is calculated as follows: $\Delta U_{htr} = \frac{dU_{htr}}{dT}.\left(T_{t\arg et} - T_{\exp erimental}\right)$

The first part of the expression is the wave from step 6 whereas the second part is the wave from step 4 (cf. figure 29).

In the following step, we add ΔU_{htr} of step 7 to the voltage wave of step 2. The new voltage wave is represented by the violet curve on figure 33.

The green curve is the initial voltage wave applied in the first step. The violet curve corresponds to the corrected voltage wave after the first PID iteration.

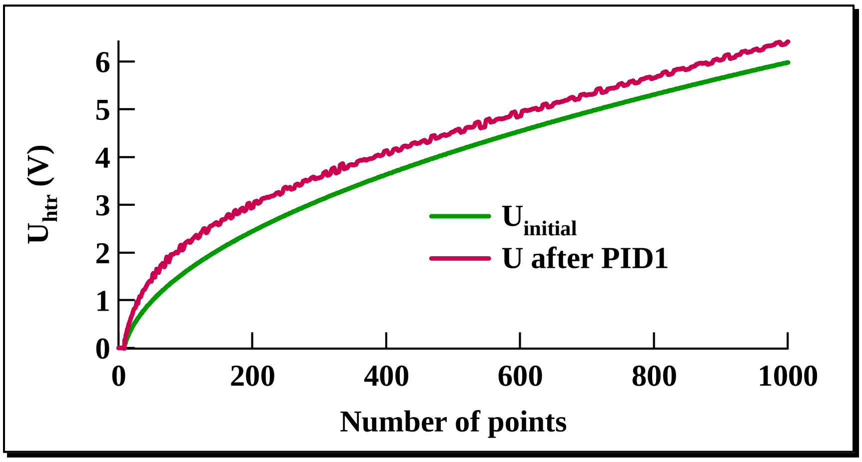

Figure 33. Step 8, corrected voltage waveform after the PID procedure.

The new voltage wave is applied on the sensor.

On figure 34, the first experimental ramp is the green curve, the black curve is the target temperature, and the violet curve is obtained after the first PID correction. We observe that the difference between the experimental and target curves is drastically decreased. Nevertheless there is still a curvature at the beginning of the curve. Therefore a second PID iteration still has to be performed.

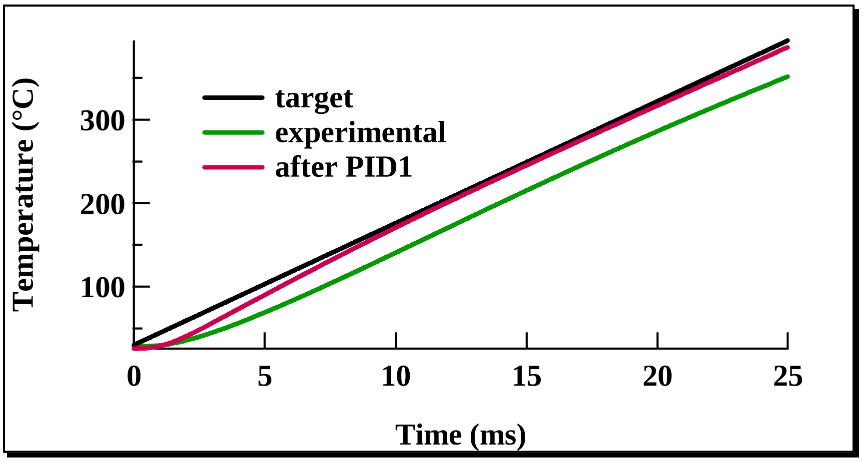

Figure 34. Experimental, target and corrected temperature ramps.

3.5. Temperature gradient on the sensors

The temperature gradient is measured by placing an indium microparticle at different places on the membrane. The particle is used as a temperature probe: the onset melting temperature of the particle is brought up at each places on the sensor membrane. For the given example the membrane has a size of 100 x 100 µm² (sensor XEN-3972) and the indium microparticle measures 9 µm. The particle is placed with the help of a micromanipulator.

Figures 35 shows the places where the particle was placed inside and outside the measurement area delimited by the thermocouples.

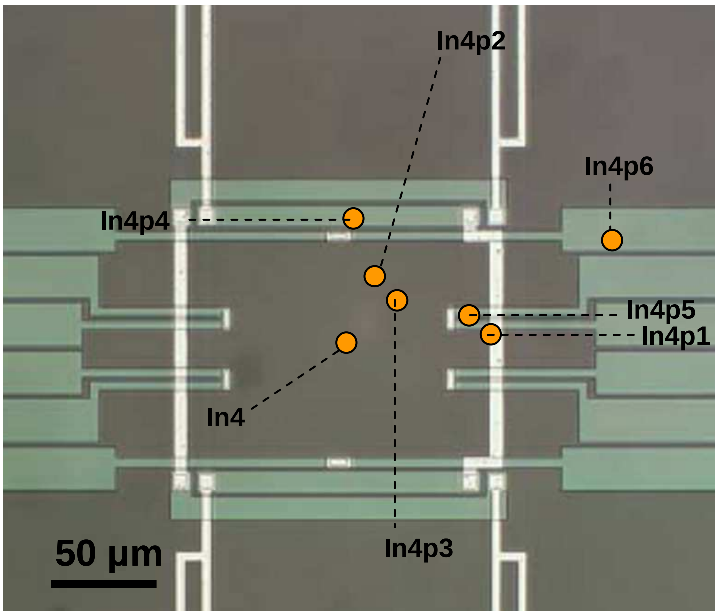

Figure 35. Indium microparticle of 9 µm on the sensor membrane.

The particle size is in the range of the scheme on figure 35.

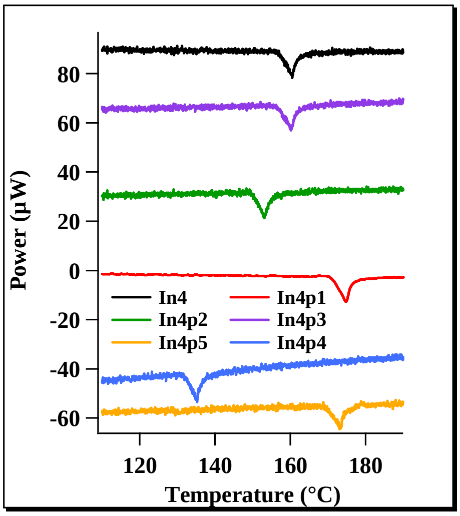

Name	Position (µm)	Melting enthalpy $.10^{-8}$ (J)	$T_{melting}$ (℃)	ΔT (℃)
In4	(0 ; 0)	6.2	156.5	0
In4p1	(60 ; 3)	6.05	171.7	-15.2
In4p2	(9.1 ; 27.3)	6.13	148	8.5
In4p3	(18.2 ; 18.2)	6.16	152.6	3.9
In4p4	(0 ; 54.5)	6.05	130.7	25.8
In4p5	(50 ; 9.1)	6.05	166	-9.5
In4p6	(130 ; 40)	_	_	_

Figure 36. Nanocalorimetric curves obtained at 39,000 °C/min and corresponding thermoanalytical data for a 9 µm indium microparticle positioned at different places inside the measurement area.

The nanocalorimetric curves of the 9 µm indium particle placed inside the measurement area are shown on figure 36, the melting enthalpy and melting temperature for each places of the particle are listed in the table from figure 36. The experiments are performed at a heating rate of 39000 °C/min (= 0.65 °C/ms). We choose this relatively slow heating rate for the melting temperature of indium particle to not being influenced significantly by the heating rate.

Delta T is calculated as follow: $\Delta T = 156.5 - T_{melting}$.

We don’t observe the melting of the particle placed far from the measurement area (In4p6 on figure 35), so the curve corresponding to the fast heating experiment of the sensor with the particle at such place is not represented on figure 36.

Figure 36 shows that melting enthalpy of the indium particle is independent of its position, i.e. it equals (6.11 ± 0.07) 10^{-8} J. However, the melting temperature does show a dependence from the particle position: the melting temperature onset varies in vertical and horizontal directions.

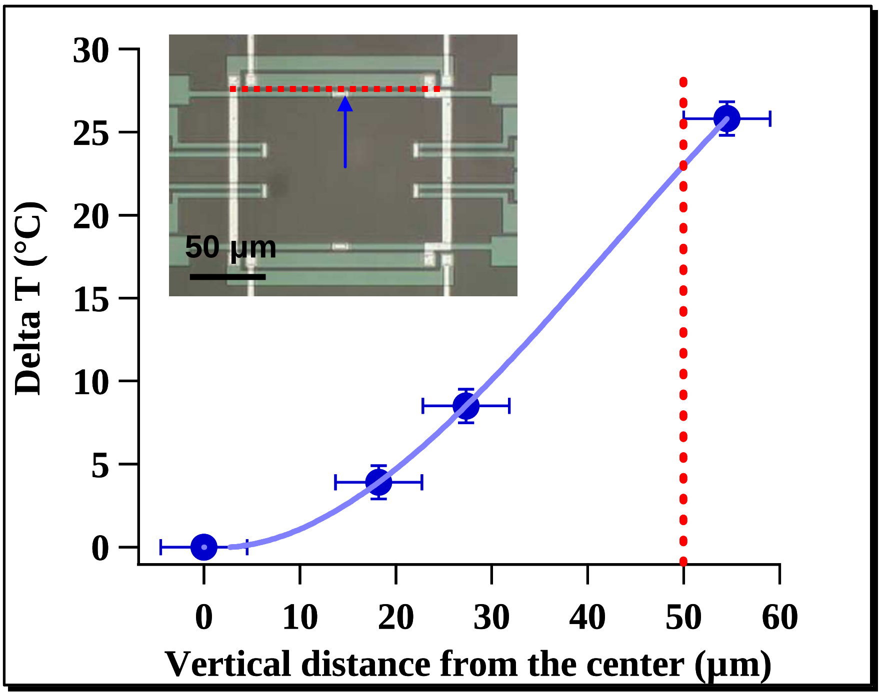

Figure 37. Delta T as a function of the vertical displacement. The vertical axis and the active area limits are shown in the insert.

The temperature variation (delta T) from the center to the heater (vertical direction) is shown on figure 37. When the particle is close to the center (at a distance smaller than 20 µm from the center), delta T is low (5°C). For a distance in the range of 20 µm to 50 µm, delta T increases almost linearly. The heaters are warmer than the center of the measurement area, which explains why the temperature increases with the heater proximity.

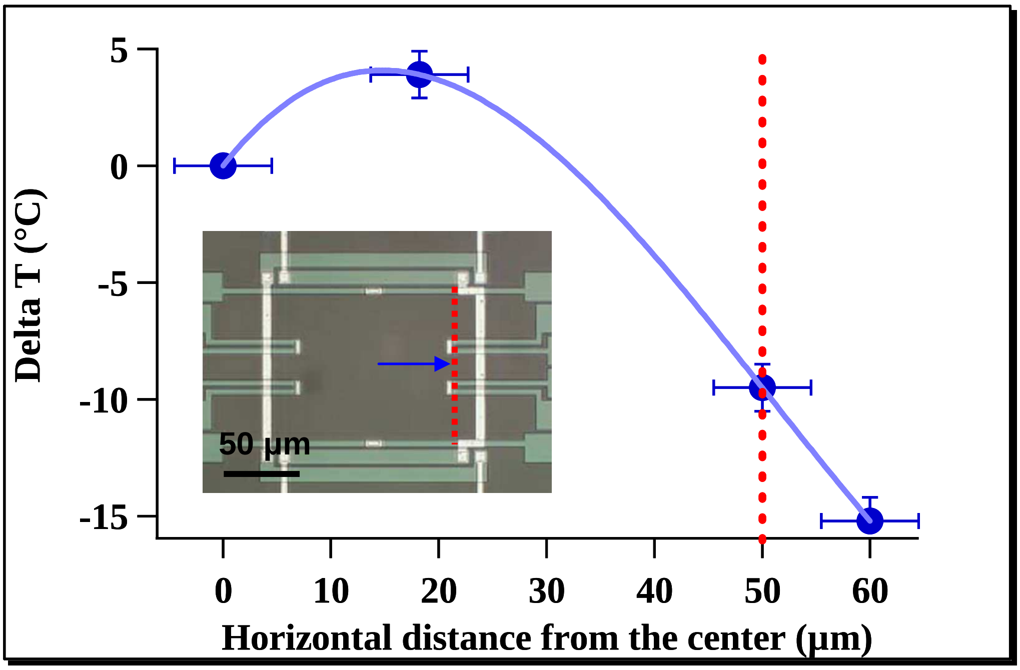

Figure 38. Delta T as a function of the horizontal displacement. The horizontal axis and the active area limits are shown in the insert.

Figure 38 gives the temperature variation from the center to the edge of the measurement area along the horizontal direction. The second point is due to the vertical offset of this point and not due to the horizontal offset (we don’t have much precision for this point). We observe that, along this direction, the gradient is much less steep. When the particle is placed on the edge of the measurement area at 50 µm from the center, the temperature decreases for 9.5°C. Furthermore, 60 µm away from the center the temperature is 15.2°C lower than in the membrane center. This important decrease of temperature is due to the fact that the heater strips are not infinite. Therefore, a part of the heat flux is spread radially, which explains why the heater cannot heat the edge of the measurement area as well as the center.

Concluding, we have observed through these experiments that, on the one hand, the melting enthalpy of indium microparticles is independent of their position on the membrane. On the other hand, a strong temperature gradient exists on the membrane at distances above 20 µm from the center. The temperature gradient is more important along the vertical axis than along the horizontal one.

3.6. Mass determination of unknown particles

To perform a correct calorimetric experiment, one should be able to weigh the sample. We use a method based on the cantilever resonant frequency to determine the mass of unknown particles.

AFM cantilevers are characterized by the probe dimensions (width, length, thickness) and the elastic properties (Young's modulus). For a common tipless cantilever from silicon nitride (length 350 ± 5 µm, width 35 ± 3 µm, thickness 1.0 ± 0.3 µm, $\rho = 3.1\ \mathrm{g.cm^{-3}}$) [8-9], its mass is about 39 ng. These parameters determine the main mechanical characteristics such as resonant frequency (ω) and spring constant (k). The cantilever stiffness varies with thickness and length. According to the equation given in chapter 2: $m = k_{lev} \cdot \left(\frac{1}{\omega^2} - \frac{1}{\omega_0^2} \right)$, therefore the spring constant of a cantilever is the key factor for determination of the unknown particle mass.

In our work, the first objective was to determine the spring constant of tipless cantilevers in order to use them afterwards as a microbalance for the mass determination of the explosive compounds. To calibrate the cantilevers, the melting enthalpy of an indium microparticle is measured by the nanocalorimeter to determine the mass of the particle. Then this particle is fixed at the end of the cantilever. The spring constant of cantilever is determined from the mass of the indium particle, the resonant frequency of the unloaded cantilever and that of the cantilever loaded with the particle.

Experimentally, we measure the spring constant of two types of cantilevers: the first are tipless cantilevers and the second are conventional rectangular cantilevers for imaging in Tapping mode. We made the measurements on 350-µm-long, 35-µm-wide tipless silicon cantilevers from Mikromasch. The nominal value of the cantilevers spring constant is 0.03 N/m. According to the Mikromasch specifications, the spring constant vary between 0.01 to 0.08 N/m. The rectangular cantilevers with a tip are RTESP probes from Veeco. These cantilevers have a resonant frequency between 267 – 320 kHz and their spring constants vary from 20 to 80 N/m.

Optical micrographs reveal different sizes and shapes of indium microparticles (cf. chapter 2).

An indium microparticle is placed on the nanocalorimetric sensor by micromanipulation (figure 39), then several fast-heating measurements are performed.

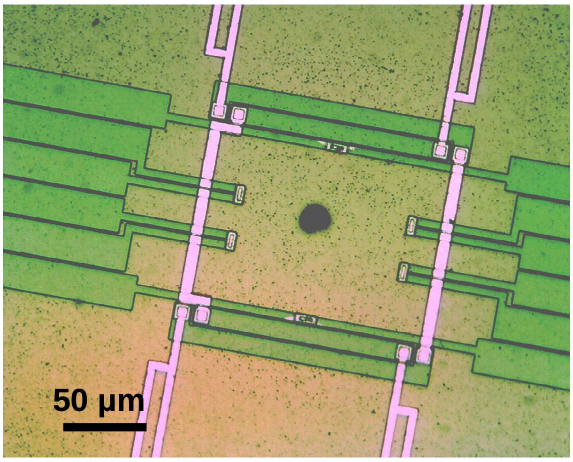

Figure 39. Indium microparticle positioned in the center of the nanocalorimetric sensor.

After the determination of particle mass by nanocalorimetry, the indium microparticle is fixed at the end of the tipless cantilever (figure 40) by placing the sensor in the AFM and by pushing the cantilever against the particle.

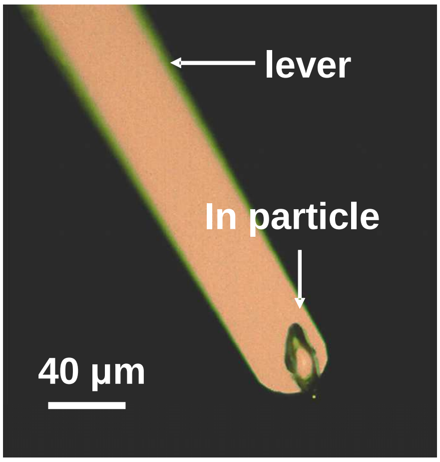

Figure 40. Indium microparticle on a tipless cantilever.

The spring constant of cantilevers with a tip is determined without destroying or touching the surface with the tip. For this measurement, the cantilever is loaded upside down into the tip holder. Thus the tip of the cantilever is directed towards the laser and the backside of the cantilever is directed toward the sample surface. If the laser is focused on the tip, it gets diffracted by the tip, so one cannot obtain a single laser spot on the photodiode. The laser beam is placed near the tip as shown on figure 41.

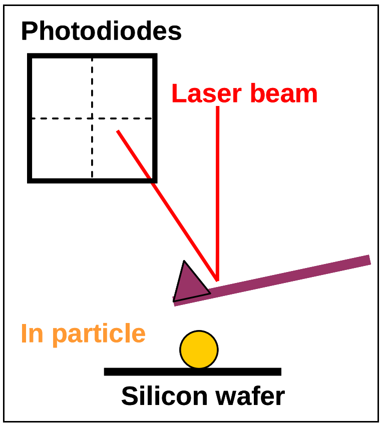

Figure 41. Cantilever with a tip placed in the AFM.

The resonant frequencies of the unloaded cantilever and of the cantilever with the particle are measured by AFM. Nine autotunes are performed on the cantilever, the averaged curve is fitted with a lorentzian (4):

$$y = A + B * x + \frac{C * Q}{\sqrt{Q^2 * (1-(\frac{x}{f_0})^2)^2 + (\frac{x}{f_0})^2}} \qquad (4)$$

In equation (4), Q is the quality factor, A is a constant, B is the slope (the resonant peak is a little asymmetric), C is a proportionality coefficient, f_0 is the resonant frequency of the unloaded cantilever. The fit allows one to extract the quality factor and the resonant frequency.

Six fast heating measurements were performed on each of several indium particles to determine the melting enthalpy of the particles. The mass of the particles was calculated from the melting enthalpy measured on the nanocalorimetric curves using the melting enthalpy of the pure material (28.62 J/g).

The graph on figure 42 is obtained on an indium microparticle at several heating rates from 32380 °C/min to 216640 °C/min.

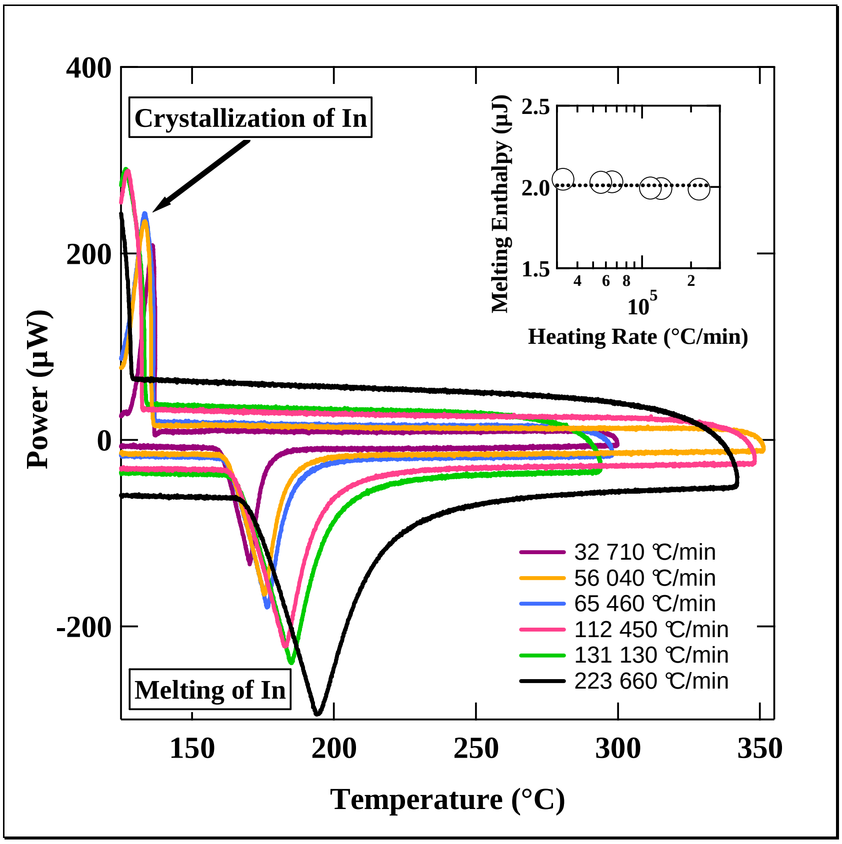

Figure 42. Nanocalorimetric curves of a indium particle of 70.30 ± 0.90 ng.

In this case, the indium particle has a mass of 70.30 ± 0.90 ng. The nanocalorimetric experiments are performed on nine indium particles with the masses listed in table 2. They change in the range from 2.08 ng to 90 ng.

Particle	In4	InA	InB	InC	InD	InE	InF	InG	InH	InI	InJ
Mass (ng)	2.08	90	68.34	70.30	32.93	17.69	43.03	29.25	11.20	7.43	11.11
Accuracy (ng)	0.16	1.30	2.51	0.90	0.92	0.29	1.05	0.65	0.12	0.11	0.47

Table 2. Masses of indium particles used to calibrate the cantilevers

The accuracy on the mass is determined using the standard deviation based on six fast heating measurements. The precision on the resonant frequency is about 2 – 3 Hz.

Figure 43 presents on the left the four amplitude-frequency curves corresponding to cantilever E before (1) and after loading with In particles of different masses (2 to 4). We observe that the frequency is decreasing when the particle mass increases as expected. Furthermore the Lorentzian from equation (4) in red on figure 43 fits with the experimental curves. The dependence of the added mass on the square of reciprocal resonant frequency of the same cantilever is given in the right panel of the figure. The linear relation is satisfied in the whole range of particle masses. The spring constant of cantilever E can thus be obtained from the slope of the curve, and equals 0.0454 N/m, i.e. within the nominal range. From the error-bars on the particle masses, the standard deviation of the spring constant is determined, which is better than 1%. The effective mass of the cantilever is 8.12 ± 0.18 ng. The latter is the equivalent point mass concentrated at the end of the cantilever.

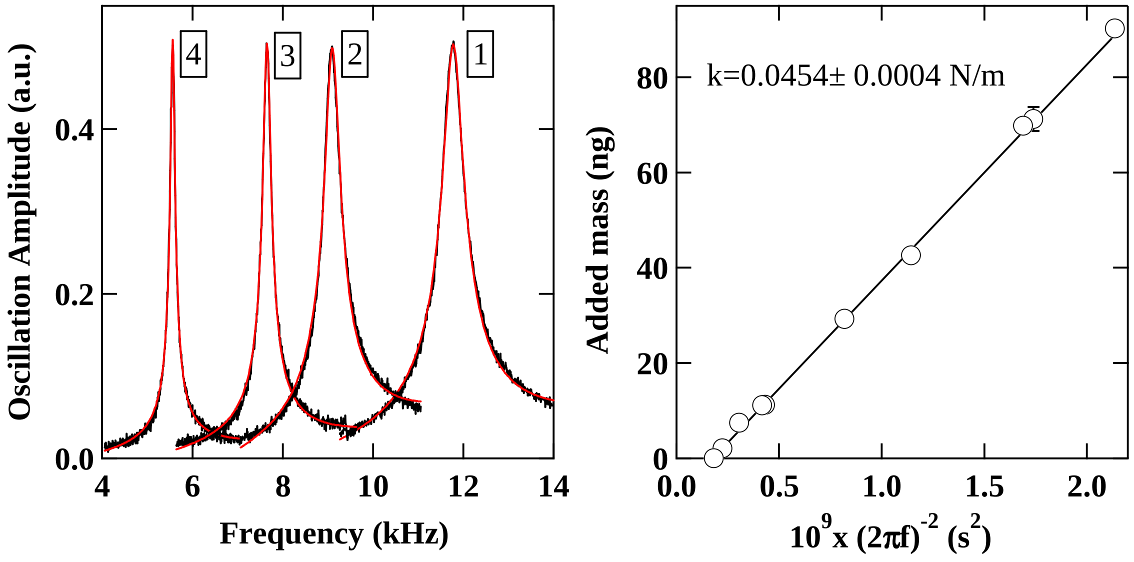

Figure 43. *Left:* amplitude-frequency curves corresponding to cantilever 2E before (1) and after loading with In particles of 7.43 ± 0.11 ng (2), 11.20 ± 0.12 ng (3) and 29.25 ± 0.25 ng (4). Black and red lines correspond to the experimental data and fits with Lorentzian functions, respectively. *Right:* added mass as a function of square of reciprocal resonant frequency for the same cantilever successively loaded with nine different In particles. The effective mass of the cantilever is 8.12 ± 0.18 ng.

The spring constant of nine others cantilevers are determined by the same method. It is noteworthy that all cantilevers come from the same batch. The graphs determining the spring constant for each cantilever are given in appendix 3.3.

The effective mass of these studied cantilevers is shown on figure 44.

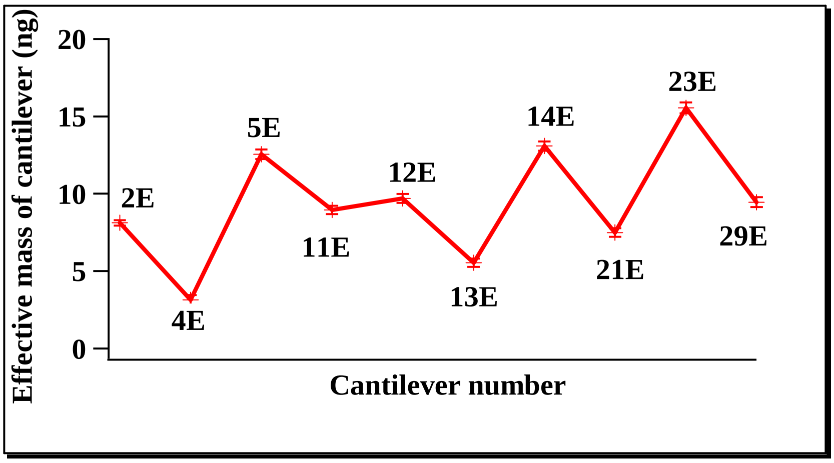

Figure 44. Effective mass of ten cantilevers.

The average of the effective mass is 9.12 ± 1.83 ng.

The quality factor Q is measured for unloaded cantilevers and for the cantilevers with a particle of 11.11 ng.

Name	2E_empty	2E_In	4E_empty	4E_In	5E_empty	5E_In	11E_empty	11E_In
Q	27.495	45.893	31.584	44.225	31.529	48.327	22.358	39.623
Accuacy	0.345	0.319	0.364	0.496	0.220	0.315	0.175	0.305

12E_empty	12E_In	13E_empty	13E_In	14E_empty	14E_In	21E_empty	21E_In
24.480	45.686	25.052	46.047	29.265	46.972	17.747	35.007
0.270	0.335	0.209	0.312	0.226	0.366	0.433	0.326

23E_empty	23E_In	29E_empty	29E_In
21.591	31.924	26.465	45.273
0.208	0.259	0.180	0.322

Table 3. Quality factor for unloaded and In-loaded cantilevers.

The quality factors of loaded cantilever are higher than that of the unloaded ones because the mass of the system (cantilever with the particle) increases but the frictional damping remains the same.[10]

The determination of the cantilever spring constant with the Nanocalorimetry has several advantages in comparison with other methods presented in chapter 1. First, there is no uncertainty on the geometric dimensions (length, width, thickness) of the particle measured by optical microscopy. The main error source for Cleveland's and Sader's methods is the precision on the dimensions of the object which is the diameter of the beads for Cleveland's method and the cantilever dimensions for the Sader's method. Then, the optical sensitivity of the laser is not used in our measurements as for the thermal noise method. Also, we are not limited by the sampling rate which is the case of the thermal noise method so even the spring constant of cantilevers with high frequency can be successfully calibrated. Moreover, there is no stick-slip phenomena as for the reference lever method proposed by Torii, so our method is applicable for determination of the spring constant of tipless cantilevers.

Determination of the spring constant of a cantilever with a tip through an example. The cantilever is placed in the tip holder as shown on figure 41. According to the average of autotune curves corresponding to the empty cantilever, the resonant frequency of the empty cantilever is 307.89 kHz. The resonant frequency of the cantilever with the indium particle InI is 219.12 kHz. The mass of the particle InI is 8.22 ± 0.29 ng. The cantilever spring constant is therefore determined according to equation (5):

$$k = \frac{m_{InI}}{\left(\frac{1}{4\pi f^2} - \frac{1}{4\pi f_0{}^2}\right)} \quad (5)$$

The spring constant of the cantilever is calculated to be 31.57 N/m. This value is within the frequency range given by Veeco (20 < k < 80 N/m).

Application to the mass measurement to studies of the explosives: the case of CL-20. The determination of extremely small amounts of explosives is really important in the field of explosives detection. Some explosives such as PETN and RDX melt before the decomposition point so it is possible to determine the mass of such kind of energetic materials according to their melting enthalpy. Others energetic materials such as CL-20 don't melt before the decomposition as shown on the following DSC curves.

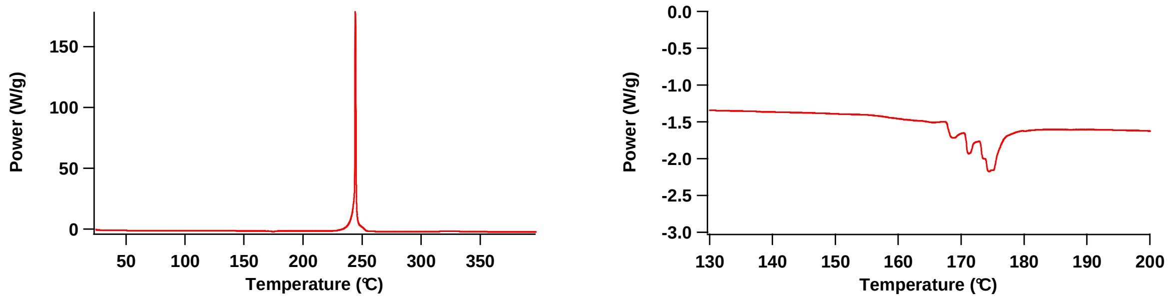

Figure 45. DSC curves of CL-20 measured at 10 °C/min.

On DSC curves on figure 45 we observe an exothermic peak at 230°C which corresponds to decomposition of CL-20, and an endothermic peaks at 170°C corresponding to a polymorphic transition (see chapter 4).

Furthermore, the decomposition enthalpy and the polymorphic transition enthalpy of CL-20 depends on several external parameters such as pressure and environment[11]. Therefore it is quite useful for the experimentalist to know the mass of the crystal.

For the experiment on figure 46, the mass of the CL-20 crystal is determined with cantilever 2E (k = 0.0454 N/m). The frequency of the unloaded cantilever is 11.767 kHz and the frequency of cantilever with the CL-20 crystal is 6.675 kHz, so the mass of the crystal equals 12.96 ng.

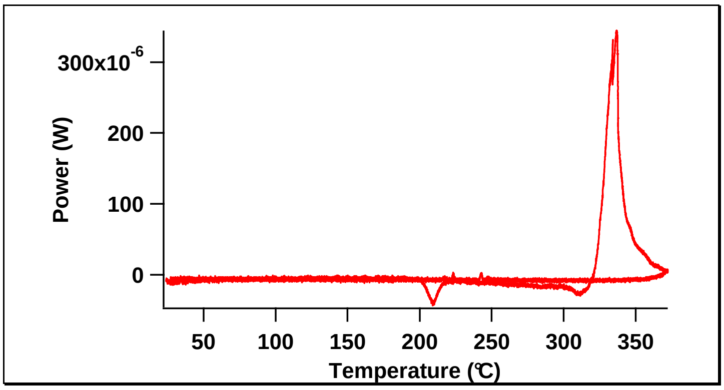

Figure 46. Nanocalorimetric curve of a CL-20 crystal of 12.96 ng.

It was found that the decomposition enthalpy is not constant with the heating rate as shown on figure 47.

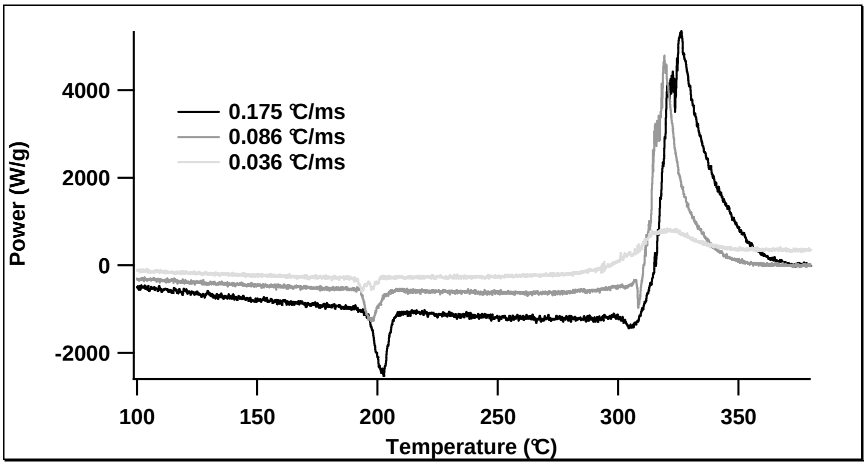

Figure 47. Nanocalorimetric curves of CL-20 measured at different heating rates.

For the nanocalorimetric experiments shown on figure 47, the mass of the CL-20 crystals are 9.89 ± 0.63 ng, 15.73 ± 1.91 ng and 13.46 ± 1.99 ng and the heating rates are 0.175 °C/ms, 0.086 °C/ms, and 0.036 °C/ms, respectively. Each particle mass is determined with three different cantilevers 29E, 23E, 21E. We observe on this graphic that the decomposition enthalpy depends on the heating rate: for the experiments at 0.0175 °C/ms and at 0.086 °C/ms, the decomposition enthalpy is 834.88 and 813.46 J/g, respectively, whereas for the experiment at 0.036 °C/ms the enthalpy is only of 629.31 J/g. The influence of the heating rate on the decomposition enthalpy of CL-20 was reported previously by Turcotte at conventional heating rates of DSC (1, 2, 5, 10 °C/min).

As far as the polymorphic peak is concerned, it can be single or double. The last observation can be assigned to the purity[11] of CL-20, so in this case we cannot determine the crystal mass from the enthalpy of this transition.

3.7. Conclusions

This chapter is focused on establishing the procedure to calibrate the calorimetric sensors. The originality of the temperature calibration procedure resides in the use of the melting temperature of metallic microparticles (In and Zn) to cross-check the temperature measured by the Nanocalorimeter. This cross-checking is done for heating ramps in modulation (slow heating rates) and for ramps at fast-heating rates.

The measurements of temperature gradient are also performed with an indium microparticle placed on a XEN-3972 sensor (active area of 100 x 100 μm^2). We observe that the melting temperature of the indium particle measured by the Nanocalorimeter changes with its position on the membrane and that the melting enthalpy is constant when the particle is placed inside the measurement area.

To improve the quality of the linear heating ramps at high heating rates we propose an iterative PID-based method.

To perform quantitative calorimetric measurements, we weigh unknown particles using the resonant frequency of tipless AFM cantilevers. Before the mass determination, the spring constant of the cantilever has to be determined with precision. Chapter 2 gives an overview of the different methods designed to measure the spring constants. In this chapter, we propose the Nanocalorimeter as a new experimental tool for such measurements. In particular, the Nanocalorimeter presents several advantages compared to other methods. Thus it is free from uncertainties on the object size, it is not limited by the sampling rate as it is the case of the thermal noise method, it is not dependent on the laser optical sensitivity, and does not suffer from problems due to stick-slip phenomena as is the case of the reference lever method. Experimentally, indium particles of different size are placed successively on a sensor. Then several fast-heating experiments are performed in order to melt the indium particle and to determine its mass through its melting enthalpy. The cantilever spring constant corresponds to the slope of the line representing the added mass on the cantilever as a function of $\frac{1}{(2.\pi.f)^2}$. Once the determination of the cantilever spring constant is completed, the unknown particle is placed on the cantilever, and its mass is measured using the following equation $m = k.\left(\frac{1}{\omega^2} - \frac{1}{\omega_0^2}\right)$ where k is the cantilever spring constant, ω is the angular frequency of the cantilever loaded with the particle, and ω_0 is the angular frequency of the unloaded cantilever.

The precision of this method is about 3%, the main error comes from the melting enthalpy determination of the indium particles.

---

[1] Efremov, M.Yu.; Olson, E.A.; Zhang, M.; Lai, S.L.; Schiettekatte, F.; Zhang, Z.Z.; Allen, L.H. *Thermochimica Acta* **2004**, *412*, 13 – 23.

[2] Kwan, A.T.; Efremov, M.Yu.; Olson, E.A.; Schiettekatte, F.; Zhang, M.; Geil, P.H.; Allen, L.H. *Journal of Polymer Science, Part. B. Polymer physics* **2001**, *39*, 1237-1245.

[3] http://www.xensor.nl/pdffiles/sheets/nanogas3939.pdf

[4] http://www.xensor.nl/pdffiles/sheets/nanogas-olderversions.pdf

[5] http://www.periodni.com/fr/sn.html

[6] Minakov, A.A.; Adamovsky, S.A.; Schick, C. *Thermochimica Acta* **2005**, *432*, 177 – 185.

[7] Conductivité thermique, cours de Prof. H. HOFMANN (EPFL), laboratoire de technologie de poudres, http://mxsg3.epfl.ch/ltp/Cours

[8] http://www.spmtips.com/csc/c12/tipless

[9] http://www.polytech-lille.fr/cours-atome-circuit-integre/CstSiN4.htm

[10] Cleveland, J.P.; Manne, S.; Bocek, D.; Hansma, P.K. *Review of Scientific Instruments* **1993**, *64* (2), 403 – 405.

[11] Turcotte, R.; Vachon, M.; Kwok, Q.S.M.; Wang, R.; Jones, D.E.G. *Thermochimica Acta* **2005**, *433*, 105-115.

4. Study of explosives

This chapter is devoted to the thermal behaviour of energetic materials during nanocalorimetric experiments. First, DSC analysis are performed on RDX and PETN to determine their activation energy of decomposition, then the sublimation of RDX and PETN single crystals deposited on a nanocalorimetric chip is evidenced. The activation energies of sublimation are extracted from the nanocalorimetric measurements and a model of a single RDX crystal sublimation is proposed. After that, the evaporation of RDX and PETN during fast heating experiments is studied. The thermal behaviour of nanoRDX/TNT blends addressed with the nanocalorimeter allows to confirm the presence of RDX nanoparticles in the blend. The last part of this chapter is focused on the thermal behaviour of CL-20 single crystals.

4.1. Micro RDX and PETN

The two energetic materials studied in the first part of the chapter are single micro-crystals of RDX and PETN. The study starts from a DSC analysis in the bulk, then the thermal behaviour of individual crystals is analyzed with nanocalorimetry to address the sublimation and evaporation processes.

4.1.1. DSC Analysis

DSC experiments on RDX and PETN are performed in closed crucibles. On figure 1, DSC traces of RDX were recorded during heating between 25°C and 380°C at six heating rates: 2, 5, 10, 20, 40 and 60°C/min.

An endothermic transition is observed on all curves at 204°C, this event is immediately followed by an exothermic transition. The endothermic transition is assigned to the RDX melting, while the exothermic peak corresponds to the RDX decomposition. Table 1 summarizes temperatures and enthalpies characteristic from the RDX used in this study.

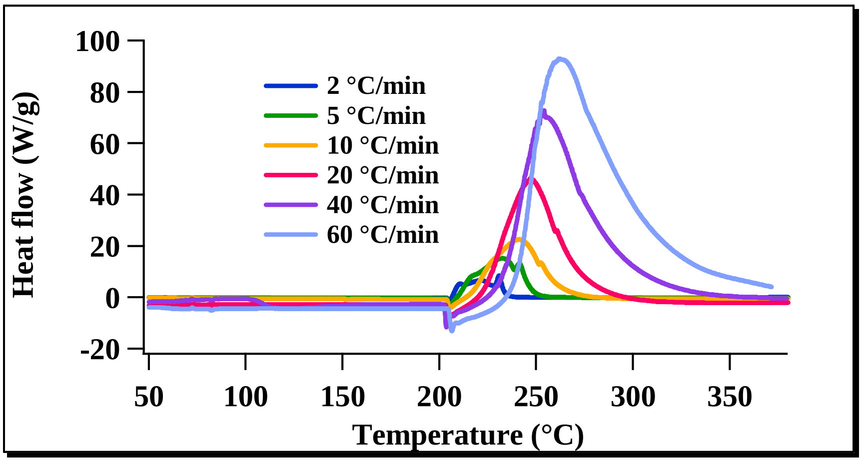

Figure 1. DSC curves of RDX in closed crucibles measured at 2°C/min, 5°C/min, 10°C/min, 20°C/min, 40°C/min, 60°C/min.

Thermal analysis with the differential isoconversional method is performed using this data to determine the activation energy of the RDX decomposition. A short description of the isoconversional method is given in appendix 4.1. In this method, the activation energy is computed from the reaction rate at each conversion.

Heading rates (°C/min)	$\Delta H_{melting}$ (J/g)	$T_{melting}$ (°C)	$\Delta H_{decomposition}$ (J/g)	$T_{decomposition}$ (°C)
2	98.9	204.2	4670	206.3
5	94.6	204.2	4970	209.4
10	85.8	204.3	4340	216.2
20	87.8	203.7	5070	222.6
40	92.0	203.1	4620	233.7
60	89.7	204.7	4840	240.4

Table 1. Thermoanalytical parameters of RDX, as measured in closed crucibles at several heating rates.

The activation energy of RDX decomposition for several degrees of conversion is given on figure 2.

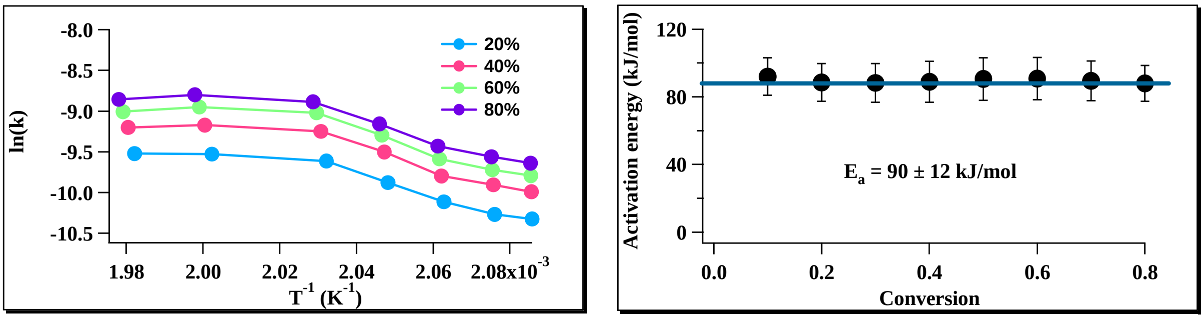

Figure 2. Activation energy of RDX decomposition measured in closed crucibles.

According to the experiments, the activation energy of RDX decomposition is 90 ± 12 kJ/mol. In the literature, the experimental and theoretical activation energy of RDX is in the range of 96 to 219 kJ/mol. The discrepancy for activation energy can be explained for example by kinetic compensation effects.[1] The kinetic compensation effect consists in the fact that E_a correlates with the pre-factor. When E_a increases, the reaction rate is not necessarily decreases inevitably because A increases to compensate for E_a. So the activation energy of RDX decomposition is strongly dependent on the sample characteristics (e.g., sample mass, particle size, heating rate, self-heating of the sample) and the experimental conditions (characteristics of the surrounding atmosphere, shape and material of construction of the sample holder). Thus, the activation energy of RDX is known to increase when the sample density decreases [2].

Independently of the compensation effects, some experiments in closed and open pans proved that there is a competition between evaporation and decomposition[3]. Thus in closed crucibles, the activation energy of decomposition is 200 kJ/mol, the decomposition occurs in the liquid phase. In open crucibles the E_a becomes 140 kJ/mol because of the competition with evaporation and the decomposition of the gaseous RDX (figure 3).

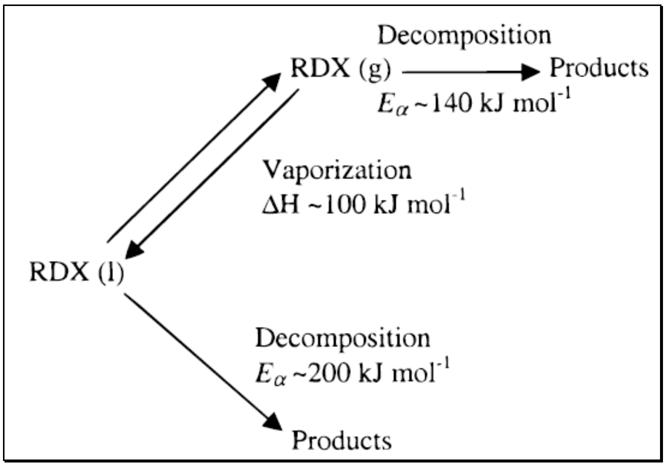

Figure 3. A kinetic scheme for the thermal decomposition of liquid RDX.

The mechanisms of the gas phase unimolecular decomposition of RDX are explained by a N – NO_2 bond rupture and by a concerted ring fission to three methylenenitramine molecules as illustrated in figure 4.[4]

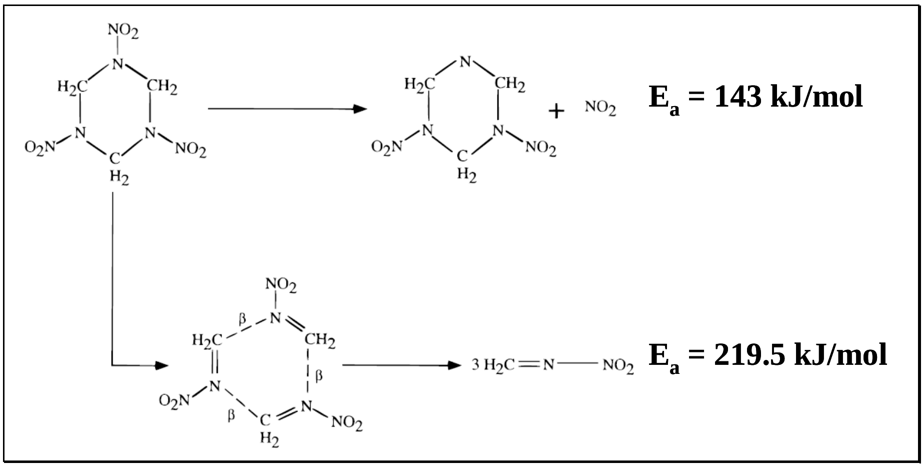

Figure 4. Schematic drawing of RDX dissociation via N – NO_2 bond. rupture (E_a = 143 kJ/mol) and symmetric ring-fission (E_a = 219.5 kJ/mol).

DSC traces of PETN on figure 5 were recorded during heating between 25°C and 400°C at six heating rates: 2, 5, 10, 20, 40 and 60°C/min.

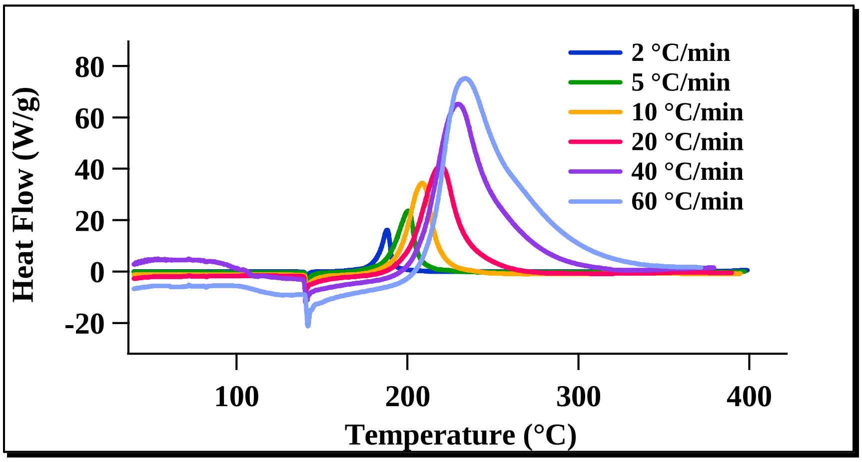

Figure 5. DSC curves of PETN in closed crucibles measured at 2°C/min, 5°C/min, 10°C/min, 20°C/min, 40°C/min, 60°C/min.

The DSC curves on figure 5 exhibit an endothermic transition at 140°C and an exothermic transition in the range of 180 to 200°C. The endothermic peak corresponds to the PETN melting and the exothermic peak corresponds to the PETN decomposition.

Table 2 summarizes temperatures and enthalpies characteristic of the thermal behaviour of PETN used in this study.

Heating rates (°C/min)	$\Delta H_{melting}$ (J/g)	$T_{melting}$ (°C)	$\Delta H_{decomposition}$ (J/g)	$T_{decomposition}$ (°C)
2	154.7	140.3	4320	181.5
5	148.0	140.0	4110	187.5
10	145.9	140.4	3940	194.2
20	135.3	140.0	3500	199.1
40	112.7	140.5	3970	206.9
60	87.7	140.3	3780	212.0

Table 2. Thermoanalytical parameters of PETN, as measured in closed crucibles at several heating rates.

The analysis with the isoconversional method has been also performed on this data to determine the activation energy of the PETN decomposition. The latter is given as a function of conversion on figure 6.

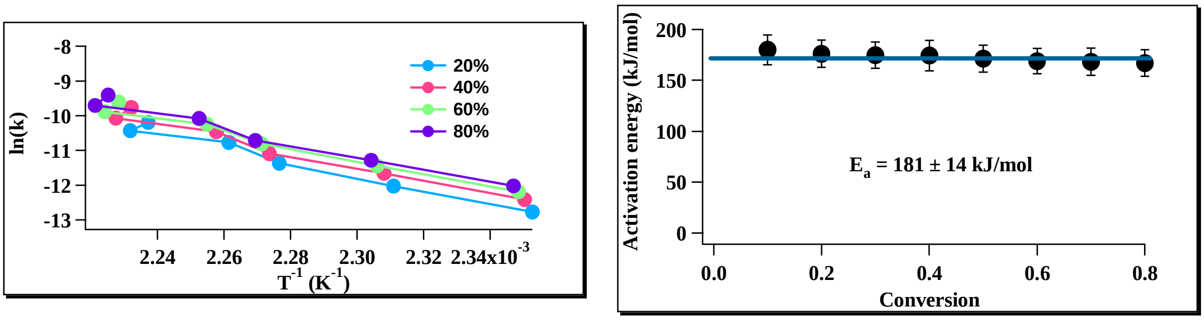

Figure 6. Activation energy of PETN decomposition measured in closed crucibles.

According to the experiments, the activation energy of PETN decomposition is constant and equal 181 ± 14 kJ/mol. The activation energy reported in the literature is in the range of 132.7 to 197.5 kJ/mol.[5] Therefore our values are in good agreement with the literature. The decomposition process is believed to follow a four-step model which is summarized on figure 7.[6]

reactions	E_a (kJ/mol)	lnZ (s^{-1})
PETN → Condensed Phase Intermediates	196.6	41.59
PETN + Condensed Phase Intermediates → Gaseous Intermediates	178.3	41.95
Condensed Phase Intermediates → Gaseous Intermediates	149.7	36.00
Gaseous Intermediates → Final Gaseous Products (CO_2, H_2O, N_2, CO, etc)	126.8	32.00

Figure 7. Four-step decomposition model of PETN.

4.1.2. Sublimation

The following section is focused on the sublimation phenomenon observed for RDX and PETN microcrystals. First, we identify the sublimation process, and then we study the kinetics of sublimation for each of the two explosives.

1. Evidence for the RDX and PETN sublimation

- Evidence of the RDX sublimation.

The following optical micrographs on figure 8 are taken every 10s during an isotherm at 130°C on a single RDX crystal. The time on each picture is the time given by the nanocalorimeter during the isotherm. The isotherm starts at time t = 4s. The nanocalorimeter operational parameters are 0.1 mA for the amplitude, 0.3 mA for the DC offset and 75 Hz for the modulation frequency.

The first micrograph at 4s shows a RDX crystal in the center of the measurement area. At 30s, we observe the crystal size decreases and some particles appear around the measurement area. At 60s, the crystal becomes smaller and the amount of particles around the measurement area increases. At 100s, there is no RDX in the center anymore but an increasing amount of particles around the measurement area.

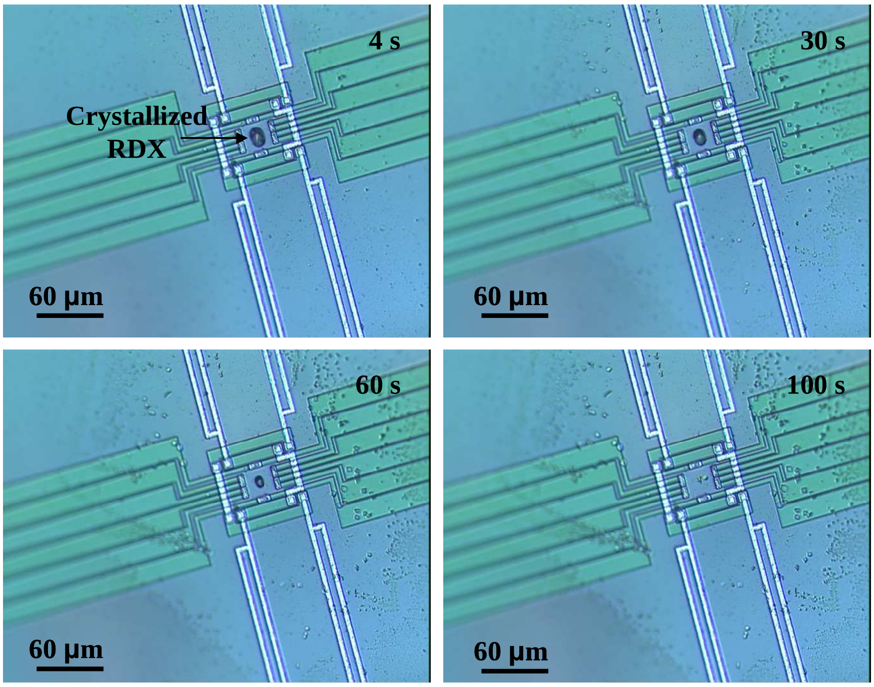

Figure 8. Optical micrographs of a RDX crystal on a sensor chip during isotherm at 130°C.

The AC amplitude curve corresponding to this isotherm is shown on figure 9.

We observe on figure 9 a raise of the amplitude during the isotherm. This change in the amplitude takes about 92s to occur (from 4s to approx. 96s on figure 9), then the curve stays at an almost constant value after 104s. By

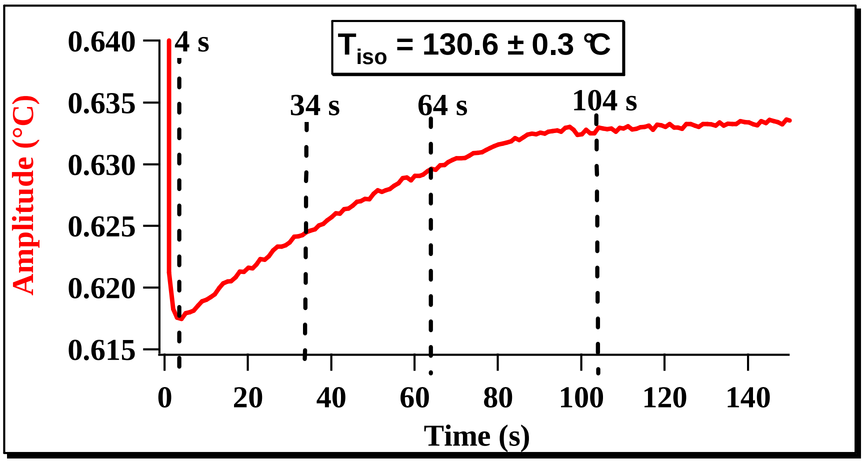

Figure 9. Quasi-isothermal nanocalorimetric curve corresponding to a single RDX crystal at 130°C (the experiment starts at 4 s).

comparing the optical micrographs on figure 8 and the nanocalorimetric curves on figure 9, we assign the change in the AC amplitude to a progressive removal of the RDX crystal from the center of the measurement area.

To know if the material located outside the measurement area is crystalline or not, we performed a heating ramp on RDX crystals deposited on a sensor which has a hole behind the 1 μm thick membrane. This makes measurements in transmitted polarized light feasible on such a sensor.

On the micrographs on top of figure 10 we observe RDX particles which are strongly birefringent, i.e. crystalline. These micrographs correspond to the sample before the heating ramp. The two micrographs on the bottom of figure 10 are taken after heating of the RDX crystals at 20°C/min. It can be seen that nothing remains on the membrane, while the material appeared outside the measurement area is crystalline.

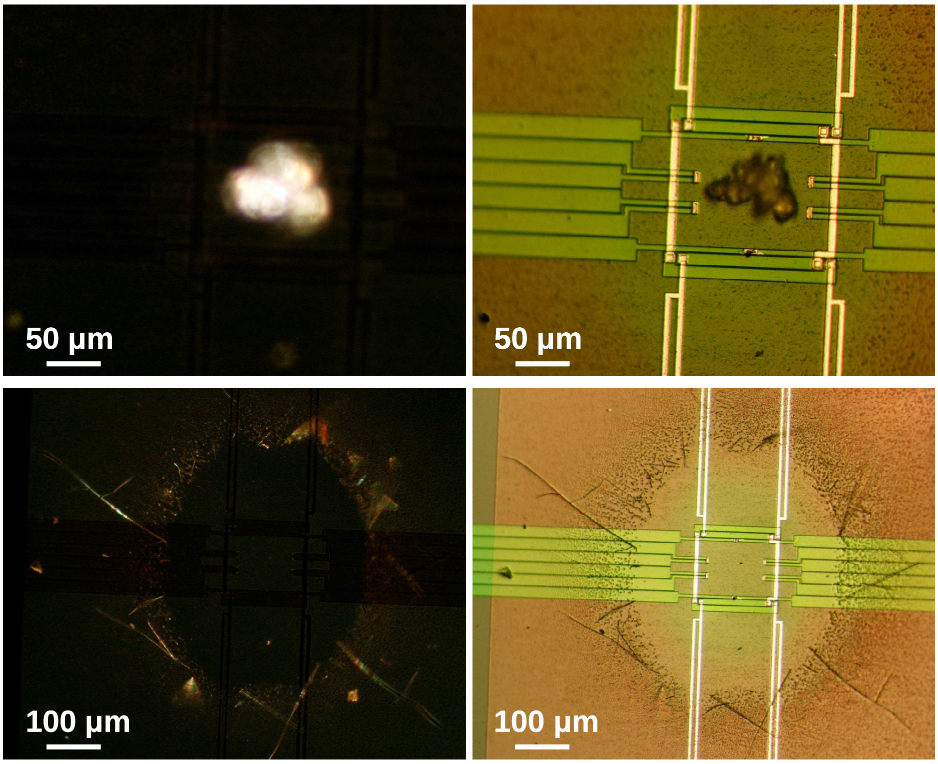

Figure 10. View of RDX crystals in reflected and transmitted polarized light before and after a heating ramp at 20 °C/min.

Raman analysis is performed on RDX crystals located in the centre of the measurement area before the heating ramp and on particles outside the measurement area after the completion of the heating ramp to identify the nature of these particles. The Raman spectrum on figure 11 is performed on one isolated RDX crystal. On figure 11, the Raman spectrum of the RDX crystal exhibits an intense peak at 884 cm^{-1} associated to the aromatic ring stretching mode. The weak peak at 848 cm^{-1} is assigned to NO_2 deformation and the three intense peaks around 3000 cm^{-1} are due to CH_2 stretching mode. According to the literature[7], this Raman spectrum is the signature of the α-RDX. The Raman spectrum on figure 12 is measured on a particle formed after the heating ramp.

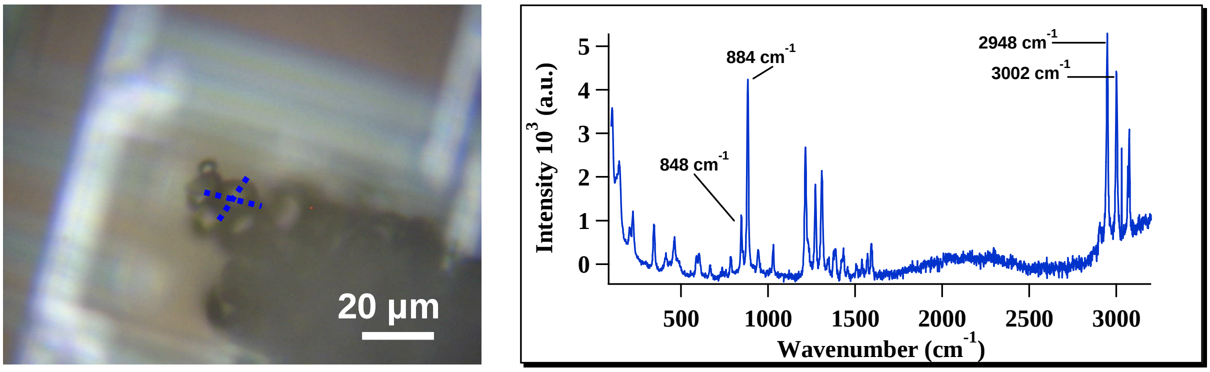

Figure 11. RDX crystal (left) and its Raman spectrum (right).

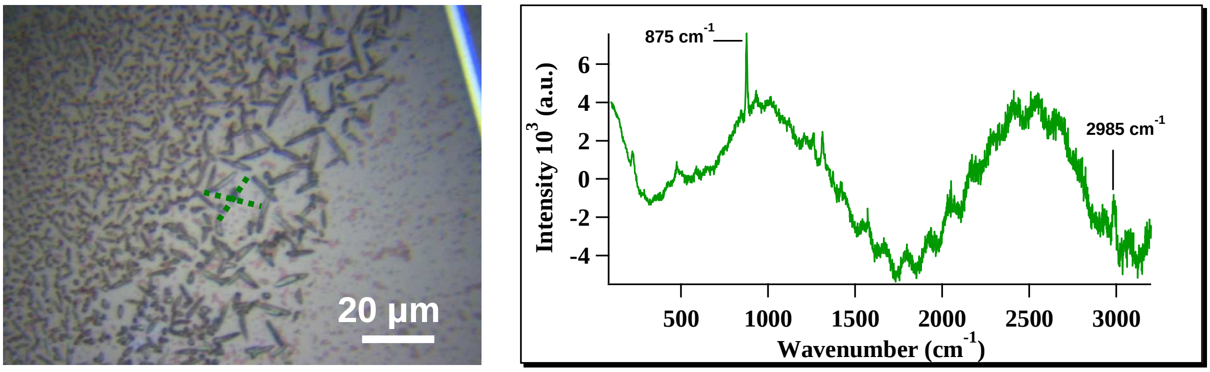

Figure 12. Particles obtained outside the active area after a heating ramp of the RDX crystals at 20 °C/min (on the left) and its Raman spectrum (on the right).

The measured Raman signal is not very intense because of a small amount of material and small thickness of the particle but one sees that the spectrum is clearly dominated by an intense peak at 875 cm^{-1} (9 cm^{-1} away from that of the α-RDX spectrum). This peak is characteristic of the β-RDX.[8-9] Besides, the rod shape of the particles on figure 12 is characteristic of the β-RDX.[10] P. Torres et al. have found that formation of β-RDX can be induced by the substrate surface.

- Evidence for the PETN sublimation.

Similar experiments were performed on a single PETN crystal with the same nanocalorimeter parameters. The optical micrographs given in figure 13 were taken with one PETN single crystal every 15s during an isotherm at 146.4°C. The isotherm starts at t = 21s.

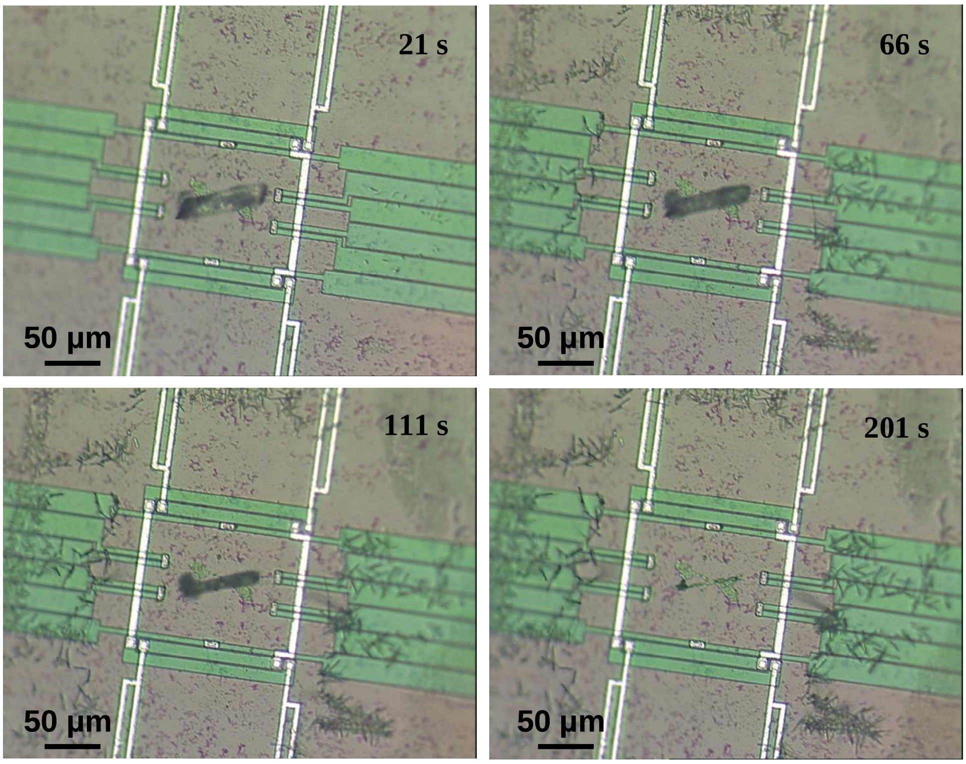

Figure 13. Optical micrographs showing a single PETN crystal on a chip sensor during isotherm at 146.4°C.

We observe on figure 13 that, during isotherm the PETN crystal in the center of the measurement area becomes smaller, whereas some rod-shaped particles appear around the measurement area. At 201s, the PETN crystal is not visible anymore whereas a lot of particles appeared outside the measurement area. The nanocalorimetric curve corresponding to the isotherm of the PETN crystal at 146.4°C is given on figure 14.

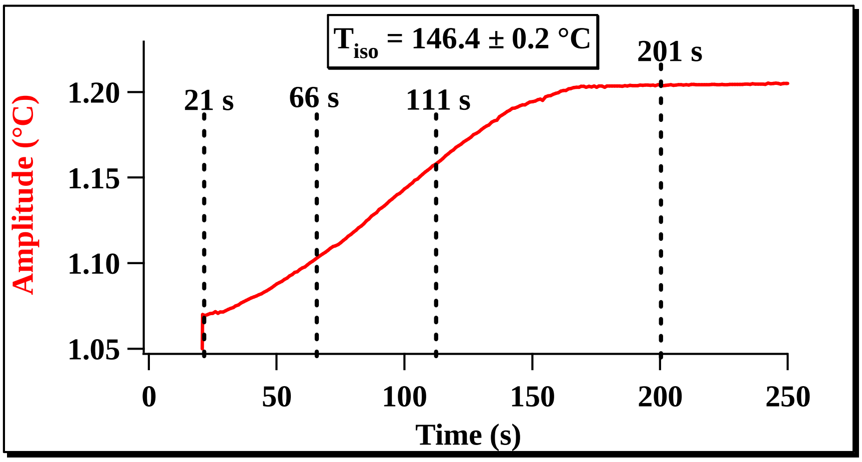

Figure 14. Quasi-isothermal nanocalorimetric curve corresponding to a single PETN crystal at 146.4°C (the experiment starts at 21 s).

As with RDX, we observe that the increasing values of the AC amplitude correspond to a decrease of the PETN crystal size.

The optical micrographs of the PETN crystal in polarized light are on figure 15.

Before the heating ramp (cf. micrograph on top of figure 15) one can see crystalline PETN. After the heating ramp, the PETN has disappeared from the center of the measurement area and a lot of rod-shaped particles are present around the measurement area.

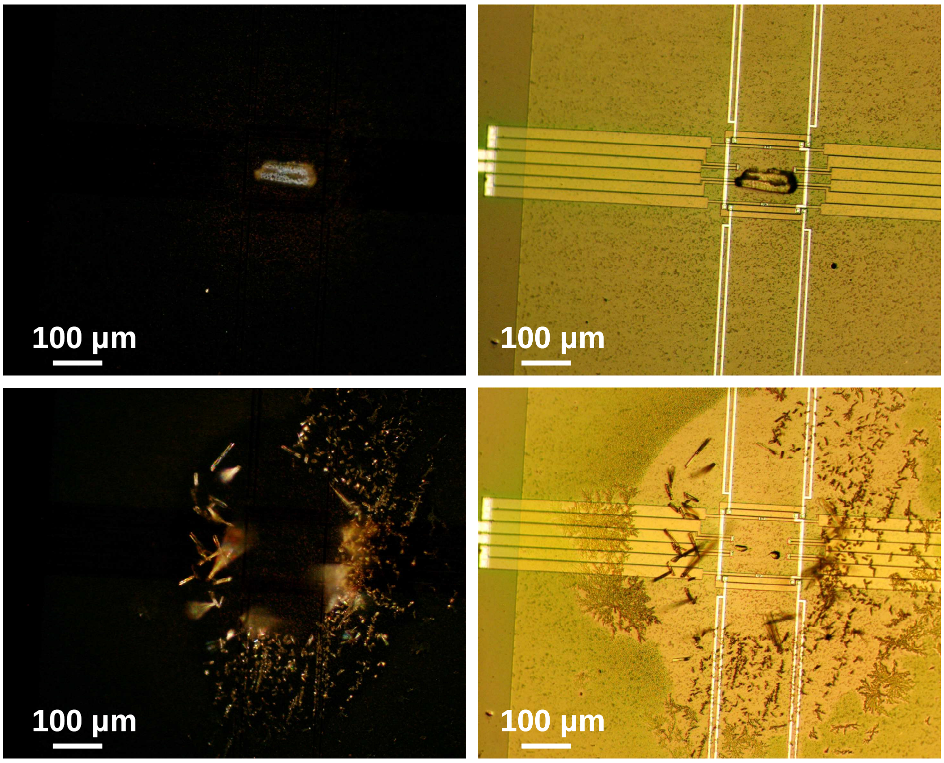

Figure 15. View of PETN crystals in reflected light and in transmitted polarized light before and after the heating ramp at 20 °C/min.

Raman measurements are performed on PETN crystal and on particles around the measurement area which appeared during the heating ramp. Figure 16 shows the PETN crystal used to measure the Raman spectra.

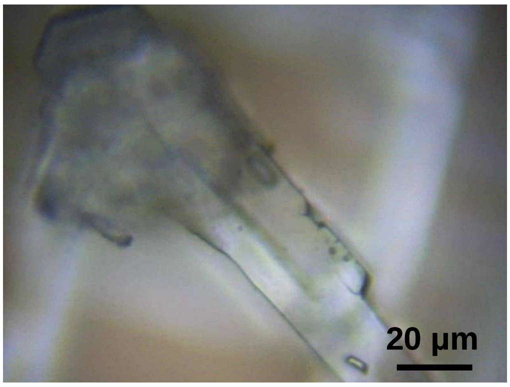

Figure 16. Optical micrograph of a single PETN crystal used for the Raman analysis.

Figure 17 shows the particles appeared during the heating ramp at 20°C/min.

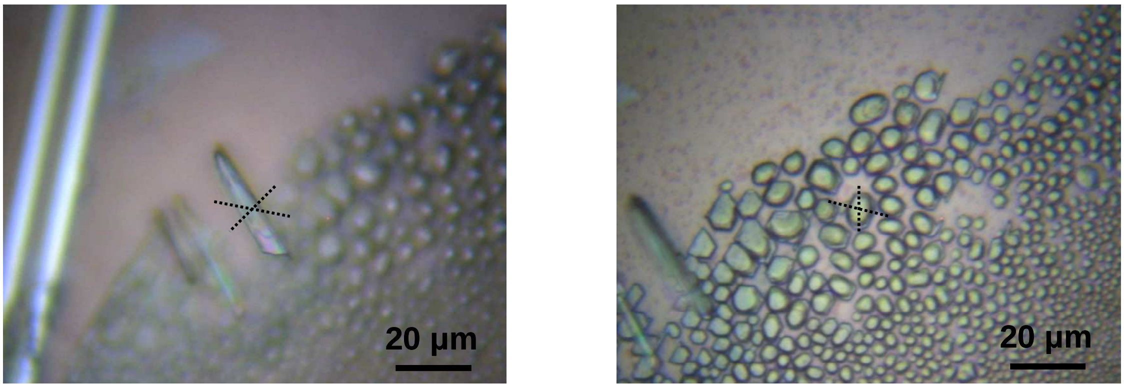

Figure 17. Optical micrographs of particles appeared during the heating ramp on PETN crystal.

We observe needle-shaped and spherical particles around the measurement area after completion of the heating of PETN crystal at 20°C/min.

The Raman spectra of these three kinds of particles are shown on figure 18.

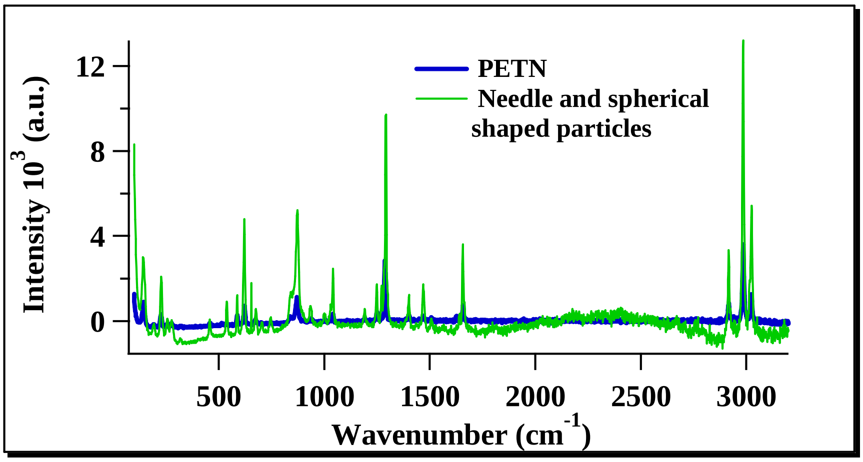

Figure 18. Raman spectrum of a single PETN crystal and of the particles after its heating ramp.

The Raman spectra of the initial PETN crystal is given in blue, the one of the particles obtained after its heating ramp is given in green. We observe that the curves are superposed so the particles around the measurement area are PETN crystals, furthermore the PETN phase has not changed after sublimation. The intensity of the PETN spectrum is lower than the intensity of the spectrum of sublimated PETN, probably because the focussing of the beam was not exactly on the PETN crystal. Renishaw has already performed Raman analysis on PETN[11], his data is identical to that on figure 18. The peaks around 3000 cm^{-1} are assigned to the symmetric and asymmetric C – H bond stretching. The intense broad peak at 870 – 890 cm^{-1} is assigned to NO stretching modes, the symmetric and asymmetric stretching vibrations of the nitro groups are at 1280 – 1300 cm^{-1} and 1630 – 1670 cm^{-1}, respectively.[12]

Through these different observations, we come to the conclusion that RDX and PETN crystals are recrystallized outside the measurement area after a heating ramp at 20°C/min or after an isotherm. Therefore the sublimation process of RDX and PETN is taking place. Besides, the sublimation of the α-RDX crystals leads to its crystallization in the form of β-RDX.

2. *Kinetics of sublimation*

The activation energy of sublimation is determined for single crystals of RDX and PETN. This is done through quasi-isothermal experiments illustrated on figures 9 and 14. The increase of amplitude is caused by a decrease of the crystal weight since the amplitude at constant pressure is expressed as a function of the heat capacity of the membrane and the added mass as reads:

$$\Theta = \frac{P}{\sqrt{(mc\omega)^2 + Q^2}} \qquad (1)$$

where Θ is the amplitude of the temperature modulation, m, c, T are the mass, heat capacity and sample temperature, respectively. Q is the heat exchange parameter, ω is the angular frequency of modulation.

The activation energy of sublimation of single RDX crystals is calculated using the data of five quasi-isothermal experiments performed at different temperatures in the range of 96.3°C to 159.7°C. The temperature accuracy is 0.3°C. It is noteworthy that at 20°C/min we are not able to detect the enthalpy of sublimation during a heating ramp. The crystals used for each isothermal experiment have to be more or less similar, i.e. to have ca. circular shape and a diameter of 15 µm. This is required to avoid the size effects.

The temperature dependence of the sublimation rate constant can be described by modified Eyring equation [13] :

$$k_s(T) = F[\upsilon / (kT)] \exp[-E_a / (RT)]$$

where $F[\upsilon / (kT)]$ is a frequency factor dependent on intermolecular bond vibrations (υ) in the solid and absolute temperature (T), E_a is activation energy, k the Boltzmann's constant and R is the gas constant. Eyring equation is similar to Arrhenius law but Arrhenius law is only applicable to gas-phase reactions whereas Eyring equation is designed for solids. During sublimation, the RDX particle goes from the solid state (crystal) to the gaseous phase, and then eventually to the solid state again when it recrystallizes on a cold surface. According to Eyring law, the slope of $\ln(k) = f(1/T)$ is equal to $-E_a / R$.

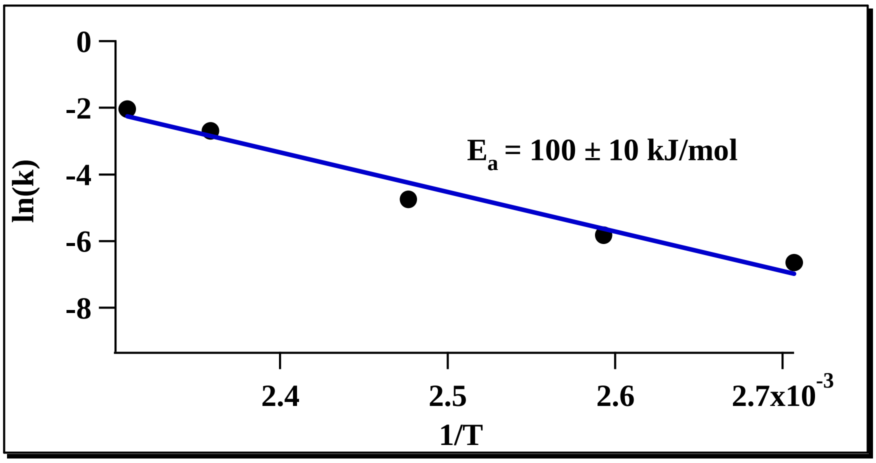

Figure 19. Rate of the RDX sublimation at a conversion of 50% measured for a single RDX crystal.

Figure 19 shows a typical plot allowing to determine the activation energy of sublimation. For each quasi-isothermal experiment, an appropriate crystal was selected under the microscope.

The activation energy of RDX sublimation determined experimentally by nanocalorimetry is 100 ± 10 kJ/mol. The literature gives different values of the RDX sublimation enthalpy in the range of 97,8 to 132 kJ/mol.[14-15-16] According to Hess law, the activation energy of sublimation is equal or superior to the enthalpy of sublimation $(E_a \geq \Delta H_{subl} = \Delta H_{evap} + \Delta H_{melting})$. So the experimental value is in agrees with the literature.

To build a simple model of the sublimation process, we assume that the process takes place at the surface of the particle. So the rate of the mass decrease can be linked to the surface and the rate (K) through expression (2):

$$\frac{dm}{dt} = -K.S(t) \qquad (2)$$

The particle mass (m) and of surface (S) for a sphere are:

$$m = \frac{4}{3}.\pi.R^3.\rho \qquad S = 4.\pi.R^2 \approx m^{2/3}$$

where R is the radius of the particle and ρ is its density. Expression (2) can be rearranged as follow:

$$\frac{dm}{dt} = -K.m^{2/3}(t)$$

After integration: $m(t) = (-K.t + m_0^{1/3})^3$ (3) (at t = 0s, m = m_0)

$$\boxed{\sqrt[3]{m(t)} = \sqrt[3]{m_0} - K.t} \, (4)$$

The plot of equation (4) should be a line with a slope corresponding to K (rate), the ordinate at the origin is $m_0^{1/3}$.

Figure 20 shows an optical micrograph of a single RDX crystal on the left and its mass evolution as a function of the isotherm time on the right. A linear fit is given in red. The temperature of the isotherm is 112.5°C.

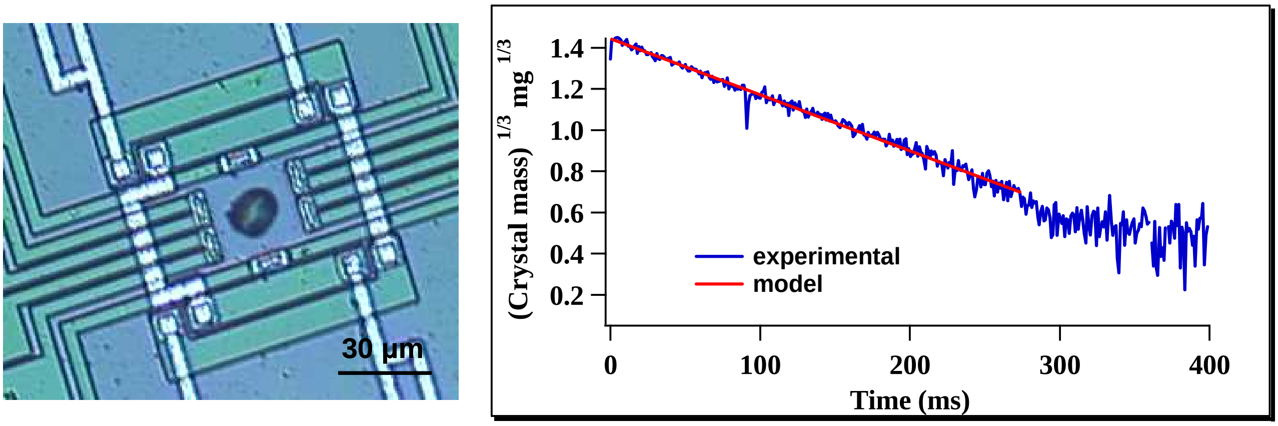

Figure 20. Mass evolution of a single RDX crystal (see text for more details).

According to expression (4), the mass to the power of 1/3 scales linearly with time. It is the case on the example on figure 20 so the sublimation process is well described by this model. For each isothermal experiment, the fit of $\sqrt[3]{m(t)} = f(t)$ gives the rate (K) and the initial mass of the particle (m_0). These values are summarized in table 3.

Temperature of the isotherm (°C)	Initial mass of RDX (ng)	K (10^{-3} s^{-1})
96.3	2.12	1.004
112.5	3.03	2.760
130.6	6.17	10.673
150.9	6.19	45.337

Table 3. Initial mass and constant K for each isothermal experiment.

Figure 21 shows the plot allowing to determine the activation energy of sublimation of a single RDX crystal thanks to equation (4).

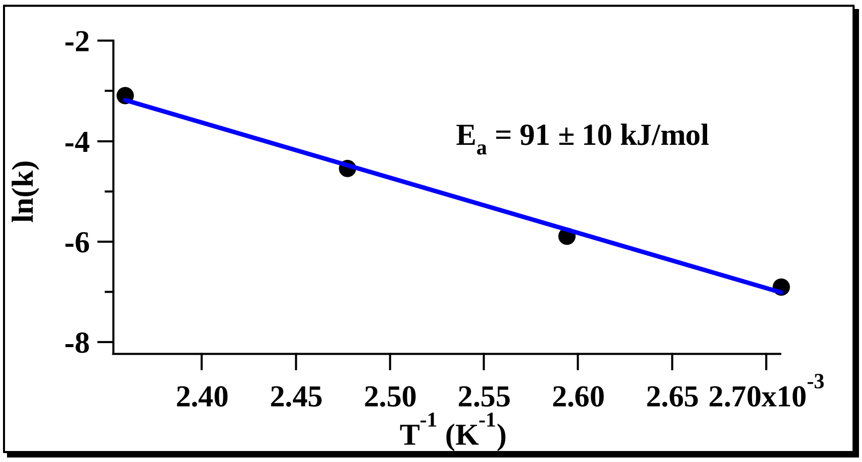

Figure 21. Rate of the sublimation of a single RDX crystal according to the model.

The model gives the activation energy of sublimation of 91 kJ/mol. This value is close to the one determined from nanocalorimetric curves at conversion of 50%. So the sublimation of a single RDX crystal is well described by the model of a sphere.

The kinetics of the PETN sublimation was also investigated through quasi-isothermal experiments. The sublimation enthalpy was also not detectable during a heating ramp at 20°C/min. The activation energy of a PETN single crystal was determined based on nine quasi-isothermal experiments. The temperature of the quasi-isothermal experiments are in the range of 126.6°C to 159.2°C. The accuracy on the temperature is 0.3°C.

Figure 22 shows a typical plot for determination of the activation energy of a single PETN crystal at a conversion of 50%. The activation energy determined experimentally is 173 ± 15 kJ/mol.

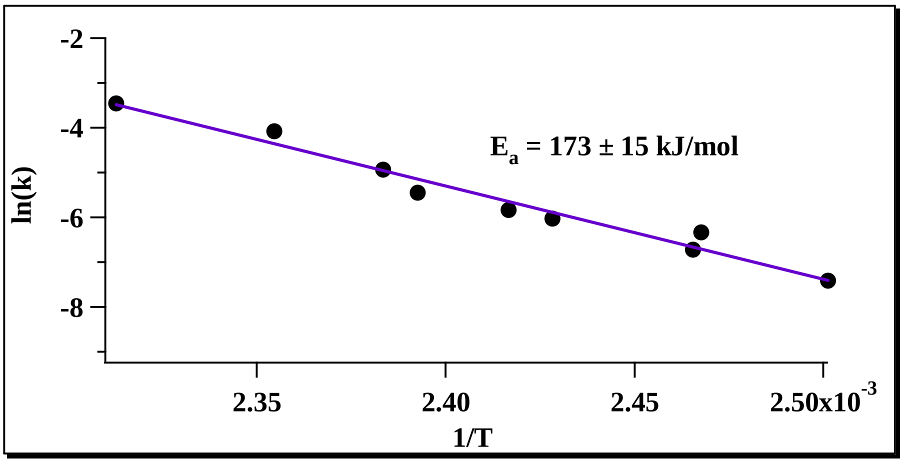

Figure 22. Rate of the PETN sublimation measured for a single PETN crystal.

In the literature[17-18], AFM analysis on PETN crystals give an activation energy of sublimation of 140 ± 26 kJ/mol. Kai H. Lau et al. using the torsion-effusion method determined the activation energy of sublimation of 157.4 ± 3.2 kJ/mol, such activation energy stems from the fact that the sublimation process is governed by the sublimation of monomeric $C(CH_2ONO_2)_4$ and not by sublimation of polymeric vapour species.[19] Our experimental value is close to this value if we take into consideration the accuracy of our measurements. We don’t have a model for the sublimation of PETN because the evolution of the crystal height during the sublimation is unknown. (The three dimensions of the crystal are composed together in the total crystal mass). Some isothermal experiments should be performed at low temperatures in order to have a low rate of sublimation. A confocal microscope could give us the height of the crystal during the sublimation. Figure 23 shows the time-evolution of the single PETN crystal size.

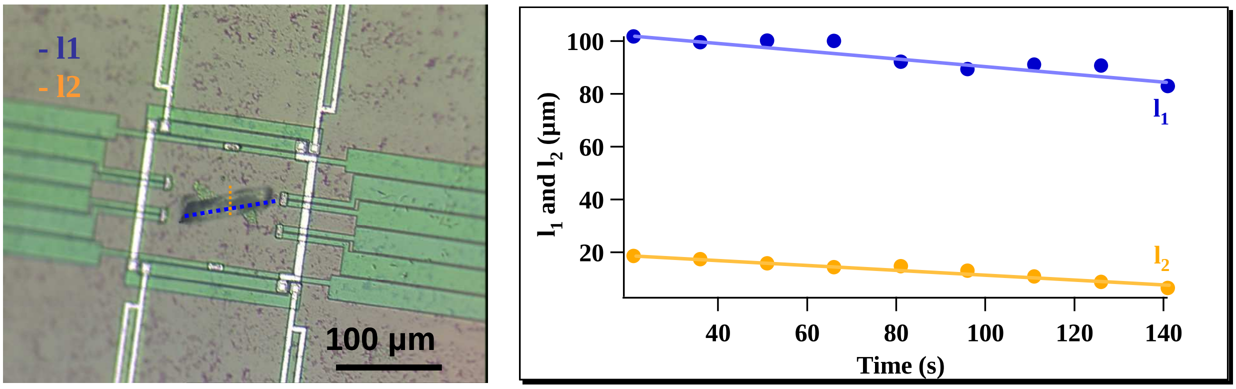

Figure 23. Micrograph of a PETN crystal and time-evolution of its dimensions at 146.4 °C.

The crystal length l_1 and width l_2 are shown as a function of the dwelling time. The two lines have the same slope, so the sublimation rate is identical in both dimensions of the PETN crystal and it is constant.

Figure 24 shows the time-evolution of the two dimensions l_1 and l_2 for all isothermal experiments. The isotherms are performed in the range of 126.7°C to 151.5°C.

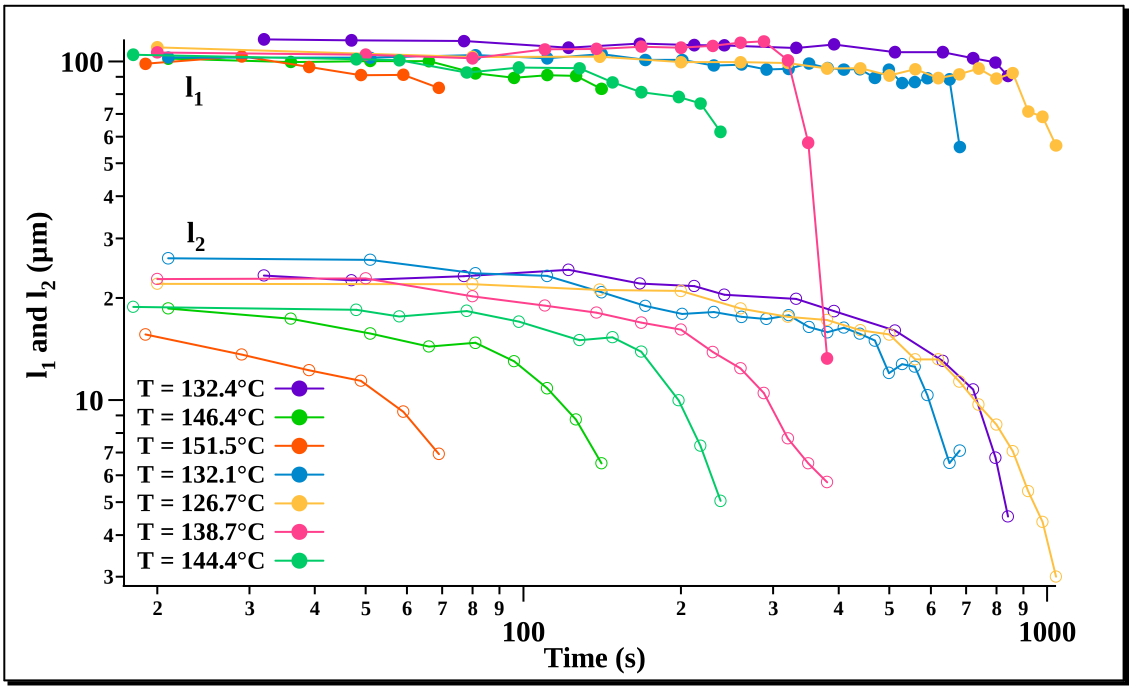

Figure 24. Time-evolution of l_1 and l_2.

Figure 25 (left) presents the time-evolution of l_1 and l_2 at 132.4°C and 144.4°C, which is largely linear. The right panel of the same figure gives the mass measured by nanocalorimetry together with the product $l_1.l_2$.

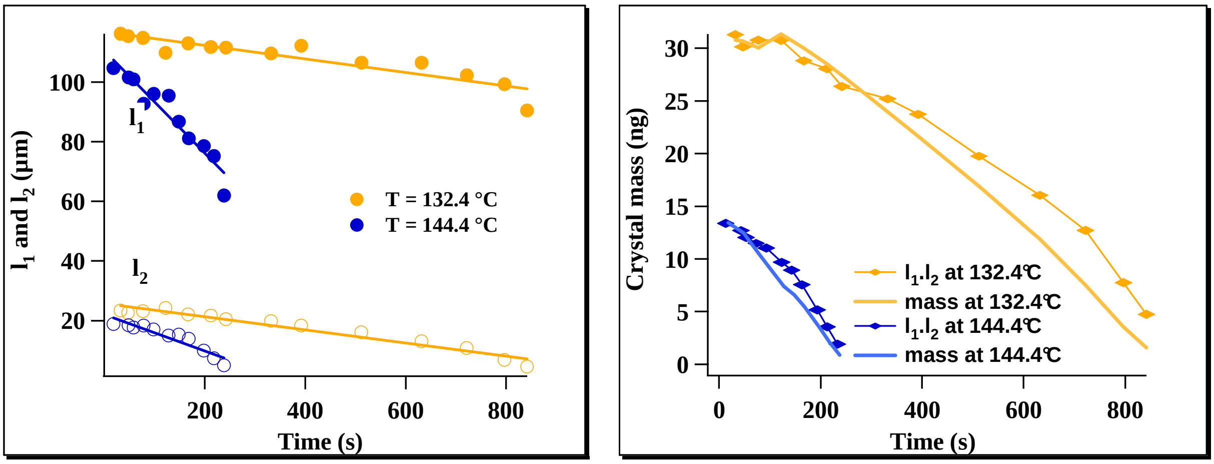

Figure 25. Time evolution of l_1 and l_2 at 132.4°C and 144.4°C.

It can be seen that the mass of the PETN measured by the nanocalorimeter approximately follows the product $l_1.l_2$. As expected, the sublimation rate is higher for isothermal experiments at higher temperature. Figure 26 gives the rate of sublimation of PETN based on the time variation of l_1 and l_2.

.

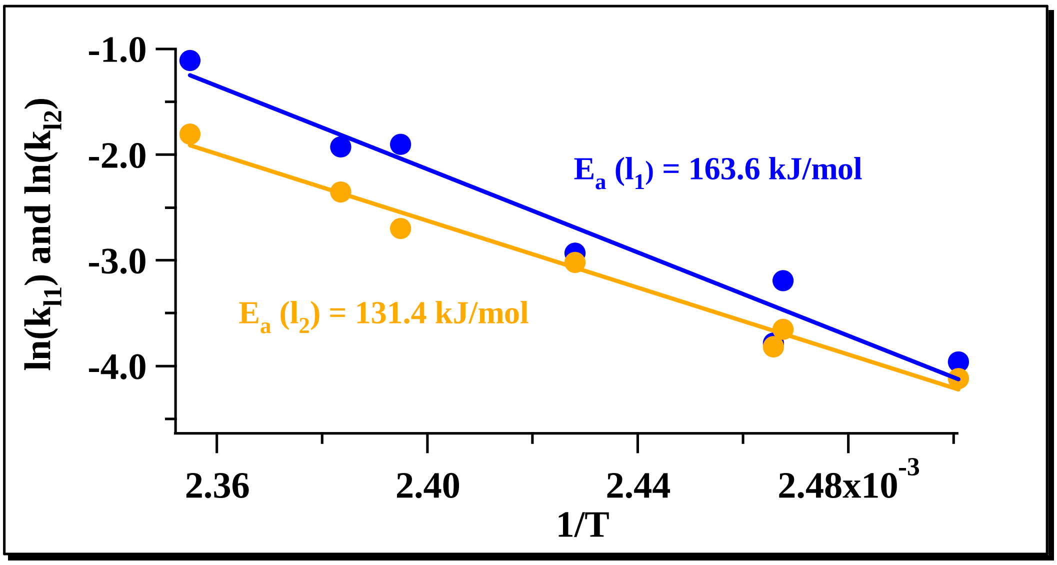

Figure 26. Rate of sublimation of a single PETN crystal measured from its dimensions l_1 and l_2.

The accuracy on the activation energy is about 20 kJ/mol. So if one takes it in consideration, the activation energy of sublimation is the same in both dimensions. The values determined from dimensions l_1 and l_2 are comparable to the value determined experimentally by nanocalorimetry, which is 173 ± 15 kJ/mol (cf. figure 22).

4.1.3. Evaporation

1. Evidence of evaporation

- *RDX.*

A fast heating experiment performed at 4420 °C/s on RDX crystals was monitored by a fast CCD camera. The trigger of the nanocalorimeter allows starting the camera just 0.3 ms before the start of the nanocalorimeter. This synchronization allows us associating each image taken by the camera to a point on the nanocalorimetric curve. A sensor XEN-3971 is used for this experiment (active area = 60 x 60 μm^2).

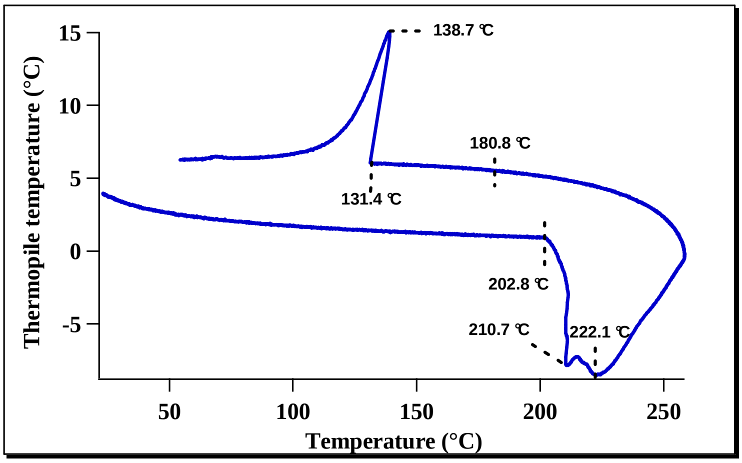

Figure 27. Nanocalorimetric curve of RDX corresponding to thermal cycle at 4 420 °C/s.

The nanocalorimetric curve measured in the experiment is given on figure 27.

During this experiment, the RDX crystals are heated until the end of the melting process, then the molten crystals are immediately cooled down. Such experiment would be impossible to realize with a DSC because the RDX is immediately decomposed after the melting (see figure 1).

On figure 27 one observes a melting peak at 202.8 °C and the crystallization peak at 131.4°C. The optical micrographs recorded at the temperatures marked on the nanocalorimetric curve are shown on figure 28 (images taken during the heating ramp) and figure 29 (images taken during the cooling ramp).

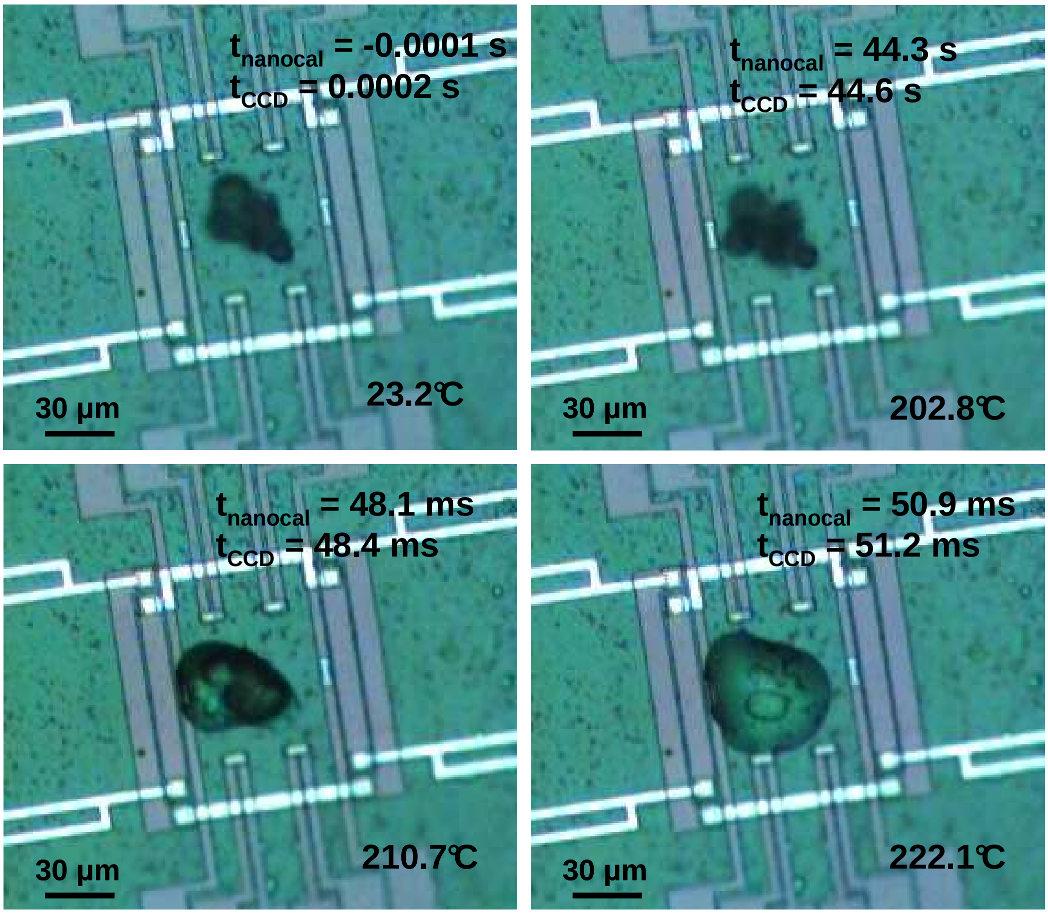

Figure 28. Micrographs corresponding to the melting process of RDX.

On the first micrograph of figure 28 one observes the RDX crystals used for the experiment, they are placed in the center of the active area. According to the nanocalorimetric curve, the RDX crystals start melting at 202.8°C. On the micrograph taken at 202.8°C the RDX crystals have slightly moved, this displacement can be probably due to formation of a thin liquid layer under the RDX aggregate which mechanically destabilizes the aggregate. As the RDX aggregate has moved toward the heater, the melting temperature measured by nanocalorimetry is 2°C lower than the melting temperature measured by DSC. The nanocalorimetric curve on figure 27 shows two minima at 210.7°C and 222.1°C within the melting peak. The image on figure 28 taken at 210.7°C shows that a part of RDX crystals has molten at this temperature. The image on figure 28 taken at 222.1°C shows a transparent droplet of molten RDX: almost all RDX crystals are molten at this temperature, there is just a little crystal remaining which is visible in the middle of the droplet. Figure 29 shows the micrographs taken during cooling of the RDX droplet.

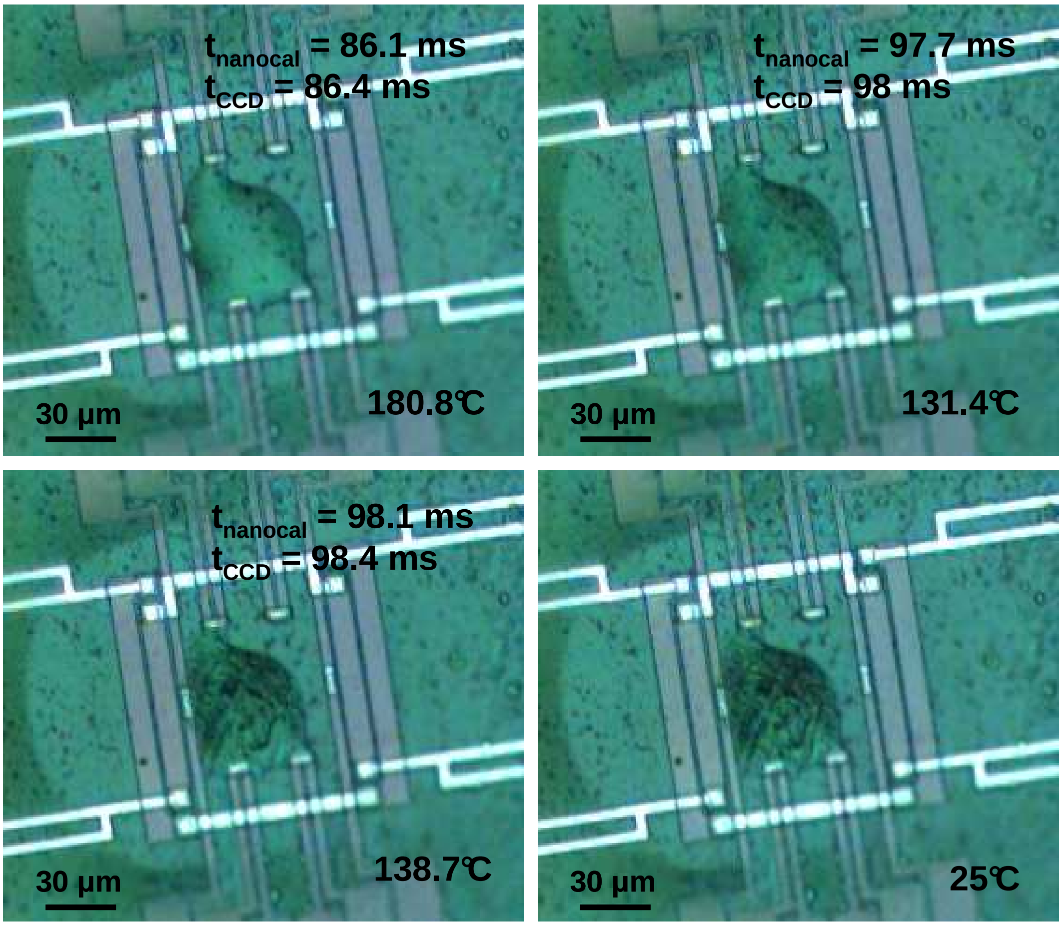

Figure 29. Micrographs corresponding to the crystallization process of RDX.

The first micrograph of figure 29 shows the droplet of molten RDX in the active area and some material outside the active area where the membrane looks darker. As the experiment is really fast (100 ms), the material around the active area can be only RDX. At 131.4°C, when the crystallization starts according figure 27, the molten RDX becomes darker than at 180.8°C on figure 29. At 138.7°C, i.e. at the maximum of the crystallization peak on figure 27, the micrograph reveals the crystallized RDX. The last micrograph on figure 29 shows the crystallized RDX in the active area and RDX outside the active area. The described experiment showed evaporation of RDX during a fast heating experiment at 4420 °C/s. The following part is focused on the evaporation of PETN.

- PETN.

The ramp profile on figure 30 is applied on a single PETN crystal.

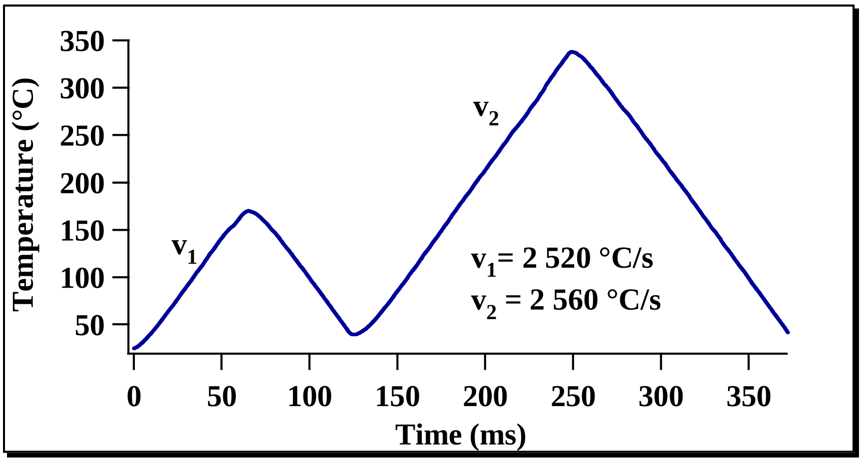

Figure 30. Temperature profile applied to a PETN crystal.

The first part of the ramp is from 25°C to 170°C at a heating rate of 2520°C/s, then the sample is cooled from 170°C to 39°C at a cooling rate of 2520°C/s. This cooling is immediately followed by a heating ramp from 39°C to 340°C at a heating rate of 2560°C/s. The last cooling of the sample is performed from 340°C to 40°C at a cooling rate of 2560°C/s.

Figure 31 presents the nanocalorimetric curve of a PETN crystal which was submitted to this temperature profile.

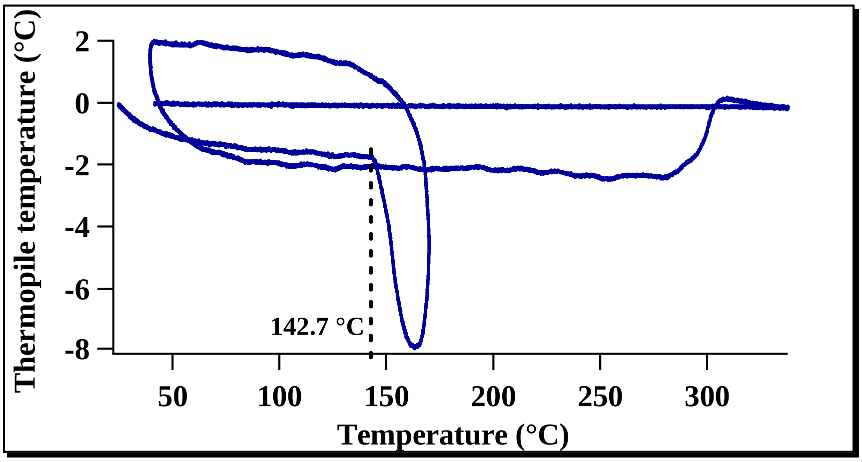

Figure 31. Nanocalorimetric curve obtained by applying the ramp profile shown on figure 28 to a single PETN crystal.

The melting peak occurs at 142.7°C during the heating ramp. There is no crystallization peak during the cooling segment. The nanocalorimetric curve does not come back to the baseline during cooling because the PETN stays molten. During the second heating ramp, no melting peak can be observed. A step occurs at 290°C, then the nanocalorimetric curve returns to the baseline during the cooling ramp, which means that no added mass is present on the membrane during this second cooling ramp. At the beginning of the second heating ramp, the PETN is in the molten state, and during the cooling ramp which follows immediately this heating ramp, nothing remains on the membrane. So we can assign the broad endothermic peak from 39°C to 307°C to evaporation of PETN.

2. *Kinetics of evaporation*

- RDX.

To determine the activation energy of the RDX evaporation, several heating and cooling cycles at fast rates have been carried out on RDX crystals. The fast heatings are performed at 4160°C/s until the end of the melting peak, the isotherm time is 4.2 ms, then the coolings are performed at 4060°C/s.

The following graph (figure 32) shows 11 cycles performed on RDX crystals. The micrographs show the RDX before and after the first cycle.

.

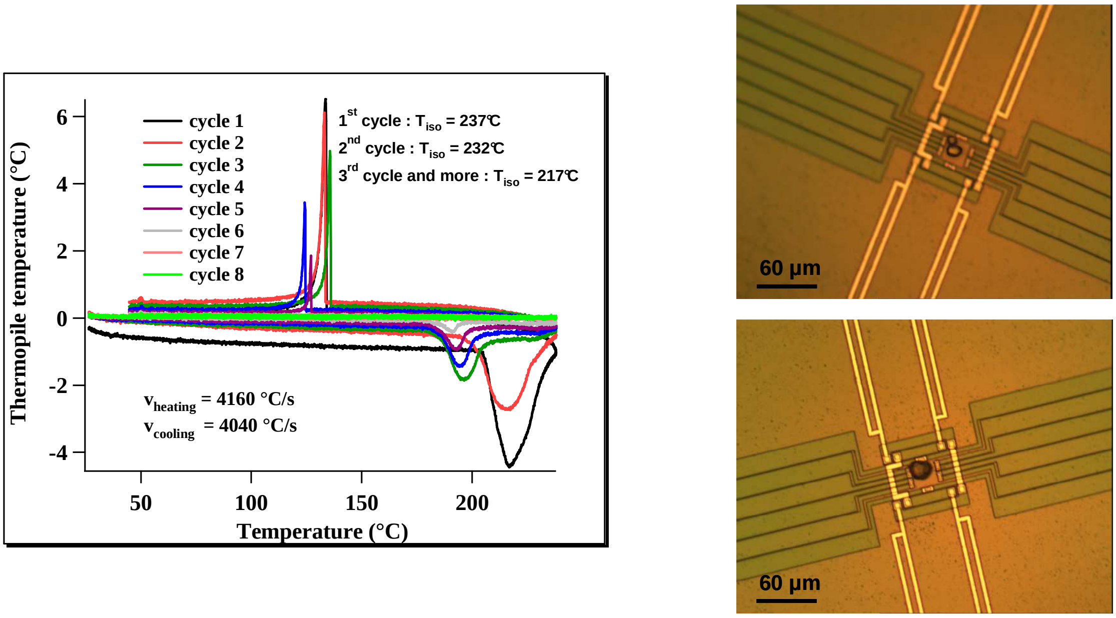

Figure 32. Cycles of heating and cooling on RDX (left), RDX particles before and after the first cycle (right).

The graph on figure 32 shows that the melting onset temperature of the first cycle equals 205 °C, which corresponds to melting temperature of RDX. At the second cycle, the melting temperature shifts towards lower temperatures (200 °C). This shift is due to a displacement of the molten particle during the first cycle: the micrographs show that the particle is at the membrane centre before the first cycle and after this cycle, the particle is moved near the heater resistance. By correcting the temperature of the isotherm, the following graph is obtained (for a better understanding the two first cycles are not represented on the graph 33).

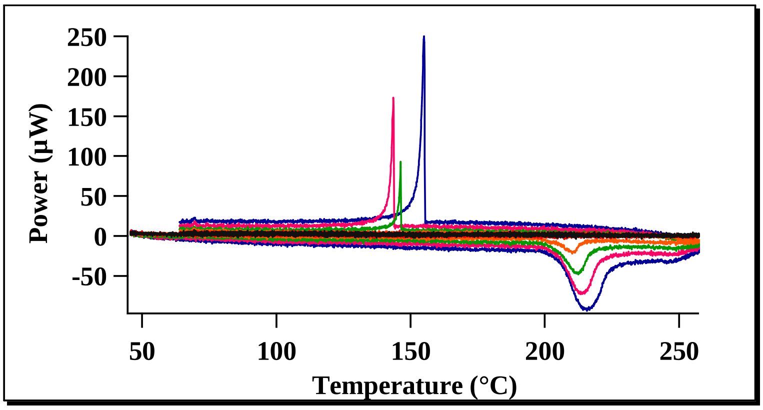

Figure 33. Heating and cooling segments for RDX, T_{iso} = 256.5 °C.

The mass of the crystalline and molten RDX is calculated by integrating the crystallisation and melting peaks of each experiment cycle and normalizing them by the specific melting enthalpy of RDX (161 J/g). The evaporated mass corresponds to the mass difference between the molten and the crystallised RDX particle corresponding to the same cycle.

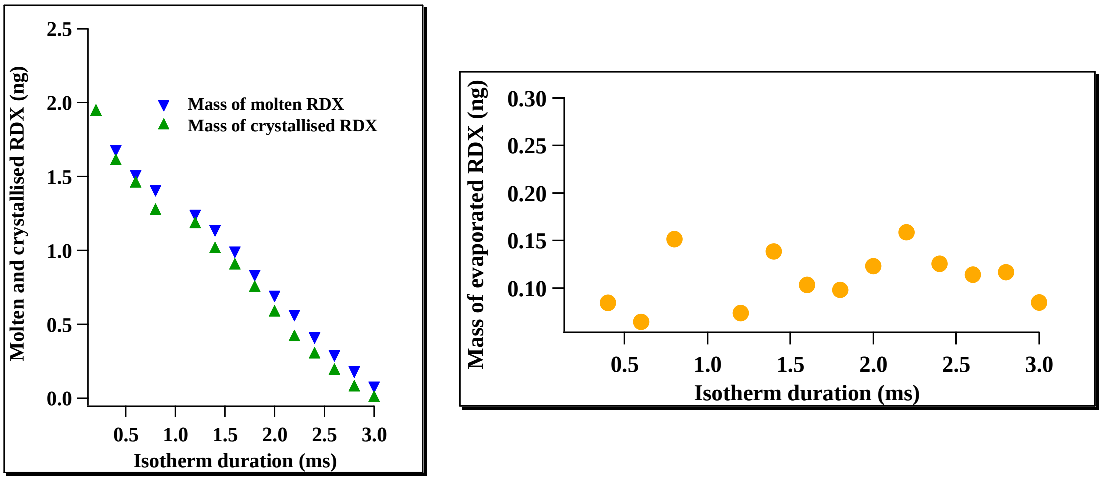

Figure 34. Mass of molten and crystallised RDX (a), mass of evaporated RDX (b) for the experimental curves shown on figure 31.

On figure 34, the points corresponding to the two first cycles on figure 32 are removed. We observe on figure 34 that the mass of evaporated RDX stays almost the same during the cycles which follow the first cycle. According to experiments performed by moving an indium particle on the membrane, the differences of evaporated mass are not due to the particle position on the membrane. Indeed, the area of the melting peak is independent of the indium particle position insofar that the particle stays in the active area. This difference can be due to the shape modification of the particle upon recrystallisation. We observe on the micrographs from figure 32 that the particle is more spherical for the second cycle than for the first one. The activation energy of RDX evaporation is determined thanks to the evaporated mass of RDX during the isotherm. Figure 35 shows the determination of activation energy of RDX evaporation.

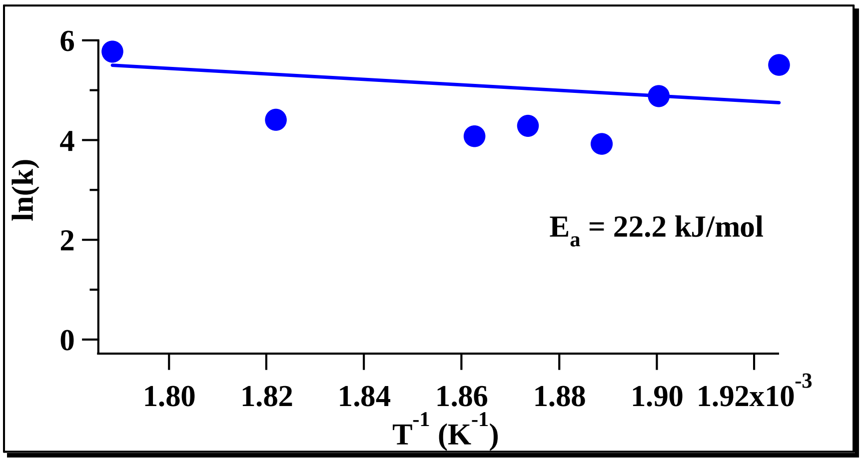

Figure 35. Determination of activation energy of RDX evaporation.

We find an activation energy of 22.2 kJ/mol. According to the literature[3], the activation energy should be 100 kJ/mol. Clearly, in this case we do not have enough precision to determine the activation energy of RDX evaporation with this method.

4.2. Blends of nano-RDX / TNT

4.2.1. Morphology

Blends of nano-RDX / TNT are obtained by a process of nanocrystallization patented by ISL. This process generates by ultrasonic waves an aerosol of small droplets of solvent/explosive. After the evaporation of the solvent in an oven, the particles are reduced via Cottrell precipitation. The SEM micrographs of TNT and RDX microcrystals are on figure 36.

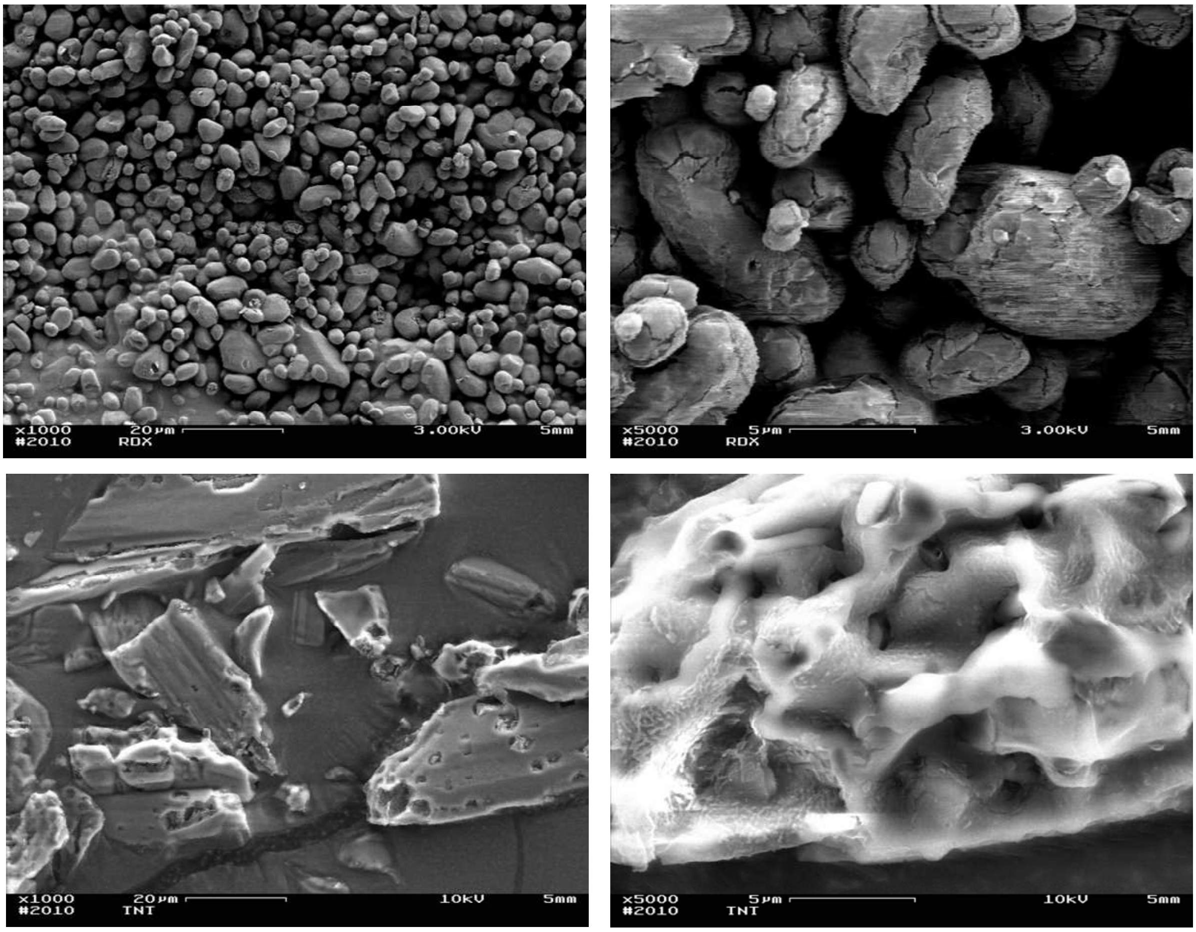

Figure 36. SEM micrographs of RDX (on the top) and TNT (on the bottom) microcrystals.

The RDX microcrystals have granular appearance and have a polydisperse distribution in size. The SEM micrograph on the top right shows RDX crystals which have cracks. These cracks are due to the SEM beam which decomposes the RDX at this magnification. The TNT microcrystals are flat and also have different sizes. One can see on the SEM micrograph on the bottom right panel that the surface of TNT crystal is not smooth.

Figure 37 gives the SEM micrographs of TNT/RDX blends (50/50) obtained after the crystallization process. The proportion of each compound at the beginning of the process is 50/50 in weight.

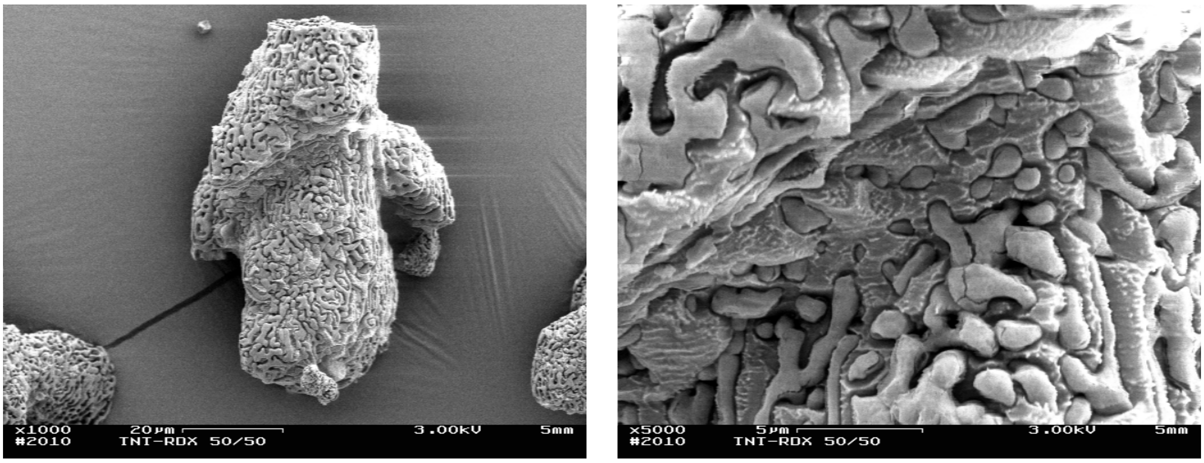

Figure 37. SEM micrographs of TNT/RDX blends (50/50).

Figure 37 shows that one can obtain micrometric particles after the process. As one can see on the right panel of figure 37, these particles seems to be composed of two phases. The matrix looks rough as TNT crystals on figure 36 whereas the inclusion particles look much smoother. Therefore, we can suppose that the RDX crystals are embedded in a TNT matrix. The particle sizes range from several micrometers to a few hundreds of nanometers.

In figure 38, the proportion of each compound at the beginning of the nanocrystallization is 30% for TNT and 70% for RDX.

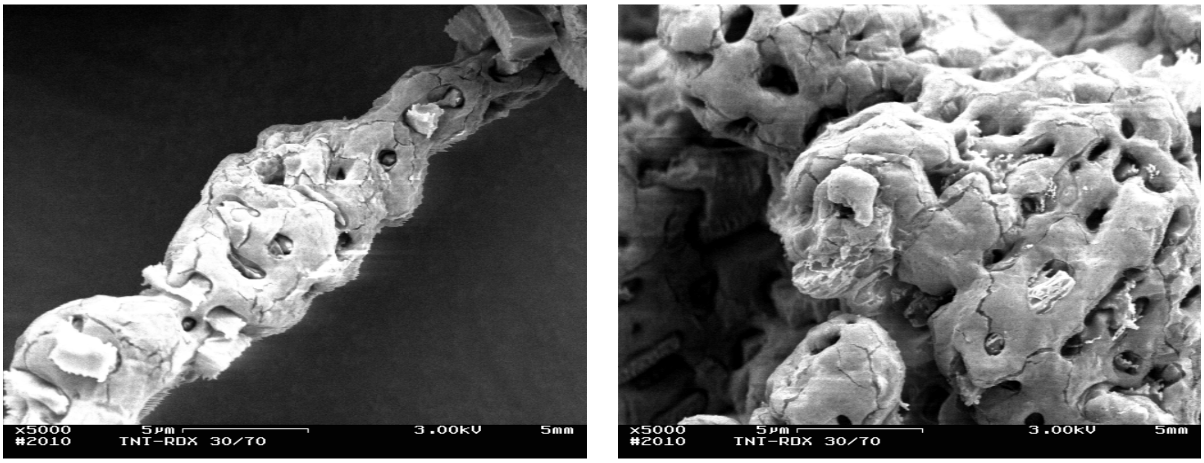

Figure 38. SEM micrographs of TNT/RDX blends (30/70).

According to figure 38, we obtain microparticles after the process performed on a blend 30% of TNT and 70% of RDX. In this case, the matrix looks smooth in comparison to the matrix on figure 37. Moreover some cracks can be noticed at higher magnification, these cracks are similar on those on RDX microcrystals from figure 36. Some holes in the matrix on the right of the figure 38 contain rough particles, which resemble small TNT crystals from figure 36. We can suppose through these observations that the TNT crystals are embedded in a RDX matrix.

4.2.2. Nanocalorimetry on TNT/RDX blends

The TNT/RDX blends obtained after the nanocrystallization process are studied using a XEN-3970 sensor at 78000°C/min. DSC experiments at 5°C/min are also performed on the TNT/RDX blends in closed crucibles.

Figure 39 presents the DSC traces of the TNT and RDX used in the process of nanocrystallization.

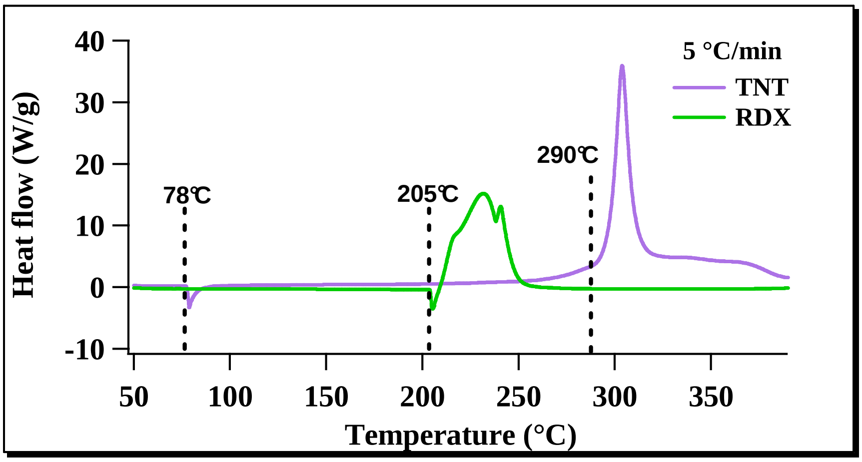

Figure 39. DSC curves of TNT and RDX in closed crucibles measured at 5°C/min.

The first endothermic peak at 78°C on the trace of TNT is assignated to the melting of TNT, the decomposition peak of TNT occurs at 290°C. The DSC trace of RDX shows the melting of RDX at 205°C which is immediately followed by the decomposition peak. The nanocalorimetric and DSC traces are shown on figure 40.

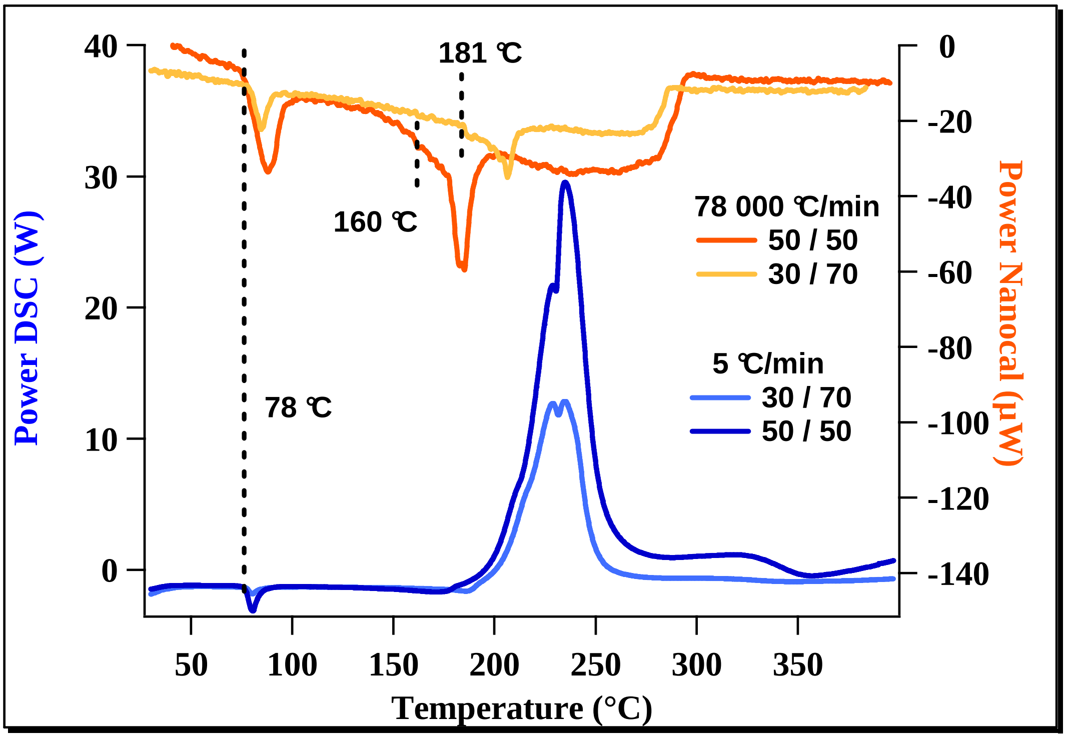

Figure 40. DSC and nanocalorimetric curves of the TNT/RDX blends.

The endothermic peak at 78°C corresponds to melting of TNT. This peak is visible on both, the nanocalorimetric and DSC curves from figure 40. It can serve as internal standard to check the temperature calibration of the sensor. On DSC curves from figure 40, we observe an exothermic peak at 190°C which is assigned to decomposition of the blends. It is noteworthy that the melting peak of RDX is not visible on DSC traces. The melting is hided or impeded by the decomposition process.

On the nanocalorimetric curves, we observe an endothermic peak at 160°C for the 50/50 blend and at 181°C for the TNT/RDX 30/70 blend. These endothermic peaks are assigned to the melting of RDX. On DSC curves from figure 39, the melting peak starts at 205°C. Therefore the low melting events observed on the nanocalorimetric curves can be attributed to the presence of RDX nanoparticles in the blends. The step at 290°C is due to evaporation of the blends. No exothermic peak of decomposition can be visualized on the nanocalorimetric curves. Neither can we see the decomposition peak of RDX or TNT.

These experiments show that the absence of the decomposition peak on the nanocalorimetric curves allows observing the melting of RDX. The depression of the RDX melting temperature confirms the presence of small RDX crystals in the blends obtained by nanocrystallization.

4.3. CL-20

4.3.1. Evidence for CL-20 sublimation during calorimetric experiments

In this section, we focus on the sublimation of CL-20, which is studied with a combination of polarized light microscopy in transmission and Raman spectroscopy.

A heating ramp at 20°C/min is performed on a single crystal of CL-20 using flat sensor XEN-3971. Optical micrographs are taken in reflected and polarized transmitted light before and after the heating ramp (cf. figure 41).

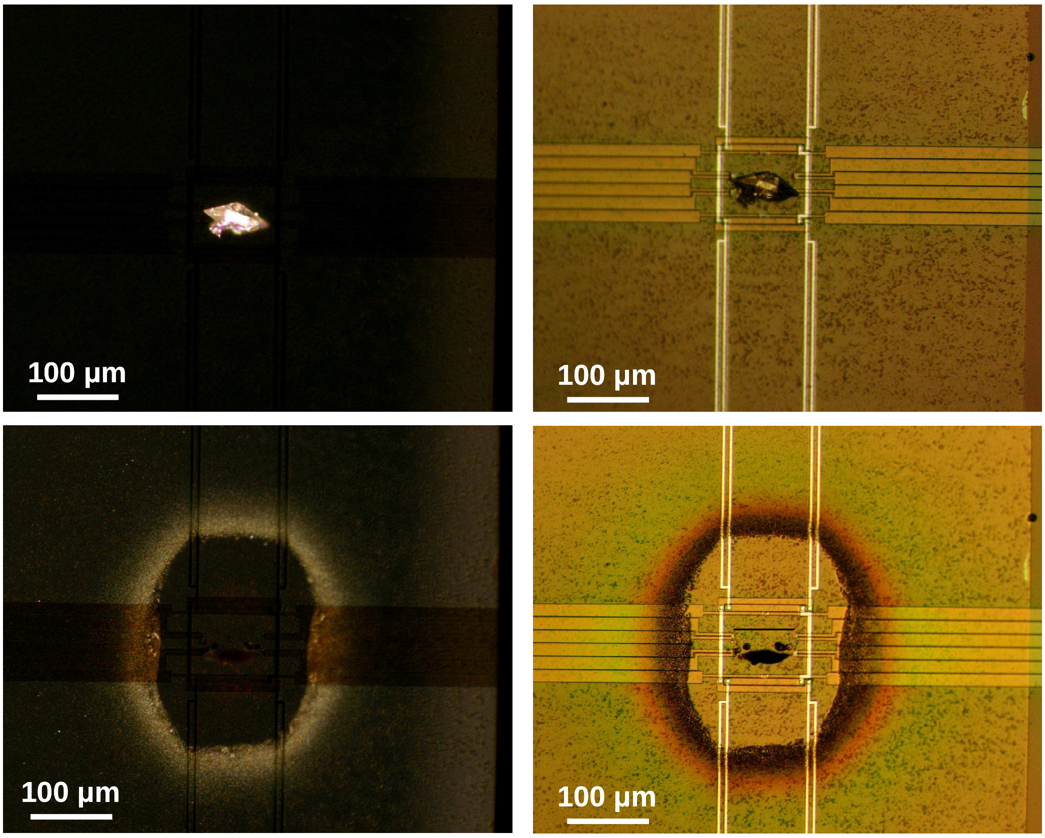

Figure 41. Views of a CL-20 crystal in reflected and transmitted polarized light before and after heating ramp at 20 °C/min.

On figure 41 one can see that the CL-20 particle before the heating ramp is well crystalline (birefringent) while the sensor membrane is dark. After heating ramp, the micrographs on bottom of figure 41 show that the regions surrounding the active area look brighter than the active area itself. The CL-20 crystal and the material outside the active area are analyzed by Raman. Figure 42 gives the Raman spectrum for a CL-20 crystal used in this study.

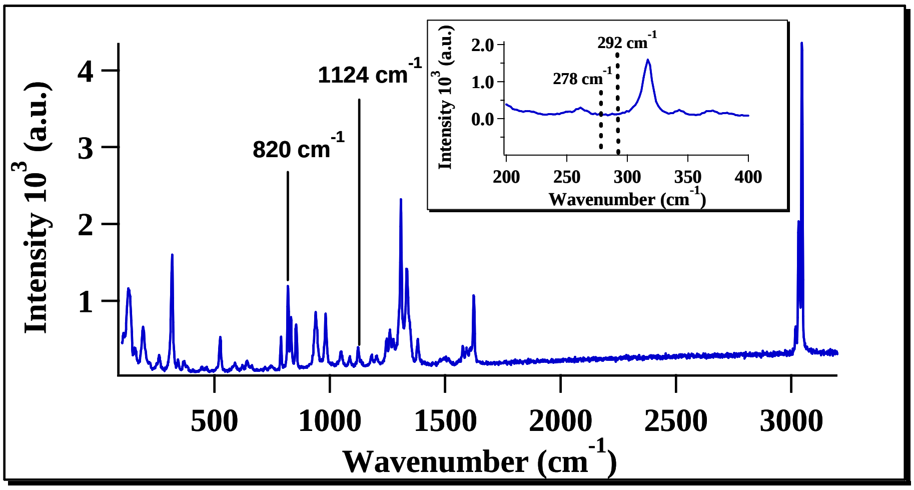

Figure 42. Raman spectrum of a CL-20 crystal.

The insert in figure 42 is a zoom of the spectrum area between 200 and 400 cm^{-1}. The absence of peaks in the region of 280 cm^{-1} to 290 cm^{-1} confirms that the CL-20 sample is pure: according to literature[20], there are characteristic peaks for three of the four stable polymorphs (α, β, γ, ε) in this area except ε. The peak at 820 cm^{-1} corresponding to the ring stretch and the peak at 1124 cm^{-1} are characteristic peaks of the ε polymorph.

Figure 43 shows the Raman spectrum of the material outside the active area.

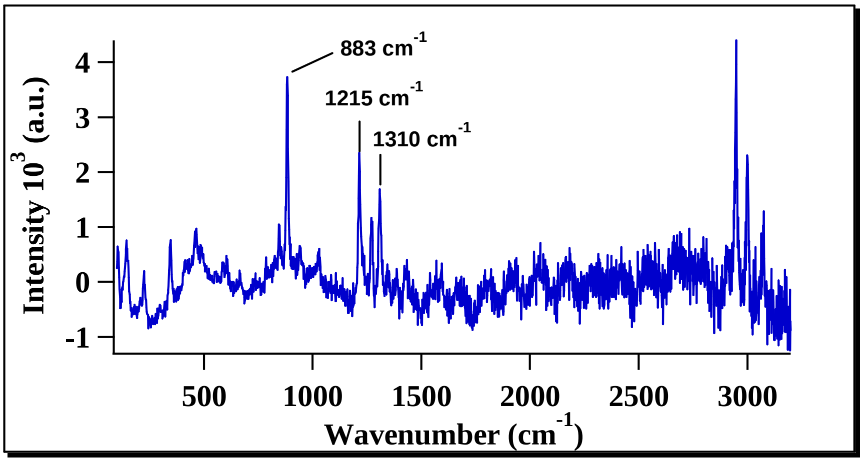

Figure 43. Raman spectrum of CL-20 obtained outside the active area after a heating ramp of a CL-20 crystal at 20 °C/min.

One observes a few particles outside the active area, which look rather thin. This could explain why the Raman spectrum on figure 43 is noisy. However, the two spectra are different. A peak at 883 cm^{-1} visible on figure 43 was not on the spectrum of CL-20 on figure 42 (we were not able to identify this peak from the literature). On figure 43, there is no peak in the area from 280 cm^{-1} to 290 cm^{-1} and the characteristic peaks from the ε polymorph are not on this spectrum. Nevertheless, we observe the peaks corresponding to the C-H stretch in the region of 3000 cm^{-1}, the peaks corresponding to the symmetric NO_2 stretch in the area from 1215 cm^{-1} to 1310 cm^{-1}: these peaks are characteristic of CL-20 but we cannot determine the polymorph based on the spectrum of figure 43.

4.3.2. Decomposition of CL-20

DSC analysis on CL-20 are performed in unsealed crucibles at 1, 2, 5, 10, 20°C/min. Nanocalorimetric traces are obtained on CL-20 at 5200°C/min, 17380°C/min, 82000°C/min. These analysis are on figure 44. Nanocalorimetric experiments are performed on sensor XEN-3972, the size of the CL-20 crystal is about 50 µm.

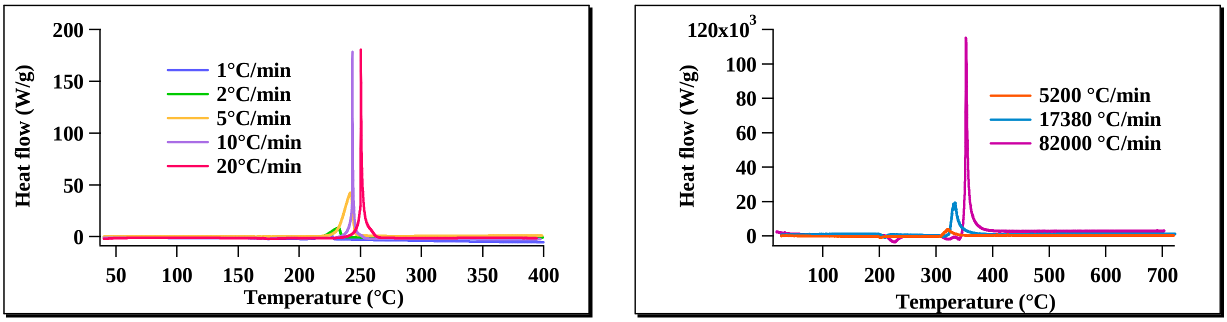

Figure 44. DSC curves of CL-20 in unsealed crucibles measured at 1°C/min, 2°C/min, 5°C/min, 10°C/min, 20°C/min (on the left) and nanocalorimetric curves at 5200°C/min, 17380°C/min and 82000°C/min.

One endothermic transition occurs between 160°C and 200°C, this transition is assignated to the $\varepsilon \rightarrow \gamma$ transition. The exothermic peak which takes place at temperature superior to 200°C is the CL-20 decomposition.

Table 4 summarizes temperatures and enthalpies characteristic of the CL-20 used in this study at several heating rates. We can see that the enthalpy of decomposition varies with the heating rate.

Heating rates (°C/min)	$\Delta H_{decomposition}$ (J/g)	$T_{decomposition}$ (°C)
1	2707	200
2	2575	205
5	4543	216
10	1480	225
20	1200	231
5220	770	300
17400	1020	310
81600	540	340

Table 4. Thermoanalytical parameters of CL-20 at several heating rates .

A nanocalorimetric experiment performed at 850°C/s is monitored by a high-speed CCD camera triggered by the nanocalorimeter to observe what happens to the crystal during the heating ramp. The nanocalorimetric curve is on figure 44. A sensor XEN-3971 is used.

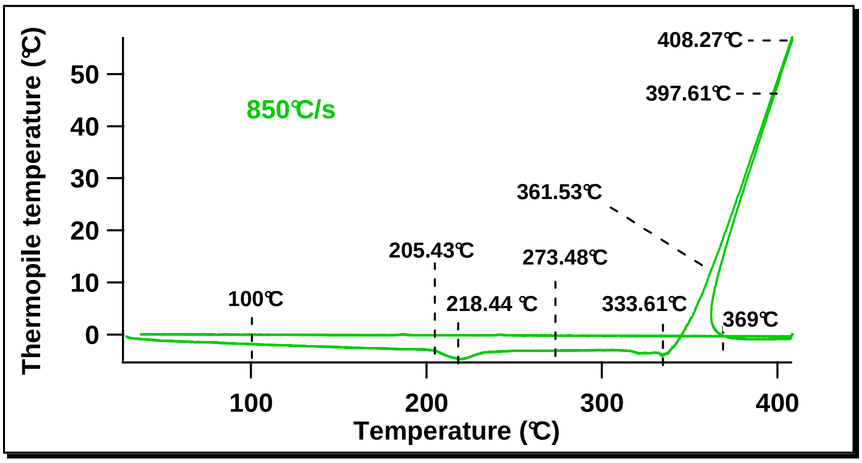

Figure 45. Nanocalorimetric curve of a CL-20 crystal at a heating rate of 850°C/s.

We observe on figure 45 that the transition ε→γ occurs at 205.43°C and that the decomposition peak is at 333.61°C. The marked temperatures correspond to temperatures for which the optical micrographs are given on figures 46 and 47. The decomposition peak on figure 45 is sloped to the right probably because the CL-20 crystal is too big relatively to the size of the active area so the decomposition heats the thermocouples around the active area too much (the thermocouple measures the temperature of the membrane and the heat released by the decomposition increases this temperature). The importance of the decomposition peak shows that the sensor could detect CL-20 crystals which are much smaller than the crystal on figure 46.

The optical micrographs taken at temperatures in the range of 100°C to 333.61°C are given on figure 46.

According to figure 45, the transition ε→γ occurs at 205.43°C. No modification corresponding to this transition is observed by optical microscope on figure 46.

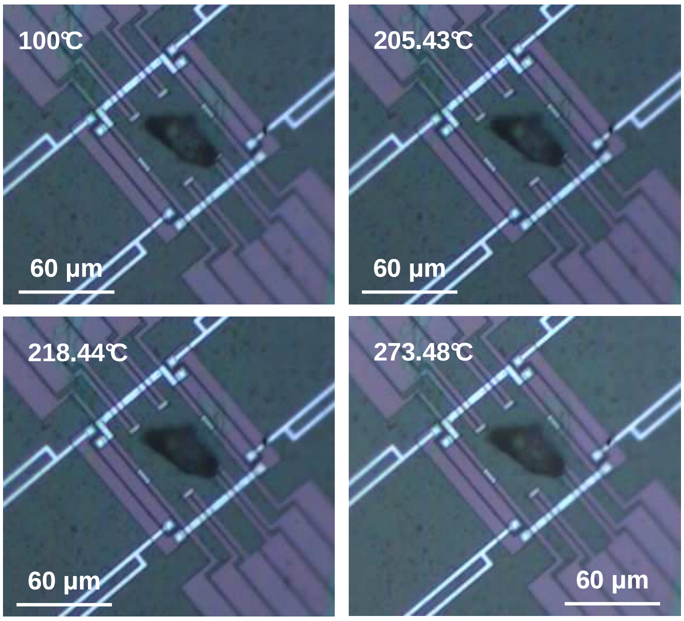

Figure 46. Optical micrographs taken from 100°C to 273°C during the heating ramp at 850°C/s.

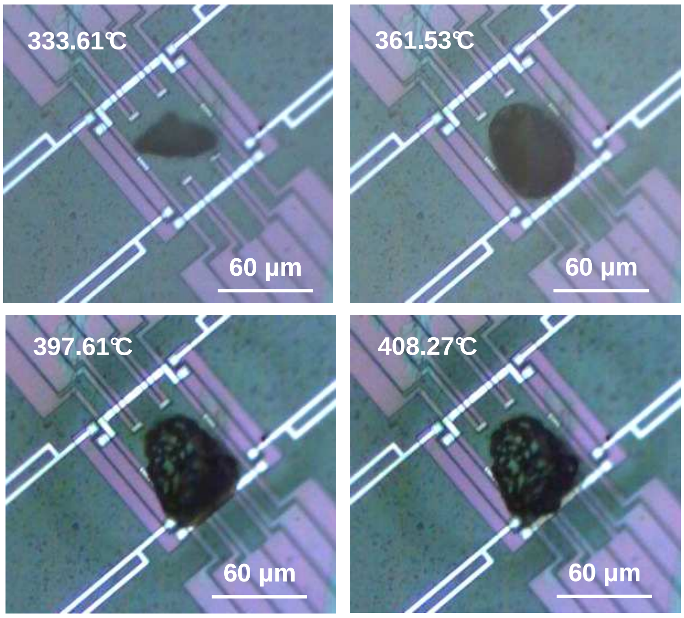

Figure 47. Optical micrographs taken during the decomposition peak.

The optical micrographs taken during the decomposition peak are shown on figure 46. According to the nanocalorimetry, the decomposition occurs in ca. 36 ms. On figure 47, the micrograph at 333.61°C is taken at the onset decomposition temperature of the CL-20 crystal. By comparing the first micrograph of figure 47 with the last micrograph of figure 47 we observe that the crystal has rotated by about 30° at the decomposition onset temperature: this rotation can be due to a thin gas layer formed during the first moment of the decomposition.

On figure 47, we observe that the CL-20 crystal becomes a bigger at 361.53°C. According to nanocalorimetric curve on figure 45, the end of the decomposition peak occurs at 369°C. The last micrograph of figure 47 shows that a residue remains on the active area. According to the formula of CL-20, the oxygen balance of CL-20 is negative so the decomposition is not total. This residue is already observable at 397.61°C on figure 47 when the decomposition peak is not yet finished (cf. figure 45).

The residue at the end of the CL-20 decomposition is analyzed by Raman (cf. figure 48).

The spectrum is similar to the one found in the literature[21-22]. It shows that the residue contains mainly carbon, some amides and a small amount of unreacted CL-20.

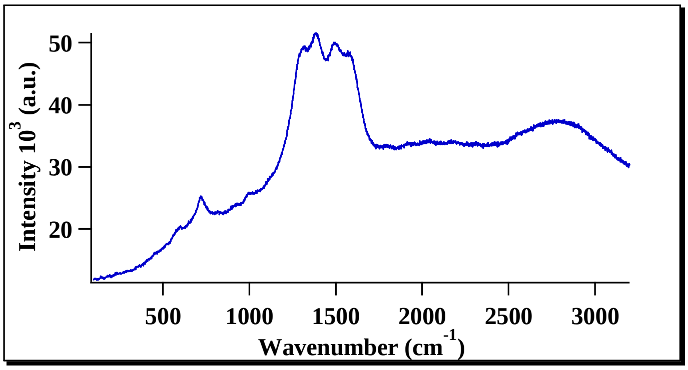

Figure 48. Raman spectrum of CL-20 residue obtained after a fast heating ramp of a CL-20 crystal .

4.4. Conclusions

This chapter describes our nanocalorimetric results on explosive micro crystals such as RDX, PETN and CL-20. Also blends of nanoRDX / TNT are addressed.

The first part of this chapter is focused on the sublimation and evaporation of RDX and PETN microcrystals. We observe that the sublimation of α-RDX leads to its recrystallisation in β-RDX on a cold part of the calorimetric chip. The sublimated PETN does not change its phase upon recrystallization. The activation energy of the α-RDX sublimation is 100 ± 10 kJ/mol and the activation energy of PETN sublimation is 173 ± 15 kJ/mol. The possibility of studying evaporation of PETN and RDX is shown.

Interestingly, the RDX and PETN crystals are not undergoing decomposition during fast heating ramps on the nanocalorimetric chip whereas these energetic materials are decomposed during DSC experiments.

In the second part of the chapter, we characterize nanoRDX/TNT blends which were synthesized in a prototype of nanocrystallization. SEM micrographs of RDX and TNT allow identifying the different components obtained at the end of the process. The thermal behaviour of the blends shows a difference between DSC and the nanocalorimeter chip. On DSC curves, the melting peak of RDX is hidden or impeded by the decomposition peak occurring at 200°C whereas the nanocalorimetric curves do not show the decomposition peak of the blends, but show the melting peak of RDX. The melting of the blends obtained after nanocrystallization occurs at lower temperatures than in the initial RDX. The depression of the melting peak supports the presence of nanoRDX in the blend.

The last part of the chapter is dedicated to study of CL-20. The evidence of its sublimation during nanocalorimetric experiments is obtained with polarized light in transmission. The important exothermic peak corresponding to the CL-20 decomposition is clearly visible on the nanocalorimetric curves. This peak prompts us thinking that the nanocalorimeter chip could serve as a sensitive detector of CL-20 traces.

---

1 Brill, T.B.; Gongwer, P.E.; Williams, G.K. *J. Phys. Chem.* **1994**, *98*, 12242 – 12247.

2 Strachan, A.; Kober, E.M.; van Duin, A.C.T.; Oxgaard, J.; Goddard III, W.A. *The Journal of Chemical Physics* **2005**, *122*, 054502

3 Long, G.T.; Vyazovkin, S.; Brems, B.A.; Wight, C.A. *J. Phys. Chem. B* **2000**, *104*, 2570 – 2574.

4 Wu, C.J.; Fried, L.E.; *J. Phys. Chem. A* **1997**, *101*, 8675 – 8679.

5 Makashir, P.S.; Kurian, E.M. *Propellants, Explosives, Pyrotechnics* **1999**, *24*, 260 – 265.

6 Tarver, C.M.; Tran, T.D.; Whipple, R.E. *Propellants, Explosives, Pyrotechnics* **2003**, *28* (4)

7 Karpowicz, R.J.; Sergio, S.T.; Brill, T.B. *Ind. Eng. Chem. Prod. Res. Dev*. **1983**, *22*, 363 – 365

8 Torres, P.; Mercado, L.; Mortimer, L.; Mina, N.; Hernández, S.P.; Lareau, R.; Chamberlain, R.T.; Castro-Rosario, M.E. *Proc. SPIE* **2003**, *5089*, 1054

9 Torres, P.; Mercado, L.; Cotte, I.; Hernández, S.P.; Mina, M.; Santana, A.; Chamberlain, R.T.; Lareau, R.; Castro, M.E. *J. Phys. Chem. B* **2004**, *108*, 8799 – 8805.

10 McCrone, W.C. *Anal. Chem*. **1950**, *22*, 954

http://www.lajarda.com/tfqma/didactica/notas_aplicacion/Raman_explosivos.pdf : Explosive identification using Raman spectroscopy

12 Lipinska-Kalita, K.E.; Pravica, M.G.; Nicol, M. *J. Phys. Chem. B* **2005**, *109*, 19223 – 19227.

13 Krongauz, V.V.; Ling, M.T.K.; Woo, L.; Purohit, U. *Thermochimica Acta* **2007**, *457*, 35-40.

14 Maksimov, Y.Y. *Russian Journal of Physical Chemistry* **1992**, *66*, 540 – 542.

15 Ramirez, M.L., Thesis, University of Puerto Rico, **2009.**

16 Edwards, G. *Trans. Faraday Soc.* **1953**, *49*, 152 – 154.

17 Pitchimani, R.; Burnham, A.K.; Weeks, B.L. *Journal of Physical Chemistry B* **2007**, *111*, 9182 – 9185.

18 Burnham, A.K.; Qiu, S.R.; Pitchimani, R.; Weeks, B.L. *Journal of Applied Physics* **2009**, *105*, 104312.

19 Lau, K.H.; Hildenbrand, D.L.; Crouch-Baker, S.; Sanjurjo, A. *J. Chem. Eng. Data* **2004**, *49*, 544 – 546.

20 Goede, P.; Latypov, N.V.; Östmark, H. *Propellants, Explosives, Pyrotechnics* **2004**, *29* (4), 205 – 208.

21 Dong, L.-M.; Li, X.-D.; Yang, R.-J. *Acta Phys.-Chim Sin*. **2009**, *5*, 981 - 986

22 Korsounskii, B.L.; Nedel'ko, V.V.; Chukanov, N.V.; Larikova, T.S.; Volk, F. *Russian Chemical Bulletin* **2000**, *49* (5), 812 – 818.

5. Perspectives of energetic materials detection

A wide range of detection devices based on different physical properties exist already. Some of them have been introduced in chapter 1. Here, we are going to evaluate the capacities of the nanocalorimetry with regard to differentiating the energetic materials, as well as with regard to the detection limits and compare it to the existing methods. The performance criteria on which security screening technologies are judged are accuracy (high detection), speed and cost. Systems must also be sufficiently automated for nontechnical security personnel to operate.

Two kinds of energetic materials are taken as representative examples: the crystals of low molecular mass explosives (RDX, PETN, CL-20) studied in chapter 4 and a polymer explosive (nitrocellulose thin film).

5.1. AC experiments with nanocalorimetry

In chapter 4, we observed that RDX, PETN, CL-20 crystals sublimate during a heating ramp at 20°C/min in the AC mode (frequency = 75Hz, amplitude = 0.1 mA, offset = 0.3 mA). For the nanocalorimetric curves on figure 1, each experiment is performed in the AC mode at 20°C/min on a single crystal placed in the center of the active area of a XEN-3970sensor.

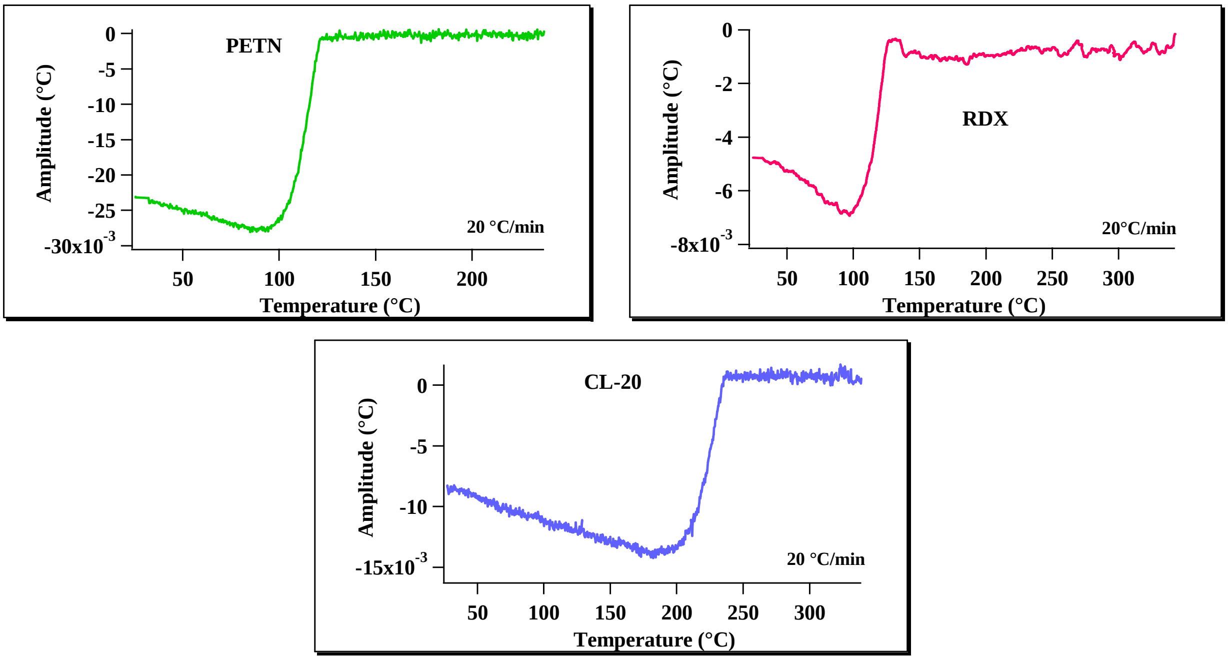

Figure 1. Nanocalorimetric traces of PETN, RDX and CL-20 heated at 20°C/min.

Figure 1 does not reveal melting peaks of RDX and PETN, neither it is the case of polymorphic transition of CL-20. For PETN and RDX the sublimation occurs at 100 °C, at 200 °C for CL-20. PETN and RDX are sublimated at the same temperature because they have similar vapour pressure whereas CL-20 has a lower vapour pressure (see figure 11 in chapter 1). In such conditions, the only parameter which can differentiate PETN and RDX through AC calorimetric experiments is their activation energy. In our experiments on nitrocellulose films, we deposited by spin-coating the acetone solutions of the three grades of nitrocellulose on XEN-3970 sensors which have a measurement area of 30 x 30 µm². The nanocalorimetric curves corresponding to the three grades of nitrocellulose films measured on heating at 20 °C/min are given on figure 2.

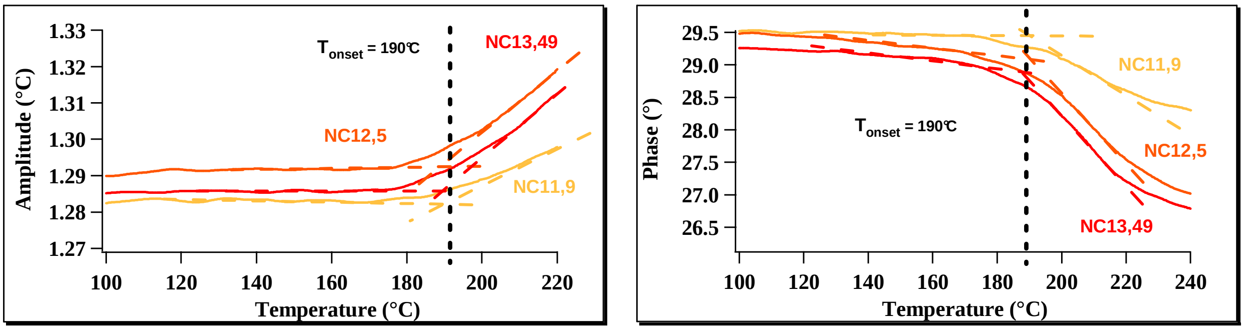

Figure 2. Amplitude and phase curves of spin-coated nitrocellulose films corresponding to modulated heating at 20 °C/min.

We observe that the amplitude increases and the phase decreases starting from 190°C. There is no exothermic peak which could be attributed to the nitrocellulose decomposition. The modifications visible on amplitude and phase curves could be attributed either to decomposition or sublimation of the nitrocellulose films. The decomposition temperature measured by the calorimetric chip is 190°C for the three nitrocellulose grades. This temperature is close to the one measured by DSC in a high pressure crucible (see appendix 2.4). There is no difference observable by nanocalorimetry between the three grades of nitrocellulose. According to figures 1 and 2, it is not possible to differentiate each tested explosives through AC calorimetry because the only transition visible on nanocalorimetric curves is the sublimation. The sublimation of PETN, RDX, CL-20 was bringing to light in chapter 4 through isothermal experiments.

In the described experiments the sample weights of PETN, RDX, CL-20 and nitrocellulose thin films are 30 ng, 5 ng, 20 ng and 15.6 ng, respectively. Table 1 shows the noise for each experiment determined from figure 1. The table 1 gives the height of the sublimation step of each materials, the noise on the nanocalorimetric curve and the lowest detectable mass. It was assumed that the lowest detectable mass should have a sublimation step equal to three times the noise level.

	RDX	PETN	CL-20	NC13.49
Mass (ng)	5	30	20	15.6
Sublimation step (°C)	0.0059	0.027	0.015	0.30
Noise (°C)	0.0009	0.0003	0.0007	0.004
Lowest detectable mass (ng)	2.3	1.0	2.8	0.6

Table 1. Determination of the lowest mass expected to detect with AC experiments at 20°C/min.

The lowest expected mass per active area of the chip XEN-3970 is determined here by calculation as it is difficult to check experimentally for the low molecular weight explosives in the form of single crystals. However it is feasible for nitrocellulose films the mass of which can be controlled by the thickness of the deposited films. To verify our predictions for nitrocellulose, we deposited NC13.49 films of different thicknesses by spin-coating. The nanocalorimetric curves for each of the prepared NC13.49 films are presented on figure 3.

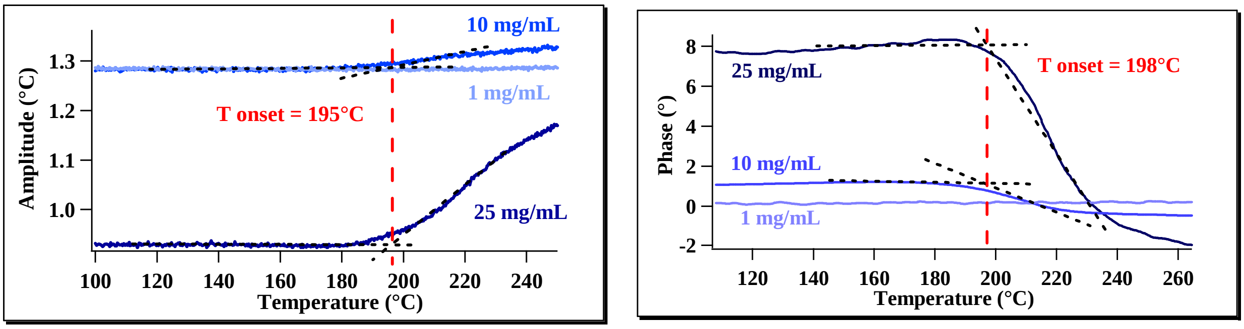

Figure 3. Amplitude curves of spin-coated nitrocellulose (NC13,49) films of different thicknesses corresponding to modulated heating at 20 °C/min.

It can be seen that the steps in amplitude and in phase are decreasing while decreasing the film thickness. However, the decomposition temperature of the nitrocellulose films does not depend on the thickness. The masses of deposited and decomposed nitrocellulose are calculated with the equation explained in chapter 1:

$$\Theta = \frac{P}{\sqrt{(mc\omega)^2 + Q^2}} \quad (1).$$

They are summarized in table 2.

Concentration of NC solution used for spin-coating	Thickness of NC film (nm)	Deposited mass (ng)	Decomposed mass (ng)	Percentage of decomposition
25 mg/mL	250	15.59	12.65	81 %
10 mg/mL	200	1.35	1.03	76%
1 mg/mL	90	less than 1 ng		

Table 2. Deposited and decomposed masses of spin-coated nitrocellulose films of several thicknesses.

If one calculates the deposited masses according to the film thickness, the values of the masses will be smaller than the ones computed from equation (1). This discrepancy can be due to the membrane roughness (higher than wafer roughness) and to the effect of wires sputtered on the sensor which prevent the solution spreading during spin-coating. The mass of the nitrocellulose film with a thickness of 90 nm cannot be determined precisely. According to table 2 and to figure 3, the lowest mass of the nitrocellulose film detected by the Nanocalorimeter is less than 1 ng per active area of the chip XEN-3970 (30 x 30 μm²). This value is in good agreement with the expectation (cf. table 1). Besides, we observe that all nitrocellulose is not decomposed after a heating ramp. We check this observation by coupling the Nanocalorimeter with the AFM (cf. appendix 5.1).

5.2. Fast heating experiments by nanocalorimetry

Fast heating experiments are performed on RDX and PETN crystals at a heating rate of 2500°C/s (figure 4) on sensors XEN-3970.

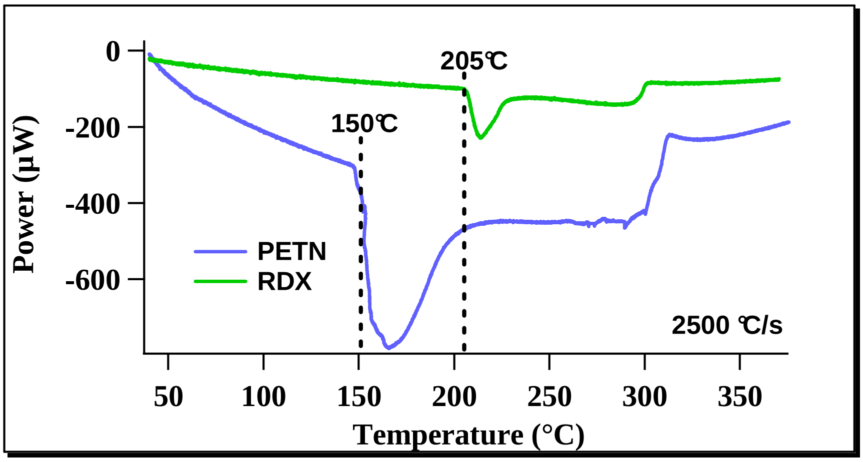

Figure 4. Nanocalorimetric curves of RDX and PETN corresponding to thermal cycle at 2500°C/s.

The RDX crystal melts at 205°C and the PETN crystal at 150°C as in the DSC experiments described in chapter 4. The step in the heat capacity due to the evaporation occurs at approx. 300°C for both energetic materials. According to melting enthalpy, RDX has a mass of 7.3 ng and PETN has a mass of 35.1 ng. One can clearly distinguish RDX and PETN (cf. figure 4) based on their difference in the melting temperature. Figure 5 presents a nanocalorimetric curve of a CL-20 crystal measured at 1400°C/s on a XEN-3971 sensor. According to the mass determination with AFM cantilever, the sample mass is 13.9 ng.

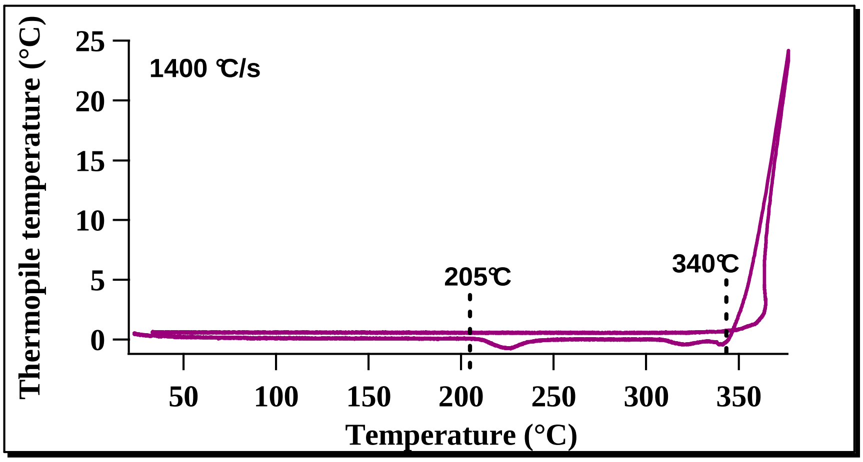

Figure 5. Nanocalorimetric curve of CL-20 corresponding to thermal cycle at 1400°C/s.

The polymorphic transition[1] which is the transition from ε phase to γ phase occurs at 205°C as it is the case of a DSC experiment. We observe an exothermic peak at 340°C attributed to the decomposition of the CL-20 crystal. Contrary to RDX and PETN crystals, the exothermic peak of CL-20 decomposition is observable by nanocalorimetry. The low vapour pressure of CL-20 compared to those of RDX and PETN can explain the fact that the decomposition peak is observable for CL-20 and not for RDX and PETN. Figure 6 shows nanocalorimetric curves of nitrocellulose (NC13.49) films heated at 350°C/s, 710°C/s and 1430°C/s on a XEN-3972 sensor.

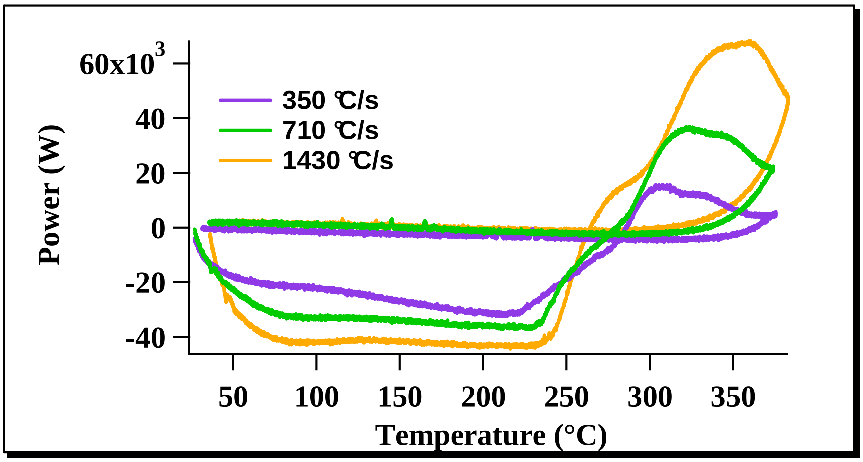

Figure 6. Nanocalorimetric curves of NC13.49 spin-coated films corresponding to thermal cycle at 350°C/s, 710°C/s, 1430°C/s.

The endothermic transition between 50°C and 240°C is attributed to evaporation of residual acetone in the nitrocellulose films. The exothermic peak, which occurs at 250°C, is the decomposition peak of nitrocellulose. The curves don’t come back at zero after the decomposition peak because there is still some nitrocellulose on the sensor after the heating ramp.

According to figures 4, 5, 6, it can be seen that it is possible to differentiate each tested explosives thanks to fast heating experiments:

- RDX and PETN crystals are distinguishable from the others explosives based on their melting point and the step of evaporation, furthermore their nanocalorimetric curves have no exothermic peaks,
- CL-20 crystal has an endothermic peak attributed to the polymorphic transition at 205°C and an important exothermic peak at higher temperature,
- Nitrocellulose films exhibit a decomposition peak at high temperature.

The lowest masses of each tested energetic materials one can detect through fast heating experiments by nanocalorimetry are given in table 3.

	RDX	PETN	CL-20	NC13.49
Mass (ng)	7.3	35.1	13.9	16
Melting or decomposition peak (°C)	2.45	10.9	24.6	6.64
Noise (°C)	0.028	0.025	0.020	0.021
Lowest detectable mass (ng)	0.25	0.24	0.03	0.15

Table 3. Determination of the lowest detectable mass with fast heating experiments at 2500°C/min (for RDX and PETN) and 1400°C/min (for CL-20 and NC13.49).

The height of the melting peaks are measured for RDX and PETN, the height of the decomposition peaks are measured for CL-20 and NC13,49. Decomposition releases more energy than melting absorbs, so the lowest mass detected by nanocalorimetry corresponds to energetic materials which exhibit a decomposition peak in their nanocalorimetric curves. *Based on these considerations, one should be able to detect a CL-20 crystal of only 30 pg with a XEN-3971 sensor.*

Table 4 gives the lowest mass of nitrocellulose NC13.49 films which should be detectable at three heating rates.

Heating rate (°C/s)	350	710	1430
Mass (ng)	15	18	16
Decomposition peak (°C)	2.8	4.4	6.64
Noise (°C)	0.026	0.022	0.021
Lowest detectable mass (ng)	0.42	0.27	0.15

Table 4. Determination of the lowest mass of nitrocellulose detectable by nanocalorimetry at different heating rates.

We observe in table 4 that the lowest mass could be reduce by nearly a factor 2 if the heating rate is multiply by a factor 2. So the lowest mass of nitrocellulose which could be detected at 1,000,000 °C/s (the higher heating rate) should be 0,2 pg.

Table 5 gives the lowest mass of tested explosives which could be detected at the higher heating rate reaches by the nanocalorimeter i.e. 1,000,000 °C/s. We assume that the noise level is independent of the heating rate and is equal to 0.02°C.

	RDX	PETN	CL-20
Lowest expected mass at given heating rate (ng)	0.25	0.24	0.03
Heating rate (°C/s)	2500	2500	1400
Lowest detectable mass at 1,000,000 °C/s (pg)	0.6	0.6	0.04

Table 5. Determination of the lowest mass of explosive detectable by nanocalorimetry at 1 million °C/s.

According to these predictions, at a heating rate of 1 million °C/s one should be successful in detection energetic materials with mass in the range of a few tenths of a picogram. The lowest mass of CL-20 should be 40 femtograms.

5.3. Nanocalorimetry as compared to the existing detection methods

As mentioned in chapter 1, an explosives detection device must have a high detection sensitivity (i.e., be able to detect very low masses), a quick analysis time, be automated and have a low cost. In the next section, we evaluate the advantages and disadvantages of the nanocalorimeter compared to the existing detecting methods in terms of sensitivity, selectivity, sample placement and time of analysis.

5.3.1. Sensitivity and analysis time

The explosives detection device developed by Thundat and al. is able to detect 70 pg (10^{-12} g) of TNT. It uses heated cantilever (see chapter 1).

The mass spectrometry is usually employed in airports to detect energetic materials, the lowest mass detectable by such device is in the range to those developed by Thundat. The limit of detection for TNT, RDX and PETN are about 1, 5, 20 pg respectively, with the analysis time on the order of a few seconds.

The best detection device developed nowadays Fido XT has the same limit of detection than dogs and is faster than dogs. It can detect a few femtograms (10^{-15} g) of explosives in only 30s.

The lowest mass of explosive expected to be detectable by nanocalorimetry at 1 million °C/s is in the range of several hundreds of femtograms. The limit of detection by nanocalorimetry depends on the particular energetic material and on the heating rate: the limit of detection is 40 fg for CL-20 and some hundreds of femtograms for other energetic materials such as PETN and RDX heated at 1 million °C/s, with the analysis time of a few milliseconds. In reality, the analysis time is much longer if one takes in account the time of the sample preparation (some minutes to one hour). The sensitivity of the nanocalorimeter is enhanced if the energetic material exhibits a decomposition peak. In order to reach a heating rate of 1 million °C/s during a linear ramp, it is necessary to use nanocalorimetric sensors with a small active area. The sample must have a good thermal contact between itself and the membrane, otherwise it won’t generate any nanocalorimetric signal, and the detection will fail. So according to the predictions, the nanocalorimeter has a good sensitivity for the explosives detection.

5.3.2. Detection selectivity

The differentiation of energetic materials by nanocalorimetry is possible at high heating rates (DC experiments), otherwise the materials are sublimated during slower AC experiments. The differentiation is possible thanks to the thermal transitions present in the energetic materials during nanocalorimetric experiments. The materials do not exhibit the same thermal behaviour in a nanocalorimeter than in a DSC. Indeed, we have shown that PETN and RDX crystals are evaporated at high heating rates whereas CL-20 and nitrocellulose films are decomposed. Instead, in DSC experiments in closed crucibles all of these explosives are decomposed. It is thus necessary to do screening of all explosives at the same heating rate in order to be able to differentiate each explosive from its nanocalorimetric curve.

As shown on figure 4, one can distinguish PETN from RDX thanks to their different melting temperature. The sample must be placed in the center of the active area of the sensor, otherwise the gradient on the sensor can shift the melting temperature of the tested energetic material (see the measurements of the temperature gradient in chapter 3). In the case of unknown sample, an exothermic peak during a high heating ramp can prove that the sample is an energetic material. If the material is evaporated, one cannot conclude if it is an energetic material or not without a standard curve to compare it in the same conditions (heating rate and atmosphere).

5.3.3. Sample preparation

In nanocalorimetry, the sample must be placed in the center of the active area of the sensor, otherwise the temperature measurements can be in error and the identification of the material becomes impossible. This inconvenient can be bypassed by using sensor with a thin aluminium coating which is used to homogenize the temperature on the sensor.[2] The temperature homogeneity on the sensor can be checked with an indium particle as presented in chapter 2. The thermal contact between the sample and the surface of the membrane must be good enough to have a nanocalorimetric signal during analysis. The nanocalorimetric sensors used in this study can analyse only sample in solid form. Another complication stems from the fact that the sample must not move during analysis: all external disturbances (electrostatic, air flow, wind) must be avoid as well as internal stress presents in the particle (see the fast heating experiments with the tin particle in chapter 3).

As for other detection devices, it is necessary to guide the energetic material particle directly onto the center of the sensor membrane.

5.4. Conclusions

At the present time, the Fido-XT device remains the best method to detect energetic materials. Actually, this device is sensitive (detection of a few femtograms), portable, easy to manipulate and it can be fixed on a robot which is conduct to the explosive device in order to disarm it. The nanocalorimetry is one of the techniques which can be used in the future for the explosives detection but some technical issues have to be solved. The membrane should be modified to enhance the thermal contact between the sample and the membrane. The experiments on blends of nanoRDX/TNT have proven that the nanocalorimeter can be used to analyze nanoparticles of energetic materials too.

---

[1] Chukanov, N.V.; Dubikhin, V.V.; Raevskii, A.V.; Golovina, N.I.; Korsunskii, B.L.; Nedel’ko, V.V.; Aldoshin, S.M. *Russian Journal of Physical Chemistry* **2006**, *80* (2), 281 – 287.

[2] www.xensor.nl/pdffiles/sheets/nanogas-oldversions.pdf

6. Summary

Calorimetry is one of the main techniques of thermal analysis. Most of physical or chemical modifications of material are associated with thermal effects whereby heat is absorbed (i.e., endothermic phenomena such as melting) or released (i.e., exothermic phenomena such as thermal decomposition). For such transitions, calorimetry allows determining the associated thermodynamic and kinetic parameters and characteristic temperatures.

Typically, calorimetric experiments are performed with Differential Scanning Calorimetry (DSC), which measures the heat flux absorbed or released by the sample following the same temperature program as a reference material. In these experiments, measurements are typically carried out on a few milligrams of sample. However, for many applications one has to handle nanograms or even picograms of sample. One of such applications is relevant to studies of materials which can release a significant amount of energy during their decomposition (energetic materials). The release of energy is obtained by mechanisms of intra-molecular oxido-reduction. Different treatments can trigger this release such as heating the materials to the decomposition temperature, impact, friction. Moreover, calorimetry able to handle nanograms of sample could find potential applications in the field of explosives detection. ***Nanocalorimetry allows to heat small amounts of sample (a few nanograms to a few hundred picograms) at extreme heating rates, i.e. up to one million °C/s.***

The temperature increase can initiate several phenomena in energetic materials, therefore the calorimetry could be an appropriate technique to characterize and to detect energetic materials. ***The energetic materials used in this study are nitrocellulose (NC), hexogen (RDX), 2,4,6,8,10,12-hexanitro-2,4,6,8,10,12-hexaazaisowurtzitane (CL-20) and penthrite (PETN).***

The manuscript presents our results on the ***nanocalorimeter calibration***, on the thermal behaviour of the ***explosives studied with nanocalorimetry*** and also includes an evaluation ***of nanocalorimetry as a tool for explosives detection.***

Chapter 3 is focused on establishing the ***procedure to calibrate the calorimetric sensors*** which is an essential step for calorimetric measurements. The calibration we propose contains five steps. First, we calibrate the temperature of the heater resistances, then we determine the dependence of the heater voltage on its temperature. The internal thermopile sensitivity is then calibrated by heating the sensor with a heater resistance, and the heater temperature is linked to the voltage on the thermopile. The AC amplitude correction function is eventually determined. Eventually, the calibration is cross-checked with melting temperatures of indium and zinc microparticles. ***The originality of the temperature calibration procedure resides in the use of the melting temperature of metallic microparticles (In and Zn) to cross-check the temperature measured by the Nanocalorimeter.*** This is done for heating ramps in AC modulation (slow heating ramps) and for DC ramps at fast-heating rates. Usually, an external thermocouple is placed approx. 1 cm away from the measurement area, which could introduce a significant error if there is a temperature gradient between the external thermocouple and the elements of the active area (e.g., heaters resistances, thermopiles). Positioning of a metallic microparticle in the center of the active area allows circumventing this problem. An example of the calibration procedure is done with a XEN-3972 sensor which has a measurement area of 100x100 μm². The calibration depends on the membrane size, membrane type (the membrane can be fabricated e.g. from bare silicon nitride or contain aluminium coating) and the sensor batch.

The measurements of the ***temperature gradient*** are also performed with a help of an indium microparticle placed on a XEN-3972 sensor (active area of 100 x 100 μm²). The ***particle is used as a temperature probe***: the onset melting temperature of the particle is evaluated for different places on the sensor membrane. We observe that the melting temperature of the indium particle measured by the Nanocalorimeter changes with its position on the membrane and that the ***melting enthalpy is independent of its position*** on the membrane. A strong temperature gradient exists on the membrane at distances above 20 μm from the center. It is steeper along the vertical axis than along the horizontal one.

To improve the quality of the linear heating ramps at high heating rates we propose an iterative method based on the principle of a PID. Generally, a ***PID regulator allows adjusting the measurement signal relative to the programmed signal***. The error signal here is defined as the difference between the two signals. The PID regulator can undertake three actions to minimize the error signal: proportional action (the error signal is multiplied by a respective gain), integral action (the error signal is integrated with respect to time, then it is multiplied by a respective gain), differential action (the error signal is first differentiated with respect to time, then it is multiplied by a respective gain). In this work, the ***proportional action*** is found sufficient for refining the linear heating ramps at high heating rates. An example of such refinement is given for sensor XEN-3970.

To perform quantitative calorimetric measurements, ***we weigh unknown particles using the resonant frequency of tipless AFM cantilevers.*** Before the mass determination, the spring constant of the cantilever has to be determined with precision. Chapter 2 gives an overview of the different methods designed to measure the spring constants (the Cleveland method, the Sader method, the reference lever method of spring constant calibration, the thermal noise method). We propose the Nanocalorimeter as a new experimental tool for the calibration of cantilever spring constant. In particular, the Nanocalorimeter presents several advantages compared to other methods. Thus it is free from uncertainties on the object size, it is not limited by the sampling rate as it is the case of the thermal noise method, it is not dependent on the laser optical sensitivity, and does not suffer from problems due to stick-slip phenomena as it is the case of the reference lever method. Experimentally, indium particles of different size are placed successively on a sensor. Then several fast-heating experiments are performed in order to melt the indium particle and to determine its mass through its melting enthalpy. The cantilever spring constant corresponds to the slope of the line representing the added mass on the cantilever as a function of $\frac{1}{(2.\pi.f)^2}$. Once the determination of the cantilever spring constant is completed, the unknown particle is placed on the cantilever, and its mass is measured using the following equation $m = k.\left(\frac{1}{\omega^2} - \frac{1}{\omega_0^2}\right)$ where k is the cantilever spring constant, ω is the angular frequency of the cantilever loaded with the particle, and ω_0 is the angular frequency of the unloaded cantilever. ***The precision of this method is about 3%, the main error comes from the melting enthalpy determination of the indium particle.***

Chapter 4 presents our nanocalorimetry data on explosive micro crystals which are ***RDX, PETN and CL-20***. Some ***blends of nanoRDX / TNT*** are also studied. In the first part of the chapter, DSC analysis is performed on RDX and PETN to determine the activation energy of decomposition. According to the experiments, the activation energy of RDX decomposition is 90 ± 12 kJ/mol. In the literature, the experimental and theoretical activation energy of RDX is in the range of 96 to 219 kJ/mol. The activation energy of PETN decomposition is 181 ± 14 kJ/mol (in the literature, it is in the range of 132.7 to 197.5 kJ/mol). Therefore our values for PETN is in good agreement with the literature. A possible discrepancy for activation energy of RDX can be explained by several reasons such as the RDX density, the competition with evaporation and the decomposition of the gaseous RDX. The wide range of value of decomposition activation energy can also be explained by kinetic compensation effects. The kinetic compensation effect is the correlation of E_a with the pre-factor A. When E_a increases, the reaction rate is not necessarily decreasing because A can increase to compensate for E_a. So the activation energy of RDX decomposition is strongly dependent on the sample characteristics (i.e., sample mass, particle size, heating rate, self-heating of the sample) and on the experimental conditions (i.e., characteristics of the surrounding atmosphere, shape and material of construction of the sample holder).

The second part of the chapter is focused on the ***sublimation and evaporation of RDX and PETN microcrystals on the nanocalorimetric chip***. During quasi-isothermal experiments, we observe that the crystal size of RDX or PETN decreases and some particles appear around the measurement area. At the end of the experiment, there is no crystal in the center anymore. Instead there is a significant amount of particles around the measurement area. The AC amplitude increases during the isotherm. By comparing the optical micrographs and the nanocalorimetric curves, we assign the change in the AC amplitude to a progressive removal of the crystal from the center of the measurement area. Transmitted polarized light and Raman analysis confirm that the particles outside the active area are sublimated RDX and PETN. ***The sublimation of α-RDX leads to its recrystallisation into β-RDX on cold parts of the chip. By contrast, the sublimated and subsequently recrystallized PETN does not change the phase. The activation energy of α-RDX sublimation is 100 ± 10 kJ/mol and the activation energy of PETN sublimation is 173 ± 15 kJ/mol.*** The principal possibility of studying evaporation of PETN and RDX is also shown. Importantly, the RDX and PETN crystals are not decomposed during fast heating ramps on the nanocalorimetric chip whereas these energetic materials are decomposed during DSC experiments.

In the third part of the chapter, we characterize ***nanoRDX/TNT blends*** which were synthesized by a process of nanocrystallization patented by ISL. This process uses ultrasonic waves to generate an aerosol of small droplets of solvent/explosive. After evaporation of the solvent in an oven, the particles are reduced via Cottrell precipitation. SEM micrographs of RDX and TNT used before the process allow identifying the different components of the final blend. ***The thermal behaviour of the blends shows a different behaviour when studied by DSC or the nanocalorimetric chip.*** On DSC curves, the melting peak of RDX is hidden or impeded by the decomposition peak which occurs at 200°C whereas ***the nanocalorimetric curves do not show the decomposition peak. Instead, the melting peak of RDX is clearly visible.*** The melting of RDX in the blends obtained after nanocrystallization occurs at lower temperatures than in the initial RDX. The depression of the RDX melting peak supports the presence of nanoRDX in the blend.

The last part of the chapter is dedicated to studies of ***CL-20***. The evidence of its sublimation is also obtained using transmitted polarized light microscopy coupled to the nanocalorimeter. The intense exothermic peak corresponding to the CL-20 decomposition is clearly visible on nanocalorimetric curves. The enthalpy of this peak prompts us thinking that the nanocalorimeter chip has a potential in detecting the traces of CL-20.

Chapter 5 describes the ***perspectives of detection of energetic materials by nanocalorimetry.*** In this chapter, we evaluate the lowest detectable mass of explosives and the possibility to perform selective detection.

Heating ramps at 20°C/min in AC modulation (frequency = 75 Hz, amplitude = 0.1 mA, offset = 0.3 mA) show that RDX, PETN and CL-20 microcrystals undergo sublimation. RDX and PETN are sublimated at the same temperature because they have similar vapour pressures. Nitrocellulose films of different grades deposited on a XEN-3970 sensor do not show differences between them, which could be observable by nanocalorimetry.

The lowest detectable mass in AC experiments at 20°C/min is 2.3 ng for RDX, 1.0 ng for PETN, 2.8 ng for CL-20, 0.6 ng for nitrocellulose.

In the DC mode (fast heating experiments) one can differentiate between RDX and PETN based on the difference in the melting temperature. The nanocalorimetric curve of CL-20 presents an endothermic peak at 205 °C attributed to the transition from ε phase to γ phase, the exothermic peak at 340 °C is assigned to the CL-20 decomposition. The nanocalorimetric curves of nitrocellulose films show an endothermic peak between 50°C and 240°C which is attributed to evaporation of residual acetone. The decomposition of nitrocellulose occurs at 250°C. According to these observations, ***it is possible to differentiate each tested explosives thanks to their characteristic thermal transitions during fast heating experiments.*** Furthermore, the nanocalorimeter should be able to detect in the same conditions 250 pg of RDX, 240 pg of PETN, 30 pg of CL-20 and 150 pg of NC13.49. ***By extrapolation at a heating rate of one million °C/s, we should be able to detect 0.6 pg of RDX, 0.6 pg of PETN, 0.04 pg of CL-20 and 0.2 pg of NC13.49.*** Therefore the nanocalorimetry has a ***good sensitivity*** compared to other detection devices if we extrapolate our measurements at one million °C/s. For comparison, the best detection device developed nowadays (Fido XT) having the same limit of detection as dogs can detect a few femtograms (10^{-15} g) of explosives in only 30s.

In terms of ***detection selectivity***, the differentiation of energetic materials by nanocalorimetry is possible at high heating rates (DC experiments), otherwise the materials are sublimated during slower AC experiments. ***The differentiation is possible based on the thermal transitions present in the energetic materials***, so it is necessary to make a thermal database of the existing explosives in order to be able to identify them. In the case of unknown explosives, an exothermic peak detected during a high heating ramp could indicate that the sample is an energetic material.

In terms of ***sample preparation***, the nanocalorimetry presents a technical difficulty in the sense that the sample must be placed in the center of the active area of the sensor. The nanocalorimetric sensors used in this study can analyse only samples in the solid state. Another complication stems from the fact that the sample must not move during analysis: all external disturbances (electrostatic, air flow, wind) must be avoid as well as internal stress presents in the particle

At the present time, the Fido-XT device remains the best tool to detect energetic materials. Actually, this device is sensitive (detection of a few femtograms), portable, easy to manipulate and it can be fixed on a robot which is conduct to the explosive device in order to disarm it. ***The nanocalorimetry is one of the techniques which can be used in the future for the explosives detection but some technical issues have to be solved.*** The membrane should be modified to enhance the thermal contact between the sample and the membrane. The experiments on blends of nanoRDX/TNT have proven that the nanocalorimeter can be used to analyse nanoparticles of energetic materials as well.

7. Résumé

Un nanocalorimètre permet l'analyse thermique de très faibles quantités d'échantillons (quelques nanogrammes ou quelques centaines de picogrammes), ainsi que l'étude de films minces dont l'épaisseur varie de quelques nanomètres à plus d'un micron. Les vitesses de chauffe et de refroidissement sont nettement plus élevées que celles réalisées avec une DSC classique : ***les vitesses de chauffe peuvent atteindre*** 10^3 ***à*** 10^6 ***K/s.*** Par conséquent, les mesures réalisées avec ce type d'appareil sont très rapides (quelques millisecondes). Du fait de sa sensibilité élevée, des vitesses de chauffe rapides atteintes et de l'acquisition rapide des données, le nanocalorimètre peut-être utilisé pour la caractérisation et la détection de ***quelques nanogrammes*** de matériaux énergétiques.

Les objectifs de cette thèse sont d'une part de mettre au point une procédure de calibration des capteurs nanocalorimétriques (calibration de la température, de la puissance, de la masse du microcristal à analyser) et d'autre part de caractériser des matériaux énergétiques afin de pouvoir effectuer des analyses quantitatives en vue d'applications pour la détection d'explosifs. Les matériaux énergétiques étudiés sont ***des films de nitrocellulose, des cristaux de penthrite, d'hexogène (principal constituant du C4), de 2,4,6,8,10,12-hexanitro-2,4,6,8,10,12-hexaazaisowurtzitane (Cl20), et des nano-cristaux d'explosifs***.

Le travail réalisé a montré qu'il est possible de différencier rapidement des explosifs par leurs températures de fusion, de décomposition et d'évaporation. Il est aussi possible de déterminer des ***paramètres cinétiques d'un cristal isolé d'explosif***. Le nanocalorimètre a aussi permis de ***calibrer la constante de raideur des leviers AFM*** utilisés pour déterminer la masse de microcristaux d'explosifs.

Le **chapitre 3** présente une ***procédure originale pour calibrer les capteurs nanocalorimétriques***. La calibration est une étape primordiale pour ensuite pouvoir effectuer des mesures nanocalorimétriques. La calibration que nous proposons comporte cinq étapes. Premièrement, nous calibrons la température des résistances chauffantes, ensuite nous déterminons la dépendance de la tension de la résistance chauffante sur sa température. La sensibilité de la thermopile interne est ensuite calibrée en chauffant le capteur avec les résistances chauffantes, puis la température de la résistance chauffante est reliée à la tension sur la thermopile. Pour finir, la calibration est vérifiée en faisant fondre des microparticules d'indium et de zinc au centre de la membrane. ***L'originalité de cette procédure de calibration réside dans l'utilisation de la température de fusion de microparticules métalliques (indium et zinc) pour vérifier la température mesurée par le nanocalorimètre***. Cette vérification est réalisée en effectuant des rampes en température à 20°C/min et à des vitesses de chauffe élevées. Habituellement, un thermocouple externe est placé à environ 1 cm de l'aire de mesures, ce qui peut introduire une erreur significative s'il y a un gradient de température entre le thermocouple externe et les éléments de l'aire de mesure (i .e. les résistances chauffantes et les thermocouples). Le placement de microparticules métalliques au centre de l'aire de mesure permet de contourner ce problème. Un exemple de la procédure de calibration est faite sur un capteur XEN-3972 qui a une aire de mesure de 100 x 100 µm². Les paramètres de calibration dépendent de la taille de la membrane, du type de membrane utilisée (uniquement en nitrure de silicium ou avec un film mince d'aluminium) et du lot de capteur.

Le ***gradient thermique*** est mesuré en plaçant une microparticule d'indium sur un capteur XEN-3972 (aire de la zone de mesure = 100 x 100 µm²). ***La particule est utilisée comme une sonde thermique*** : la température onset de fusion de la particule est relevée à chaque endroit de la particule sur la membrane. Nous observons d'une part que la température de fusion de la particule change en fonction de l'emplacement de la particule sur la membrane et d'autre part que ***l'enthalpie de fusion est indépendante de la position de la particule sur la membrane.*** Un important gradient thermique existe sur la membrane à une distance de 20 µm du centre. Le gradient thermique est plus important selon l'axe vertical que selon l'axe horizontal.

Afin ***d'améliorer la qualité des rampes linéaires à vitesses de chauffe élevées***, nous proposons une méthode basée sur le PID. De manière générale, ***un régulateur PID permet d'ajuster le signal mesuré par rapport au signal de consigne***. Dans notre cas, le signal d'erreur est défini comme la différence entre les deux signaux. Le régulateur PID peut effectuer trois actions pour minimiser le signal d'erreur : une action proportionnelle (le signal d'erreur est multiplié par un gain), une action intégrale (le signal d'erreur est tout d'abord intégré en fonction du temps puis il est multiplié par un gain), une action différentielle (le signal d'erreur est d'abord dérivé en fonction du temps puis il est multiplié par un gain). Dans ce travail, l'action proportionnelle est suffisante pour obtenir des rampes linéaires aux vitesses de chauffe élevées employées. Cette méthode est illustrée par un exemple sur un capteur XEN-3970.

Pour effectuer des mesures calorimétriques quantitatives, ***les particules inconnues sont pesées avec un levier AFM dépourvu de pointe.*** Avant de déterminer la masse de la particule, la constante de raideur du levier doit être déterminée avec précision. Le chapitre 2 donne une vue d'ensemble des différentes méthodes utilisées pour déterminer la constante de raideur d'un levier AFM (méthode de Cleveland, méthode de Sader, méthode utilisant des leviers de référence, méthode du bruit thermique). Dans ce chapitre, nous proposons le nanocalorimètre comme un nouvel outil expérimental pour la calibration de la constante de raideur d'un levier. Le nanocalorimètre présente plusieurs avantages par rapport aux autres méthodes : les imprécisions sur la taille de l'objet ne sont pas prises en compte, il n'y a pas de limite de la fréquence d'échantillonnage comme c'est le cas dans la méthode du bruit thermique, la mesure est indépendante de la sensibilité optique du laser, et il n'y a pas de problème relatif au phénomène de stick-slip comme c'est le cas dans la méthode des leviers de référence. Expérimentalement, des particules d'indium de différentes tailles sont placées successivement sur le capteur nanocalorimétrique. Ensuite, plusieurs chauffes rapides sont effectuées afin de fondre la particule d'indium et d'en déterminer la masse à partir de l'enthalpie de fusion de la particule. La constante de raideur du levier correspond à la pente de la droite représentant la masse ajoutée sur le levier en fonction de $\frac{1}{(2.\pi.f)^2}$. Une fois que la détermination de la constante de raideur du levier est faite, la particule inconnue est placée sur le levier et sa masse est mesurée en utilisant l'équation $m = k.\left(\frac{1}{\omega^2} - \frac{1}{\omega_0{}^2}\right)$ où k représente la constante de raideur du levier, ω est la fréquence angulaire de résonnance du levier chargé avec la particule et ω_0 est la fréquence angulaire de résonance du levier non chargé. ***La précision de cette méthode est d'environ 3%, la principale source d'erreur vient de la détermination de l'enthalpie de fusion de la particule d'indium.***

Le **chapitre 4** présente nos résultats sur les expériences nanocalorimétriques effectuées sur des microcristaux d'explosifs de ***RDX, PETN et CL-20***. Des ***mélanges de nanoRDX/TNT*** sont aussi étudiés par nanocalorimétrie.

Dans la première partie de ce chapitre, des analyses DSC sont effectuées sur RDX et PETN pour déterminer leur énergie d'activation de décomposition. D'après les mesures, l'énergie d'activation de décomposition du RDX est de 90 ± 12 kJ/mol. Dans la littérature, les valeurs expérimentales et théoriques de l'énergie d'activation de décomposition du RDX sont comprises entre 96 et 219 kJ/mol. L'énergie d'activation de décomposition de PETN est de 181 ± 14 kJ/mol (dans la littérature, la valeur est comprise entre 132.7 et 197.5 kJ/mol). Notre valeur pour PETN est donc en accord avec la littérature. Les différences dans les valeurs d'énergies d'activation de décomposition du RDX peuvent être dues à la densité du RDX, à la compétition existante entre l'évaporation et la décomposition du RDX gazeux. La grande plage de donnée des valeurs d'énergie d'activation de décomposition du RDX peut aussi être expliqué par des effets cinétiques de compensation. L'effet cinétique de compensation est le fait qu'il existe un grand nombre de paires E_a – lnA dépendant de beaucoup de conditions. Lorsque l'énergie d'activation augmente, le taux de réaction ne décroit pas forcément car le pré-facteur A augmente pour compenser l'énergie d'activation. L'énergie d'activation de décomposition du RDX d'un couple E_a – lnA dépend fortement des caractéristiques de l'échantillon (masse de l'échantillon, taille de particule, vitesse de chauffe, auto-échauffement de l'échantillon) et des conditions expérimentales (caractéristiques de l'atmosphère environnant, forme et matériau de construction du porte échantillon).

La deuxième partie porte ***sur la mise en évidence de la sublimation et de l'évaporation des microcristaux de RDX et de PETN sur le capteur nanocalorimétrique***. Lors d'expériences quasi-isothermes, nous observons que la taille du cristal (RDX ou PETN) décroît et que des particules apparaissent autour de l'aire de mesure. A la fin de l'expérience, il n'y a plus de cristal au centre de la membrane, cependant beaucoup de particules se trouvent autour de l'aire de mesure. La courbe d'amplitude correspondante à l'expérience augmente au cours de l'isotherme. En comparant les images de microscopie optique avec la courbe nanocalorimétrique, le changement de l'amplitude peut être attribué à la disparition progressive du cristal au centre de la membrane. Les images en lumière polarisée et les analyses Raman confirment que les particules à l'extérieur de l'aire de mesure sont du RDX et de la PETN sublimés. De plus, ***nous observons d'une part que la sublimation du α-RDX conduit à la cristallisation du β-RDX sur les zones froides du capteur ; d'autre part, la PETN sublimée n'a pas changé de phase. L'énergie d'activation de sublimation du α-RDX est de 100 ± 10 kJ/mol et l'énergie d'activation de sublimation de PETN est de 173 ± 15 kJ/mol.*** L'évaporation de PETN et RDX est aussi mise en évidence. Une tentative de la détermination de l'énergie d'activation d'évaporation du RDX est présentée. Les cristaux de RDX et PETN ne sont pas décomposés pendant les chauffes rapides faites sur les capteurs nanocalorimétriques cependant ces matériaux énergétiques sont décomposés en DSC.

Dans la troisième partie, des ***mélanges nanoRDX/TNT*** sont caractérisés. Ces mélanges ont été synthétisés par un procédé de nanocristallisation breveté par l'ISL. Ce procédé génère par ondes ultrasoniques un aérosol de petites gouttes de solvant/explosifs. Après évaporation du solvant dans un four, les particules sont précipitées. Les images MEB du RDX et du TNT utilisés avant le procédé permettent d'identifier les différents composants des particules obtenues à la fin du procédé. ***Le comportement thermique de ces particules est***

différent en DSC qu'en nanocalorimétrie. Sur les courbes DSC, le point de fusion du RDX est caché par le pic de décomposition du mélange qui a lieu à 200°C alors que ***les courbes nanocalorimétriques du mélange ne présentent pas de pic de décomposition, la fusion du RDX est clairement visible.*** La fusion de RDX dans les mélanges obtenus après le procédé de nanocristallisation a lieu à des températures plus basses que celle du micro RDX. La dépression du point de fusion du RDX dans les mélanges est une preuve de la présence de nanoRDX.

La dernière partie de ce chapitre est dédiée à l'étude du ***CL-20***. La mise en évidence de la sublimation du CL-20 est aussi faite par microscopie en lumière polarisée. L'important pic exothermique correspondant à la décomposition du CL-20 est clairement visible sur les courbes nanocalorimétriques. L'importance du pic montre que le nanocalorimètre pourrait détecter une masse de CL-20 beaucoup plus faible.

Le chapitre 5 présente les ***perspectives dans la détection de matériaux énergétiques par nanocalorimétrie***. Dans ce chapitre, il est essentiel de déterminer la masse minimale d'explosif que l'on peut détecter et de trouver un moyen de différencier chaque explosif testé.

Des chauffes en modulation à 20°C/min montrent que les microcristaux de RDX, PETN, CL-20 sont sublimés. RDX et PETN sont sublimés à la même température car ils ont des pressions de vapeur similaires. ***Dans ces conditions, la détermination de leur énergie d'activation de sublimation est le seul moyen de les différencier***. Des films de nitrocellulose de différents grades sont déposés sur des capteurs XEN-3970, il n'y a pas de différence observable en nanocalorimétrie entre ces trois grades. ***La masse minimale d'explosif que l'on pourrait détecter à 20°C/min est de 2.3 ng pour le RDX, 1 ng pour PETN, 2.8 ng pour CL-20 et 0.6 ng pour la nitrocellulose.***

Des expériences à des vitesses de chauffe élevées sont faites sur les mêmes matériaux énergétiques. La vitesse de chauffe est de 2500°C/s pour RDX et PETN, 1400°C/s pour CL-20 et 350°C/s, 710°C/s, 1430°C/s pour les films de nitrocellulose de grade NC13.49. D'après les expériences, nous pouvons différencier RDX et PETN grâce à leur température de fusion. La courbe nanocalorimétrique de CL-20 présente un pic endothermique à 205°C attribué à la transition de la phase ε à la phase γ, le pic exothermique à 340°C correspond à la décomposition de CL-20. La courbe nanocalorimétrique des films de nitrocellulose montre un pic endothermique entre 50°C et 240°C qui est attribué à l'évaporation de l'acétone résiduelle dans le film de nitrocellulose. Le pic de décomposition a lieu à 250°C. D'après ces observations, ***il est possible de différencier les explosifs testés grâce à leur transitions thermiques caractéristiques lors des chauffes à des vitesses rapides***. De plus, le nanocalorimètre devrait être capable de détecter dans les mêmes conditions 250 pg de RDX, 240 pg de PETN, 30 pg de CL-20 et 150 pg de NC13.49. ***En extrapolant à une vitesse de chauffe de 1 000 000 °C/s, nous devrions être capable de détecter 0.6 pg de RDX, 0.6 pg de PETN, 0.04 pg de CL-20 et 0.2 pg de NC13.49.***

En terme de ***sensibilité***, la nanocalorimétrie possède ***une bonne sensibilité*** comparée aux autres techniques si nous extrapolons nos résultats à une vitesse de chauffe d'un million de °C/s. Cependant, le meilleur appareil de détection d'explosifs développé jusqu'à présent (Fido XT) a la même limite de détection que le chien et est plus rapide que le chien. Cet appareil peut détecter quelques femtogrammes (10^{-15} g) d'explosifs en seulement 30s.

En terme de ***sélectivité***, la différentiation des matériaux énergétiques par nanocalorimétrie est possible à des vitesses de chauffes élevées (DC mode), sinon les explosifs sont sublimés pendant les expériences en mode AC. ***La différentiation est possible grâce aux transitions thermiques présentes dans les matériaux énergétiques pendant les expériences de nanocalorimétrie,*** il est donc nécessaire d'effectuer un screening des explosifs existants pour pouvoir les différencier par la suite. Dans le cas d'un échantillon inconnu, un pic très exothermique lors d'une chauffe à vitesse élevée peut prouver que l'échantillon est un explosif.

En terme de ***préparation d'échantillon***, l'échantillon doit être placé au centre de la membrane. Le capteur nanocalorimétrique utilisé dans cette étude peut analyser seulement des échantillons sous forme solide. Une autre difficulté vient du fait que l'échantillon ne doit pas bouger pendant l'analyse : toutes les perturbations externes (électrostatique, flux d'air, vent) doivent être évité aussi bien que les contraintes internes présentes dans la particule.

Pour le moment, l'appareil Fido-XT reste la meilleure méthode pour la détection de matériaux énergétiques. En effet, c'est un appareil avec une sensibilité élevée (détection de quelques femtogrammes), portable, facile à manipuler et il peut être fixé sur un robot pour pouvoir désarmer des engins explosifs. ***La nanocalorimétrie est une des techniques pouvant être utilisée dans le futur pour la détection d'explosifs mais des problèmes techniques doivent être résolus.*** Les expériences sur les mélanges de nanoRDX/TNT ont prouvé que le nanocalorimètre peut être utilisé pour analyser aussi des nanoparticules de matériaux énergétiques.

8. APPENDICES

8.1. APPENDICES TO CHAPTER 2

8.1.1. APPENDIX 2.1. DSC curves of RDX in closed crucibles

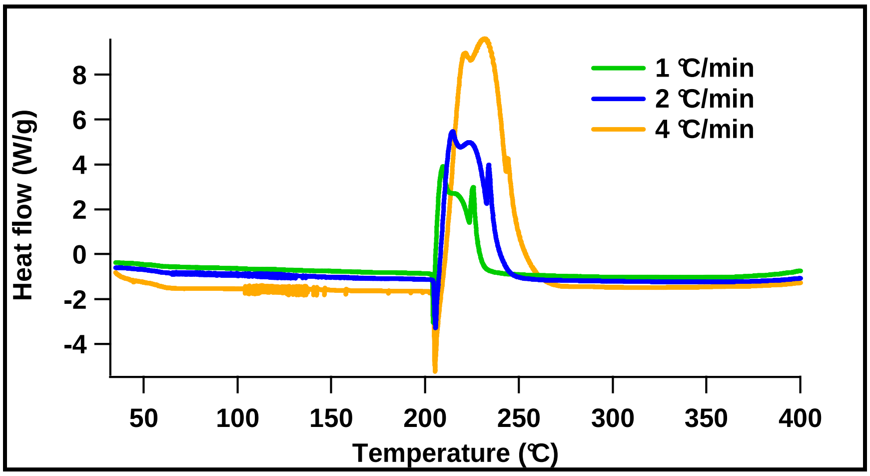

Figure 1. DSC curves of RDX at 1°C/min, 2°C/min and 4°C/min.

Heating rate (°C/min)	$T_{melting}$ (°C)	Melting enthalpy (J/g)	$T_{decomposition}$ (°C)	Decomposition enthalpy (J/g)
1	203.9	92.98	205.2	4688
2	204.6	95.96	207.5	4775
4	204.7	97.72	208.7	5041

Table 1. Melting and decomposition data of RDX.

8.1.2. APPENDIX 2.2. DSC curves of PETN in closed crucibles

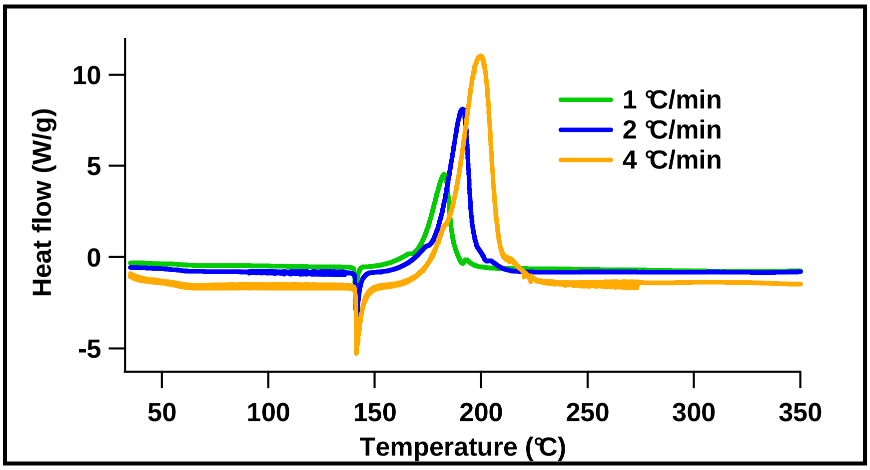

Figure 2. DSC curves of PETN at 1°C/min, 2°C/min and 4°C/min.

Heating rate (°C/min)	$T_{melting}$ (°C)	Melting enthalpy (J/g)	$T_{decomposition}$ (°C)	Decomposition enthalpy (J/g)
1	140.5	154.22	171	3838
2	140.8	164.56	179	3840
4	141	152.61	184	3750

Table 2. Data on melting and decomposition of PETN.

8.1.3. APPENDIX 2.3. DSC curves of CL-20 in closed crucibles

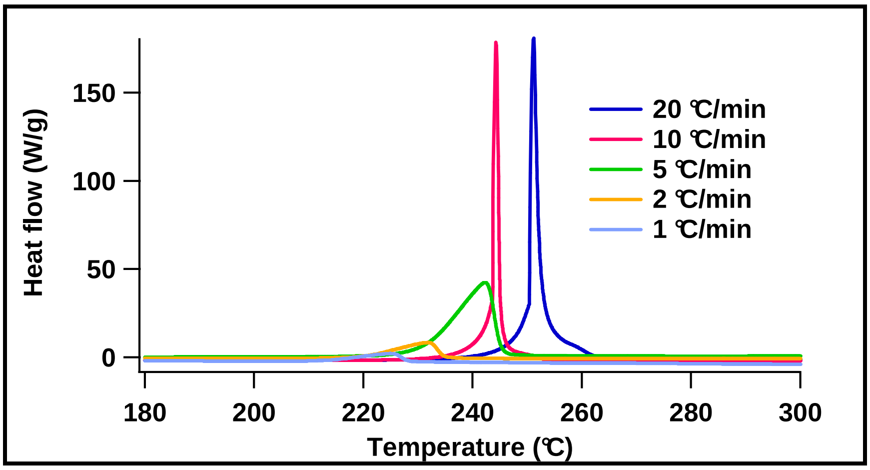

Figure 3. DSC curves of CL-20 at 1°C/min, 2°C/min, 5°C/min, 10°C/min and 20°C/min.

Heating rate (°C/min)	$T_{decomposition}$ (°C)	Decomposition enthalpy (J/g)
1	200	2707
2	205	2575
5	216	4542
10	225	1480
20	231	1200

Table 3. Decomposition temperature and enthalpy of CL-20.

8.1.4. APPENDIX 2.4. DSC analysis of nitrocellulose in closed crucibles

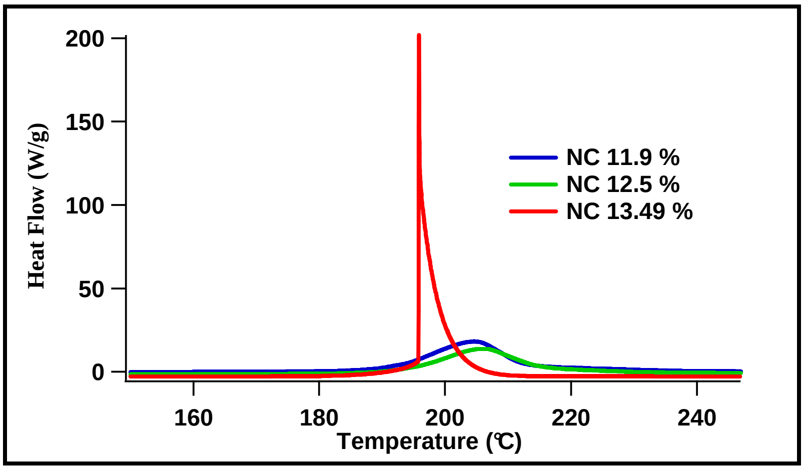

Figure 4. DSC curves of the three grades of nitrocellulose measured at 10°C/min.

Nitrocellulose	$T_{decomposition}$ (°C)	Decomposition enthalpy (J/g)
NC 11,9 %	192.1	1767
NC 12,5 %	193.6	1518
NC 13,49 %	195.5	2308

Table 4. Decomposition temperature and enthalpy of the three nitrocellulose grades.

8.1.5. APPENDIX 2.5. Resonance curves of the used AFM cantilevers

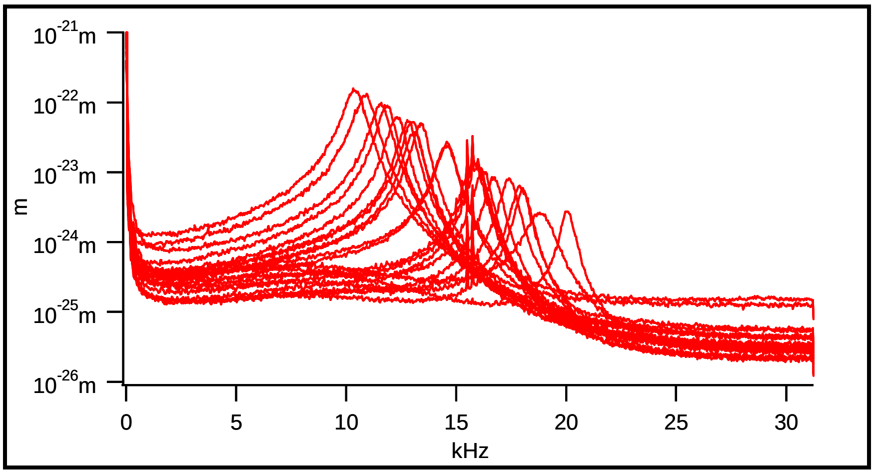

Figure 5. Resonant frequency of cantilevers D.

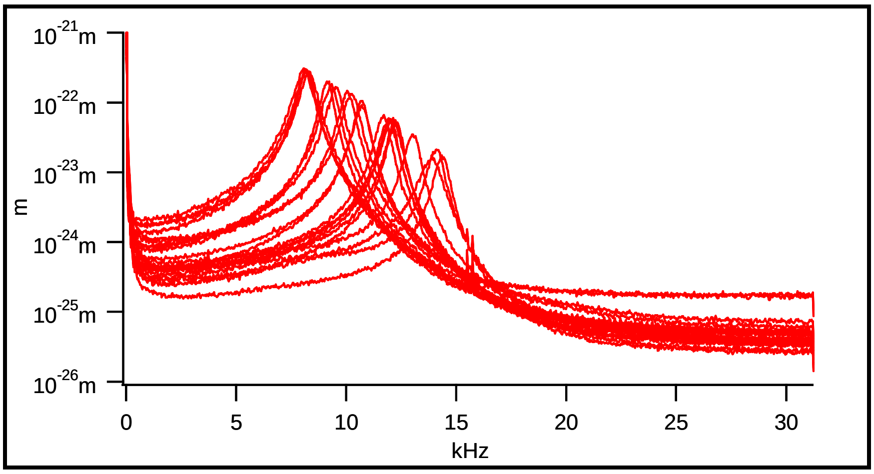

Figure 6. Resonant frequency of cantilevers E.

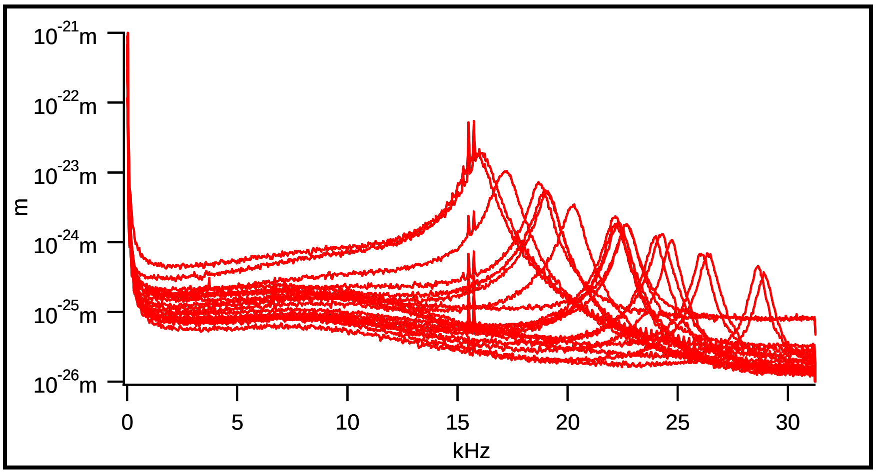

Figure 7. Resonant frequency of cantilevers D

8.2. APPENDICES TO CHAPTER 3

8.2.1. APPENDIX 3.1. Two ways to measure the heater resistance

The simple measurement of the resistance is termed “static resistance” and is noted T_{htr}. For a precise measurement of the heater resistance a trimming resistor circuit has been implemented (cf figure 1). R_1 is an external variable resistor and R_2 is the internal heater of the sensor.

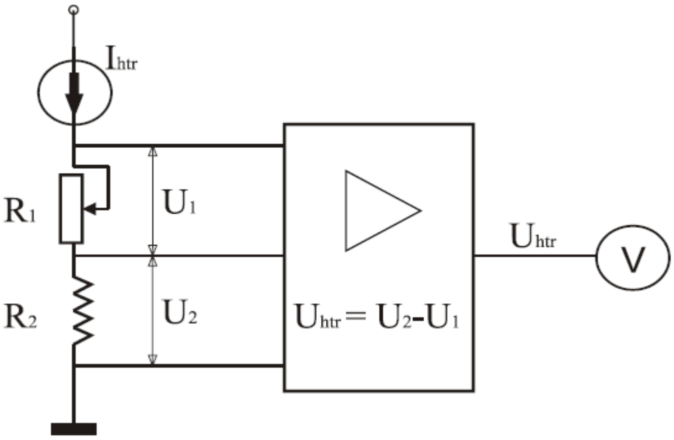

Figure 1. Trimming resistance scheme designed to measure the temperature of the heater.

At the minimum temperature and minimum current (I_{htr}) the user should set R_1 value equal to R_2 (as $U_{htr} = 0$). As the resistance of heater R_2 will increase almost linearly with temperature the value $R_{htr} = U_{htr} / I_{htr}$ will be proportional to the heater temperature.

The second way to measure heater temperature consists in performing AC experiments. This is done by applying a modulating current and measuring the voltage signal on the U_{htr} output. The relation of the RMS amplitudes of voltage and current modulation is proportional to the heater resistance, which is called dynamic and noted T_{htrd}.

8.2.2. APPENDIX 3.2. Circuitry of the sensor holder

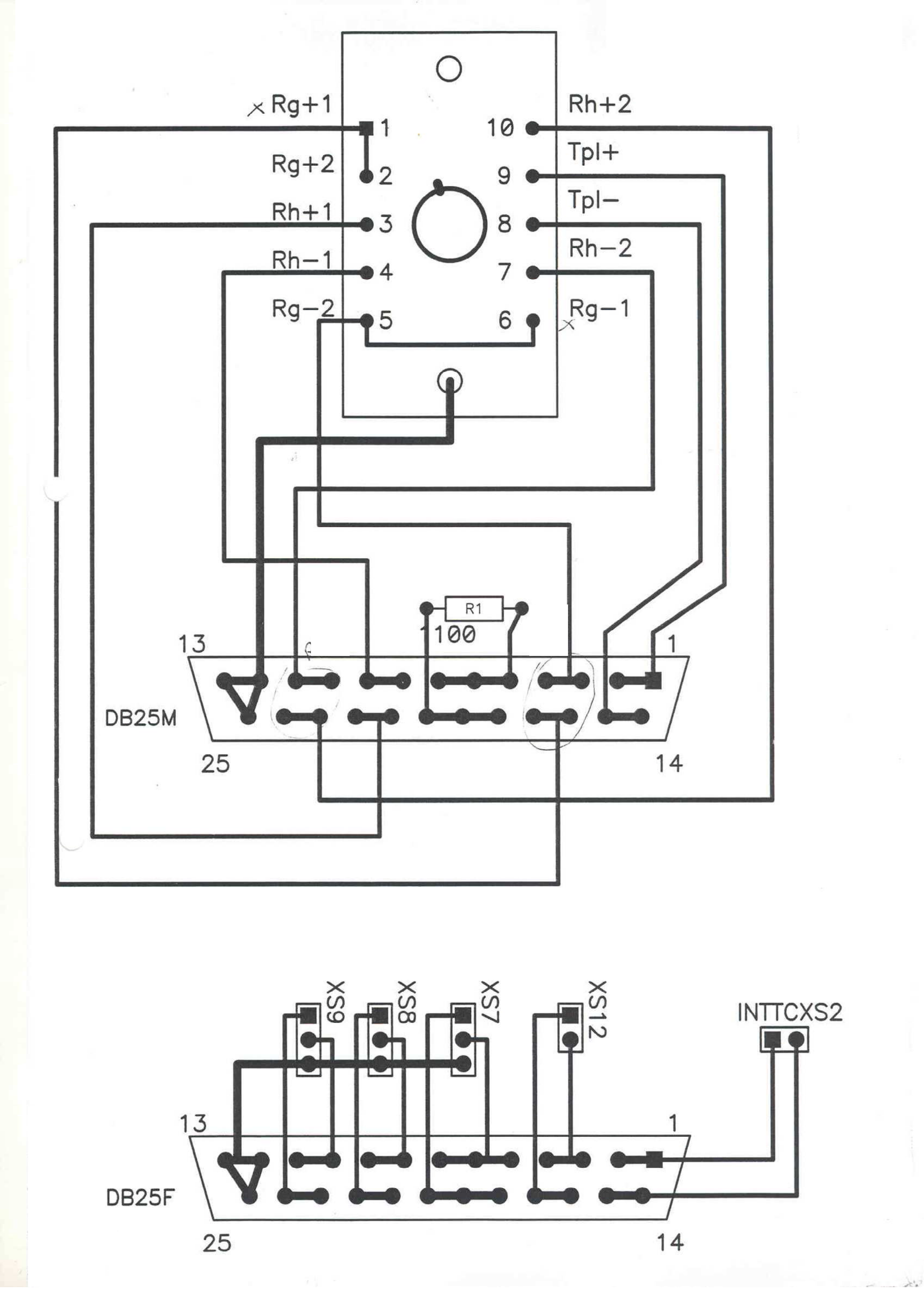

8.2.3. APPENDIX 3.3 Determination of the spring constant for several tipless cantilevers

The following figures were used to compute the spring constant of the cantilevers. On the graphs, the parameter *a* stands for the inverse of the effective mass of the cantilever in nanograms, *b* is the spring constant of the cantilever in 10^{-2} N/m.

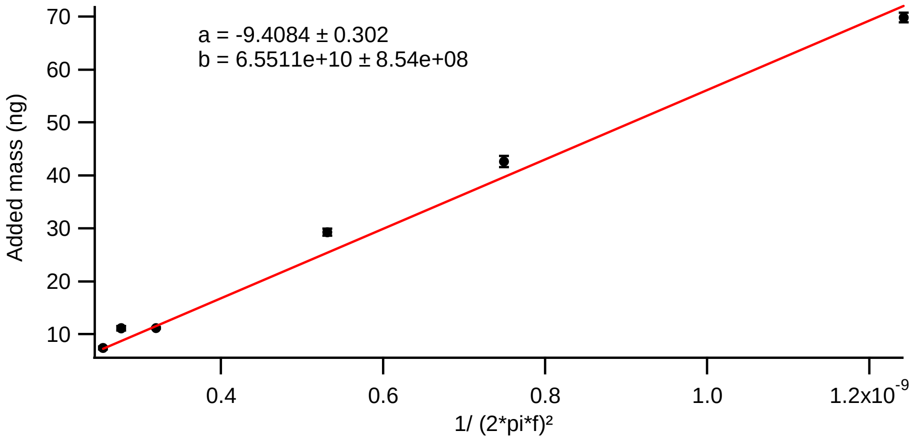

Figure 2. Spring constant and effective mass for cantilever 4E.

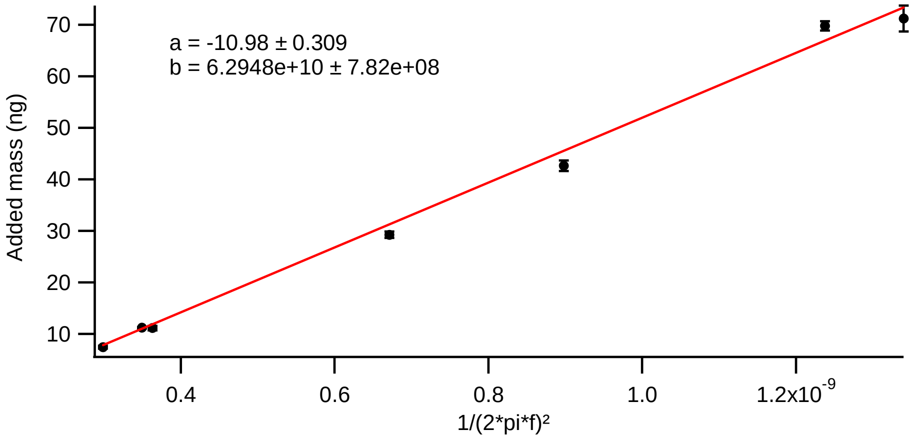

Figure 3. Spring constant and effective mass for cantilever 5E.

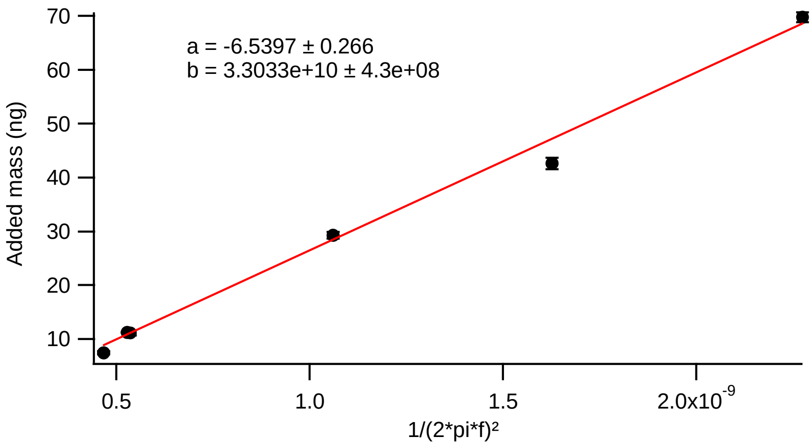

Figure 4. Spring constant and effective mass for cantilever 11E.

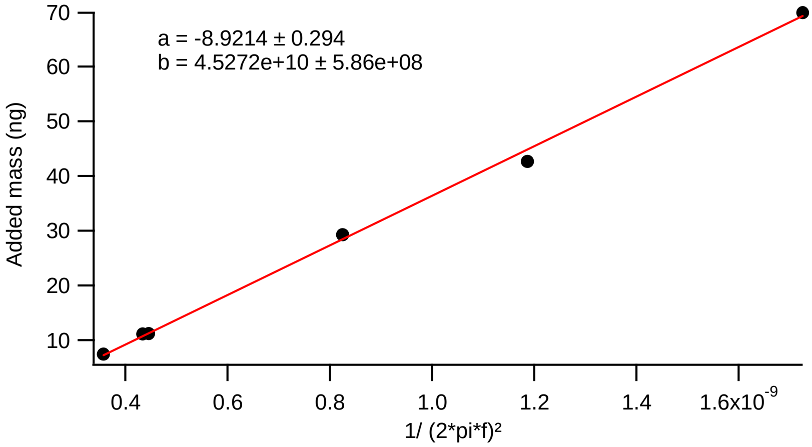

Figure 5. Spring constant and effective mass for cantilever 12E.

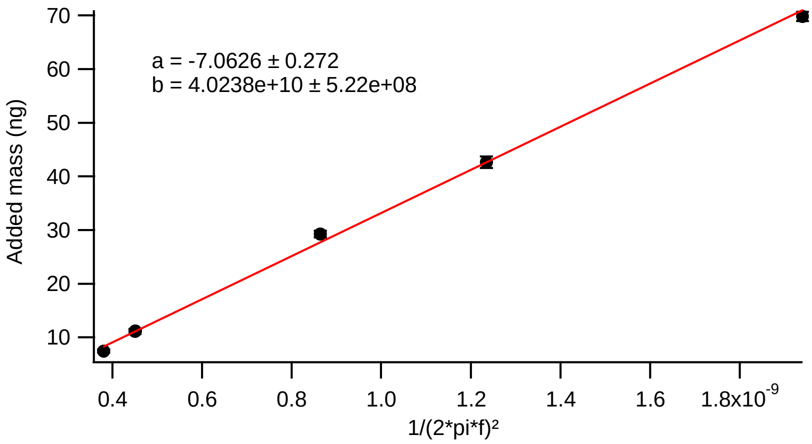

Figure 6. Spring constant and effective mass for cantilever 13E.

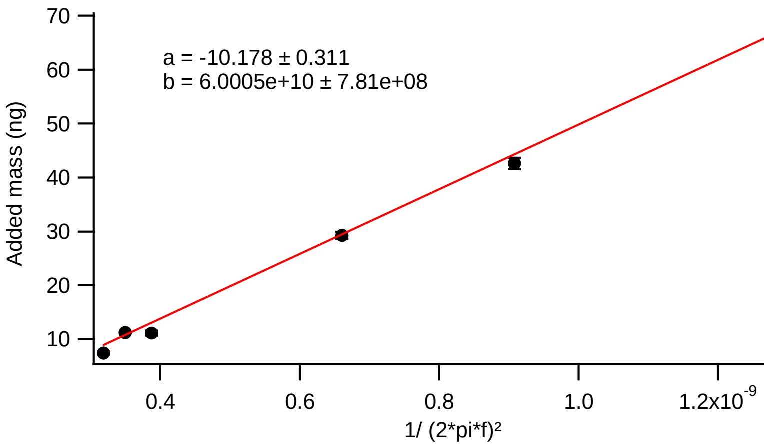

Figure 7. Spring constant and effective mass for cantilever 14E.

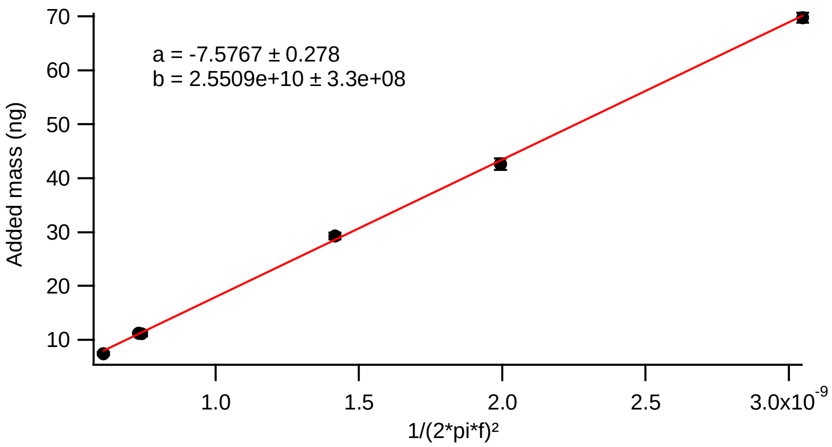

Figure 8. Spring constant and effective mass for cantilever 21E.

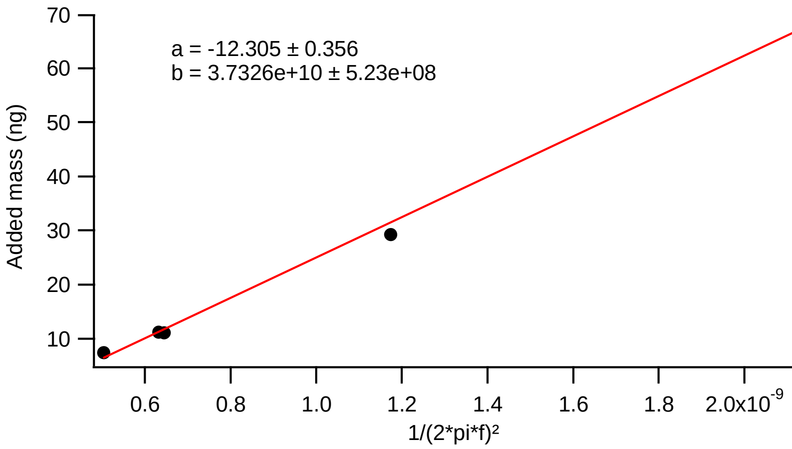

Figure 9. Spring constant and effective mass for cantilever 23E.

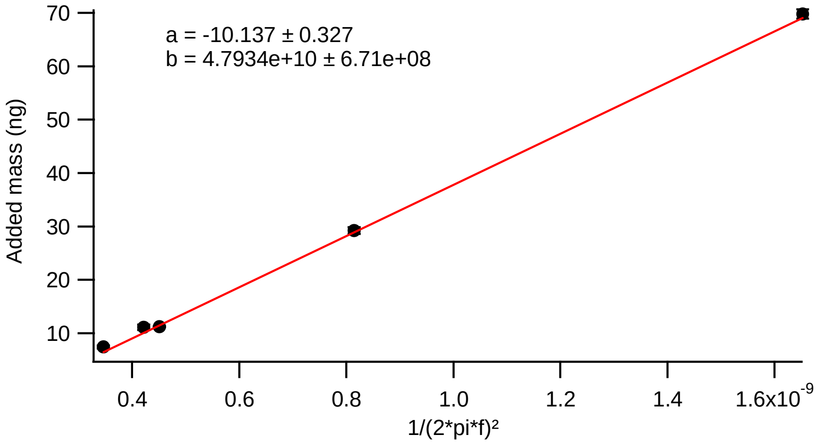

Figure 10. Spring constant and effective mass for cantilever 29E.

8.2.4. *APPENDIX 3.4. Comparison of the different methods of mass determination*

The mass of an indium particle is determined by three methods. The first one used the frequencies of a tipless cantilever loaded with the particle and of the same cantilever without the particle. This method is used for unknown particle.
The second and third ones are based on calorimetric measurements performed at high heating rates: the particle mass is determined thanks to the melting enthalpy of the particle and thanks to the heat capacity measurement of the particle.

13.99 ± 2.80 ng

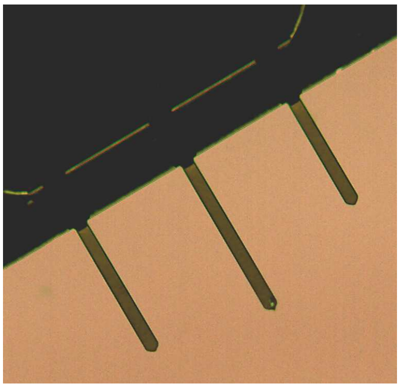

Frequency shift

↑

mass of an In particle

↙ ↘

Melting enthalpy

Heat capacity (C_p)

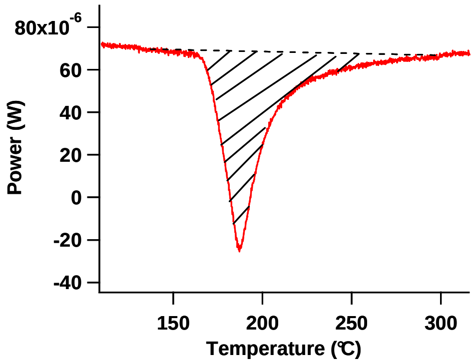

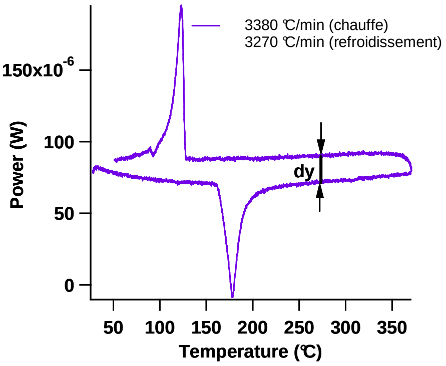

13.20 ± 0.95 ng

11.41 ± 0.90 ng

We observe that the three methods are in good agreement with each other.

8.3. APPENDIX TO CHAPTER 4

8.3.1. APPENDIX 4.1. Isoconversional method.[1-2]

Aim: determination of the activation energy for each conversion of the reaction.

Assumption: a single-step kinetic equation (1) is applicable only to a narrow temperature region.

$$\frac{d\alpha}{dt} = k(T)f(\alpha) \qquad (1)$$

α is the conversion, T is the temperature, f(α) is the reaction model and t is the time.

The rate k(T) in (1) is replaced by the Arrhenius equation:

$$\frac{d\alpha}{dt} = A\exp\left(-\frac{E_a}{RT}\right)f(\alpha) \qquad (2)$$

where A is the pre-exponential factor, E_a is the activation energy.

The isoconversional principle states that at a constant extent of conversion, the reaction rate is only a function of temperature. According to this principle, eq. (2) becomes:

$$\left[\frac{d\ln\left(d\alpha/dt\right)}{dT^{-1}}\right]_\alpha = -\frac{E_\alpha}{R} \qquad (3)$$

Experimentally, several experiments are performed in DSC by varying either the heating rates or the isothermal temperature, in this way we obtain data on varying rates at a constant conversion. Thanks to this method, the kinetics of a complex process can be separated in several single-step kinetic equations.

The rearrangement of equation (2) leads to the following equation:

$$\ln\left(\frac{d\alpha}{dt}\right)_{\alpha,i} = \ln[A_\alpha f(\alpha)] - \frac{E_\alpha}{RT_{\alpha,i}} \qquad (4)$$

---

[1] Vyazovkin, S.; Sbirrazzuoli, N. *Macromolecular rapid communications* **2006**, *27*, 1515 – 1532.

[2] Vyazovkin, S.; Wight, C.A. *Thermochimica Acta* **1990**, *340 – 341*, 53 – 68.

Equation (4) is the foundation of the **differential isoconversional method** of Friedman, i is the different heating rates. The Friedman method is applied to integral data, it requires numerical differentiation of the experimental α versus T curves that results in quite noisy data and, thus, unstable E_α values. This problem is avoided by using **integral conversional method**.

The integration of equation (2) gives:

$$g(\alpha) \equiv \int_0^\alpha \frac{d\alpha}{f(\alpha)} = A.\exp\left(-\frac{E}{RT}\right)t \qquad (5)$$

where g(α) is the integral form of the reaction model. Rearrangement of equation (5) gives eq. (6):

$$-\ln t_{\alpha,i} = \ln\left[\frac{A_\alpha}{g(\alpha)}\right] - \frac{E_\alpha}{RT_i} \qquad (6)$$

The E_α dependence is determined from isothermal runs performed at different temperatures T_i.

For nonisothermal conditions, the equation (7) is used:

$$\ln\left(\frac{\beta_i}{T_{\alpha,i}^2}\right) = const. - \frac{E_\alpha}{RT_{\alpha,i}} \qquad (7)$$

8.4. APPENDICES OF CHAPTER 5

8.4.1. APPENDIX 5.1. Nanocalorimeter – AFM

The combination of the Nanocalorimeter and Multimode AFM is presented on figure 1.

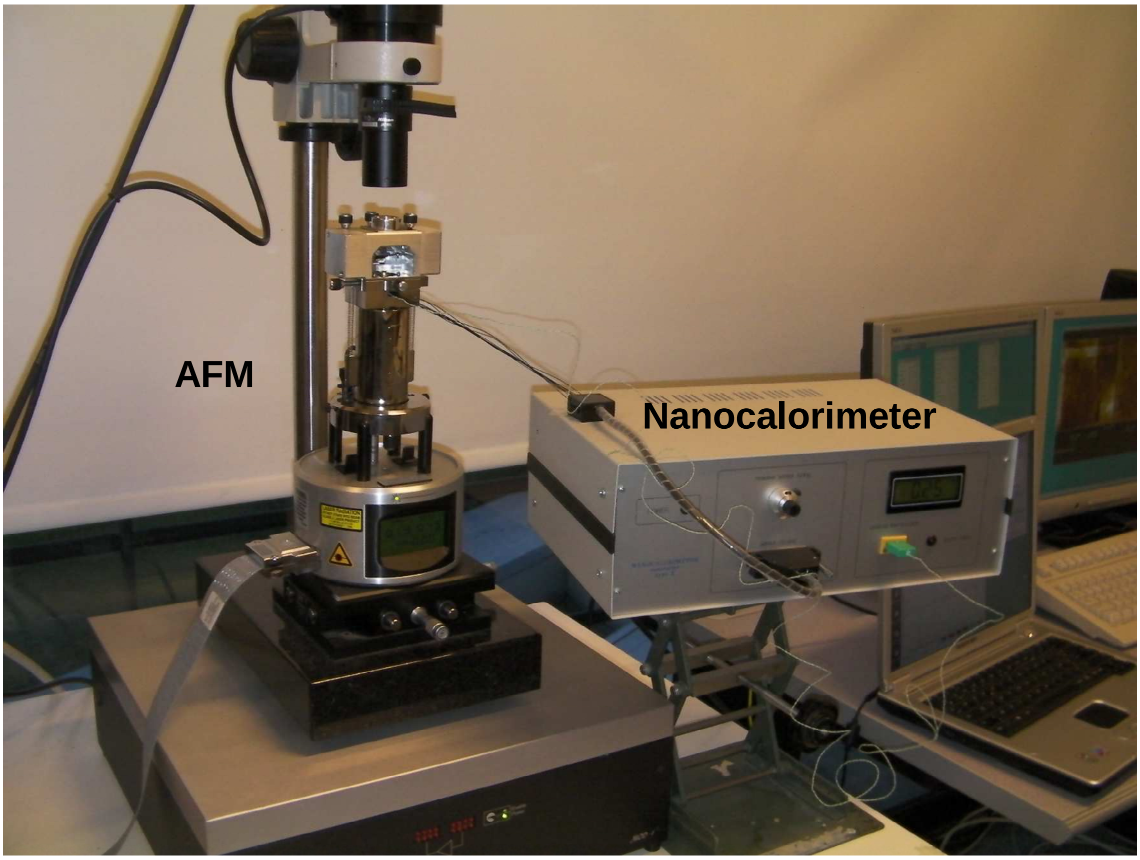

Figure 1. Nanocalorimeter coupled to AFM

The nanocalorimetric chip is placed in the AFM as shown on figure 2.

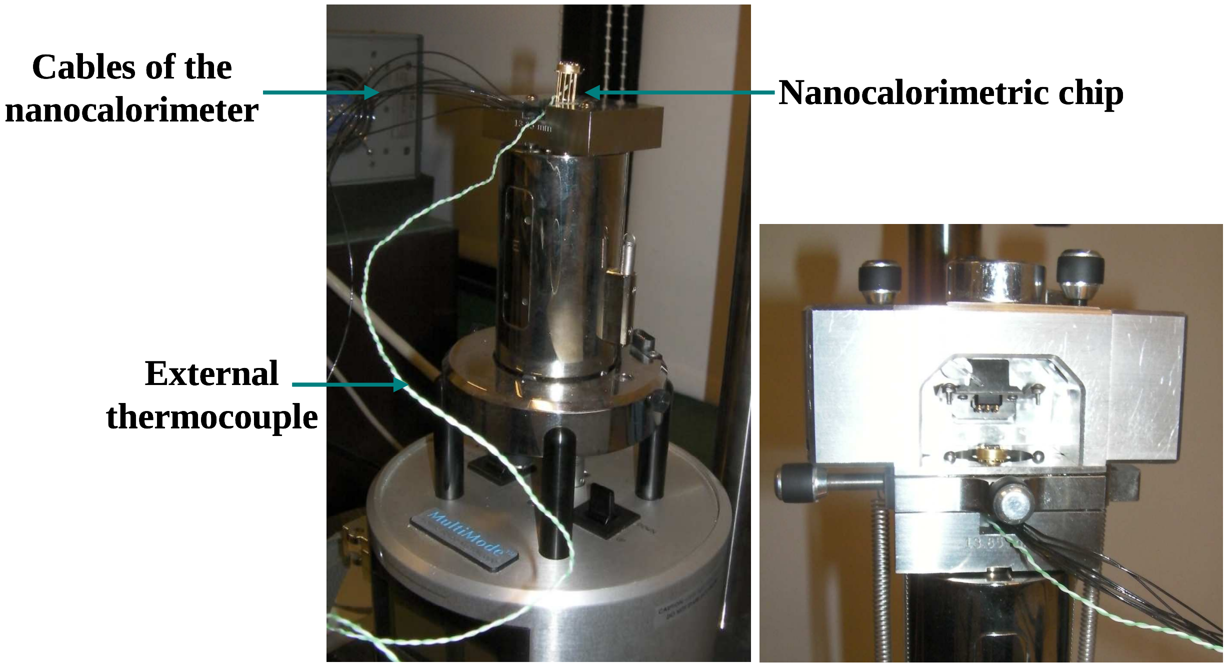

Figure 2. Nanocalorimetric chip in the AFM.

To understand what happens with the nitrocellulose film during a heating ramp, we performed AFM images after nitrocellulose spin-coating deposition (figure 3), after heating ramp at 150°C (figure 4), 200°C (figure 5) and after decomposition of nitrocellulose (figure 6).

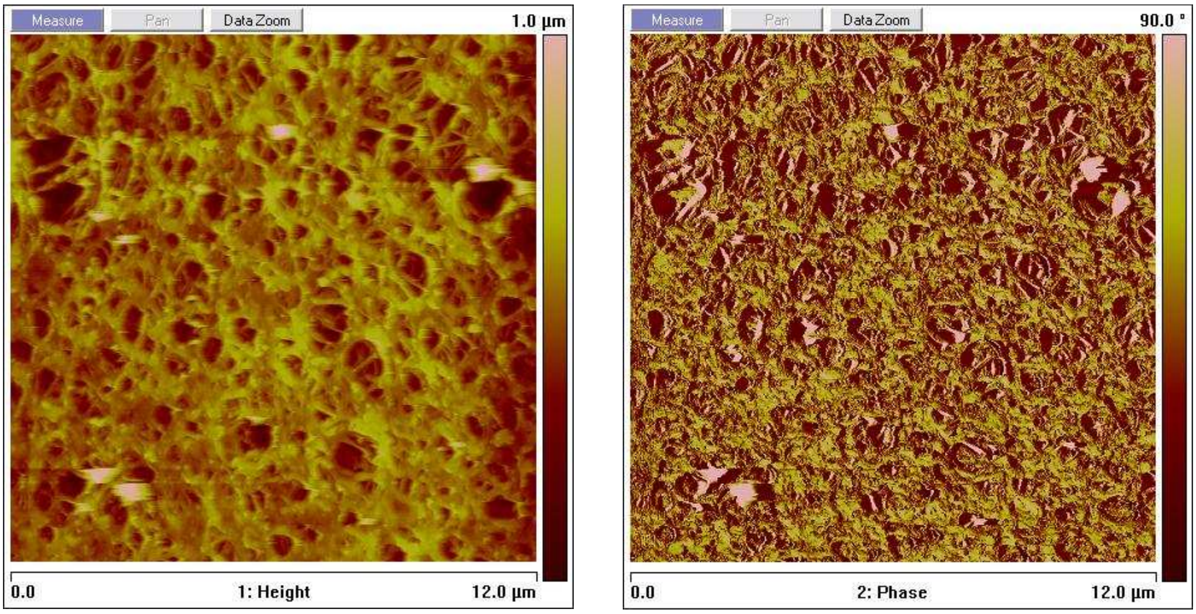

Figure 3. Tapping mode AFM topographic and phase images of a NC13.49 spin-coated film at 25°C.

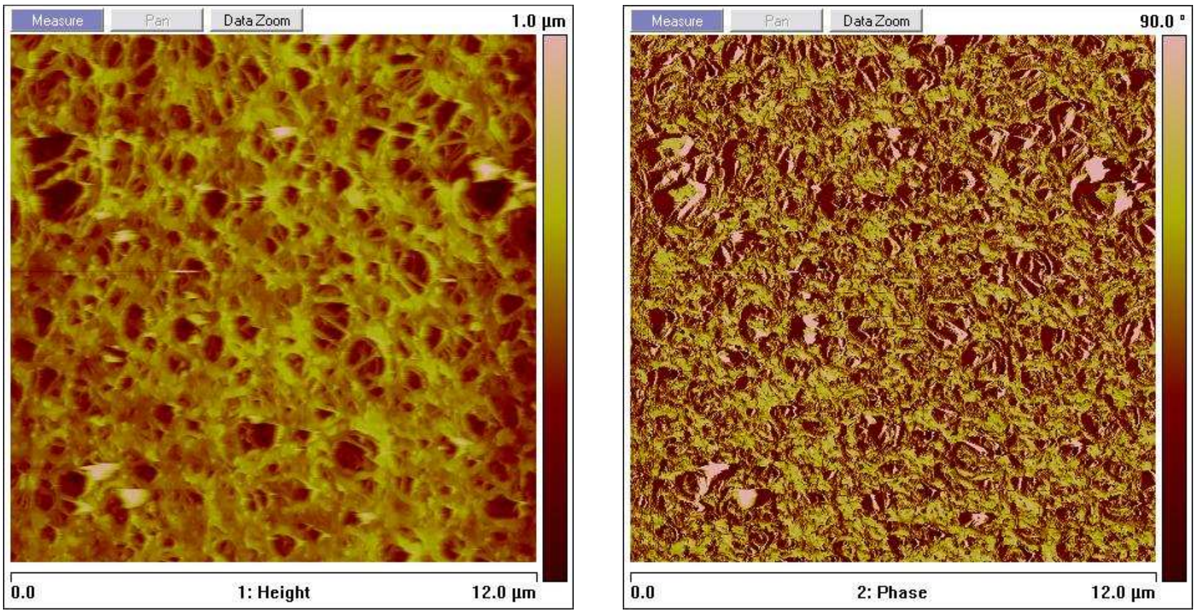

Figure 4. Tapping mode AFM topographic and phase images of a NC13.49 spin-coated film at 150°C.

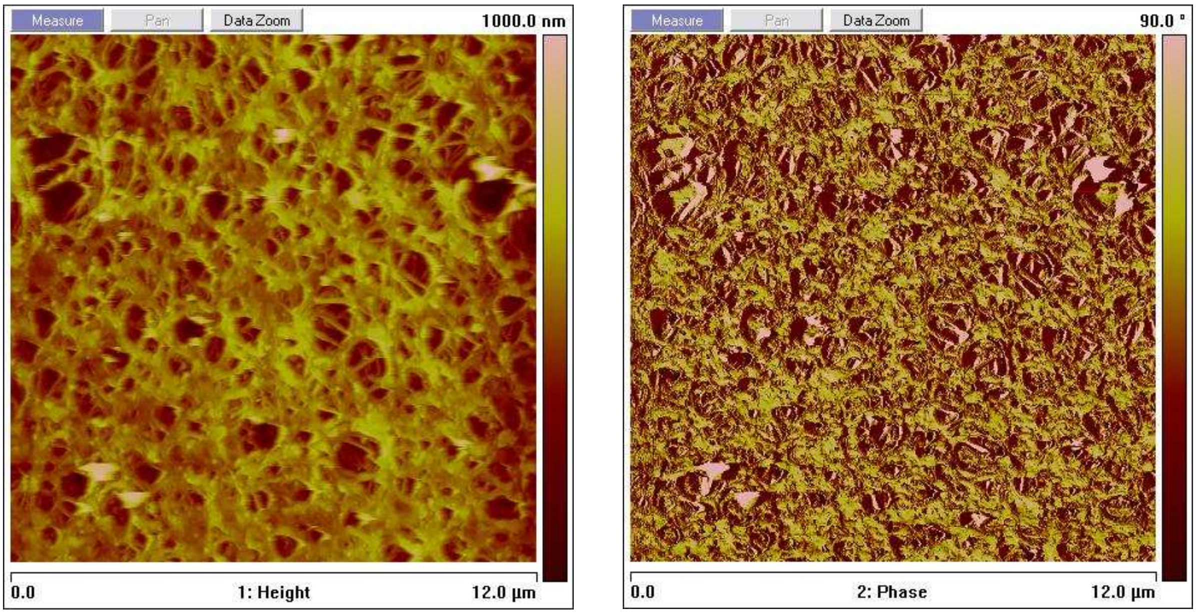

Figure 5. Tapping mode AFM topographic and phase images of a NC13.49 spin-coated film at 200°C.

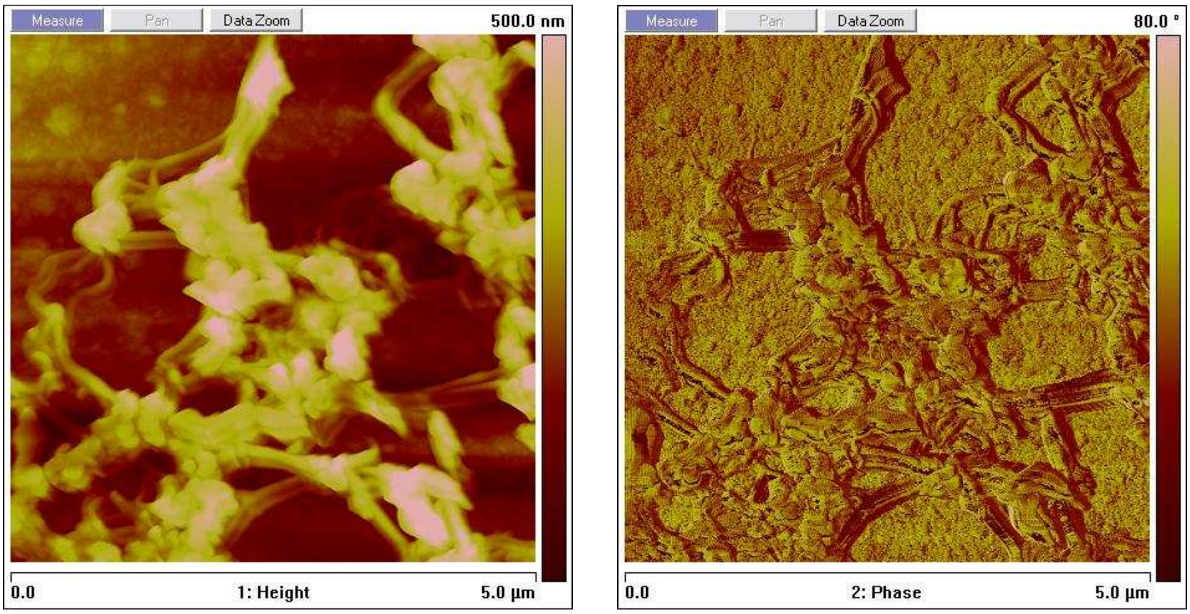

Figure 6. Tapping mode AFM topographic and phase images of a sensor membrane after decomposition of NC13.49.

The AFM micrographs on figures 3, 4, 5 show that the nitrocellulose film morphology does not change after heating ramp at 150°C and 200°C with a heating rate of 20°C/min. The images of the membrane obtained after decomposition of NC13.49 (figure 6) show a residue of the nitrocellulose decomposition on the surface. The heating ramp was performed until 250°C.